

SUPERCAPACITOR ELECTRODE MATERIALS FROM HIGHLY POROUS
CARBON NANOFIBERS WITH TAILORED PORE DISTRIBUTIONS

by

Nimali Chathurika Abeykoon

APPROVED BY SUPERVISORY COMMITTEE:

John P. Ferraris, Chair

Kenneth J. Balkus Jr.

Mihaela C. Stefan

Ronald A. Smaldone

Copyright 2017
Nimali Chathurika Abeykoon
All Rights Reserved

To my loving father, mother and my husband, Thilina

SUPERCAPACITOR ELECTRODE MATERIALS FROM HIGHLY POROUS
CARBON NANOFIBERS WITH TAILORED PORE DISTRIBUTIONS

by

NIMALI CHATHURIKA ABHEYKON, BS

DISSERTATION

Presented to the Faculty of
The University of Texas at Dallas
in Partial Fulfillment
of the Requirements
for the Degree of

DOCTOR OF PHILOSOPHY IN
CHEMISTRY

THE UNIVERSITY OF TEXAS AT DALLAS

May 2017

ACKNOWLEDGMENTS

I extend great gratitude to my advisor Dr. John P. Ferraris, for his kind supervision, support and encouragement throughout the research period. I am greatly indebted to him for helping me immensely to make this project a success and gain knowledge and experience through this research period. I also thank my supervisory committee, Dr. Kenneth J. Balkus Jr., Dr. Mihaela C. Stefan and Dr. Ronald A. Smaldone for their helpful suggestions and support. Many thanks go to Dr. Anvar Zakhidov for giving me the opportunity to contribute to some of his research work. Thank you for giving me the opportunity to work with research expertise in the field from Kazakhstan.

I also thank Dr. Manuel Quevedo-Lopez (Department of Materials Science and Engineering) for extending his raman facility to me and Isable Pinter for giving me training on the raman system. I would like to extend my thanks to Dr. Yves Chabal, Dr. Jean-Francois Veyan, and Jeremy Cure (Department of Materials Science and Engineering) for helping with XPS analysis. I also thank Dr. Christina Thompson, Dr. Sajani Basnayake and Sampath Alahakoon for helping with surface area analysis and Dr. Benjamin Batchelor and Dr. Samsuddin Mahmood for helping with TGA-MS analysis and Wijayantha Perera for helping with TEM analysis. My grateful appreciation goes to Dr. Lissa Magel from Solarno for her valuable suggestions. I am grateful to Dr. Jeliza Bonso for teaching me about fabrication of carbon fibers and electrochemical characterizations.

I would also like to acknowledge the past and present Ferraris group members, Dr. Grace Kalaw, Dr. Sumudu Wijenayake, Dr. Pathum Panapitiya, Dr. Dulip Perera, Dr. Emir Hubijar, Sahila Perananthan, Rangana Jayawickramage, Samitha Panangala, Chamaal Karunaweera, Do Nguyen, Juan Garcia for assistance and friendship during this research period. Also, the contributions of my undergraduate (Zoha Khan, Eli Sanchez, Velia Garcia, Mai Khong, John Charlton and

Akshay Walia) and high school (Shashwat Chaturvedi) students to this work is greatly appreciated. Especially, to Zoha, Eli and Velia, Thank you very much helping me with the polymer synthesis. I would like to convey my gratitude to Dr. Winston Layne, Dr. George McDonald and Dr. Hein Nguyen for technical support and guidance whenever I need their help with lab instruments. I would also like to thank the staff of the department of chemistry and biochemistry for their helpfulness and friendliness. To all of my Sri Lankan friends, Thank you all for your friendship and the memorable moments shared together.

To my father Navarathne Abeykoon, my mother Dayawathie Abeykoon, my sister Anusha Abeykoon and my brother Manoj Abeykoon, thank you very much for your endless love and encouragement. Without your help, none of this would have been possible. Above all, I would like to thank my husband, Thilina Weerakoon, for his never-ending love, understanding, wholehearted support and unlimited patience throughout this journey. Thank you for being there always for me and making me stronger to overcome every challenges in my life. Without you, I would not be the person I am today and I will be forever grateful for your presence in my life.

March 2017

SUPERCAPACITOR ELECTRODE MATERIALS FROM HIGHLY POROUS CARBON NANOFIBERS WITH TAILORED PORE DISTRIBUTIONS

Nimali Chathurika Abeykoon, PhD
The University of Texas at Dallas, 2017

Supervising Professor: John P. Ferraris

Environmental and human health risks associated with the traditional methods of energy production (e.g., oil and gas) and intermittency and uncertainty of renewable sources (e.g., solar and wind) have led to exploring effective and alternative energy sources to meet the growing energy demands. Electricity based on energy storage devices are the most promising solutions for realization of these objectives. Among the energy storage devices, electrochemical double layer capacitors (EDLCs) or supercapacitors have become an attractive research interest due to their outstanding performance, especially high power densities, long cycle life and rapid charge and discharge times, which enables them to utilize in many applications including consumer electronics and transportation, where high power is needed. However, low energy density of supercapacitors is a major obstacle to compete with the commercially existing high energy density energy storage device such as batteries. The fabrication of advanced electrodes materials with very high surface area from novel precursors and utilization of electrolytes with higher operating voltages are essential to enhance energy density of supercapacitors. In this work, carbon nanofibers (CNFs) from different polymer precursors with new fabrication techniques are explored to develop

highly porous carbon with tailored pore distributions to match with employed ionic liquid electrolytes (which possess high working voltages), to realize high energy storage capability. Novel electrode materials derived from electrospun immiscible polymer blends and synthesized copolymers and terpolymers were described. Pore distributions of CNFs were tailored by varying the composition of polymers in immiscible blends or varying the monomer ratios of copolymer or terpolymers.

Chapter 1 gives the detailed introduction of supercapacitors including history and storage principle of EDLCs, fabrication of carbon nanofiber based electrodes and electrolytes employed for EDLCs. It also explains the necessity and the advantages of tailored high surface area nanofibers as an electrode materials for supercapacitors.

Chapter 2 describes the preparation of high surface area carbon nanofibers using polymer blends containing PAN and PMMA and introduces an effective and simple strategy to improve the surface area of CNFs by using a sacrificial polymer, PMMA.

Chapter 3 describes blending of high fractional free volume polymer, 6FDA-DAM: DABA (3:2) into PBI to increase surface area and by using the higher etch rate of 6FDA-DAM: DABA in the blend to optimize pore distribution of CNFs.

Chapter 4 introduces a novel approach to increase surface area of CNFs without any physical or chemical activation by using an *in situ* porogen containing copolymer P(AN-*co*-IA). The concept developed here avoids unnecessary and complex extra activation steps when fabricating carbon nanofibers which leads to lower char yield and uncontrollable pore sizes.

Chapter 5 describes enhancement of surface area by using terpolymer P(AN-VIM-IA) to develop a new precursor. This approach is further advantageous since terpolymer can combine superior electrochemical properties of homopolymer, PAN and P(AN-*co*-IA) and P(AN-*co*-VIM).

Chapter 6 describes the use of commercially available small molecule compatibilizer 2-MI to tailor pore architecture of carbon fiber derived from the immiscible blend of PBI/6FDD to match with the ion sizes of ionic liquid electrolytes thereby increasing the surface area of the CNFs that is accessible to electrolytes.

TABLE OF CONTENTS

ACKNOWLEDGMENTS.....	v
ABSTRACT	vii
LIST OF FIGURES.....	xiii
LIST OF TABLES.....	xx
CHAPTER 1 INTRODUCTION	1
1.1 Electrochemical double layer capacitors (EDLCs).....	3
1.2 Electrode materials for supercapacitors	7
1.3 Carbon fiber manufacturing process	9
1.4 Electrolytes for EDLCs.....	12
1.5 References	15
CHAPTER 2 SUPERCAPACITOR PERFORMANCE OF CARBON NANOFIBER ELECTRODES DERIVED FROM IMMISCIBLE PAN/ PMMA POLYMER BLENDS	20
2.1 Abstract	21
2.2 Introduction.....	21
2.3 Experimental	24
2.4 Results and discussion	27
2.5 Conclusion	41
2.6 References.....	42
CHAPTER 3 NOVEL BINDER-FREE ELECTRODE MATERIALS FOR SUPERCAPACITORS UTILIZING HIGH SURFACE AREA CARBON NANOFIBERS DERIVED FROM IMMISCIBLE POLYMER BLENDS OF PBI/6FDA-DAM:DABA	46
3.1 Abstract	47
3.2 Introduction.....	47
3.3 Experimental	51
3.4 Results and discussion	57
3.5 Conclusion	75
3.6 Appendix - Supporting Information.....	76
3.7 References.....	78

CHAPTER 4 ELECTROSPUN POLY(ACRYLONITRILE- <i>CO</i> -ITACONIC ACID) AS A POROUS CARBON PRECURSOR FOR HIGH PERFORMANCE SUPERCAPACITOR: STUDY OF THE POROSITY INDUCED BY IN SITU POROGEN ACTIVITY OF ITACONIC ACID.....	83
4.1 Abstract	83
4.2 Introduction.....	84
4.3 Experimental	87
4.4 Results and discussion	91
4.5 Conclusion	110
4.6 Appendix - Supporting Information.....	112
4.7 References	115
CHAPTER 5 HIGH SURFACE AREA CARBON NANOFIBER SUPERCAPACITOR ELECTRODES DERIVED FROM AN <i>IN SITU</i> POROGEN CONTAINING TERPOLYMER: POLY(ACRYLONITRILE- <i>CO</i> -1-VINYLMIDAZOLE- <i>CO</i> -ITACONIC ACID)	118
5.1 Abstract	118
5.2 Introduction.....	119
5.3 Experimental	122
5.4 Results and discussion	127
5.5 Conclusion	140
5.6 Appendix - Supporting Information.....	141
5.7 References	147
CHAPTER 6 COMPATIBILIZATION OF IMMISCIBLE POLYMER BLENDS USING SMALL MOLECULES TO TAILOR PORE DISTRIBUTION OF CARBON FIBERS FOR SUPERCAPACITOR ELECTRODES.....	151
6.1 Abstract	151
6.2 Introduction.....	152
6.3 Experimental	155
6.4 Results and discussion	160
6.5 Conclusion	174
6.6 Appendix - Supporting Information.....	176
6.7 References	180

BIOGRAPHICAL SKETCH.....	183
CURRICULUM VITAE	

LIST OF FIGURES

Figure 1.1. Ragone plot showing energy density vs. power density for various energy storage devices.....	2
Figure 1.2. Spider chart showing relative features of select energy storage devices.....	3
Figure 1.3. Schematic diagram of a conventional capacitor.	5
Figure 1.4. Schematic of an electrochemical double-layer capacitor.	6
Figure 1.5. Schematic of electrospinning of nanofibers from precursor solution.	10
Figure 1.6. Custom-built electrospinner.	11
Figure 1.7. Chemical structures of (a) 1-ethyl-3-methylimidazolium bis(trifluoromethane sulfonyl)imide (EMITFSI) and (b) <i>N</i> -butyl- <i>N</i> -methylpyrrolidinium bis(trifluoromethanesulfonyl)imide (PYR ₁₄ TFSI).	15
Figure 2.1. Schematic illustration of the porous carbon nanofiber formation using PAN/PMMA immiscible polymer blends. During carbonization, PMMA decomposes creating pores in PAN nanofibers.....	24
Figure 2.2. SEM images of electrospun (a) neat PAN, (b) PAN:PMMA (95:5), (c) PAN:PMMA (90:10) and (d) PAN:PMMA (75:25) nanofiber mats.	28
Figure 2.3. SEM images of carbon nanofiber mats of (a) neat PAN, (b) PAN:PMMA (95:5) , (c) PAN:PMMA (90:10) and (d) PAN:PMMA (75:25).....	29
Figure 2.4. SEM images of carbon nanofiber mats from (a) neat PAN, (b) PAN:PMMA (95:5), (c) PAN:PMMA (90:10) and (d) PAN:PMMA (75:25).....	30
Figure 2.5. SEM images of the surface morphology of the PMMA extracted (a) PAN:PMMA (95:5) (b) PAN:PMMA (90:10) and (c) PAN:PMMA (75:25) films.	30
Figure 2.6. (a) TGA analysis and (b) FTIR analysis of PMMA, as-spun mat of PAN and blends.	31
Figure 2.7. Raman spectra of CNFs derived from (a) neat PAN (b) PAN:PMMA (95:5) (c) PAN:PMMA (90:10) and (d) PAN:PMMA (75:25).....	33

Figure 2.8. Nitrogen adsorption–desorption isotherms and (b) pore size distribution for CNFs derived from (a) PAN, (b) PAN/PMMA (95:5), (c) PAN/PMMA (90:10) and (d) PAN/PMMA (75:25).....	34
Figure 2.9. Cyclic voltammograms of carbonized nanofibers derived from (a) PAN, (b) PAN/PMMA (95:5), (c) PAN/PMMA (90:10) and (d) PAN/PMMA (75:25).	36
Figure 2.10. (a) Ragone plots (b) galvanostatic discharging curves at a constant current density of 1 A g^{-1}	38
Figure 2.11. Nyquist plots for the CNF samples prepared from the PAN and PAN/PMMA blends in EMITFSI ionic electrolyte.	39
Figure 2.12. Capacitance retention of PAN : PMMA (95 : 5) over 1000 charge/discharge cycles at a current density of 1 A g^{-1}	41
Figure 3.1. Schematic illustration of the fabrication of the phase separated nanofibers using PBI/6FDD polymer blends and structures of PBI and 6FDD.....	51
Figure 3.2. Carbonization and CO_2 activation protocol.	54
Figure 3.3. SEM images of electrospun (a) PBI, (b) PBI:6FDD(90:10), (c) PBI:6FDD(70:30) and (d) PBI:6FDD(50:50) nanofiber mats.	58
Figure 3.4. SEM images of carbonized and activated (a) PBI, (b) PBI:6FDD(90:10), (c) PBI:6FDD(70:30) and (d) PBI:6FDD(50:50) nanofiber mats.	59
Figure 3.5. SEM images of the cross-section of the 6FDD extracted (a) PBI:6FDD(70:30) and (c) PBI:6FDD(50:50) films that were cast directly from electrospinning solutions and TEM images of electrospun fiber of (b) PBI:6FDD(70:30) and (d) PBI:6FDD(50:50).	60
Figure 3.6. TEM images of electrospun (a) PBI, (b) PBI:6FDD(90:10), (c) PBI:6FDD(70:30), (d) PBI:6FDD(50:50) nanofibers and carbonized and activated (e) PBI, (f) PBI:6FDD(90:10), (g) PBI:6FDD(70:30), (h) PBI:6FDD(50:50) nanofibers.	61
Figure 3.7. TGA analysis (a) of as-spun mat of PBI and blends (b) and FTIR analysis.	62
Figure 3.8. Raman spectra of CNFs derived from (a) PBI, (b) PBI:6FDD(90:10), (c) PBI:6FDD(70:30) and (d) PBI:6FDD(50:50).	64
Figure 3.9. XRD patterns of CNFs derived from PBI and PBI:6FDD blends.....	65

Figure 3.10. (a) XPS survey spectra of all CNFs samples (inset , (a) PBI, (b) PBI:6FDD (90:10), PBI:6FDD (70:30) and (d) PBI:6FDD (50:50), High-resolution deconvoluted (b) C 1s, (c) O 1s, and (d) N 1s, XPS spectra of CNFs derived from PBI:6FDD(70:30).	66
Figure 3.11. (a) Nitrogen adsorption/desorption isotherms and (b) pore size distribution for CNFs derived from ((a) PBI, (b) PBI: 6FDD(90:10), (c) PBI:6FDD(70:30) and (d) PBI:6FDD(50:50).	67
Figure 3.12. Cyclic voltammograms of carbonized nanofibers derived (a) PBI, (b) PBI:6FDD (90:10), (c) PBI:6FDD(70:30) and (d) PBI:6FDD(50:50).	70
Figure 3.13. (a) Ragone plots (b) galvanostatic discharging curves at a constant current density of 1 A g^{-1} (c) galvanostatic discharging curves for PBI:6FDD(70:30) at different current densities from 1 to 10 A g^{-1} (d) Nyquist plot of carbonized nanofibers derived from PBI and PBI:6FDD blends with different compositions.	72
Figure 3.14. Specific capacitance retention of PBI:6FDD(70:30) as a function of cycle number.	74
Figure S3.1. Synthesis of 6FDA-DAM:DABA.	76
Figure S3.2. Characterizations of 6FDA-DAM:DABA (a) NMR, (b)TGA and (c) FT-IR.	77
Figure S3.3. High-resolution (a) C 1s, (b) O 1s, and (c) N 1s, XPS spectra of CNFs derived from PBI.	77
Figure S3.4. High-resolution (a) C 1s, (b) O 1s, and (c) N 1s, XPS spectra of CNFs derived from PBI:6FDD(90:10).	78
Figure S3.5. High-resolution (a) C 1s, (b) O 1s, and (c) N 1s, XPS spectra of CNFs derived from PBI:6FDD(50:50).	78
Figure 4.1. Schematic for the strategy of producing porous carbon nanofiber using <i>in situ</i> porogen activity of P(AN- <i>co</i> -IA) copolymer over conventional CO ₂ activation. During carbonization, CO ₂ gases produce by decomposition of itaconic acids, which create pores on nanofibers.	86
Figure 4.2. Synthesis of P(AN- <i>co</i> -IA).	88
Figure 4.3. FTIR analysis of (a) electrospun fibers (b) stabilized fibers of PAN homopolymer and its copolymers with different ratio of IA.	92
Figure 4.4. (a) DSC analysis in N ₂ atmosphere (b) TGA analysis in air atmosphere and (c) TGA analysis in N ₂ atmosphere of electrospun samples.	94

Figure 4.5. SEM images of electrospun (a) PAN (b) P(AN- <i>co</i> -IA)-2 (c) P(AN- <i>co</i> -IA)-5 (d) P(AN- <i>co</i> -IA)-8, carbonized (e) PAN (f) P(AN- <i>co</i> -IA)-2 (g) P(AN- <i>co</i> -IA)-5 (h) P(AN- <i>co</i> -IA)-8, CO ₂ activated (i) PAN (j) P(AN- <i>co</i> -IA)-2 (k) P(AN- <i>co</i> -IA)-5 (l) P(AN- <i>co</i> -IA)-8 fibers.	95
Figure 4.6. The simultaneous TGA -MS spectra of electrospun fibers as a function of IA monomer ratio (a) PAN (b) P(AN- <i>co</i> -IA)-2 (c) P(AN- <i>co</i> -IA)-5 (d) P(AN- <i>co</i> -IA)-8.	98
Figure 4.7. (a) CO ₂ ion intensity and (b) COOH ion intensity of electrospun fibers as a function of IA monomer ratio derived from TGA-MS spectra.	99
Figure 4.8. Raman spectra of (a) CNF and (b) ACNF.	99
Figure 4.9. (a) Nitrogen adsorption/desorption isotherms and (b) pore size distribution for CNFs	101
Figure 4.10. (a) Optical image of flexible carbonized mat derived from copolymer P(AN- <i>co</i> -IA)-8, cyclic voltammograms of CNFs derived from (b) P(AN- <i>co</i> -IA)-2 (c) P(AN- <i>co</i> -IA)-5 (d) P(AN- <i>co</i> -IA)-8.	105
Figure 4.11. (a) Specific capacitance (b) Ragone plot (c) Galvanostatic discharging curves at a constant current density of 1 A g ⁻¹ (d) Nyquist plots for the CNF samples.	106
Figure 4.12. Cyclic voltammograms of ACNFs derived from (a) PAN (b) P(AN- <i>co</i> -IA)-2 (c) P(AN- <i>co</i> -IA)-5 (d) P(AN- <i>co</i> -IA)-8.	108
Figure 4.13. (a) Specific capacitance (b) Ragone plot (c) Galvanostatic discharging curves at a constant current density of 1 A g ⁻¹ (d) Nyquist plots for the ACNF samples.	109
Figure S4.1. ¹ H-NMR analysis of P(AN- <i>co</i> -IA)-2.	112
Figure S4.2. ¹ H-NMR analysis of P(AN- <i>co</i> -IA)-5.	112
Figure S4.3. ¹ H-NMR analysis of P(AN- <i>co</i> -IA)-8.	113
Figure S4.4. SEC analysis of the synthesized polymers.	114
Figure S4.5. Cyclic voltammograms of carbonized nanofibers derived from PAN homopolymer.	114
Figure 5.1. Synthesis of PVI terpolymer.	123

Figure 5.2. SEM images of (a-c) electrospun fibers from (a) PVI-5 (b) PVI-10 (c) PVI-23, (d-f) carbonized nanofiber from (d) PVI-5 (e) PVI-10 (f) PVI-23 (g-i) CO ₂ activated nanofibers from (g) PVI-5 (h) PVI-10 (i) PVI-23 samples.	128
Figure 5.3. FTIR analysis of electrospun samples derived from PVI terpolymers.....	129
Figure 5.4. TGA analysis of PAN homopolymer and electrospun PVI terpolymer samples in (a) air atmosphere and (b) N ₂ atmosphere respectively.	130
Figure 5.5. The simultaneous TGA and mass spectrometry of electrospun terpolymers.	131
Figure 5.6. Raman spectra of (a) CNF and (b) ACNF derived from PVI copolymers.	132
Figure 5.7. Nitrogen adsorption/desorption isotherms and pore size distribution for (a, b) CNFs	133
Figure 5.8. Cyclic voltammograms of CNFs derived from (a) PVI-5 (b) PVI-10 (c) PVI-23 (d) Specific capacitance of CNF derived from PVI terpolymers and PAN homopolymer as a function of the scan rate.	136
Figure 5.9. Cyclic voltammograms of ACNFs derived from (a) PVI-5 (b) PVI-10 (c) PVI-23 (d) Specific capacitance of ACNF derived from PVI terpolymers and PAN homopolymer as a function of the scan rate.	137
Figure 5.10. (a) Ragone plots of electrode materials measured at various current densities (b) Nyquist plots for the samples prepared from both CNFs and ACNFs.	138
Figure S5.1. ¹ H NMR of PVI-5 terpolymer.	142
Figure S5.2. SEC analysis of the synthesized polymers.	143
Figure S5.3. Optical images of the electrospun of PVI-5 nanofiber mat (top) and stabilized nanofiber mats of PVI-5 at different temperature (bottom).	144
Figure S5.4. FTIR analysis of stabilized fibers of PVI-5 at different stabilized temperature. ...	144
Figure S5.5. Cyclic voltammograms of CNF derived from PVI-5 terpolymer stabilized at (a) 220 °C (b) 240 °C (c) 260 °C and (d) Specific capacitance of CNF derived from PVI-5 terpolymers at different stabilization temperatures.	145
Figure S5.6. SEM images of (a) electrospun (b) carbonized (c) CO ₂ activated nanofibers from PAN homopolymer.	146

Figure S5.7. Cyclic voltammograms of CO ₂ activated nanofibers derived from PAN homopolymer (ACNF-PAN).....	147
Figure 6.1. Schematic illustration of for electrospinning PBI:6FDD (50:50) blends with and without small molecule (2-MI) compatibilizers and their corresponding microstructures on fibers.	155
Figure 6.2. SEM images of electrospun fibers derived from (a) BL-0, (b) BL-5 (c) BL-10 and (d) BL-20.	161
Figure 6.3. SEM images of carbonized fibers derived from (a) BL-0, (b) BL-5 (c) BL-10 and (d) BL- 20.	162
Figure 6.4. SEM images of the cross-section of the membranes cast from electrospinning solutions of PBI:6FDD blends compatibilized with (a) 0 wt% (b) 5 wt% (c) 10 wt% and (d) 20 wt% 2-MI after extraction with THF.	163
Figure 6.5. TEM images of electrospun fibers derived from (a) BL, (b) BL-5 (c) BL-10 and (d) BL-20.	164
Figure 6.6. TEM images of carbonized fibers derived from BL-0 (a)100 nm, (b) 20 nm and BL-20	166
Figure 6.7. TGA curves of electrospun fibers derived from blend without 2-MI and blends compatibilized with different weight percentages of 2-MI.....	167
Figure 6.8. Raman spectra of ACNFs derived from (a) BL-0, (b) BL-5 (c) BL-10 and (d) BL-20.....	168
Figure 6.9. Cyclic voltammograms of ACNFs derived (a) BL-0, (b) BL-5 (c) BL-10 and (d) BL-20.....	170
Figure 6.10. (a) Specific capacitance with five different scan rates (b) Ragone plots (c) galvanostatic discharging curves at a constant current density of 1 A g ⁻¹ (d) Nyquist plot of carbonized nanofibers derived from BL with different wt% of 2-MI.	172
Figure S6.1. Synthesis of 6FDA-DAM:DABA(3:2).	176
Figure S6.2. ¹ HNMR spectrum of 6FDD.....	177
Figure S6.3. FTIR spectrum of 6FDD.	177
Figure S6.4. TGA curve of 6FDD.	178

Figure S6.5. Size distribution by intensity of BL-0 and BL-5 using DLS analysis.....	179
--	-----

LIST OF TABLES

Table 2.1. Ratios of peak intensities of CNFs derived from PAN and the PAN/PMMA blends ..	34
Table 2.2. Surface area and pore volume of PAN and PAN/PMMA based carbon nanofibers	35
Table 2.3. Specific capacitance $F\ g^{-1}$ of the CNFs derived from the PAN and the PAN/PMMA blends at five different scan rates.....	37
Table 2.4. Energy densities and the power densities of the CNF derived from PAN and PAN/PMMA blends.....	39
Table 3.1. Average fiber diameter of PBI and the PBI/6FDD blends.	58
Table 3.2. Chemical composition of C 1s, N 1s and O 1s obtained from the XPS spectra.	67
Table 3.3. Surface area and pore volume of PBI and PBI/6FDD based carbon nanofibers	68
Table 3.4. Specific capacitance of the CNFs derived from the PBI and the PBI/6FDD blends at five different scan rates	71
Table 3.5. Energy densities and the power densities of the CNFs derived from PBI and the PBI/6FDD blends at current densities of $1\ A\ g^{-1}$ and $10\ A\ g^{-1}$	73
Table 4.1. Average diameters of electrospun fibers, CNF and ACNF	96
Table 4.2. Surface area and pore volume of PAN and P(AN- <i>co</i> -IA) based CNFs and ACNFs..	103
Table 4.3. Specific capacitance, energy density and power density of carbonized nanofibers (CNFs).....	107
Table 4.4. Specific capacitance, energy density and power density of carbonized nanofibers (ACNFs).....	110
Table S4.1. Molecular weights of the synthesized polymers.....	179
Table 5.1. Average diameters of derived from electrospun fibers, CNF and ACNF of PAN homopolymer and different ratio of PVI terpolymers.	129
Table 5.2. Surface area and pore size analysis of carbonized nanofibers (CNFs) and CO_2 activated carbon nanofibers (ACNFs) derived from PVI terpolymers.....	134

Table 5.3. Electrochemical performance of CNFs and ACNFs electrodes derived from PAN and PVI terpolymers in EMITFSI	139
Table S5.1. Summary of NMR analysis of P(AN-VIM-IA) terpolymers.....	142
Table S5.2. Molecular weights of the synthesized polymers.....	143
Table 6.1. Ratios of peak intensities of ACNFs derived from blends with different ratio of 2-MI.....	169
Table 6.2. Specific capacitance of the ACNFs derived from blends with different ratio of 2-MI at five different scan rates	171
Table 6.3. IR drops obtained for the he ACNFs derived from blends with different ratio of 2-MI.....	173
Table 6.4. Energy densities and the power densities of the CO ₂ activated fibers derived from blends with different loading of 2-MI	174
Table S6.1. Z- Average particle size obtained from DLS analysis.....	179

CHAPTER 1

INTRODUCTION

The traditional methods of energy production using oil and gas are unsustainable due to the ever growing demands of a growing population.¹ Additionally oil and gas production and consumption pose major environmental and human health risks. Furthermore, disadvantages associated with traditional methods of energy production such as depletion of fossil fuel resources, unpredictability of oil price, local pollution and global warming and geopolitical tensions lead to finding effective and alternative energy sources.² Renewable energy sources such as wind and solar energy are being deployed as low cost alternative energy sources to overcome the problem of traditional methods of energy production.³ Also renewable energy sources are also suitable for application in rural areas.⁴ Unfortunately, these renewable energy sources cannot produce energy in times of need because solar can produce energy mostly in the day time and wind can only produce energy while wind is blowing, which is mostly at night.^{5,6} Intermittency and uncertainty of renewable sources disrupt the electrical power grid's operation in a number of ways and have resulted in the search for more efficient energy storage systems which can store the electrical energy from primary sources and effectively meet the peak power demand whenever it is needed.⁷ Consequently, electrochemical devices for energy storage such as batteries, fuel cells, flywheels and supercapacitors have been researched and developed over the last decade to use as more sustainable energy devices.⁸ Among them, the supercapacitor has developed as a new technology with the potential to enable major advances in energy storage.⁹

Batteries produce energy by converting chemical energy to electrical energy via oxidation reduction reactions within voltaic cells.¹⁰ But as demonstrated by the Ragone plot (see Figure 1.1), they have high energy densities but low power density. Supercapacitors have emerged as a potential high power electrochemical device with long cycle life. However, supercapacitors offer higher power densities but lower energy densities than batteries.¹¹

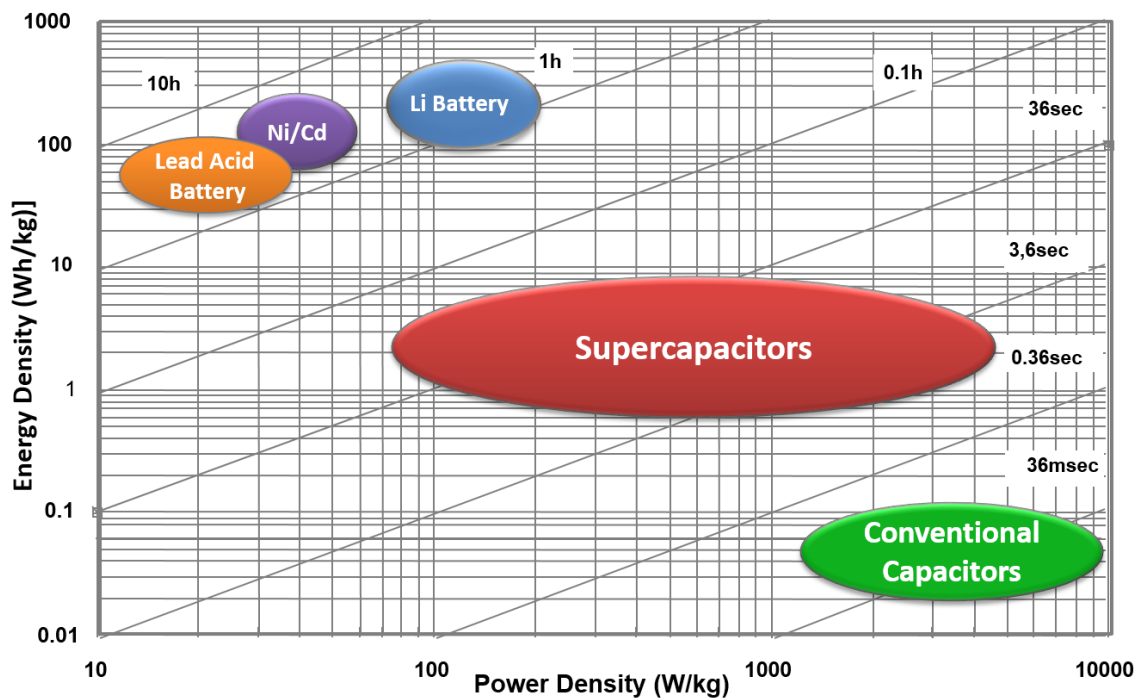


Figure 1.1. Ragone plot showing energy density vs. power density for various energy storage devices.

Figure 1.2 demonstrates a spider plot comparing the characteristics of different energy storage devices.¹² Currently, batteries are the more common energy storage device because of the high energy densities they offer. However, as demonstrated by Figure 1.2, batteries have lower cycle stability, power density, safety, and recycling capability than supercapacitors. On the other hand,

supercapacitors can deliver greater power densities and show long cycle life, have ability to be charged or discharged within a few seconds to milliseconds, have wide working potential and broader temperature range of operation than lithium-ion batteries, though they are unable to store as much energy as batteries.¹³ As a result, supercapacitors are an attractive power solution for an increasing number of applications that require high charge and discharge rates such as consumer electronics, tramways, and energy harvesting systems. Increasing supercapacitor energy density while maintaining capacitance and power density is essential for expanding their feasibility.¹⁴

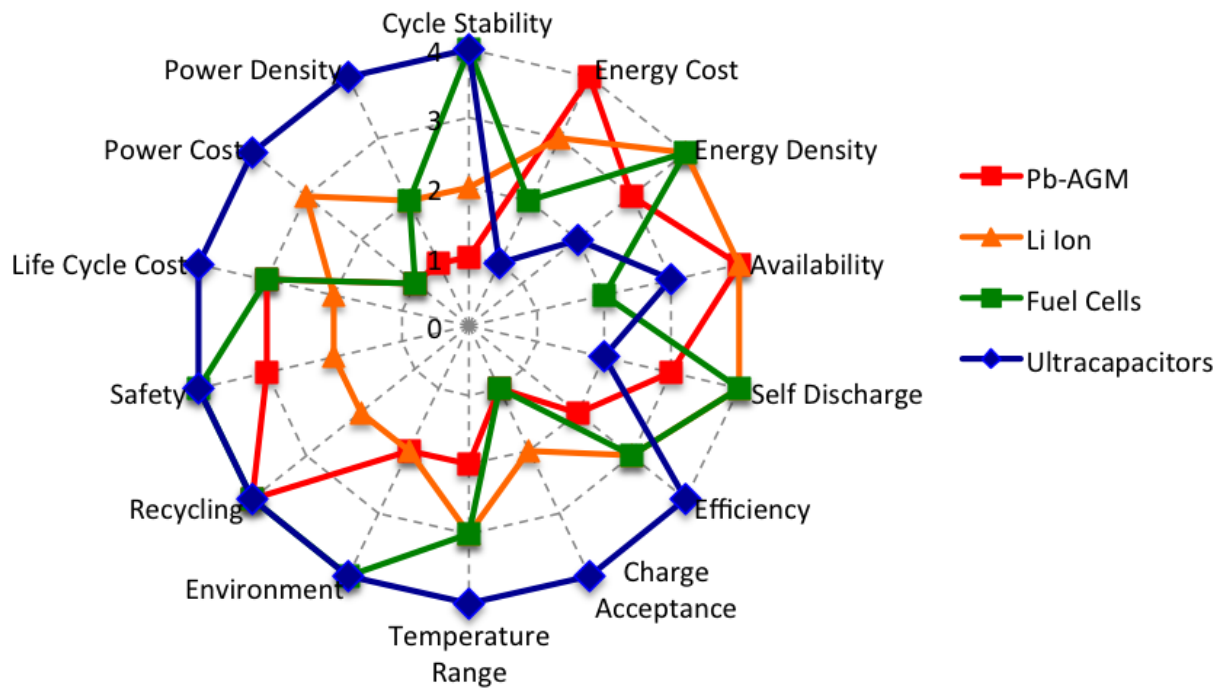


Figure 1.2. Spider chart showing relative features of select energy storage devices.

1.1 Electrochemical double layer capacitors (EDLCs)

Electric double layer capacitors (EDLCs) also known as supercapacitors or ultracapacitors were first made in the 1950s by General Electric using from activated carbon electrodes in an aqueous

electrolyte as described in the 1957 patent by H.I. Becker of General Electric.¹⁵ Unfortunately, General Electric never commercialized this work because of impracticability this device since both electrodes needed to be immersed in a container of electrolyte as a flooded battery.¹⁶ In 1996, R.A. Rightmire, a chemist at the Standard Oil Company of Ohio (SOHIO) invented and patented the device format now commonly used.¹⁷ Later in 1971, SOHIO, licensed the technology to NEC (Japan) corporation, who marketed the electrochemical capacitors (ECs) to provide backup power for computer memory. After Panasonic introduced their “Goldcaps” brand energy source for memory backup applications in 1978 the market expanded rapidly. The coin cell configuration used to design ECs was then developed by Panasonic. The major differences between the NEC and Panasonic products were the electrolyte used. NEC used ‘pasted electrode’ in an aqueous electrolyte with bipolar cell assembly, while Panasonic used non-pasted electrode in a nonaqueous electrolyte in the cell assembly.¹⁶ At the same time, ELNA, in collaboration with Asahi Glass of Japan, entered the market by producing their own organic electrolyte based EDLCs under the name “Dynacap”. Since then supercapacitors have gained attention and popularity throughout the world as energy storage devices, due to their interesting characteristics discussed below.¹⁸

1.1.1 Storage principles

Conventional capacitors store energy between two conducting electrodes (two metal plates) separated by a dielectric material as shown in Figure 1.3. When a voltage is applied to a capacitor, charge is stored by the separation of charge across each electrode.¹⁹ The charges are kept separate by the dielectric, thus generating an electric field that allows the capacitor to store energy.

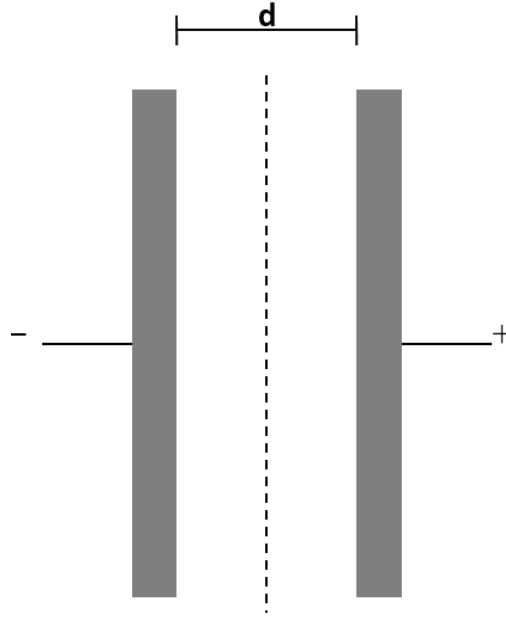


Figure 1.3. Schematic diagram of a conventional capacitor.

Capacitance, C is expressed as the ratio of stored charge Q to the applied voltage V ,

$$C = Q/V \quad 1.1$$

Capacitance also related to the geometry of the electrodes and can be expressed by equation 1.2 as is illustrated by the following relation for parallel-plate capacitors,²⁰

$$C = \epsilon_0 \epsilon_r A/d \quad 1.2$$

Where C is the capacitance, A is the surface area of two electrodes, d is the separation between the electrodes, ϵ_r is the relative permittivity of the electrode material and ϵ_0 is the permittivity of free space (8.854×10^{-14} F/cm). As demonstrated by Equation 1.2, capacitance is dependent on the surface area of the electrode material and distance between two electrodes

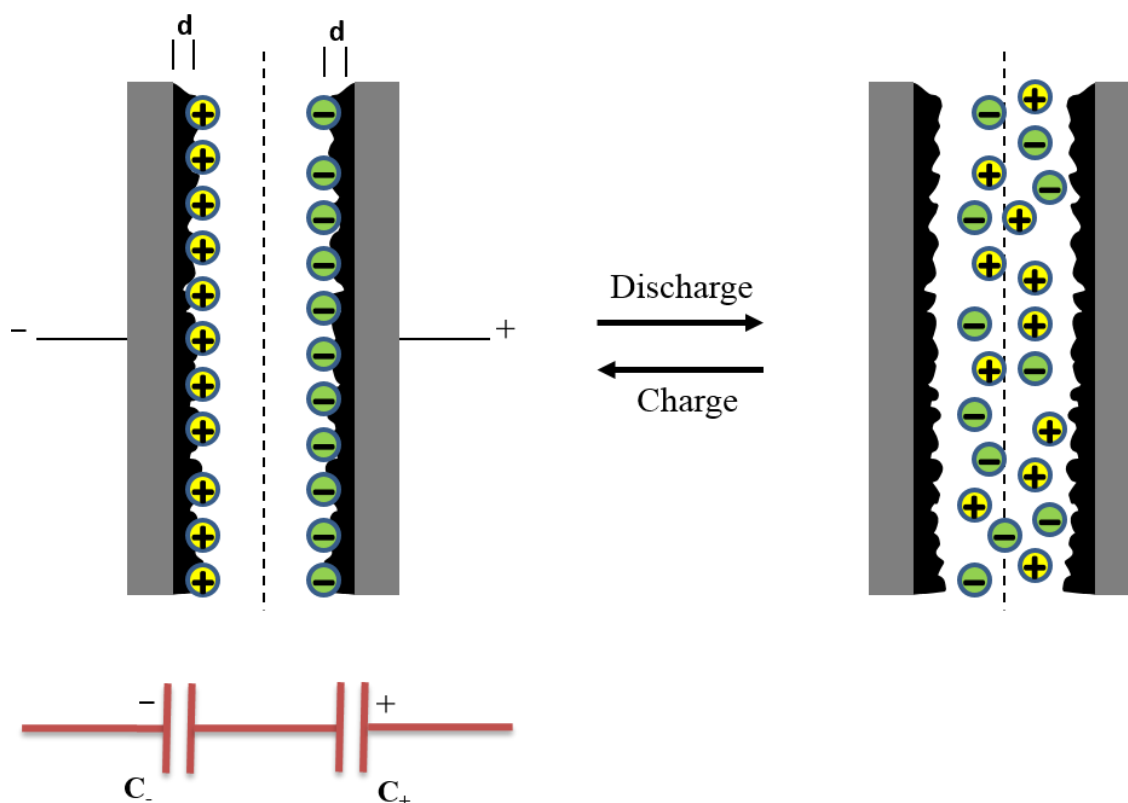


Figure 1.4. Schematic of an electrochemical double-layer capacitor.

An electrochemical double-layer capacitor (EDLC) is a type of electrochemical capacitor that consists of two porous, carbonaceous electrodes immersed in an electrolyte solution as shown in Figure 1.4. Ions are adsorbed from the electrolyte within the pores of the electrodes upon charging and are then desorbed upon discharge. Upon charging, when a voltage is applied to an EDLC polarization occurs at the electrode/electrolyte interface. This causes the positive ions in the solution to migrate to the surface of the cathode and the negative ions to migrate to the surface of the anode.¹¹ In effect, the EDLC is then functioning like two capacitors in series with the carbon electrode serving as one terminal and the ions from the electrolyte solution serving as the other in each of the two “capacitors” (Figure 1.4). In each of these “capacitors” the charge separation

distance is equal to the radius of the ions (order of a few angstroms) that have accumulated at the surface of the carbon electrode resulting in a tremendous increase in the device's capacitance.²¹ If the capacitances of the two electrodes, denoted as C_+ and C_- , respectively, the overall capacitance (C_T) of the entire cell can be expressed as equation 1.3

$$1/C_T = 1/C_+ + 1/C_- \quad 1.3$$

Capacitance and energy and power are used as indicators of supercapacitor performance. Equation 1.4, demonstrates the relationship between energy and capacitance. The energy E stored in a capacitor is directly proportional to its capacitance and quadratically proportional to the applied voltage.²² Also according to equation 1.5, power (P) is quadratically proportional to the applied voltage and inversely proportional to the equivalent series resistance (R_s). In both cases an increase of the voltage (V) causes a significant enhancement of energy (E) and power (P). One way this can be achieved by using an electrolyte having a high voltage window.

$$E = \frac{1}{2} CV^2 \quad 1.4$$

$$P = V^2/4R_s \quad 1.5$$

As capacitance is increased, so is energy. Consequently, in order for supercapacitors to be more feasible energy storage devices, the surface area of the electrode materials must increase for capacitance to improve. In this way, supercapacitors can overcome the limitations of low energy densities.

1.2 Electrode materials for supercapacitors

Materials with high surface areas are chosen to increase supercapacitor performance. Additionally, the presence of pores in the electrode material not only increases the surface area of the material

but also allows charge to be stored in these micro/meso pores. EDLC electrodes have been fabricated using several types of carbonaceous materials including activated carbons, templated carbon, carbon nanotubes (CNTs), carbon aerogel (CAGs), and graphene and carbon nanofibers (CNFs).²³

Activated carbon has been used as a common electrode material due to its very high surface area, relatively low cost and wide availability compared to other carbon materials.²⁴ Activated carbons possess different porous architectures combining micropores (< 2 nm), mesopores (2-50 nm), and macropores (>50 nm) to accomplish their high surface areas.²⁵ Micropores help to adsorb and accumulate ions in to the pores to form the double layer whereas mesopores facilitate the ion diffusion to these micropores by providing low resistive pathways for electrolyte ions to pass through the porous carbon structure.²³ Binding agents are required to fabricate electrodes from activated carbon. Addition of insulating polymeric binders lowers the mass fraction of the active materials thus lowering electrochemical performances.

Templated carbons possess precisely controlled and uniform pore sizes with highly ordered nanochannels and large surface areas.²⁶ The template carbonization method gives a better degree of control over pore size distribution than activated carbon and a maintained interconnection pore structure.²⁷ This interconnected pore structure shows better charge storage and rate capability than the materials having randomly connected pores. However, difficulty of preparation and the extra steps that are needed to remove template (silica, zeolite Y) from the samples and relatively high cost usually offset the advantages.²³ Carbon based nanotubes (CNTs), are also a common supercapacitor material due to the mechanical strength and high conductivity.^{28,25} The mesopores in CNTs are larger than the micropores in activated carbon which allows CNTs greater

accessibility to ions in electrolyte solutions. Also, electrodes prepared from carbon nanotubes show lower ESR than activated carbon because the electrolyte ions can more easily diffuse into the mesoporous network provide by its structure.²⁹ But the low surface area and high fabrication cost of CNTs has limited their commercial applicability.

Carbon aerogels (CAGs) have been used for the EDLCs due to the outstanding high specific surface area and relatively good electrical conductivity. CAGs are usually produced by a sol–gel method using resorcinol and formaldehyde aerogels.²⁵ Carbon aerogels usually possess continuous mesoporous network resulting in binderless carbon materials with low ESR.³⁰

Similarly, graphene demonstrates a strong performance due to its chemical stability, large surface area, and high conductivity as a carbon-based material. But restacking of graphene sheets is problematic when fabricating electrodes.^{31,32,33} Carbon nanofibers (CNFs) are fibers derived from carbon based polymers that are nanometers to few micrometer in diameter. These materials demonstrate greater mechanical strength, large surface area, flexibility, and relatively high conductivities. The flexibility and freestanding nature of CNFs eliminates the need for using binders, thereby increasing the mass fraction of the active materials in the device.³⁴

1.3 Carbon fiber manufacturing process

Fabrication of nanofibers was mainly done by three steps, which involves first electrospinning, which is typically followed by stabilization and carbonization with or without activation. Subsequent high temperature thermal treatment is used to convert the polymer fibers to carbonaceous fibers³⁵. During the conversion from electrospun precursor to carbon fibers, the heat treatment protocol is critically important for the quality of the resulting carbon fibers.³⁶

1.3.1 Electrospinning

Electrospinning is the most widely used method for the preparation of the CNFs.³⁷ The electrospinning process is schematically illustrated in Figure 1.5.

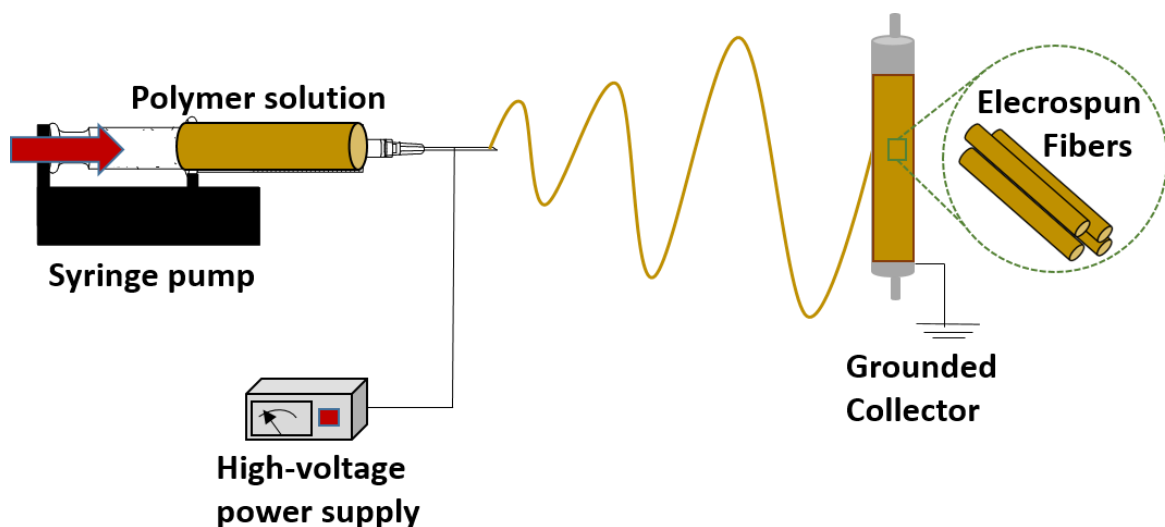


Figure 1.5. Schematic of electrospinning of nanofibers from precursor solution.

An Optical image of a custom built electrospinner is shown in Figure 1.6. In order to create nanofibers from a liquid polymer, the polymer solution is loaded onto the syringe pump and a high voltage is applied between the needle and collector so that the electrostatic repulsion caused by the voltage overcomes the surface tension of the polymer. This tension causes a distorting at the tip of the syringe that causes the liquid polymer to stretch to a fine point only a few nanometers wide. This tip is called the Taylor Cone.³⁸ The polymer fiber is sprayed from the Taylor cone and the electrostatic repulsions in the stream of polymer elongate the fiber until it lands on the collector. The resulting unwoven, flexible mat of polymer is composed of fibers ranging from nanometer to

micrometer wide.³⁹ The diameter of the electrospun fibers depends on nature of solvent, polymer nature, solution viscosity and conductivity, humidity as well as voltage, rotating speed of collector and substrate distance from the needle tip.^{40,41} Carbon fibers can be made from several precursor polymers including PAN, polyimides, cellulose, and pitch where PAN is the most often used due to its high spinnability, carbon yield and mechanical strength.^{34,42}

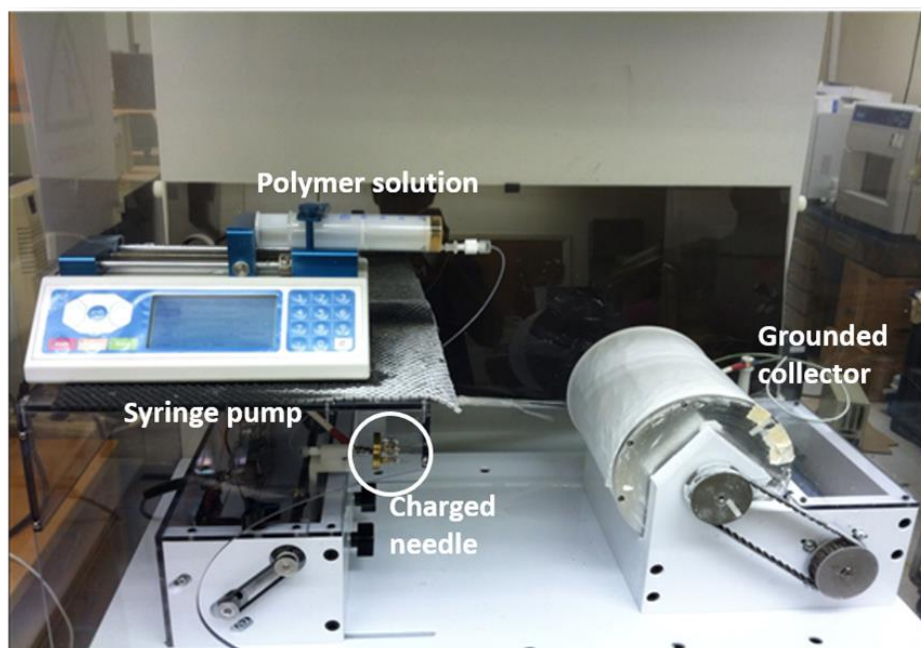


Figure 1.6. Custom-built electrospinner.

1.3.2 Stabilization

The stabilization step is the most complex stage because it is combination of several chemical reactions primarily involving dehydrogenation, oxidation and cyclization. In the stabilization process, the polymer chains are converted to cyclized ladder polymers which stabilizes the polymer backbone prior to carbonization.⁴³ This process helps to enhance the thermal stability of

the precursor to withstand higher temperature carbonization process without decomposing or melting at high temperatures and increases carbon yield.⁴⁴ Stabilization of precursors is usually conducted in the temperature range of 180 to 300 °C in an oxidative gas, typically air, and uses very slow heating rates to avoid release of large amount of heat which can cause melting of polymers. This is crucial step when making carbon fibers because most properties of the resulting carbon fibers depend on this step.

1.3.3 Carbonization

At high temperatures the oxidized precursor will be carbonized by removing hydrogen, oxygen, nitrogen, and other noncarbon elements to produce desired graphitic structures.³⁵ The carbonization step was usually carried out in the inert atmosphere at high temperatures around 800-1700 °C inside the furnace.⁴⁴

After the carbonization step, additional steps such as further carbonization at very high temperatures (higher than 2000 °C) can be carried out to increase graphite content. This is called “graphitization” step.⁴⁴ Also several activation steps (physical or chemical) can be carried out to enhance the surface area of carbon fibers further.⁴⁵

1.4 Electrolytes for EDLCs

In general, electrode materials with smaller pores have a larger surface area and demonstrate high capacitance and specific energy. However, if the pores of the electrode material are too small, the

ions in an electrolyte solution are unable to make contact with the inner surfaces of these pores.⁴⁶ Consequently, pore sizes of all electrode materials should be similar to the size of electrolyte ions to maximize the accessible surface area for electrolyte ions.⁴⁷ On the other hand, high working voltages for the electrolyte are important to increase E and P according to the equations 1.4 and 1.5. Electrolytes used in EDLCs can be mainly classified into three types: aqueous electrolyte, organic electrolyte, and ionic liquids (ILs).

Aqueous solution such as KOH, Na₂SO₄ and H₂SO₄ are used as electrolytes and can be prepared by simple procedure. Aqueous electrolytes are extensively employed for EDLCs because of inexpensiveness and also it can be easily handled without needing special conditions which simplifies the device fabrication processes.⁴⁸ These electrolytes possess smaller ionic radii thus shows higher conductivity because of high ionic concentration. However, the capacitive energy storage of aqueous electrolytes is limited by the small potential window of water due to water decomposition potential of 1.2 V.²³

On the other hand, organic electrolytes typically have a higher voltage of about 2.7 V. Currently, the majority of commercial products use organic electrolytes because of its higher voltage window. Commercial supercapacitors with organic electrolytes typically comprise conductive salts (e.g., tetraethylammonium tetrafluoroborate (TEABF₄)) dissolved in the acetonitrile (ACN) or propylene carbonate (PC).⁴⁸ However, organic electrolytes exhibit low specific capacitance, higher resistance with lower conductivity as well as higher cost than aqueous electrolytes which offset their advantages. Applicability of organic electrolytes are impeded by special safety concerns associated with toxicity, flammability and volatility of its solvents. Furthermore, organic electrolytes need complex purification procedures to remove any residual impurities and controlled

environments to remove moisture. Electrochemical stability windows of organic electrolytes decrease with increasing temperature which are not suitable for high temperature applications.⁴⁹ Further enhancement of capacitor working voltage can be realized by using ionic liquids (ILs). ILs (also known as room temperature molten salts) are synthesized by combining a bulky organic cation with different anions. ILs are characterized with high thermal and chemical stability, wide electrochemical stability window, negligible volatility and non-flammability and good conductivity at room temperature.⁵⁰ Also ILs are “solvent-free” electrolytes, which can address the safety issues associated with other electrolytes. Ionic electrolytes have high operating voltage (> 3.4 V) which significantly enhance the specific energy and power density as well as cycle stability of EDLCs.⁵¹ Furthermore, broad operational temperature ranges can be achieved by utilizing IL mixtures for supercapacitors.⁵² Imidazolium, pyrrolidinium, sulfonium, phosphonium, and quaternary ammonium are used as cations and bis(trifluoromethanesulfonyl)imide (TFSI⁻), bis(fluorosulfonyl)imide (FSI⁻), tetrafluoroborate (BF₄⁻) and hexafluorophosphate (PF₆⁻) are commonly used anion for most of ILs. But high cost and high viscosity limit their viable use in EDLCs.⁴⁸

Topics discussed in this thesis include optimization of high surface area electrode materials for supercapacitors using the ILs, 1-ethyl-3-methyl-imidazolium bis(trifluoromethanesulfonyl)imide (EMITFSI) and *N*-butyl-*N*-methylpyrrolidinium bis(trifluoromethanesulfonyl)imide (PYR₁₄TFSI). Chemical structures of EMITFSI and PYR₁₄TFSI are shown in Figure 1.7. EMITFSI has ion sizes of 4.3 x 7.6 Å (for EMI⁺) and 2.9 x 7.9 Å (for TFSI⁻) and highest working potential of 4.1 V. PYR₁₄TFSI has a larger cation ion size of 11 Å for cation (PYR⁺) and much higher working potential of 5 V.⁵⁰

- (4) Alnaser, W. E. Mobile Solar and Wind-Powered Generator (MSWPG). *Appl. Energy* **1999**, *64*, 97–105.
- (5) Daim, T. U.; Li, X.; Kim, J.; Simms, S. Evaluation of Energy Storage Technologies for Integration with Renewable Electricity : Quantifying Expert Opinions. *Environ. Innov. Soc. Transitions* **2012**, *3*, 29–49.
- (6) Dehghani, H.; Vahidi, B.; Hosseini, S. H. Wind Farms Participation in Electricity Markets Considering Uncertainties. *Renew. Energy* **2017**, *101*, 907–918.
- (7) Yekini, M.; Wazir, M.; Bashir, N. Energy Storage Systems for Renewable Energy Power Sector Integration and Mitigation of Intermittency. *Renew. Sustain. Energy Rev.* **2014**, *35*, 499–514.
- (8) Mahlia, T. M. I.; Saktisahdan, T. J.; Jannifar, A.; Hasan, M. H.; Matseelar, H. S. C. A Review of Available Methods and Development on Energy Storage ; Technology Update. *Renew. Sustain. Energy Rev.* **2014**, *33*, 532–545.
- (9) Zhang, S.; Pan, N. Supercapacitors Performance Evaluation. *Adv. Energy Mater.* **2015**, *5*(6), 1401401/1-1401401/19.
- (10) Armand, M.; Tarascon, J. Building Better Batteries. *Nature* **2008**, *451*, 652–657.
- (11) Kotz, R.; Carlen, M. Principles and Applications of Electrochemical Capacitors. *Electrochim. Acta* **2000**, *45* (15–16), 2483–2498.
- (12) Schneuwly, A. High Reliability Power Backup with Advanced Energy Storage. (https://www.tecategroup.com/white_papers/badnames/200904_WhitePaper_EDNEurope_ASchneuwly.pdf).
- (13) Winter, M.; Brodd, R. J. What Are Batteries, Fuel Cells, and Supercapacitors ? *Chem.Rev.* **2004**, *104*, 4245–4269.
- (14) Miller, J. R.; Burke, A. F. Electrochemical Capacitors : Challenges and Opportunities for Real-World Applications. *Electrochem. Soc. Interface* **2008**, *17*(1), 53-57.
- (15) Becker, H. I. Low voltage electrolytic capacitor, US patent 2800616, issued 1957-07-23.
- (16) Miller, J. R. A Brief History of Supercapacitors. *Batter. Energy Storage Technol.* **2007**, 61-78.
- (17) Rightmire, R.A., Electrical energy storage apparatus, US patent 3288641, issued 1966-11-29.

- (18) Shukla, A. K.; Banerjee, A.; Ravikumar, M. K.; Jalajakshi, A. Electrochimica Acta Electrochemical Capacitors : Technical Challenges and Prognosis for Future Markets. *Electrochim. Acta* **2012**, *84*, 165–173.
- (19) Conway, B. E. E.; Birss, V.; Wojtowicz, J. The Role and Utilization of Pseudocapacitance for Energy Storage by Supercapacitors. *J. Power Sources* **1997**, *66* (1–2), 1–14.
- (20) Simon, P.; Gogotsi, Y. Materials for Electrochemical Capacitors. *Nat. Mater.* **2008**, *7* (11), 845–854.
- (21) Beguin, F.; Presser, V.; Balducci, A.; Frackowiak, E. Carbons and Electrolytes for Advanced Supercapacitors. *Adv. Mater.* **2014**, *26* (14), 2219–2251.
- (22) Chen, S.-M.; Ramachandran, R.; Mani, V.; Saraswathi, R. Recent Advancements in Electrode Materials for the High- Performance Electrochemical Supercapacitors: A Review. *Int. J. Electrochem. Sci* **2014**, *9*, 4072–4085.
- (23) Frackowiak, E. Carbon Materials for Supercapacitor Application. *Phys. Chem. Chem. Phys.* **2007**, *9*, 1774–1785.
- (24) Abioye, A. M.; Nasir, F. Recent Development in the Production of Activated Carbon Electrodes from Agricultural Waste Biomass for Supercapacitors : A Review. *Renew. Sustain. Energy Rev.* **2015**, *52*, 1282–1293.
- (25) Davies, A.; Yu, A. Material Advancements in Supercapacitors : From Activated Carbon to Carbon Nanotube and Graphene Introduction to Supercapacitors. *Can. J. Chem. Eng.* **2011**, *89*, 1342–1357.
- (26) Wang, L.; Ding, W.; Sun, Y. The Preparation and Application of Mesoporous Materials for Energy Storage. *Mater. Res. Bull.* **2016**, *83*, 230–249.
- (27) Nishihara, H.; Kyotani, T. Templated Nanocarbons for Energy Storage. *Adv. Mater.* **2012**, *24*, 4473–4498.
- (28) Yu, Y.; Cui, C.; Qian, W.; Xie, Q.; Zheng, C.; Kong, C.; Wei, F. Carbon Nanotube Production and Application in Energy Storage. *Asia-Pac. J. Chem. Eng.* **2013**, *8*, 234–245.
- (29) Noked, M.; Soffer, A.; Aurbach, D. The Electrochemistry of Activated Carbonaceous Materials : Past, Present , and Future. *J Solid State Electrochem* **2011**, *15*, 1563–1578.
- (30) Wang, X.; Liu, L.; Wang, X.; Bai, L. Preparation and Performances of Carbon Aerogel Microspheres for the Application of Supercapacitor. *J Solid State Electrochem* **2011**, *15*, 643–648.
- (31) Xu, C.; Xu, B.; Gu, Y.; Xiong, Z.; Zhao, X. S. Environmental Science Graphene-Based Electrodes for Electrochemical Energy. *Energy Environ. Sci.*, **2013**, *6*, 1388–1414.

- (32) Zhang, X.; Zhang, H.; Li, C.; Wang, K.; Sun, X.; Ma, Y. Recent Advances in Porous Graphene Materials for Supercapacitor Applications. *RSC Adv.* **2014**, 4, 45862–45884.
- (33) Wu, H.; Zhang, Y.; Cheng, L.; Zheng, L.; Li, Y. Graphene Based Architectures for Electrochemical Capacitors. *Energy Storage Mater.* **2016**, 5, 8–32.
- (34) Lu, X.; Wang, C.; Favier, F.; Pinna, N. Electrospun Nanomaterials for Supercapacitor Electrodes : Designed Architectures and Electrochemical Performance. *Adv. Energy Mater.* 2017, **2017**, 7, 1–43.
- (35) Frank, E.; Hermanutz, F.; Buchmeiser, M. R. Carbon Fibers : Precursors, Manufacturing, and Properties. *Macromol. Mater. Eng.* **2012**, 297(6), 493–501.
- (36) Ouyang, Q.; Cheng, L.; Wang, H.; Li, K. Mechanism and Kinetics of the Stabilization Reactions of Itaconic Acid-Modified Polyacrylonitrile. *Polym. Degrad. Stab.* **2008**, 93(8), 1415–1421.
- (37) Feng, L.; Xie, N.; Zhong, J. Carbon Nanofibers and Their Composites: A Review of Synthesizing, Properties and Applications. *Materials.* **2014**, 7(5), 3919–3945.
- (38) Inagaki, M.; Yang, Y.; Kang, F. Carbon Nanofibers Prepared via Electrospinning. *Adv. Mater.* **2012**, 24 (19), 2547–2566.
- (39) Huang, Z.; Zhang, Y.; Kotaki, M.; Ramakrishna, S. A Review on Polymer Nanofibers by Electrospinning and Their Applications in Nanocomposites. *Compos. Sci. Technol.* **2003**, 63, 2223–2253.
- (40) Pillay, V.; Dott, C.; Choonara, Y. E.; Tyagi, C.; Tomar, L.; Kumar, P.; Toit, L. C.; Ndesendo, V. M. K. A Review of the Effect of Processing Variables on the Fabrication of Electrospun Nanofibers for Drug Delivery Applications. *J Nanomater.* **2013**, 789289, 22 pp.
- (41) Li, B. D.; Xia, Y. Electrospinning of Nanofibers : Reinventing the Wheel ?. *Adv. Mater.* **2004**, No. 14, 1151–1170.
- (42) Fu, Z.; Gui, Y.; Cao, C. Structure Evolution and Mechanism of Polyacrylonitrile and Related Copolymers during the Stabilization. *J Mater Sci* **2014**, 49, 2864–2874.
- (43) Nguyen-thai, N. U.; Hong, S. C. Structural Evolution of Poly (Acrylonitrile- Co -Itaconic Acid) during Thermal Oxidative Stabilization for Carbon Materials. *Macromolecules* **2013**, 46(15), 5882-5889.
- (44) Liu, Y.; Kumar, S. Recent Progress in Fabrication, Structure, and Properties of Carbon Fibers. *Polym Rev* **2012**, 52(3-4), 234-258.

- (45) Hernandez-montoya, V.; Garcia-servin, J.; Bueno-lopez, J. I. Thermal Treatments and Activation Procedures Used in the Preparation of Activated Carbons. *Lignocellul. Precursors Used Synth. Act. Carbon - Charact. Tech. Appl. Wastewater Treat. Dr. Virginia Hernández Montoya (Ed.)*, ISBN 978-953-51-0197-0, InTech, Available from <http://www.intechopen.co> **2012**.
- (46) Largeot, C.; Portet, C.; Chmiola, J.; Taberna, P.; Gogotsi, Y.; Simon, P. Relation between the Ion Size and Pore Size for an Electric Double-Layer Capacitor. *J. Am. Chem. Soc.* **2008**, *130*, 2730–2731.
- (47) Mysyk, R.; Raymundo-pin, E.; Pernak, J. Confinement of Symmetric Tetraalkylammonium Ions in Nanoporous Carbon Electrodes of Electric Double-Layer Capacitors. *J. Phys. Chem. C* **2009**, *113*, 13443–13449.
- (48) Zhong, C.; Deng, Y.; Hu, W.; Qiao, J.; Zhang, L.; Zhang, J. A Review of Electrolyte Materials and Compositions for Electrochemical Supercapacitors. *Chem. Soc. Rev.* **2015**, *44* (21), 7484–7539.
- (49) Balducci, A.; F., S.; Mastragostino, M. The Use of Ionic Liquids as Solvent-Free Green Electrolytes for Hybrid Supercapacitors. *Appl. Phys. A* **2006**, *82*, 627–632.
- (50) Pohlmann, S.; Lobato, B.; Centeno, T.; Balducci, A. The Influence of Pore Size and Surface Area of Activated Carbons on the Performance of Ionic Liquid Based Supercapacitors. *Phys. Chem. Chem. Phys.* **2013**, *15* (40), 17287–17294.
- (51) Arbizzani, C.; Beninati, S.; Lazzari, M.; Soavi, F.; Mastragostino, M. Electrode Materials for Ionic Liquid-Based Supercapacitors. *J. Power Sources* **2007**, *174*(2), 648–652.
- (52) Lin, R.; Taberna, P.; Presser, V.; Carlos, R. P.; Rupesinghe, N. L.; Teo, K. B. K.; Gogotsi, Y.; Simon, P. Capacitive Energy Storage from Å 50 to 100 °C Using an Ionic Liquid Electrolyte. *J. Phys. Chem. Lett.* **2011**, *2*, 2396–2401.

CHAPTER 2
SUPERCAPACITOR PERFORMANCE OF CARBON NANOFIBER ELECTRODES
DERIVED FROM IMMISCIBLE PAN/ PMMA POLYMER BLENDS

Authors – Nimali C. Abeykoon, Jeliza S. Bonso, John P. Ferraris

Department of Chemistry and Biochemistry

The University of Texas at Dallas

800 West Campbell Road

Richardson, Texas 75080-3021

Abeykoon, N.C.; Bonso, J.S. and Ferraris, J.P.; Supercapacitor performance of carbon nanofiber electrodes derived from immiscible PAN/PMMA polymer blends, *RSC Adv.*, 2015, **5**, 19865–19873.

Reproduced by permission of The Royal Society of Chemistry (RSC)

2.1 Abstract

Polymer blends yield carbon materials with superior performances for supercapacitor applications since blending can lead to controlled and fine pore architectures. In this study, a supercapacitor electrode material derived from an immiscible polymer blend comprising polyacrylonitrile (PAN) and polymethyl methacrylate (PMMA) was investigated. PAN was used as the carbonizing polymer while PMMA was used as the sacrificial polymer. The polymer blend solutions in DMF were electrospun to obtain free standing nanofiber mats. The resulting mat was carbonized and activated by CO₂ at 1000 °C to obtain porous carbon nanofibers (CNFs), as PAN converts to carbon and the sacrificial polymer decomposes creating pores. We demonstrated that the pore sizes can be tuned by varying the amount of PMMA loading in the blend compositions. PAN: PMMA (95:5), was found to be the optimum blend composition, affording the highest surface area of 2419 m² g⁻¹, higher degree of graphitization, higher carbon yield and lower charge transfer resistance among the blend compositions studied. Furthermore, the PAN:PMMA (95:5) CNFs showed the highest capacitance of 140 F g⁻¹ and energy densities of 67 Wh Kg⁻¹ at 3.5 V and 101 Wh Kg⁻¹ at 4V in ionic electrolyte (EMITFSI) and also showed the good cycling stability with 85% capacitance retention after 1000 cycles.

2.2 Introduction

Supercapacitors have gained a lot of attention recently as energy storage devices, due to their high power density, long cycle life, wide working potential and broad temperature range of operation.¹

Although supercapacitors have a higher energy density than conventional capacitors, they have lower energy density compared to the batteries.^{1,2}

Therefore, there has been a keen interest in the field to improve energy density of supercapacitors while retaining their high power density. The methods used to increase energy density depend on the type of the supercapacitor, since the charge storage mechanism varies with the type of supercapacitor. Mainly, these can be categorized into electrical double-layer capacitors (EDLCs), pseudocapacitors and hybrid capacitors.¹ EDLCs, studied here, are based on two carbon electrodes that electrostatically store energy in a non-faradic manner within the double layer formed between the surface of the electrode material and the electrolyte ions in the pores of electrodes.³ Therefore, high surface area and porosity of the electrode material are essential to enhance the energy density of EDLCs to achieve high performances.¹⁻⁵

The performance of EDLCs primarily depends on the types of the electrode materials used.⁶ Recently, several types of carbon materials have been reported for EDLCs, such as activated carbons,^{7,8} carbon nanofibers,⁹⁻¹¹ carbide-derived carbons (CDCs),¹² templated carbons,¹³ carbon nanotubes,¹⁴ and graphene.¹⁵ Among these, carbon nanofibers are one of the more promising candidates for EDLC because of their mechanical strength, high surface area, relatively high conductivity, freestanding nature and flexibility.^{16,17} Electrospinning is a simple and widely used technique to produce nanofibers from a wide range of polymers¹⁸. The electrolyte is also important for high supercapacitor performance, and the size of the electrolyte ions should be comparable with the pore sizes of the electrode materials.^{19,20}

Thus, the major challenge is to prepare the carbon materials which have very high surface area and suitable pore size. The polymer blend technique is a promising route to obtain carbon materials

with such fine and controlled pores. This can be achieved by blending of two immiscible polymers which allows control over the blend texture to obtain desired pore sizes.²¹ There are a few studies reported for the carbonization of nanofibers prepared from immiscible polymer blends as a precursor for supercapacitor electrode materials.²²⁻²⁴ Tran et al. reported fabrication of the porous CNFs using Nafion as a sacrificial polymer.²² They obtained CNFs with specific surface area of $1600 \text{ m}^2 \text{ g}^{-1}$ and large specific gravimetric capacitances of 210 F g^{-1} and in $1 \text{ M H}_2\text{SO}_4$ at a scan rate of 100 mVs^{-1} . Jo et al. have investigated the performance of electrode materials using carbon nanofibers derived from immiscible binary polymer blend, consisting 75 wt% of PAN as the carbonizing polymer and with 25 wt% of different sacrificial polymers such as polyacrylic acid (PAA), polyethylene glycol (PEG), polymethyl methacrylate (PMMA) and polystyrene (PS).²¹ They have correlated the pore size created on the CNFs after decomposition of sacrificial polymers with the difference in solubility parameter of the selected polymers. Also they showed that CNF prepared with controlled meso-sized pores demonstrated best cyclic voltammetry measurements. In these methods the polymer blends are comprised of two polymers with different degrees of thermal stability. The polymer with high thermal stability forms the carbon fiber, while the polymer with very low thermal stability acts as a sacrificial material, which completely decomposes at a high temperature. During the thermal decomposition, pores are generated within the carbon fibers and the pore sizes can be controlled by varying the amount of the sacrificial polymer in the blend composition.

Herein, we report the preparation of activated carbon nanofibers from electrospun immiscible PAN/PMMA polymer blends followed by thermal treatments of carbonization and activation. PAN is used as the carbon precursor of choice due to its high carbon yield, good thermal stability,

spinnability and commercial availability.²⁵ The electrospinning of the incompatible PAN/PMMA blend introduces a phase separated morphology in the fiber, which leads to porous carbonized fibers suitable as supercapacitor electrodes (Figure 2.1)

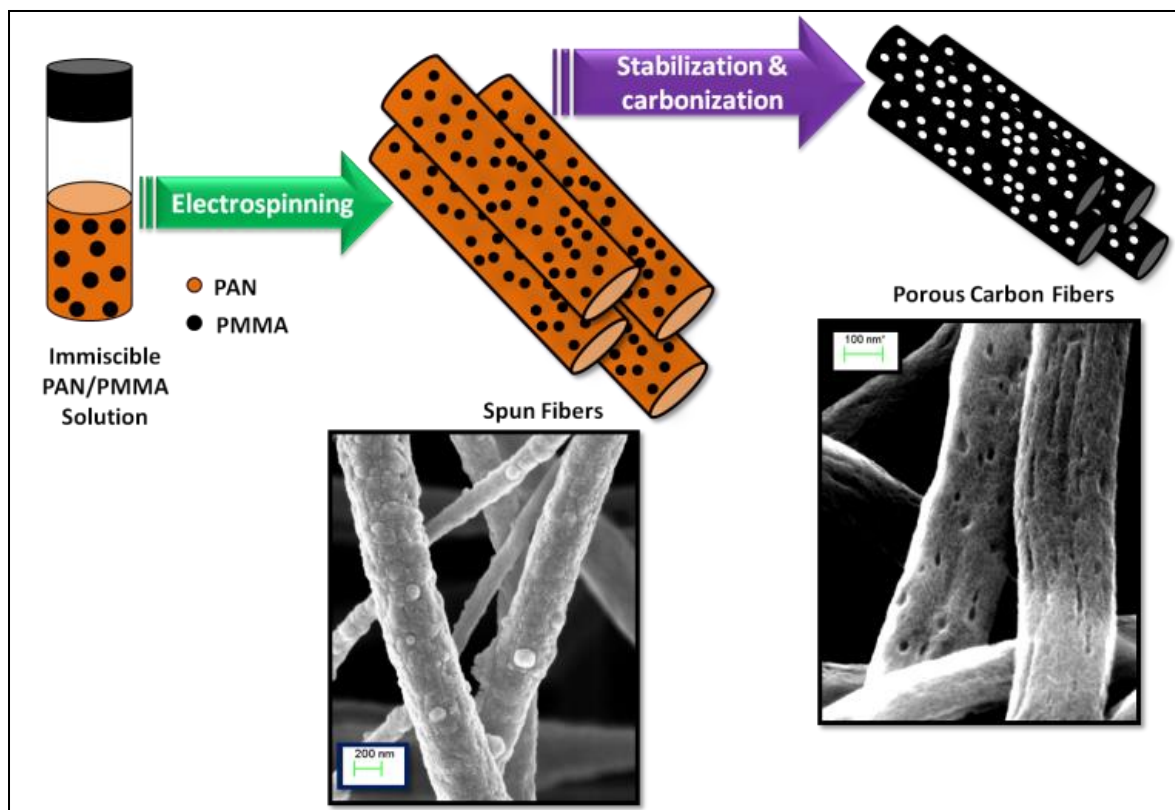


Figure 2.1. Schematic illustration of the porous carbon nanofiber formation using PAN/PMMA immiscible polymer blends. During carbonization, PMMA decomposes creating pores in PAN nanofibers.

2.3 Experimental

2.3.1 Materials

Polyacrylonitrile (PAN, $M_w = 150,000 \text{ g mol}^{-1}$), polymethyl methacrylate (PMMA, $M_w = 120,000 \text{ g mol}^{-1}$) anhydrous N,N' -dimethylformamide (DMF) were purchased from Sigma Aldrich and

used as received without further purification. Electrochemical grade ethylmethyylimidazolium bis(trifluoromethylsulfonyl) imide (EMITFSI), (99.5% purity) was purchased from IoLiTec, Inc. and was used as received. The coin cell assembly parts were obtained from Shenzhen Yongxingye Precision Machinery Mould Co. Ltd., China.

2.3.2 Preparation of carbon nanofibers

First, PAN and PMMA were dissolved in DMF in separate vials by stirring for 4h at 50 °C. Then three types of 10 wt% polymer blend solutions were prepared for electrospinning comprising PAN:PMMA (95:5), PAN:PMMA (90:10) and PAN:PMMA (75:25) blend compositions. These solutions were further stirred for 24 h at room temperature. In addition, a 10 wt% PAN control solution was also prepared by following the same procedure. The solutions were electrospun using a custom-built electrospinner under an applied voltage of 15 kV (Gamma High Voltage Research, Inc., power supply). The polymer solutions were loaded into the syringe and the attached needle tip was connected to the positive voltage of the power supply. The polymer solutions were delivered to the tip at a constant flow rate of 0.8 ml h⁻¹ controlled by a syringe pump and the grounded drum collector was placed 15 cm away from the needle tip and rotated at 300 rpm. Electrospun nanofiber mats were stabilized at 280 °C for 1 h under air flow at a heating rate of 2 °C min⁻¹ and then carbonized and CO₂ activated for 1 h at 1000 °C under helium at a heating rate of 5 °C min⁻¹.

2.3.3 Characterization

The surface morphology of as-spun, stabilized and carbonized fibers were investigated by a Zeiss SUPRA 40 Scanning Electron Microscope (SEM) with a field emission gun operating at 10 keV. As-spun and stabilized nanofibers were sputter coated using gold/palladium target before collecting data and SEM images of carbonized fibers were obtained without sputter coating. The fiber diameters were determined by averaging the diameter of 100 fibers for each sample. To investigate the phase morphology of the blends, thin film membranes were prepared by solvent-casting method. First polymer solutions were cast onto a glass substrate using a Sheen automatic applicator (1133N) equipped with a doctor blade and then PMMA polymer phase was extracted from the thin film membrane by using methylene chloride as a solvent in a Soxhelt extractor. Then the morphology of the extracted films were examined by SEM after sputter coating with gold/palladium. Fourier transform infrared (FTIR) spectra for all the samples were acquired using a Nicolet 360 FTIR spectrophotometer. Thermogravimetric analysis (TGA) for pure PMMA, as-spun fiber mat of neat PAN and the PAN/PMMA blends was done under nitrogen at a flow rate of 50 ml min⁻¹ using a TA Instruments SDT Q600 Analyzer at a heating rate of 10 °C min⁻¹ from room temperature to 1000 °C. The ratio of graphitic and amorphous carbons was determined using a JobinYvon HORIBA LabRam Raman spectrometer equipped with a 633 nm He–Ne laser. The porosity and pore volume were measured from the nitrogen adsorption isotherms at 77K (Quantachrome Instruments Autosorb-1). The specific surface area of the carbonized nanofibers was determined by the Brunauer–Emmett–Teller (BET) method. The pore size distribution was calculated using the Density Functional Theory (DFT).

2.3.4 Electrochemical tests

CR2032 coin cells were assembled to test the electrochemical performance of the obtained electrodes. First, the electrodes were punched out directly from the carbonized fiber mat. In the assembly of the coin cells, two electrodes were placed in between stainless steel spacers and two current collectors (carbon coated aluminum) and PTFE (Gore™) separator was placed in between the electrodes to separate them. EMITFSI was used as an ionic liquid electrolyte and these components were pressed together using a crimper inside the nitrogen filled glove box. To obtain electrochemical performances of the fibers, cyclic voltammetry and charge discharge tests were done using an Arbin Supercapacitor Test Station (SCTS). Electrochemical impedance spectroscopy was obtained using a PARSTAT 2273 Galvanostat (Princeton Applied Research) at 0 V DC bias in between the frequency range of 100 kHz to 10 mHz and analyzed using a PowerSuite software.

2.4 Results and discussion

2.4.1 Characterization of the material

The SEM images in Figure 2.2 show the fibrous morphology of the electrospun nanofibers obtained from neat PAN and the PAN/PMMA blends. Flexible freestanding fiber mats were obtained after electrospinning of these blend solutions. All the electrospun solutions with different weight ratios of PMMA show uniform nanofibers without beading. The fiber diameter is one of the important factors determining the electrochemical properties of carbon materials formed from

electrospun fibres. SEM images (Figure 2.2) revealed that the average diameter of fibers decreases with increasing PMMA amount in the blend compositions. The fiber diameter obtained for neat PAN was 692 ± 98 nm decreasing to 511 ± 127 nm for PAN:PMMA (95:5), 472 ± 97 nm for PAN:PMMA (90:10) and 353 ± 88 nm for PAN:PMMA (75:25). The trend can be attributed to the lower viscosity of the solutions with higher amount of PMMA compared to that of neat PAN solution.²⁶ During electrospinning, the dispersed PMMA droplets, having a lower viscosity compared to that of PAN, would be elongated more by the electrical forces and thus the fiber diameter is reduced further.²⁶

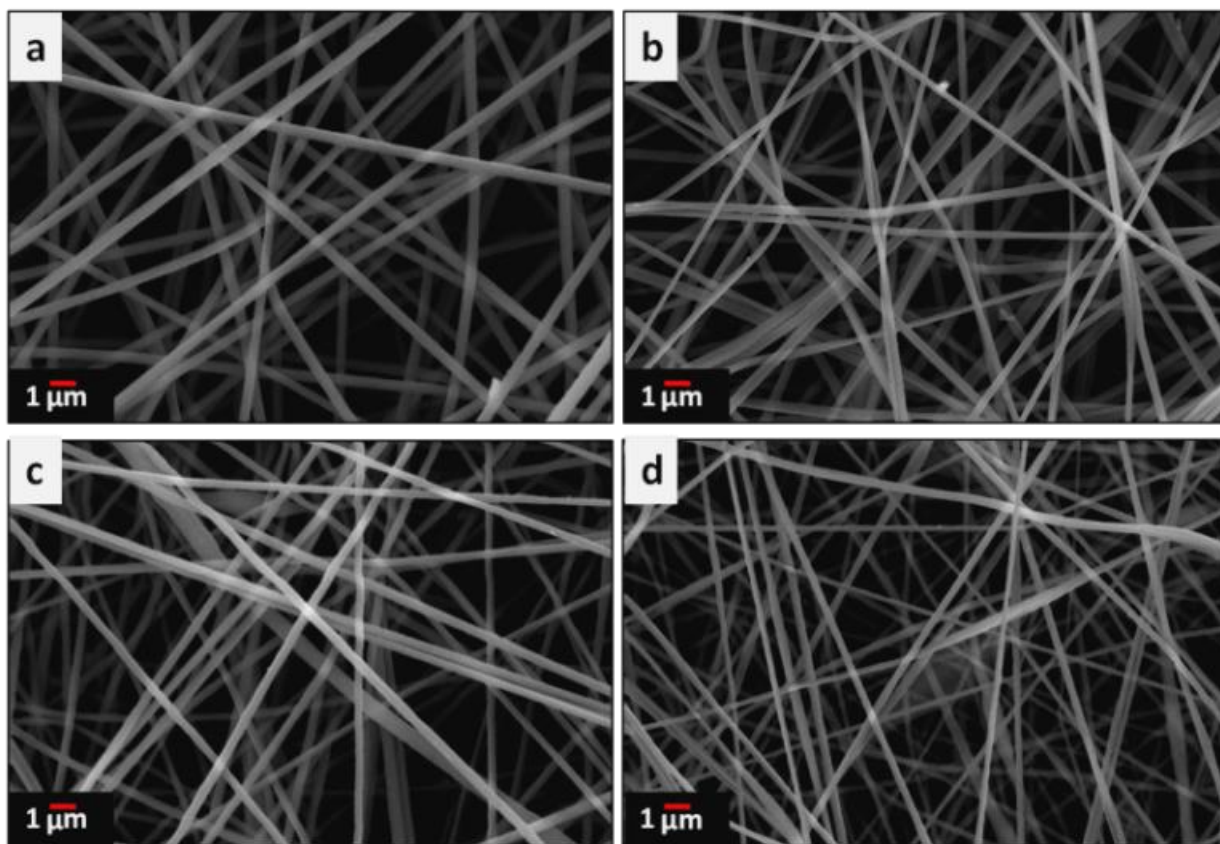


Figure 2.2. SEM images of electrospun (a) neat PAN, (b) PAN:PMMA (95:5), (c) PAN:PMMA (90:10) and (d) PAN:PMMA (75:25) nanofiber mats.

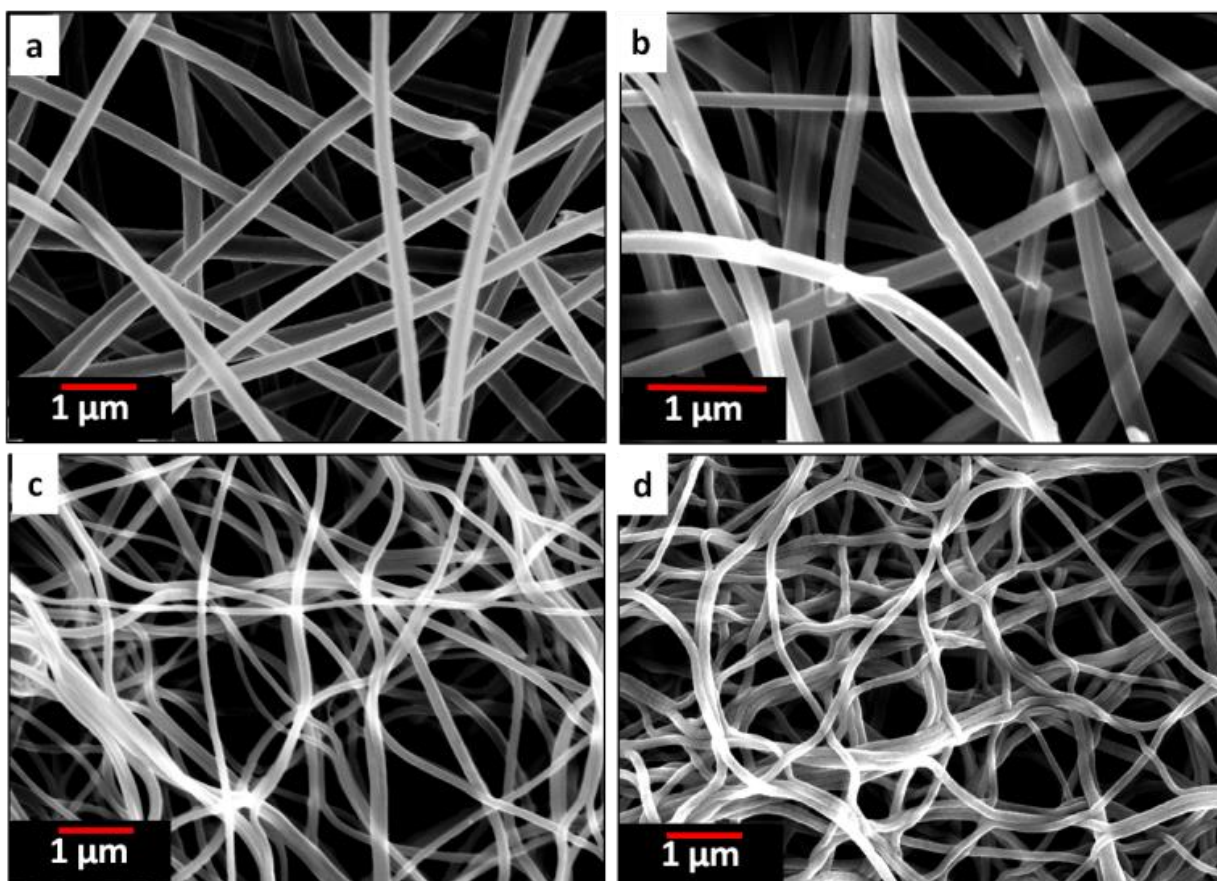


Figure 2.3. SEM images of carbon nanofiber mats of (a) neat PAN, (b) PAN:PMMA (95:5) , (c) PAN:PMMA (90:10) and (d) PAN:PMMA (75:25).

Figures 2.3 and 2.4 show the morphology of carbonized and CO₂ activated fibers at different magnifications. After the thermal treatments, the mats retained their fibrous morphology without collapsing. All the CNFs demonstrate a very uniform diameter. The fibers shrank after carbonization due to the removal of PMMA which is most obvious in PAN:PMMA (75:25). The average fiber diameter of CNFs for PAN is 260 ± 27 nm while diameters of CNFs from the PAN/PMMA blends are 197 ± 48 nm (PAN:PMMA, 95:5), 106 ± 21 nm (PAN:PMMA, 90:10), and 87 ± 19 nm (PAN:PMMA, 75: 25) nm, respectively.

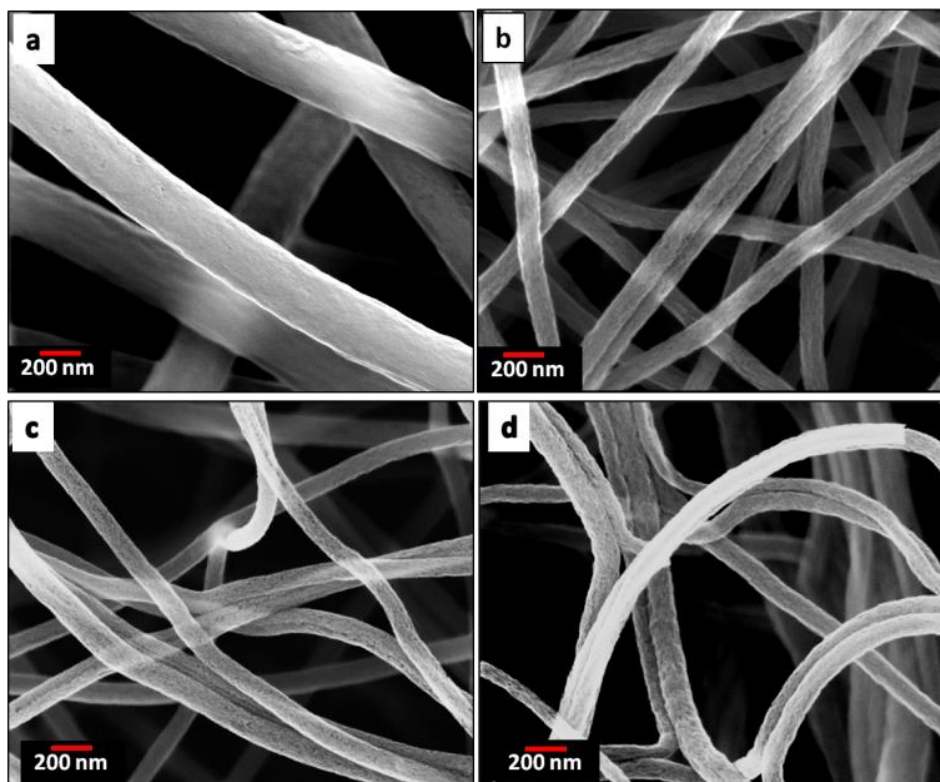


Figure 2.4. SEM images of carbon nanofiber mats from (a) neat PAN, (b) PAN:PMMA (95:5), (c) PAN:PMMA (90:10) and (d) PAN:PMMA (75:25).

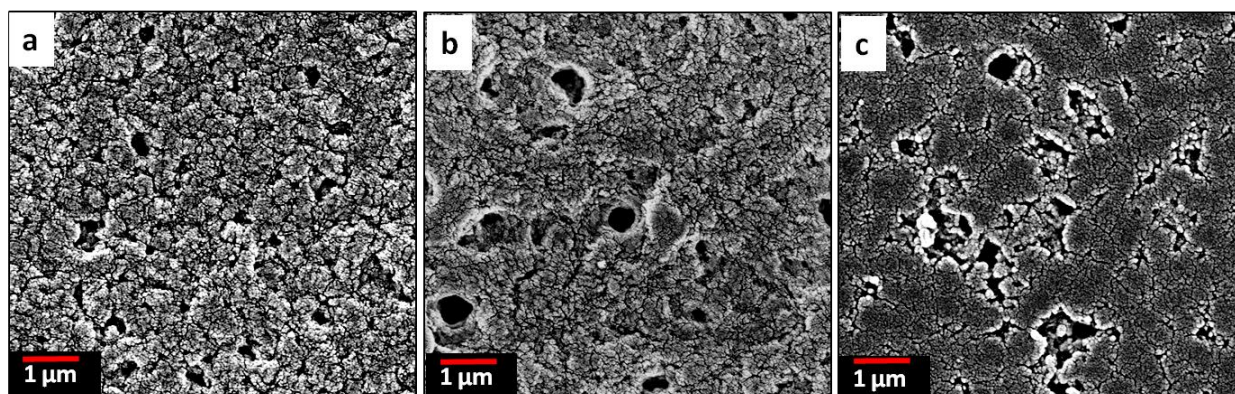


Figure 2.5. SEM images of the surface morphology of the PMMA extracted (a) PAN:PMMA (95:5) (b) PAN:PMMA (90:10) and (c) PAN:PMMA (75:25) films.

Figure 2.5 shows the SEM images of the surface morphology of the blend films in which PMMA phase has been selectively extracted with methylene chloride. In immiscible polymer blends, the

continuous phase is formed by the major component while the dispersed phase is formed with the minor component.²⁷ Similarly, here PAN became the continuous phase while PMMA became the dispersed phase as evident by the holes resulting from selective solvent extraction. As the incorporated percentage of PMMA in the blends is increased, the domain size of the dispersed phase also became larger and more irregular in shape. Whereas the PAN:PMMA (95:5) blend exhibited a fairly uniform distribution of PMMA, larger domains with irregular shapes can be observed PAN:PMMA (75:25) blend. This may be due to the enhanced coalescence of the PMMA domains occurring during the phase separation process which lowers the interfacial area by forming larger domains.²⁸ It is also possible that the higher amount of PMMA leads to aggregation of PMMA before it disperses within the PAN matrix during polymer mixing. This can account for the irregular shape of the dispersed phase. In either case, a change of blend composition leads to changes in the size and the shape of the dispersed phase and eventually allows the control of the pore size of the resulting CNFs.

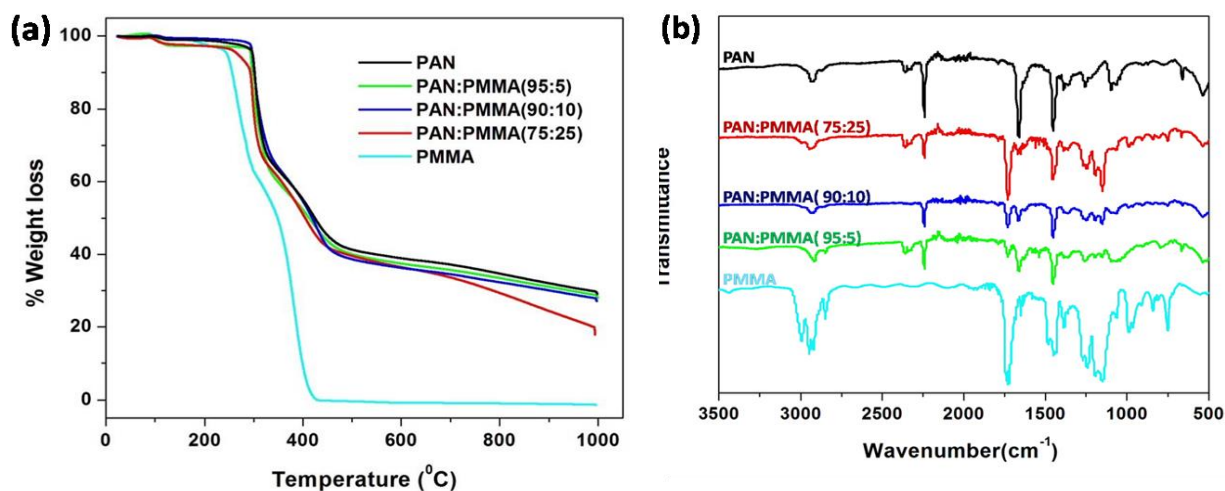


Figure 2.6. (a) TGA analysis and (b) FTIR analysis of PMMA, as-spun mat of PAN and blends.

Thermal decomposition behavior of the electrospun PAN/PMMA blends and the carbon yield at 1000 °C were studied with TGA analysis. Figure 2.6(a) shows the TGA curves of the as-spun fiber mats of PAN/PMMA blends with different PMMA loadings. Pure PMMA starts to decompose at 250 °C and it completely decomposes around 400 °C whereupon it is completely converted to volatile products.²⁹ Therefore, no residue of PMMA was observed after 400 °C on the carbonized fibers. During the pyrolysis process of the blends, porous fibers are generated as a result of the degradation of PMMA, which also accounts for a higher surface area. The weight losses mainly occurred in two temperature ranges: 250-300 °C and 300-450 °C. The first weight loss results from the cyclization of nitrile groups in the PAN.³⁰ The second weight loss arises from the decomposition of PMMA.³¹ PAN:PMMA (95:5) shows the highest carbon yield of 28.0 % among the blends studied and it is similar to that of neat PAN 29.0% at 1000 °C. The carbon yield of PAN/PMMA (90:10) was 27.1% while PAN/PMMA (75:25) shows the lowest carbon yield of 17.9%, as expected.

FTIR spectra of pure PMMA, as-spun mats of neat PAN and blends were obtained to confirm actual incorporation of PMMA into the PAN. The FTIR spectrum of PMMA is shown in Figure 2.6(b) and the characteristic absorption band of carbonyl stretching is observed at 1730 cm⁻¹.³² FTIR spectrum of neat PAN shows an absorption band at 2243 cm⁻¹, which is assigned to the –C≡N stretching of acrylonitrile unit in the polymer chain.³⁰ After blending, all the blends show the absorptions at 1730 cm⁻¹ and 2243 cm⁻¹ indicating the presence of both PMMA and PAN. Furthermore, the carbonyl stretching absorption at 1730 cm⁻¹ becomes more intense upon increasing the amount of PMMA.

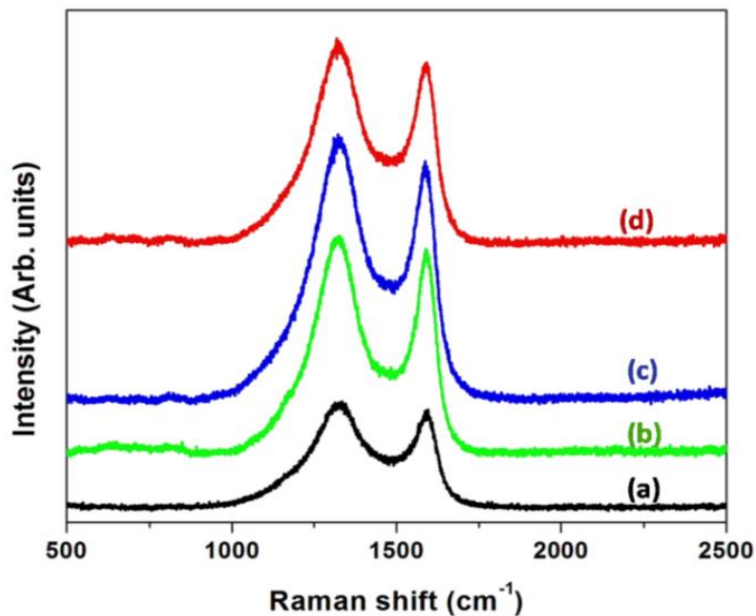


Figure 2.7. Raman spectra of CNFs derived from (a) neat PAN (b) PAN:PMMA (95:5) (c) PAN:PMMA (90:10) and (d) PAN:PMMA (75:25).

Raman spectroscopy was used to estimate the degree of graphitization of the activated samples. The band centered at 1350 cm⁻¹ is known as the "D-band" which is indicative of disordered carbonaceous structures and amorphous carbon while the band centered at 1580 cm⁻¹ is known as the "G-band" and corresponds to the ordered graphitic structures.³³ Table 2.1 shows the I_D/I_G ratios of CNFs derived from PAN and PAN/PMMA blends and these ratios are obtained based on the area of the two peaks. According to the table 2.1, CNFs derived from PAN shows the I_D/I_G Ratio of 3.33 indicating the presence of a high amount of amorphous carbon. Addition of PMMA is advantageous, since it causes the I_D/I_G ratio to decrease as a result of the formation of more ordered carbon structures. Even though the addition of PMMA to PAN increases the degree of graphitization compared to PAN, as the PMMA loading increases the degree of graphitization

decreases as evident by the I_D/I_G ratio (Table 2.1). The effect on the morphology of electrospun fibers upon incorporated of 25% PMMA in PAN/PMMA precursor blends has been reported.²⁶

Table 2.1. Ratios of peak intensities of CNFs derived from PAN and the PAN/PMMA blends

Precursor	I_D/I_G Ratio
PAN	3.33
PAN:PMMA (95:5)	2.89
PAN:PMMA (90:10)	3.02
PAN:PMMA (75:25)	3.03

2.4.2 Nitrogen adsorption and pore size analysis

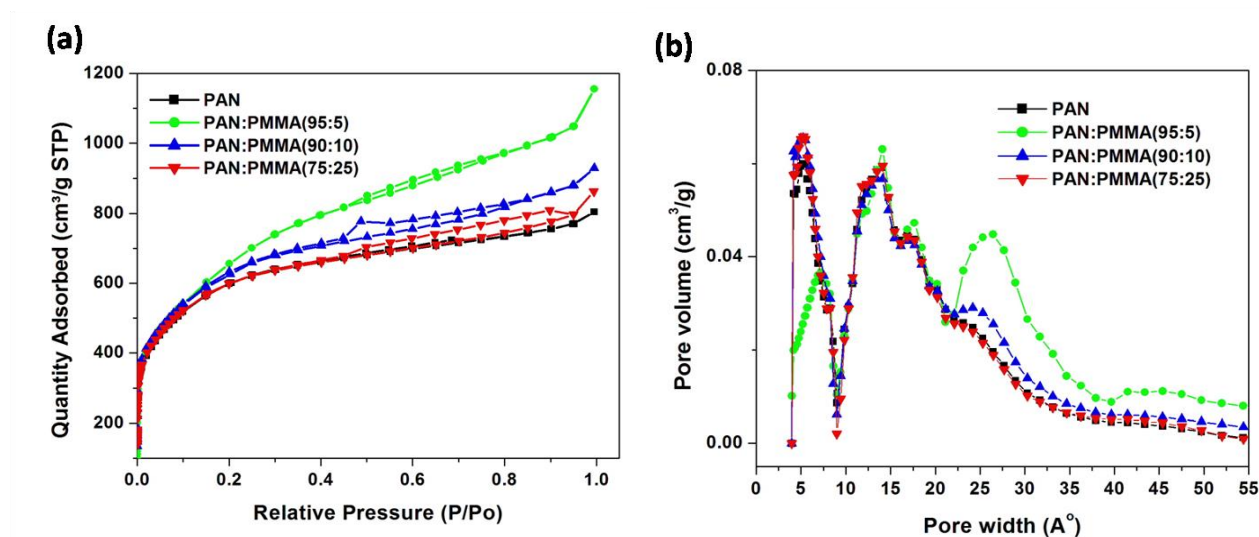


Figure 2.8. Nitrogen adsorption–desorption isotherms and (b) pore size distribution for CNFs derived from (a) PAN, (b) PAN/PMMA (95:5), (c) PAN/PMMA (90:10) and (d) PAN/ PMMA (75:25).

Figures 2.8(a) and 2.8(b) illustrate the nitrogen adsorption–desorption isotherms and the pore size distribution for the resulting activated samples, respectively. Surface area and the pore size distribution are important factors which determine the performance of the supercapacitors. According to Table 2.2, the incorporation of PMMA causes an increase in the surface area, with all the blend compositions showing higher surface areas compared to neat PAN. Among the blends PAN:PMMA (95:5) has the highest surface area. Also, it is demonstrated that the pore sizes can be tuned by varying the amount of PMMA in the blend. Incorporation of PMMA has increased the percentage of mesopores within the CNFs compared to pure PAN. Previous reports have shown

Table 2.2. Surface area and pore volume of PAN and PAN/PMMA based carbon nanofibers

	surface area (m ² /g)	Total pore Volume (cm ³ /g)	V _{micro} (cm ³ /g)	V _{meso} (cm ³ /g)	% micro pores	% meso pores	Micropore /mesopore ratio
PAN	2178	1.0035	0.6975	0.3060	69.5	30.5	2.28
PAN:PMMA (95:5)	2419	1.3128	0.6384	0.6744	48.6	51.4	0.95
PAN:PMMA (90:10)	2301	1.1061	0.7052	0.4009	63.6	36.4	1.75
PAN:PMMA (75:25)	2214	1.0062	0.7038	0.3024	69.9	30.1	2.32

that maximum double-layer capacitance can be obtained when the pore size is close to the ion size of the electrolyte.¹⁹ In this work, EMITFSI was used as the ionic liquid electrolyte. The ion sizes of the anion (TFSI) and cation (EMI) are close to each other (0.79 and 0.76 nm, respectively). In order to obtain enhanced supercapacitor performances, it is beneficial for the carbonized and activated blends with different ratios of PMMA to have their pore sizes match (or exceed) the electrolyte's ion sizes.

2.4.3 Electrochemical properties of CNFs

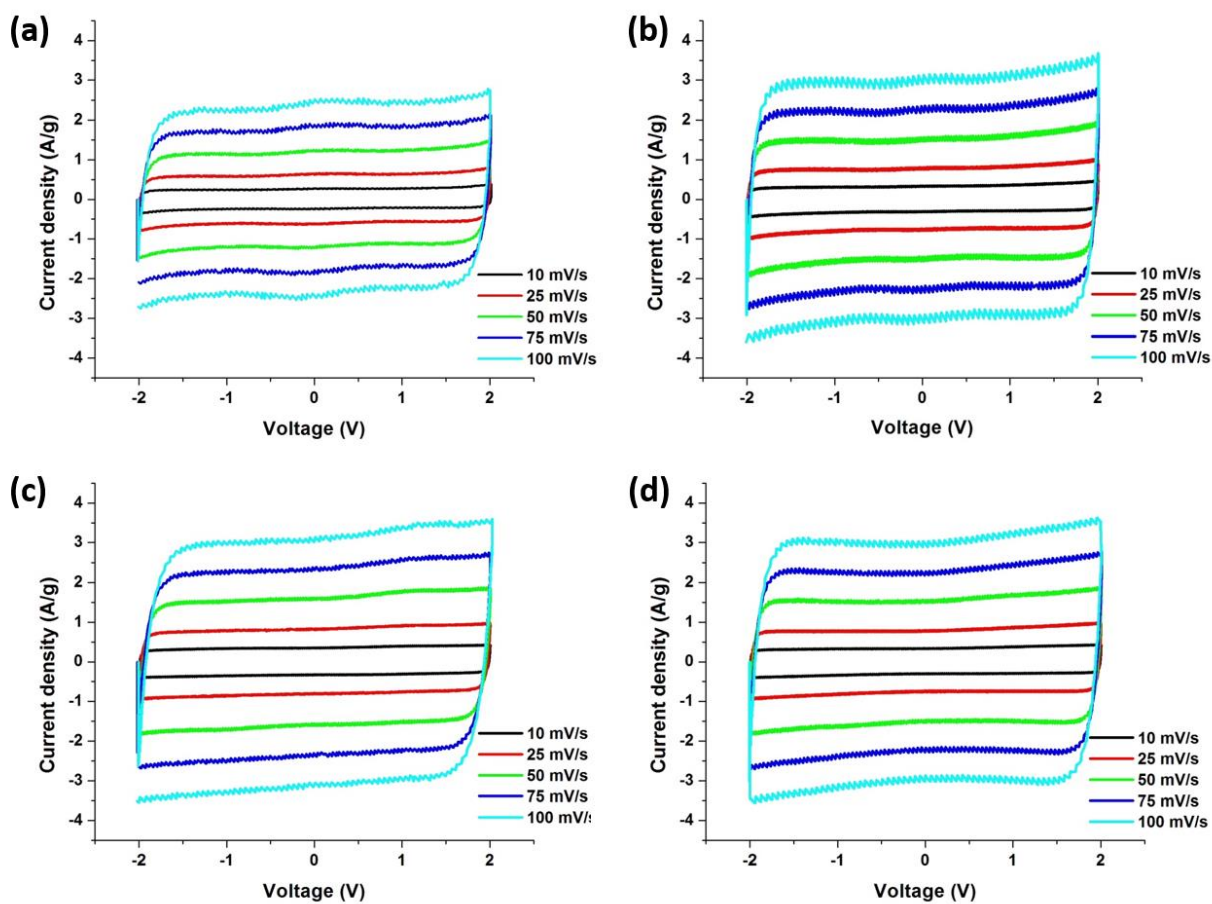


Figure 2.9. Cyclic voltammograms of carbonized nanofibers derived from (a) PAN, (b) PAN/PMMA (95:5), (c) PAN/PMMA (90:10) and (d) PAN/PMMA (75:25).

The cyclic voltammograms (CV) for the PAN/PMMA precursor blends with different ratios of PMMA are shown in Figure 2.9. CV curves were collected in the potential range -2.0 to 2.0 V at five different scan rates ranging from 10 to 100 mV s^{-1} . In EDLC, the rectangular shaped CV indicates the ideal double layer capacitive behavior. The highest specific capacitance obtained for the carbonized PAN was 91 F g^{-1} . The specific capacitances of CNFs of PAN:PMMA (95:5), PAN:PMMA (90:10) and PAN:PMMA (75:25) at the scan rate of 10 mV s^{-1} were determined to be 140, 135, and 128 F g^{-1} , respectively. PAN:PMMA (95:5), which has the highest percentage of mesopores and surface area, showed the best electrochemical performance (Table 2.3).

Table 2.3. Specific capacitance F g^{-1} of the CNFs derived from the PAN and the PAN/PMMA blends at five different scan rates

Scan rate (mV/S)	Specific capacitance (F g^{-1})			
	PAN	PAN:PMMA (95:5)	PAN:PMMA (90:10)	PAN:PMMA (75:25)
10	97.2	140.2	135.1	128.1
25	96.6	139.3	133.7	127.9
50	95.9	137.6	132.4	127.8
75	95.3	134.2	129.8	126.2
100	95.1	131.8	128.5	125.2

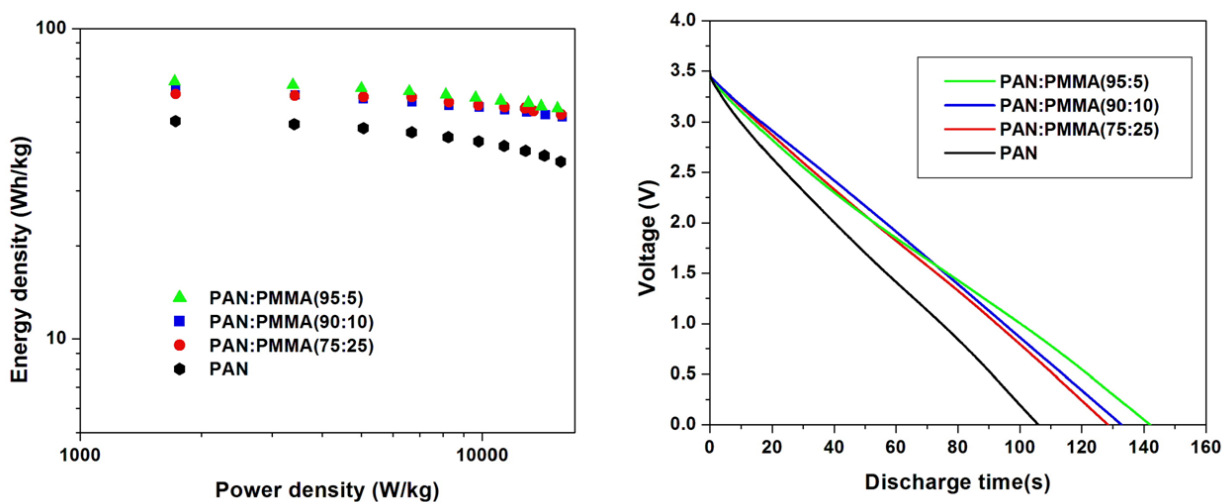


Figure 2.10. (a) Ragone plots (b) galvanostatic discharging curves at a constant current density of 1 A g⁻¹.

Energy densities were determined by discharging from 3.5 V for all the samples (Figure 2.10(a)). Table 2.4 summarizes the energy and power densities of the carbonized PAN/PMMA nanofibers at a current discharge density of 1 A g⁻¹ and 10 A g⁻¹. When the current density was increased, the energy density of the carbonized PAN dropped to 75% of that obtained at 1 A g⁻¹. In contrast, the PAN/PMMA blends retained between 82-86% of their original energy densities. The activated PAN gave an energy density of 49.4 W h kg⁻¹ and it is remarkably increased to 67.4 W h kg⁻¹ after blending with a small amount (5 wt%) of PMMA, in PAN/PMMA blend nanofibers. Also, PAN/PMMA (90:10) and PAN:PMMA (75:25) exhibit energy densities of 63.2 W h kg⁻¹ and 61.4 W h kg⁻¹ respectively. PAN:PMMA (95:5) gave an energy density of 101 W h kg⁻¹ when discharged from 4 V. Figure 2.10 (b) shows the discharge curves for PAN/PMMA blends. Discharge curves for PAN/PMMA blends are linear with no significant IR drop in contrast to PAN.

The PAN: PMMA (95:5) showed the longest discharge time followed by PAN:PMMA (90:10), PAN: PMMA (75:25) and PAN.

Table 2.4. Energy densities and the power densities of the CNF derived from PAN and PAN/PMMA blends

Current	Parameters	PAN	PAN:PMMA	PAN:PMMA	PAN:PMMA
Density			(95:5)	(90:10)	(75:25)
(A/g)					
1	Energy density (Wh/kg)	50.1	67.4	63.2	61.4
	Power density (W/kg)	1724	1715	1727	1727
10	Energy density (Wh/kg)	37.4	55.4	51.9	52.9
	Power density (W/kg)	15664	15376	15830	15707

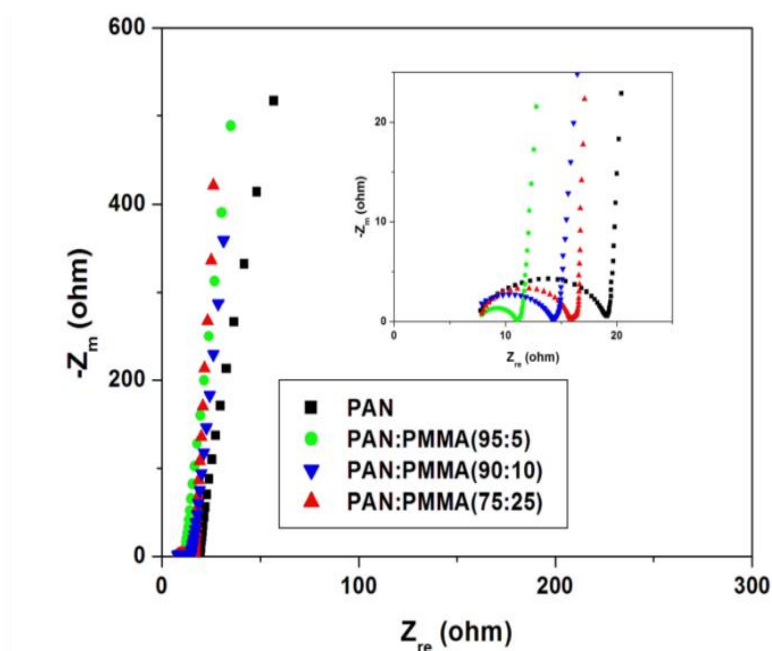


Figure 2.11. Nyquist plots for the CNF samples prepared from the PAN and PAN/PMMA blends in EMITFSI ionic electrolyte.

Figure 2.11 displays Nyquist plots for the CNF samples prepared from the PAN and PAN/PMMA blends in EMITFSI electrolyte. Electrochemical impedance spectroscopy (EIS) can provide more detailed information such as pore structure of electrode materials and kinetics in double-layer charging/discharging processes, in which a semi-circle appears in the high frequency region and an almost vertical increase in lower frequency region, indicative of ideal capacitance.³⁴ In the Nyquist plot, the x intercept at the highest frequency region is called bulk electrolyte resistance which mainly depends on the electrolyte solution. The high frequency semicircle can be assigned to two resistances, namely, the contact resistance between porous electrode and current collector or the ion transfer resistance. The semicircle of the all the CNF samples prepared from the PAN/PMMA blends were smaller than that of CNF prepared from neat PAN, which indicates that the ion transfer resistance is reduced with the incorporation of PMMA. This result can be attributed to the formation of pores that can accommodate ions as a consequence of sacrificial PMMA incorporation. The semi-circle of CNF prepared from the PAN:PMMA (95:5) blend was the smallest, indicating the lowest ion transfer resistance in the electrode/electrolyte interface. According to the pore size analysis, PAN:PMMA (95:5) shows the formation of a larger number of mesopores, which favors greater ion accessibility into the pores of electrodes which are in contact with the electrolyte.

In order to further investigate the electrochemical stability of the electrode material, the best composition of PAN:PMMA (95:5) was selected for the cycling test in ionic liquid electrolyte (EMITFSI) and result is shown in Figure 2.12. After 100th cycle 93.8% of the specific capacitance was retained while after 1000th cycle 85% of the capacitance was retained. These results demonstrate that the activated carbons derived from PAN:PMMA (95:5) exhibit a high degree of

reversibility leading to good cycle stability, making them potentially suitable electrode materials for high performing supercapacitors.

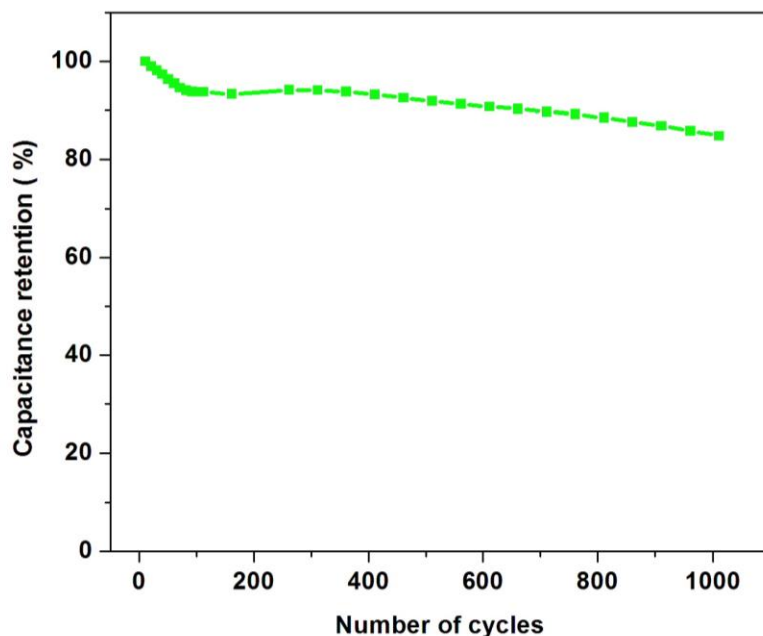


Figure 2.12. Capacitance retention of PAN : PMMA (95 : 5) over 1000 charge/discharge cycles at a current density of 1 A g^{-1} .

2.5 Conclusion

In this study, the correlation between precursor composition of immiscible PAN/PMMA blends and their electrochemical performances were studied. Polymer solutions of PAN, PAN/ PMMA (95:5), PAN/PMMA (90:10) and PAN/PMMA (75:25) were prepared, and electrospun to form free standing nanofiber mats. Porous CNFs were obtained from PAN and PAN/PMMA blends after thermal treatments. The introduction of PMMA into the PAN increases the surface area of PAN nanofibers leading to enhanced electrochemical performances of the carbon CNFs. This

improvement is attributed to the formation of pores with both microporosity and mesoporosity that afforded ready electrolyte access. PAN/PMMA (95:5) CNFs show the highest degree of graphitization, highest carbon yield, lowest charge transfer resistance, good cycle stability, highest capacitance of 140 F g^{-1} as well as energy densities of 67 W h kg^{-1} at 3.5 V and 101 W h kg^{-1} at 4 V in EMITFSI electrolyte. The preparation of PAN/PMMA immiscible polymer blends by incorporating PMMA has been found to be an effective method to increase the energy density of supercapacitors with PAN:PMMA (95:5) being especially promising.

Acknowledgements

The authors acknowledge the National Science Foundation (Grant No. IIP-1127564) for financial support. We also thank Dr. Ronald A. Smaldone and Dr. Christina Thompson and Sajani Basnayake for help with the surface area analysis. Valuable discussions with Dr. Lissa Magel (Solarno, Inc.), Dr. Nimanka P. Panapitiya and Dr. Sumudu N. Wijenayake are also greatly appreciated.

2.6 References

- (1) Winter, M.; Brodd, R. J. What Are Batteries, Fuel Cells, and Supercapacitors ? *Chem.Rev.* **2004**, *104*, 4245–4270.
- (2) Burke, A. Ultracapacitor; Why, and Where Is the Technology. *J. Power Sources* **2000**, *91*, 37–50.
- (3) Kotz, R.; Carlen, M. Principles and Applications of Electrochemical Capacitors. *Electrochim. Acta* **2000**, *45* (15–16), 2483–2498.
- (4) Qu, D.; Shi, H. Studies of Activated Carbons Used in Double-Layer Capacitors. *J. Power Sources* **1998**, *74*, 99–107.

- (5) Vix-guterl, C. Electrochemical Energy Storage in Ordered Porous Carbon Materials. *Carbon N. Y.* **2005**, *43*, 1293–1302.
- (6) Zhai, Y.; Dou, Y.; Zhao, D.; Fulvio, P. F.; Mayes, R. T. Carbon Materials for Chemical Capacitive Energy Storage. *Adv. Mater.* **2011**, *23*, 4828–4850.
- (7) Shi, H. Activated Carbons and Double Layer Capacitance. *Electrochim. Acta* **1996**, *41* (95), 1633–1639.
- (8) Bui, N. N.; Kim, B. H.; Yang, K. S.; Dela Cruz, M. E.; Ferraris, J. P. Activated Carbon Fibers from Electrospinning of Polyacrylonitrile/pitch Blends. *Carbon N. Y.* **2009**, *47* (10), 2538–2539.
- (9) Bonso, J. S.; Kalaw, G. D.; Ferraris, J. P. High Surface Area Carbon Nanofibers Derived from Electrospun PIM-1 for Energy Storage Applications. *J. Mater. Chem. A* **2014**, *2* (2), 418–424.
- (10) Jang, Y.; Amna, T.; Hassan, M. S.; Gu, J.; Kim, I. Improved Supercapacitor Potential and Antibacterial Activity of Bimetallic CNFs – Sn – ZrO₂ Nano Fibers : Fabrication and Characterization. *RSC Adv.* **2014**, *4*, 17268–17273.
- (11) Ma, C.; Song, Y.; Shi, J.; Zhang, D.; Zhong, M.; Guo, Q.; Liu, L. Phenolic-Based Carbon Nano Fiber Webs Prepared by Electrospinning for Supercapacitors. *Mater. Lett.* **2012**, *76*, 211–214.
- (12) Arulepp, M.; Leis, J.; Miller, F.; Rumma, K.; Lust, E.; Burke, A. F. The Advanced Carbide-Derived Carbon Based Supercapacitor. *J. Memb. Sci.* **2006**, *162*, 1460–1466.
- (13) Han, S.; Kim, M.; Hyeon, T. Direct Fabrication of Mesoporous Carbons Using in-Situ Polymerized Silica Gel Networks as a Template. *Carbon N. Y.* **2003**, *41*, 1525–1532.
- (14) Zhou, Z.; Wu, X.; Hou, H. Electrospun Carbon Nanofibers Surface-Grown with Carbon Nanotubes and Polyaniline for Use as High- Performance Electrode Materials of Supercapacitors. *RSC Adv.* **2014**, *4*, 23622–23629.
- (15) Stoller, M. D.; Park, S.; Yanwu, Z.; An, J.; Ruoff, R. S. Graphene-Based Ultracapacitors. *Nano Lett.* **2008**, *8* (10), 3498–3502.
- (16) Kim, C.; Yang, K. S. Electrochemical Properties of Carbon Nanofiber Web as an Electrode for Supercapacitor Prepared by Electrospinning. *Appl. Phys. Lett.* **2003**, *83* (6), 1216–1219.
- (17) Hosseini, S. S.; Peng, N.; Chung, T. S. Gas Separation Membranes Developed through Integration of Polymer Blending and Dual-Layer Hollow Fiber Spinning Process for Hydrogen and Natural Gas Enrichments. *J. Memb. Sci.* **2010**, *349* (1–2), 156–166.

- (18) Yuxuan, Du.; Xin Zhao, Zilong Huang, Y. L. and Q. Z. Freestanding Composite Electrodes of MnO_x Embedded Carbon Nano Fibers for High- Performance Supercapacitors †. *RSC Adv.* **2014**, 4, 39087–39094.
- (19) Li, B. D.; Xia, Y. Electrospinning of Nanofibers : Reinventing the Wheel ? *Adv. Mater.* **2004**, No. 14, 1151–1170.
- (20) Lazzari, M.; Mastragostino, M.; Pandolfo, G.; Ruiz, V.; Soavi, F. Role of Carbon Porosity and Ion Size in the Development of Ionic Liquid Based Supercapacitors. *J. Electrochem. Soc.* **2011**, 158 (1), A22.
- (21) Jo, E.; Yeo, J. G.; Kim, D. K.; Oh, J. S.; Hong, C. K. Preparation of Well-Controlled Porous Carbon Nanofiber Materials by Varying the Compatibility of Polymer Blends. *Polym. Int.* **2014**, 63 (8), 1471–1477.
- (22) Tran, C.; Kalra, V. Fabrication of Porous Carbon Nano Fibers with Adjustable Pore Sizes as Electrodes for Supercapacitors. *J. Power Sources* **2013**, 235, 289–296.
- (23) Dirican, M.; Zhang, X. Nano Fiber Electrodes for Symmetric and. *RSC Adv.* **2014**, 4, 59427–59435.
- (24) Kim, B.-H.; Yang, K. S.; Ferraris, J. P. Highly Conductive, Mesoporous Carbon Nanofiber Web as Electrode Material for High-Performance Supercapacitors. *Electrochim. Acta* **2012**, 75, 325–331.
- (25) Zhi, M.; Liu, S.; Hong, Z.; Wu, N. Electrospun Activated Carbon Nanofibers for Supercapacitor Electrodes†. *RSC Adv.* **2014**, 4, 43619–43623.
- (26) Hong, C. K.; Yang, K. S.; Oh, S. H.; Ahn, J.; Cho, B.; Nah, C. Effect of Blend Composition on the Morphology Development of Electrospun Fibres Based on PAN / PMMA Blends. *Polym. Int.* **2008**, 57, 1357–1362.
- (27) Nissen, E.; Yang, Y.; Springer, E.; Li, X.; Kresse, I. Morphology and Gas Permselectivity of Blend Membranes of Polyvinylpyridine with Ethylcellulose. *Polymer (Guildf)*. **2001**, 42, 6859–6869.
- (28) Panapitiya, N. P.; Wijenayake, S. N.; Huang, Y.; Bushdiecker, D.; Nguyen, D.; Ratanawanate, C.; Kalaw, G. J.; Gilpin, C. J.; Musselman, I. H.; Balkus, K. J.; Ferraris, J. P. Stabilization of Immiscible Polymer Blends Using Structure Directing Metal Organic Frameworks (MOFs). *Polymer (Guildf)*. **2014**, 55 (8), 2028–2034.
- (29) El-deen, A. G.; Barakat, N. A. M.; Khalil, K. A.; Kim, H. Y. Effective Electrosorptive Electrodes for a Capacitive Deionization Process †. *J. Mater. Chem. A* **2013**, 1, 11001–11010.

- (30) Nataraj, S. K.; Yang, K. S.; Aminabhavi, T. M. Polyacrylonitrile-Based Nanofibers - A State-of-the-Art Review. *Prog. Polym. Sci.* **2012**, 37 (3), 487–513.
- (31) Zhang, H.; Dong, F.; Fang, S.; Ye, C.; Wang, M.; Cheng, H.; Han, Z.; Zhai, S. Journal of Colloid and Interface Science Fabrication of Macroporous Titanium Dioxide Film Using PMMA Microspheres as Template. *J. Colloid Interface Sci.* **2012**, 386 (1), 73–79.
- (32) Duan, G.; Zhang, A. C.; Li, A.; Yang, X.; Lu, L.; Wang, X. Preparation and Characterization of Mesoporous Zirconia Made by Using a Poly (Methyl Methacrylate) Template. *Nanoscale Res Lett* **2008**, 3, 118–122.
- (33) M. Endo, C.Kim, T.Karaki, T.Kasai, M. J.Matthews, S. D.M. Brown, M. S. Dresselhaus, T. T. and Y. N. Structural Characterization of Milled Mesophase Pitch-Based Carbon Fibers. *Carbon N. Y.* **1998**, 36 (11), 1633–1641.
- (34) Yoo, H. D.; Jang, J. H.; Ryu, J. H.; Park, Y.; Oh, S. M. Impedance Analysis of Porous Carbon Electrodes to Predict Rate Capability of Electric Double-Layer Capacitors. *J. Power Sources* **2014**, 267, 411–420.

CHAPTER 3
NOVEL BINDER-FREE ELECTRODE MATERIALS FOR SUPERCAPACITORS
UTILIZING HIGH SURFACE AREA CARBON NANOFIBERS DERIVED FROM
IMMISCIBLE POLYMER BLENDS OF PBI/6FDA-DAM:DABA

Authors – Nimali C. Abeykoon, Velia Garcia, Rangana A. Jayawickramage, Wijayantha Perera,
Jeremy Cure, Yves J. Chabal, Kenneth J. Balkus, Jr., John P. Ferraris

Department of Chemistry and Biochemistry

The University of Texas at Dallas

800 West Campbell Road

Richardson, Texas 75080-3021

Abeykoon, N.C.; Garcia, V.; Jayawickramage, R. A.; Perera W.; Cure, J.; Chabal Y.J.; Balkus, K.J.; Ferraris and J.P.; Novel binder-free electrode materials for supercapacitors utilizing high surface area carbon nanofibers derived from immiscible polymer blends of PBI/6FDA-DAM:DABA, *RSC Adv.*, 2017, 7, 20947–20959.

Reproduced by permission of The Royal Society of Chemistry (RSC)

3.1 Abstract

Carbon nanofibers with high surface area have become promising electrode materials for supercapacitors because of their importance in increasing energy density. In this study, a high free volume polymer, 6FDA-DAM:DABA (6FDD) was blended with polybenzimidazole (PBI) in different ratios to obtain different compositions of PBI/6FDD immiscible polymer blends. Freestanding nanofiber mats were obtained via electrospinning using blend precursors dissolved in N, N-dimethylacetamide (DMAc). Subsequently, carbonization, followed by CO₂ activation at 1000 °C were applied to convert the fiber mats into porous carbon nanofibers (CNFs). The addition of 6FDD shows significant effects on the microstructure and enhancement of surface area of CNFs. The obtained CNFs show specific surface area as high as 3010 m² g⁻¹ with pore sizes comparable to those of the electrolyte ions (PYR₁₄TFSI). This provides good electrolyte accessibility to the pore of the carbon materials resulting in enhanced energy density compared to the CNFs obtained from pure PBI. Electrodes derived from PBI:6FDD (70:30) exhibited outstanding supercapacitor performance in coin cells with specific capacitance of 142 F g⁻¹ at the scan rate of 10 mV s⁻¹ and energy density of 67.5 Wh kg⁻¹ at 1 A g⁻¹ (58 Wh kg⁻¹ at 10 A g⁻¹) thus demonstrating promising electrochemical performance for high performance energy storage system.

3.2 Introduction

Supercapacitors are energy storage devices that possess high power density and good cycle stability with long lifetimes.^{1,2} Currently, supercapacitors are being used in transportation, consumer electronics and industrial applications because of these excellent characteristics.³

Electrochemical double-layer capacitors (EDLCs) are one type of supercapacitor, and are most often comprised of two porous carbon electrodes.⁴ Carbon precursor materials possessing very high surface areas are highly attractive materials to use as electrodes for EDLCs because the amount of energy that is stored and released via electrostatic adsorption and desorption of electrolyte ions on electrode surface greatly depends on the electrode's surface area.^{5,6}

Carbon nanofibers (CNFs) possess high surface areas and are an interesting alternative to the other forms of carbonaceous materials.⁷ Carbon nanofibers can be produced by electrospinning methods from a variety of polymers⁸ such as polyacrylonitrile (PAN)^{9,10}, cellulose¹¹, phenol resin¹², pitch¹³ and different types of polyimides¹⁴. Polybenzimidazole (PBI) is a promising CNF precursor polymer due to its outstanding thermal stability, high carbon yield and spinnability. Moreover, PBI is commercially available. Despite these potential advantages only a limited number of investigations using CNFs derived from PBI for electrode materials in EDLCs have been reported. Kim et al. prepared supercapacitor electrodes using PBI based carbon nanofibers activated by steam which exhibited surface areas of 500–1220 m² g⁻¹.¹⁵ Nanofibers activated at 800 °C showed a capacitance of 202 F g⁻¹ in 1 M H₂SO₄ aqueous electrolyte solution. Due to high thermal stability, PBI electrospun fibers do not require the thermal stabilization in air before carbonization that is common for PAN-based materials, thus saving time and energy. Aromatic polyimides (PI) also have potential as carbon nanofiber precursor polymers for electrode materials because of their high thermal and mechanical stabilities.¹⁶ Li et al. reported the fabrication of CNF using a heterocyclic polyimide containing benzopyrrole and benzimidazole rings.¹⁷ A volumetric capacitance of 159.3 F cm⁻³ at 1 A g⁻¹ in 1 M NaOH was reported. Much research has been carried out on producing

different forms of carbon materials, including CNFs from PIs, but very few studies report the use of PI based CNFs as supercapacitor electrodes.¹⁶

Polymer blending is a very important technique for producing new carbon materials with useful properties beyond the range that can be obtained from a single polymer.¹⁸ The domain size distribution, morphology and miscibility are influenced by the composition of polymer blends. There are several methods to make CNFs from polymer blends.¹⁹ For example two immiscible polymers having different thermal stability, where one acts as a carbonizing polymer and the second acts as a sacrificial polymer which decomposes upon carbonization, can form pores in the fiber to increase surface area.²⁰⁻²² In another case, blends have been prepared utilizing two polymers that both act as carbonizing polymers. This can increase specific properties of CNFs such as conductivity and porosity to tailor the pore size distribution of the resultant carbon fiber matrix. PBI/PI blends are examples where the specific PI component can be tuned to the application.^{23,24} Both miscible and immiscible PBI/PI blends, as well as carbonized blends of PBI/PI have been reported for gas separations.²⁵⁻²⁷ Jung et al. reported fabrication of porous CNFs from miscible PBI /Matrimid blends as electrode materials for supercapacitors. Steam activated CNFs (ACNFs) from PBI/Matrimid (75:25) showed a specific capacitance of 126 F g⁻¹, and energy and power densities of 49 Wh kg⁻¹ and 7 kW kg⁻¹ in an ionic liquid electrolyte, EMITFSI.²⁸ Recently, porous carbon fibers have been prepared from polybenzimidazole/poly-L-lactic acid (PBI/PLLA) blends. PLLA acts as a sacrificial polymer in the blends and lends increased porosity upon decomposition. Specific capacitance of 111.9 F g⁻¹ and highest energy density and power density of 36.9 Wh kg⁻¹ and 7.0 kW kg⁻¹, respectively, were reported for activated PBI/PLLA (8:2)

in EMITFSI electrolyte.²⁹ We are unaware of any reports describing the use of carbonized immiscible blends of PBI/PI for use as electrode materials for supercapacitors.

In this study, immiscible blends of PBI and 6FDA-DAM:DABA (3:2) with different ratios were used as carbon nanofiber precursors as shown in Figure 3.1. PBI was selected as one carbonizing precursor polymer because of above mentioned reasons. The aromatic polyimide, 6FDA-DAM:DABA (3:2), composed of 4,4'-hexafluoroisopropylidene diphthalic anhydride (6FDA), 2,4,6-trimethyl-1,3-phenylenediamine (DAM) and 3,5-diaminobenzoic acid (DABA) [denoted as 6FDD] was selected as the second carbonizing polymer for blend preparation based on several considerations. One of the important properties of the 6FDD polymer is its high free volume (> Ø.18) due to the bulky hexafluoropropyl bridging moiety on its backbone which restricts chain mobility and interrupts chain packing.^{30,31} The use of this high free volume polymer leads to an increase in the surface area of the resulting fiber. The ability to crosslink due to decomposition of the pendant carboxylic acid on DABA moieties of the 6FDD polymer also facilitates the carbonization processes. During carbonization, crosslinking can lock the free volume of the precursor into the carbon fiber matrix.³² After mixing of two polymers, the blend solution was electrospun to obtain phase separated nanofiber as shown in Figure 3.1. Here, we explore the possibility of using incompatible blends with two carbonizing polymers to achieve improved performance by controlling the microstructure. A uniform microstructure of 6FDD in PBI is important to tailor the micro/meso pore structure. 6FDD is more selective than PBI to CO₂ activation because of its faster etching rate (vide infra). The surface area and electrochemical performance of the resulting CNFs were investigated as a function of 6FDD/PBI ratio.

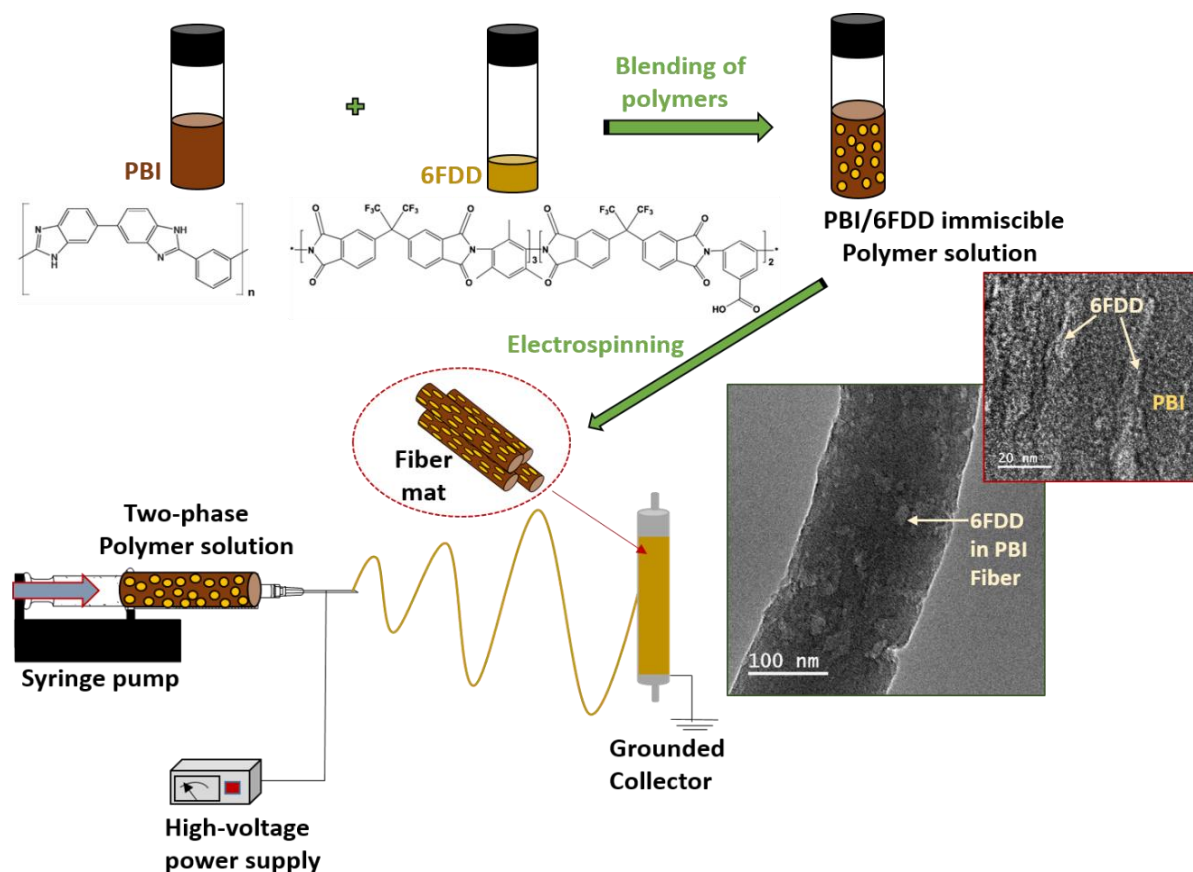


Figure 3.1. Schematic illustration of the fabrication of the phase separated nanofibers using PBI/6FDD polymer blends and structures of PBI and 6FDD.

3.3 Experimental

3.3.1 Materials

Polybenzimidazole (PBI) was purchased from PBI Performance Inc. (26 wt% in DMAc, 1.5% (w/w) LiCl, Mw 30,000) and was used as received. 4,4-Hexafluoroisopropylidene diphthalic anhydride (6FDA, >99% purity) was purchased from Akron Polymer Systems Inc. and dried at 150 °C under vacuum prior to use. 2,4,6-Trimethyl-1, 3-phenylenediamine (DAM, >97% purity) was purchased from TCI America. DAM was purified by vacuum sublimation. 3,5-

Diaminobenzoic acid (DABA, 98% purity) was purchased from Sigma Aldrich and was purified by recrystallization from water. Anhydrous 1-methyl-2-pyrrolidone (NMP, 99.8% purity) was purchased from Sigma Aldrich and was dried over activated 4A molecular sieves purchased from Sigma Aldrich. Anhydrous N, N-dimethylacetamide (DMAc, 99.8% purity) was purchased from EMD chemicals and used for the electrospinning solutions. Electrochemical grade 1-Butyl-1-methylpyrrolidinium bis(trifluoromethylsulfonyl)imide (PYR14TFSI, 99.5% purity) was purchased from IoLiTec, Inc. and ethylene carbonate (EC), (99.5% purity) and propylene carbonate PC, (99.5% purity) were purchased from Sigma Aldrich, and were used without further purification.

3.3.2 Synthesis of 6FDA-DAM:DABA (6FDD)

The 6FDA-DAM:DABA copolyimide was synthesized using monomers 6FDA, DAM and DABA with 3:2 DAM:DABA ratio by following a reported procedure.³³ Synthesis of 6FDA-DAM:DABA(3:2) via the poly(amic acid) is shown in Figure S3.1. First, a solution of 6FDA (2.000 g) in NMP (8.5 mL) was added to a solution of DABA (0.274 g) in NMP (2.5 mL) in a three-neck flask and stirred for 1 h at room temperature. A solution of DAM (0.406 g) in NMP (2.0 mL) was then added to the reaction flask and stirred at room temperature for 26 h. Next, the temperature was raised to 190 °C for 26 h and a Dean-Stark trap filled with 12 mL of o-dichlorobenzene was attached. After imidization, the polymer solution was precipitated in methanol and washed with methanol several times. The polymer was dried in a vacuum oven at 120 °C. Brown coloured polymer (91% yield) was obtained with Mw of 119 kDa and PDI of 2.5.

3.3.3 Preparation of CNF and ACNFs

20 wt% of PBI/6FDA-DAM:DABA polymer blends in DMAc were used for electrospinning. First PBI and 6FDA-DAM:DABA were dissolved in DMAc separately by stirring at 80 °C for 4 h. Then 6FDD solutions were added drop wise to PBI solutions with stirring. The blend solutions were further stirred at 80 °C for 12 h before electrospinning. The polymer ratio of PBI/6FDD was selected as 90/10, 70/30 and 50/50 by weight and denoted as PBI:6FDD(90:10), PBI:6FDD(70:30) and PBI:6FDD(50:50), respectively. Also, 20 wt% of pure PBI solution was prepared according to the same procedure as a control to compare with the blend solutions. Then electrospinning was applied to obtain fibers. A 12 mL syringe was filled with 10 mL of the blend solution. An applied voltage of 18-20 kV (Gamma High Voltage Research, Inc., power supply) was used and solutions were fed through a 20G needle at a constant rate using a syringe pump. Parameters for the electrospinning were set as follows: flow rate of 0.3 ml h⁻¹, tip-to-collector distance of 15 cm and rotating speed of grounded drum collector at 300 rpm. As-spun nanofibers were carbonized under helium atmosphere. First, the electrospun fiber samples were heated for 1h at 450 °C and then the temperature was increased up to 1000 °C at a heating rate of 5 °C min⁻¹. The carbonization process was performed at 1000 °C for 1h and then CO₂ was introduced during 30 min at this temperature to activate the samples and finally cooled to room temperature. The detailed carbonization and activation protocol is illustrated in Figure 3.2.

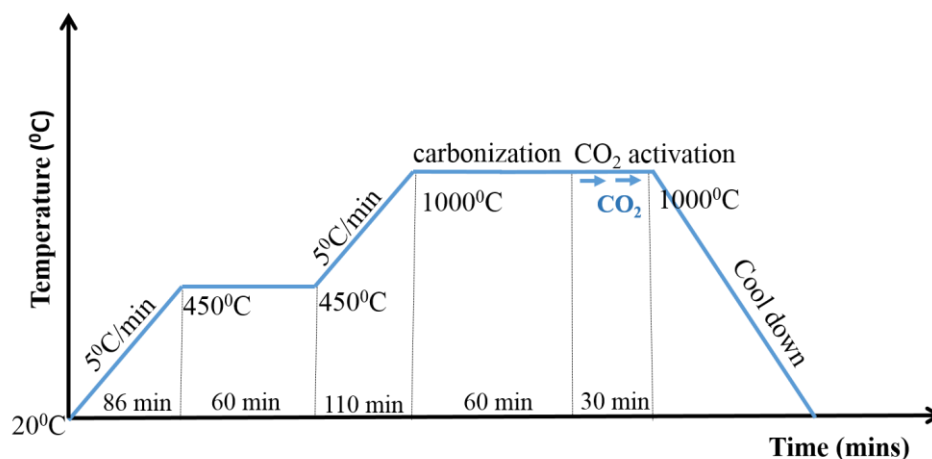


Figure 3.2. Carbonization and CO₂ activation protocol.

3.3.4 Characterization

The structure of synthesized 6FDA-DAM:DABA(3:2) was confirmed by proton NMR (¹H NMR) and attenuated total reflectance Fourier transform infrared (ATR-FTIR) spectroscopy. NMR spectra were recorded on a Bruker AVANCE III™ (500 MHz) in (CD₃)₂SO with TMS (¹H) as internal standard. FTIR spectra of the synthesized polymer and as-spun samples were acquired using a Nicolet 360 FTIR spectrophotometer. The molecular weight of as-synthesized 6FDD was determined by gel permeation chromatography (Viscotek GPCmax, VE2001) using two ViscoGEL columns in series (I-MBHMW 3078, Viscotek) and a Triple Array Detector (Module TDA 320, Viscotek). THF was used as the mobile phase at a flow rate of 1 mL min⁻¹ and polystyrene standards (Polymer Laboratories) were used for calibration. Scanning electron microscopy (SEM) was performed to characterize morphologies of samples using a Zeiss-LEO (Model 1530) Scanning electron microscope equipped with a field emission gun operating at 10 keV acceleration voltage. Gold coated samples were used for SEM imaging of the electrospun mats of the PBI and the blends whereas images of the carbonized samples were obtained without

gold coating. The average fiber diameter of the electrospun and carbonized fiber are reported based on measurements of 100 fibers and diameter distributions of the samples were obtained using the publically available ImageJ software. Transmission electron microscope (TEM) images were obtained using a JEOL JEM-2100 TEM at 200 kV (JEOL Co Ltd). Samples were prepared by dispersing electrospun fibers in methanol and the fishing technique was used to obtain fibers on to the 300 mesh Cu Lacey Carbon grid. The microstructures of the polymer blends were observed by using the thin film membranes prepared by solvent-casting the same solutions used for electrospinning onto glass substrates, employing a Sheen (1133N) automatic casting table equipped with a doctor blade. SEMs of the cross sections were taken after selectively extracting 6FDD from these prepared membranes using THF as a solvent in a Soxhlet extractor. To determine the thermal stability and the carbon yield in all blend compositions, thermogravimetric analysis (TGA) was carried out with a TA Instruments SDT Q600 Analyzer by heating from room temperature to 1000 °C at a heating rate of 10 °C min⁻¹ under a nitrogen atmosphere flow rate of 50 ml min⁻¹. Raman spectra of the carbonized materials were recorded on a Nicolet Almega XR Raman spectrometer equipped with a 780 nm laser. Surface areas and pore properties of the carbon fibers were characterized using N₂ adsorption/desorption isotherms measured at 77K using a Quantachrome Autosorb-1 analyzer. Samples were degassed at 120 °C before being analyzed. The Brunauer–Emmett–Teller (BET) method was used to calculate surface area and Density Functional Theory (DFT) was used to obtain the pore size distribution. X-ray diffraction (XRD) patterns were collected by using a RigakuUltima IV X-ray diffractometer using Cu K α radiation. X-Ray photoelectron Spectroscopy (XPS) were recorded with a Physical Electronics Quantum 2000 scanning ESCA microprobe spectrometer equipped with a monochromatic Al K α source and a

concentric hemispherical electron energy analyzer under ultrahigh vacuum (10^{-9} mbar). The samples were located at 45° with respect to the analyzer. Before the recordings of the XPS spectra, the samples were cleaned by an Argon sputtering performed at 1 KV on a 1 mm^2 surface area during 5 min. A pass energy of 23.50 eV and a resolution of 0.2 eV step over 12-20 eV regions were used during the analyses of the followings elements C 1s (280-295 eV), N 1s (394-406 eV), O 1s (526-539 eV), F 1s (679-699 eV), Si 2p (97-107 eV) and Ar 2p (235-255 eV).

3.3.5 Electrochemical tests

Supercapacitor test cells were assembled in a CR2032 coin cell configuration using two electrodes punched out from the carbonized mat. The coin cell assembly parts were obtained from Shenzhen Yongxingye Precision Machinery Mould Co. Ltd., China. Carbon coated aluminum was used as the current collectors on each side of electrodes that were separated by a Gore™ PTFE separator. The electrode performance was measured in an ionic liquid electrolyte mixture of 1-Butyl-1-methylpyrrolidinium bis(trifluoromethylsulfonyl)imide (PYR₁₄TFSI), propylene carbonate(PC) and ethylene carbonate(EC), (PYR₁₄TFSI:PC:EC) (3:3:2). All the coin cells were assembled inside a nitrogen filled glovebox (Vacuum Atmospheres Company). Coin cells were tested using an Arbin Supercapacitor Testing Station (SCTS). Cyclic voltammetry (CV) and constant current charge/discharge tests (CDC) were performed to calculate specific capacitance and energy density. CV was performed from -2 V to 2 V by varying the scan rate from 10 to 100 mV s⁻¹. CDC was obtained between 3.5 V and 0 V. Electrochemical impedance spectroscopy was done at 0 V DC bias over the frequency range of 100 kHz to 10 mHz using a PARSTAT 2273 Galvanostat (Princeton Applied Research) operated with PowerSuite software.

3.4 Results and discussion

3.4.1 Characterization of the polymer

Characterization of the 6FDD polymer is included in supplementary information. The molecular weight of the polymer (Mw) was 119 kDa with PDI of 2.5. The structure of the 6FDD was confirmed by ¹H-NMR spectroscopy (Figure S3.2 (a)), thermogravimetric analysis (TGA) (Figure S3.2 (b)) and FT-IR spectroscopy (Figure S3.2 (c)). The two absorption peaks appearing at 1780 cm⁻¹ and 1720 cm⁻¹ in the FT-IR spectrum of 6FDD (Figure S3.2 (c)), ascribed to asymmetric and symmetric stretching vibrations of the imide C=O, respectively, indicate complete conversion of the poly(amic acid) to the polyimide.³⁴

3.4.2 Characterization of the material

Electrospinning yielded free standing and flexible fiber mats of the precursor polymer blends. SEM images of as-spun fibers obtained for the different blend compositions are presented in Figure 3.3. All of the as-spun mats exhibited long, continuous nanofibers. Table 3.1 shows average fiber diameters of as-spun samples and carbonized samples, respectively. The diameter of the fibers decreases with increasing 6FDD fraction. SEM of as spun PBI shows fibers consisting of both large and small diameters with a large standard deviation of the fiber diameter compared to the blends. After blending with 6FDD, fiber diameters become more uniform for all the compositions. Figure 3.4 shows the SEM images of nanofibers carbonized and activated at 1000 °C. The fiber diameters became smaller after carbonization and the shapes of the CNFs are well maintained and retain the fibrous morphology. Diameters of the fibers decreases in the order PBI

>PBI:6FDD(90:10) > PBI:6FDD(70:30)> PBI:6FDD(50:50) as shown in Table 3.1. Smaller diameter fibers are more advantageous to obtain good performance because of their higher surface area.

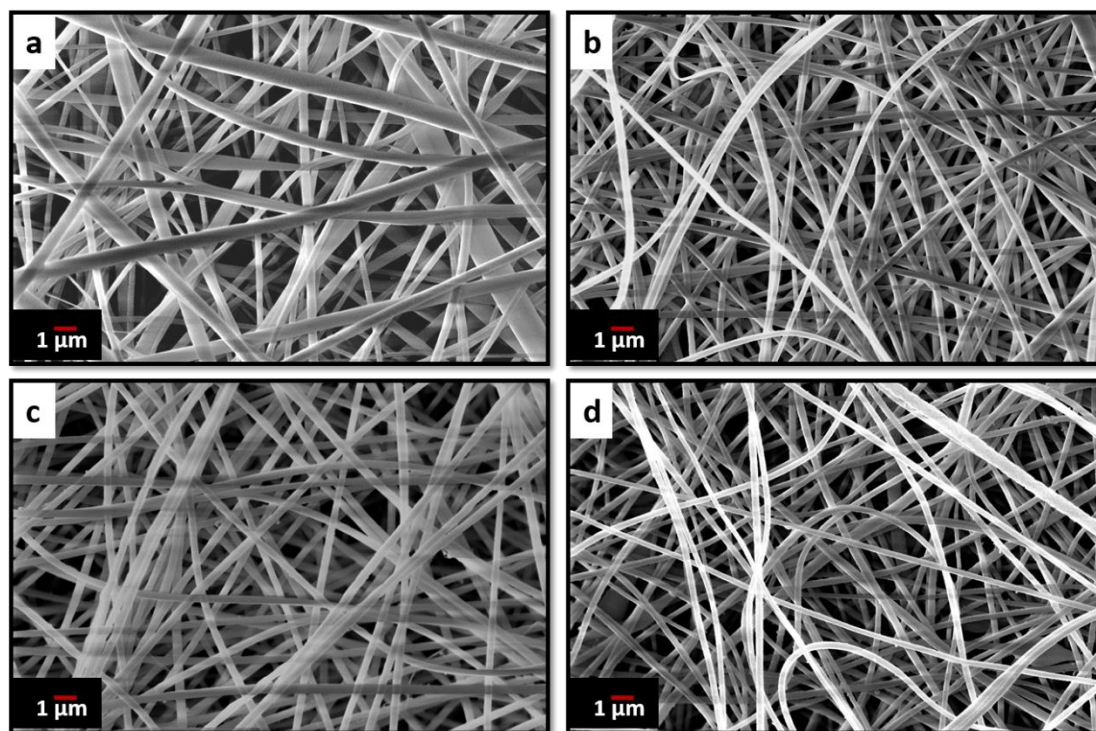


Figure 3.3. SEM images of electrospun (a) PBI, (b) PBI:6FDD(90:10), (c) PBI:6FDD(70:30) and (d) PBI:6FDD(50:50) nanofiber mats.

Table 3.1. Average fiber diameter of PBI and the PBI/6FDD blends.

Precursor	As spun fiber diameter (nm)	Carbonized fiber diameter (nm)
PBI	385±163	180±73
PBI:6FDD (90:10)	306±14	174±26
PBI:6FDD (70:30)	288±14	157±10
PBI:6FDD (50:50)	263±27	137±11

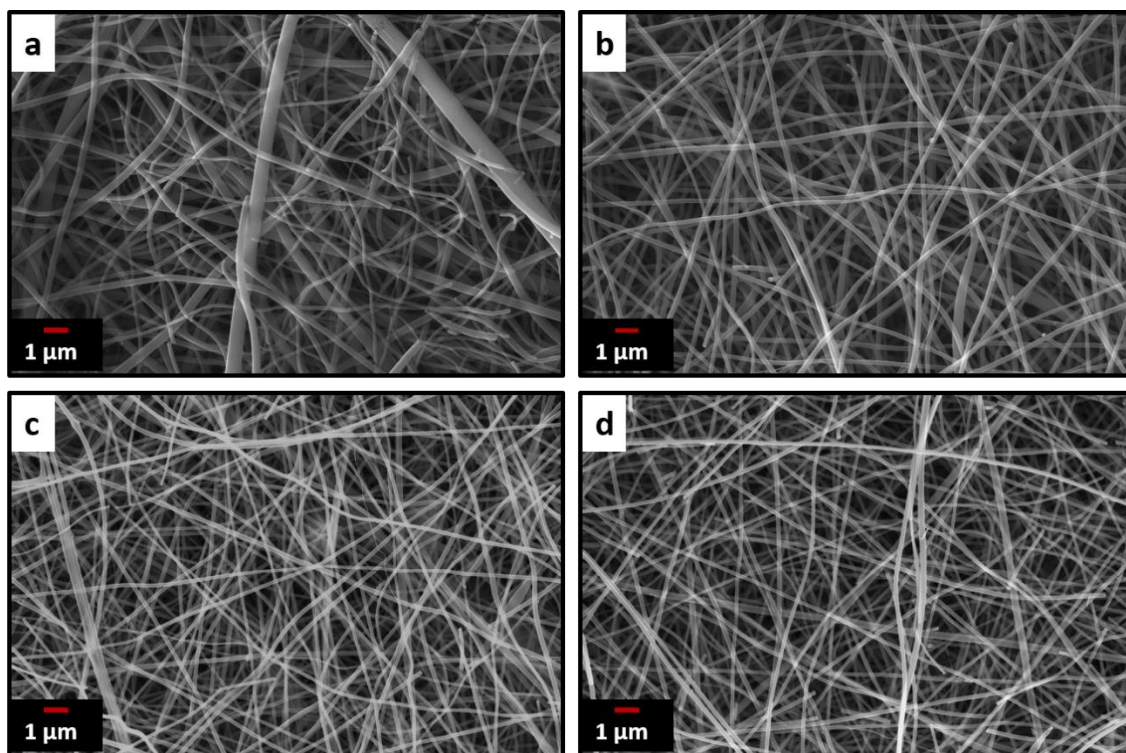


Figure 3.4. SEM images of carbonized and activated (a) PBI, (b) PBI:6FDD(90:10), (c) PBI:6FDD(70:30) and (d) PBI:6FDD(50:50) nanofiber mats.

Figure 3.5 (a) and (c) show SEMs of the cross sections of PBI/6FDD of 70/30 and 50/50 blend films, respectively, after THF-extraction of 6FDD. PBI was the continuous phase and 6FDD was the dispersed phase. The size and shape of the dispersed minor phase in the immiscible blends of PBI/6FDD changed with the ratio of the two polymers with larger domain sizes appearing at the higher amounts of 6FDD. This trend can be explained by effect of enhanced coalescence of the 6FDD domains occurring during the phase separation process. The probability of collision between droplets would increase by increasing the composition of the dispersed phase.³⁵ Because of that, at lower concentrations of 6FDD (30%), blending of two polymers resulted to a fine-size morphology with smaller domains compared to the 50% concentration of 6FDD. It is also possible

that the higher amount of 6FDD leads to aggregation of 6FDD before it disperses within the PBI matrix during polymer mixing.

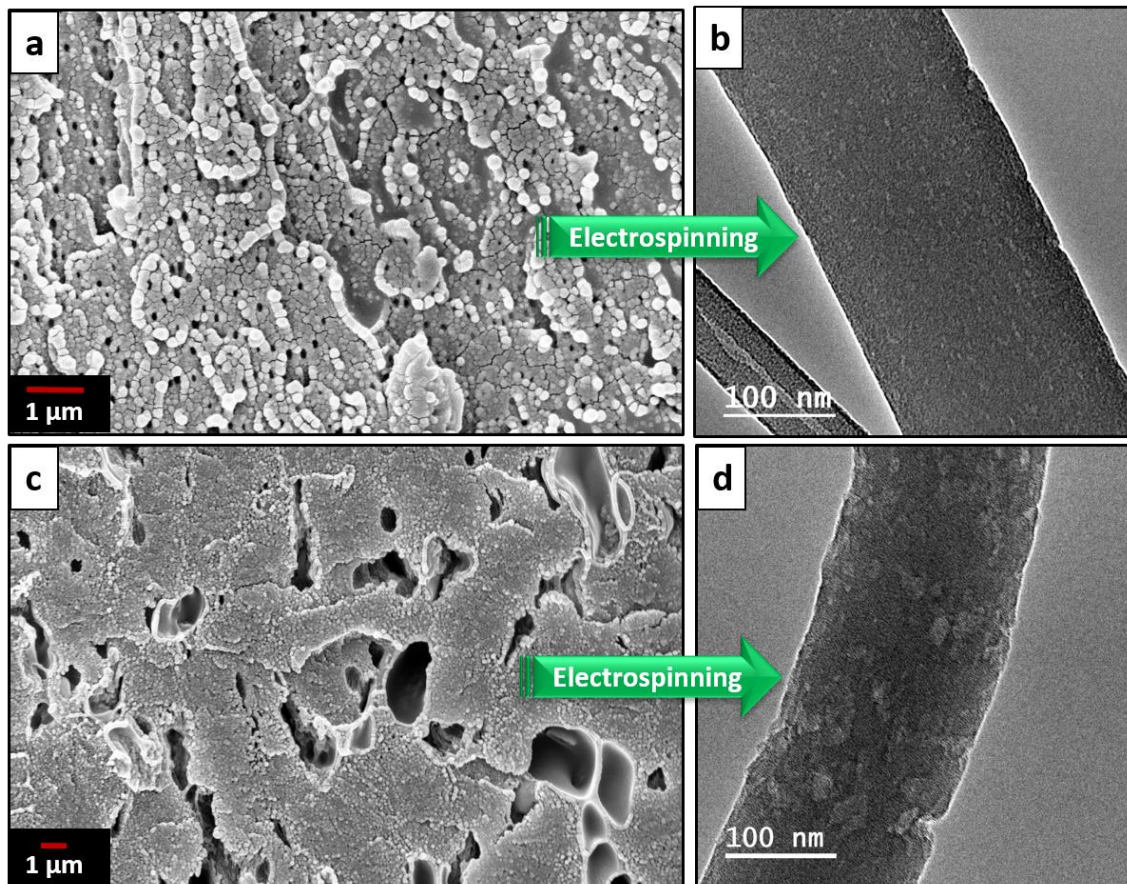


Figure 3.5. SEM images of the cross-section of the 6FDD extracted (a) PBI:6FDD(70:30) and (c) PBI:6FDD(50:50) films that were cast directly from electrospinning solutions and TEM images of electrospun fiber of (b) PBI:6FDD(70:30) and (d) PBI:6FDD(50:50).

This behaviour accounts for the different morphologies of the fibers after electrospinning of these blends as shown in TEM images of Figure 3.5 (b) and (d). The same trend of domain sizes was observed in the fiber as for the cast membranes but with somewhat more elongated domains after electrospinning. Figure 3.6 shows the TEM images of the electrospun and carbonized fibers with different compositions of PBI/6FDD. In the TEM images, all the fibers from the blend solutions

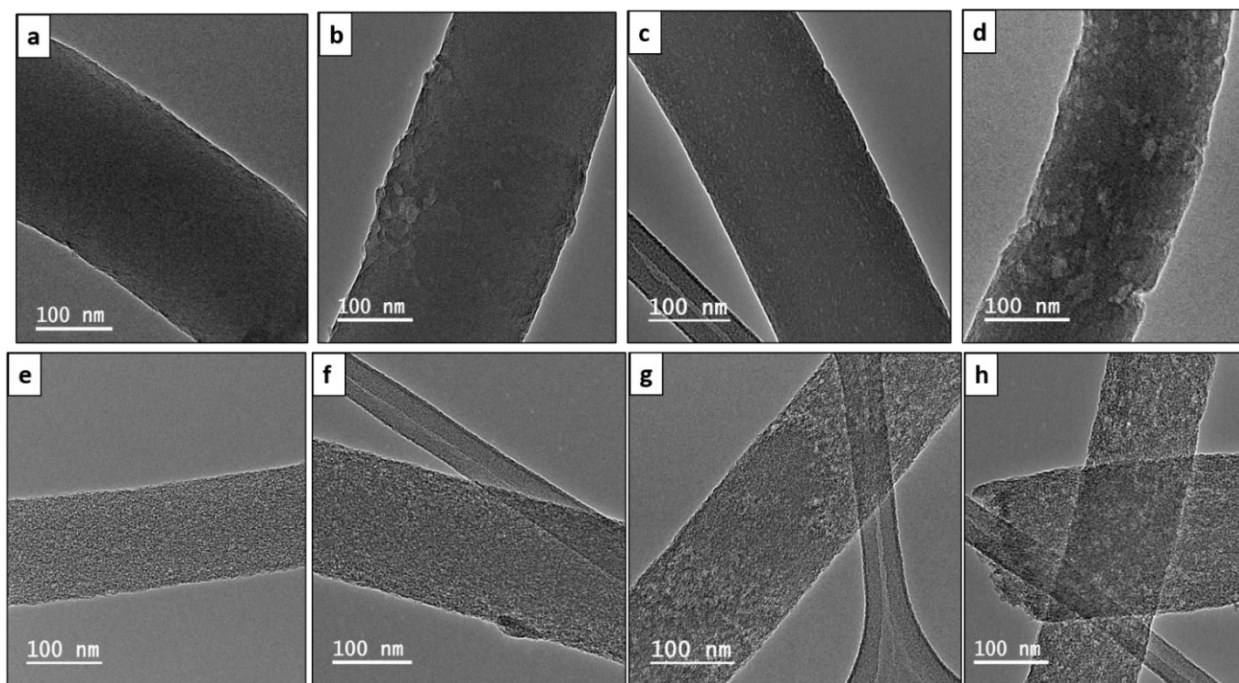


Figure 3.6. TEM images of electrospun (a) PBI, (b) PBI:6FDD(90:10), (c) PBI:6FDD(70:30), (d) PBI:6FDD(50:50) nanofibers and carbonized and activated (e) PBI, (f) PBI:6FDD(90:10), (g) PBI:6FDD(70:30), (h) PBI:6FDD(50:50) nanofibers.

exhibited nanophase-separated domains, with isolated spheres of 6FDD dispersed in the continuous phase of PBI. Also, the 70/30 blend was found to have very uniform and smaller domains (area of 6FDD domain, $45 \pm 15 \text{ nm}^2$) in contrast to the 90/10 and 50/50 immiscible blends (area of 6FDD domain, $179 \pm 149 \text{ nm}^2$). The uniformity shown by 70/30 blend was important to tailor pore size distribution because the CO_2 etch rate of the carbonized 6FDD at 1000°C is approximately 20% faster than that of the carbonized PBI. The etch rates of the individual carbonized polymers of PBI and 6FDD were measured experimentally by separately activating thin film membranes of PBI and 6FDD for 30 min with CO_2 following the same thermal treatment procedure as shown in Figure 3.2 and then measuring mass before and after CO_2 activation. Thus,

the fine morphology of 70/30 blends ultimately leads to a balance of micro and meso pores on the activated carbon fiber. These different morphologies created by immiscible blends with various compositions greatly affect the resulting surface characteristics of fibers as confirmed by surface area analysis, and ultimately the electrochemical performance of electrodes made from these carbonized fibers.

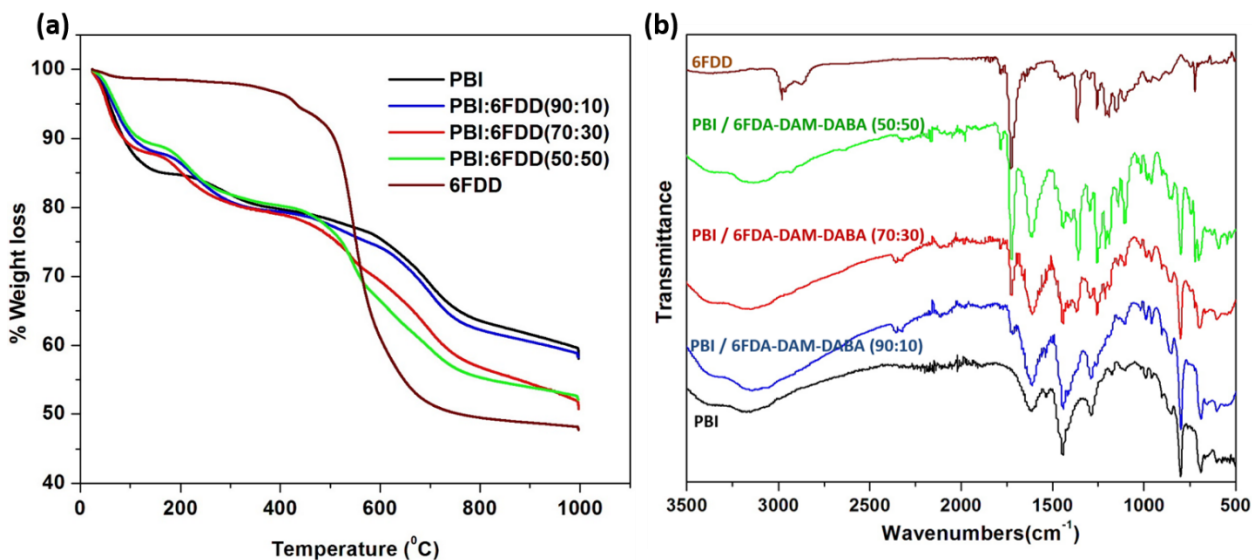


Figure 3.7. TGA analysis (a) of as-spun mat of PBI and blends (b) and FTIR analysis.

Figure 3.7(a) shows weight-loss curves obtained from TGA in a N₂ atmosphere for electrospun mats of pure PBI and PBI/6FDD blends. Pure 6FDD has a decomposition temperature around 490 °C. Three temperature regions at which mass losses occur can be clearly distinguished from the TGA profiles. These results are consistent with the previously reported thermal studies of polyimides by Kratochvil et al.³² The first weight loss up to 100 °C is associated with the evaporation of water and the second mass loss up to 250 °C is attributed to the evolution of trace amounts of residual solvent used for electrospinning. The significant amount of mass loss

associated with main backbone decomposition of the polymer initiates at about 470 °C. The TGA profile of PBI:6FDD (50:50) blend, which has the highest percentage of 6FDD clearly shows a mass loss in this temperature region. Decarboxylation of DABA occurs over the temperature range of 350-390 °C but doesn't contribute to significant weight loss (normally around 3%). The carbon yields for PBI, PBI:6FDD(90:10), PBI:6FDD(70:30) and PBI:6FDD(50:50) at 1000 °C were 58.2%, 58.1%, 50.7% and 52.1%, respectively.

FT-IR analysis shown in Figure 3.7(b) confirms the blending of PBI and 6FDD. PBI and 6FDD show characteristic peaks at 3500–2500 cm^{-1} for the N–H bond and at 1630 cm^{-1} for the C=N bond, respectively.³⁶ The band appearing at 1460 cm^{-1} is assigned to the in-plane deformation peak of the imidazole ring. Pure 6FDD shows peaks at 1780 cm^{-1} and 1720 cm^{-1} that are assigned to the symmetric and asymmetric stretching vibrations of the imide C=O, respectively. The FTIR spectra of the three blends show a combination of the peaks of the individual components in the blends. The intensities of peaks at 1780 and 1720 cm^{-1} increase with increasing composition of 6FDD in the blend from 10% to 50% and become dominant in the 50:50 blend.

Figure 3.8 shows the Raman spectra of carbonized samples. The first band around 1330 cm^{-1} (D-band) is due to presence of disordered carbon and the peak at 1590 cm^{-1} (G-band) is due to presence of highly oriented graphitic carbon.³⁷ These two bands appear in all the spectra and confirms the formation of ordered graphitic structures. The relative intensity ratio of the D-band to the G-band, represented as I_D/I_G depends on the degree of graphitization and a lower I_D/I_G ratio indicates existence of the higher amount of ordered graphitic carbon in the sample. Lorentzian equation was used for peak fitting in order to calculate the ratios of the integrated area intensity of D band to G band (I_D/I_G) of all the spectra. OriginPro 8.0 software was used to deconvolute spectra into

Lorentzian peaks and peak area obtained for D and G bands after fitting were used to calculate the I_D/I_G ratio. All blend samples showed I_D/I_G ratios in between 3.9-3.7, which are lower than pure PBI (4.01) suggesting that crosslinking of 6FDD facilitated the formation of more ordered graphitic structure during carbonization.³⁸⁻⁴⁰ Intense 2D bands observed around 2660 cm^{-1} for blends, and especially for 70/30 and 50/50 blends compared to the PBI, confirms the structural development of carbon materials after blending with 6FDD. The graphitic crystallite size (L_a) can be determine using Tuinstra-Koenig equation, $L_a \text{ (nm)} = 4.4/(I_D/I_G)$. The graphitic crystallite sizes (L_a) obtained for blends were $\sim 1.1 \text{ nm}$.⁴¹

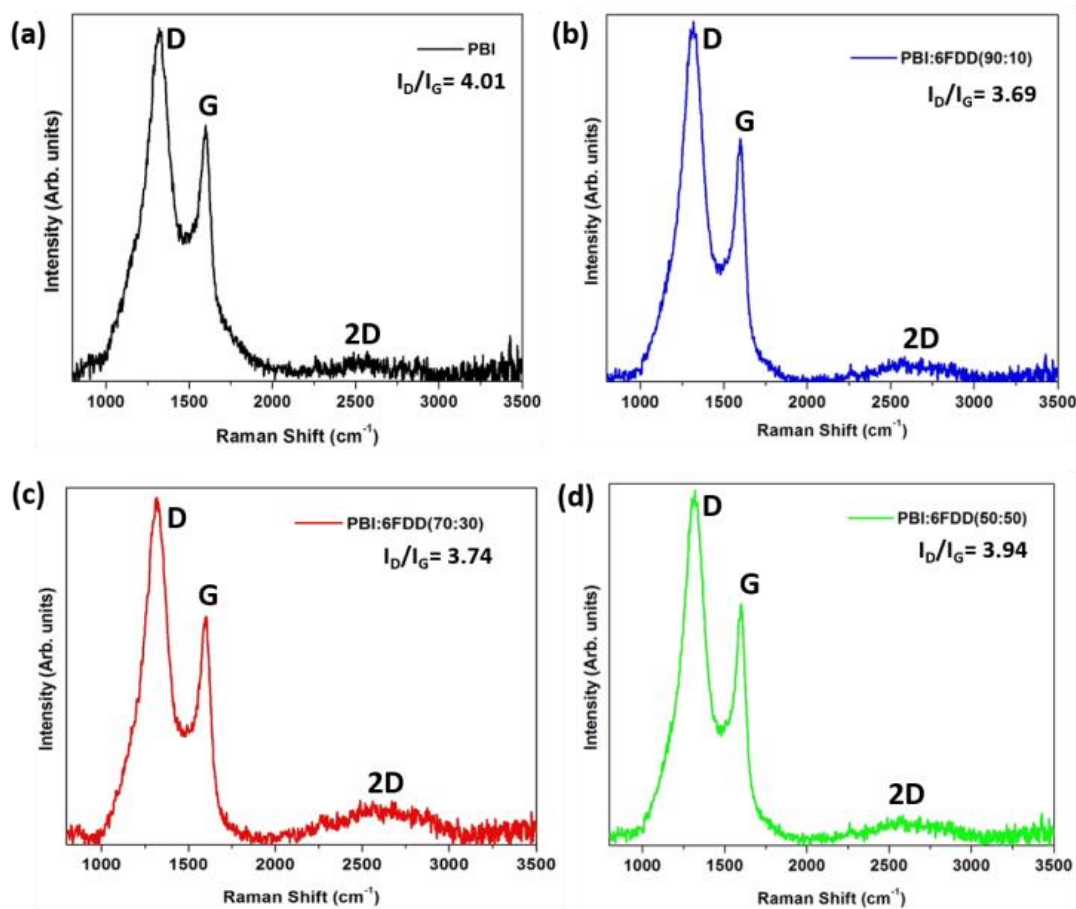


Figure 3.8. Raman spectra of CNFs derived from (a) PBI, (b) PBI:6FDD(90:10), (c) PBI:6FDD(70:30) and (d) PBI:6FDD(50:50).

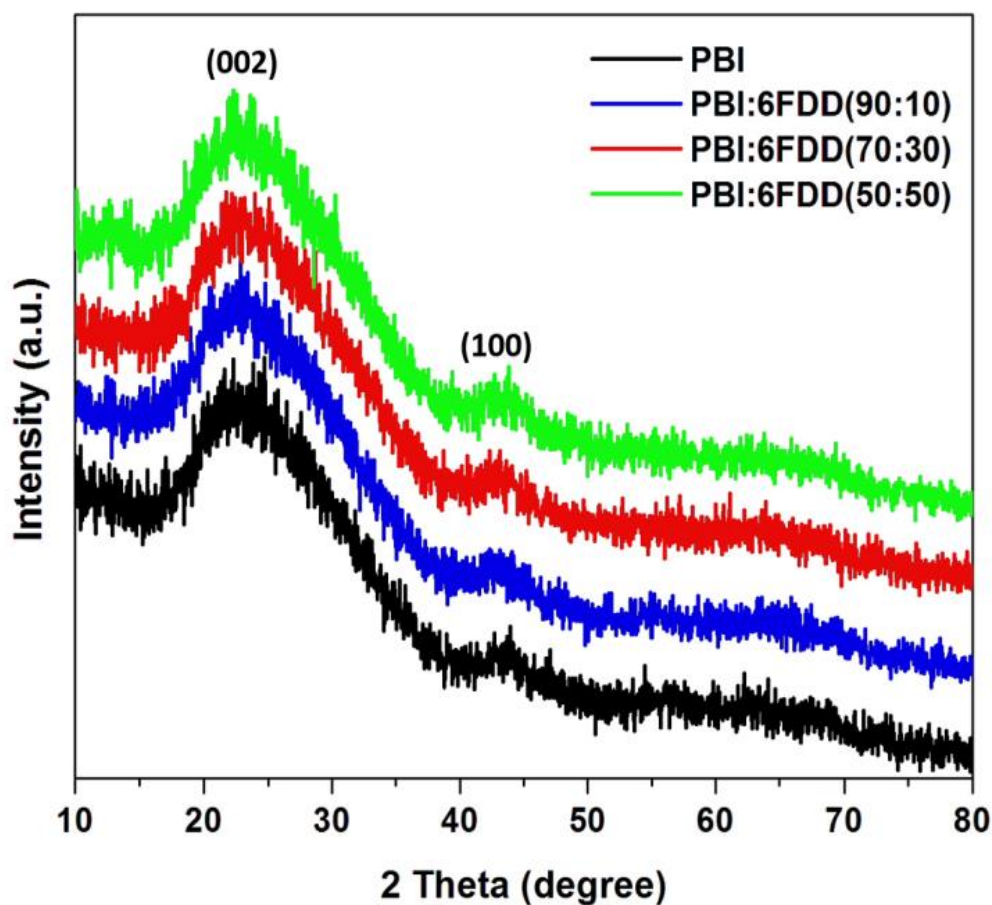


Figure 3.9. XRD patterns of CNFs derived from PBI and PBI:6FDD blends.

X-ray diffraction (XRD) patterns of all the carbonized samples were recorded as shown in Figure 3.9 to further analyze structure and degree of graphitization of all samples. The XRD pattern of all the carbonized samples consists of a broad diffraction peak centered at around 24° (2θ) and a small peak around 44° (2θ), which correspond to (002) and (100) graphite planes of carbon, respectively and which confirms that all the samples have the graphitic structure.^{42,43}

X-ray photoelectron spectroscopy (XPS) was performed to obtain surface elemental composition of carbonized samples and survey spectra were shown in Figure 3.10(a). Three distinguishing peaks for C, N and O were observed in the survey spectra of all the samples and atomic percentages

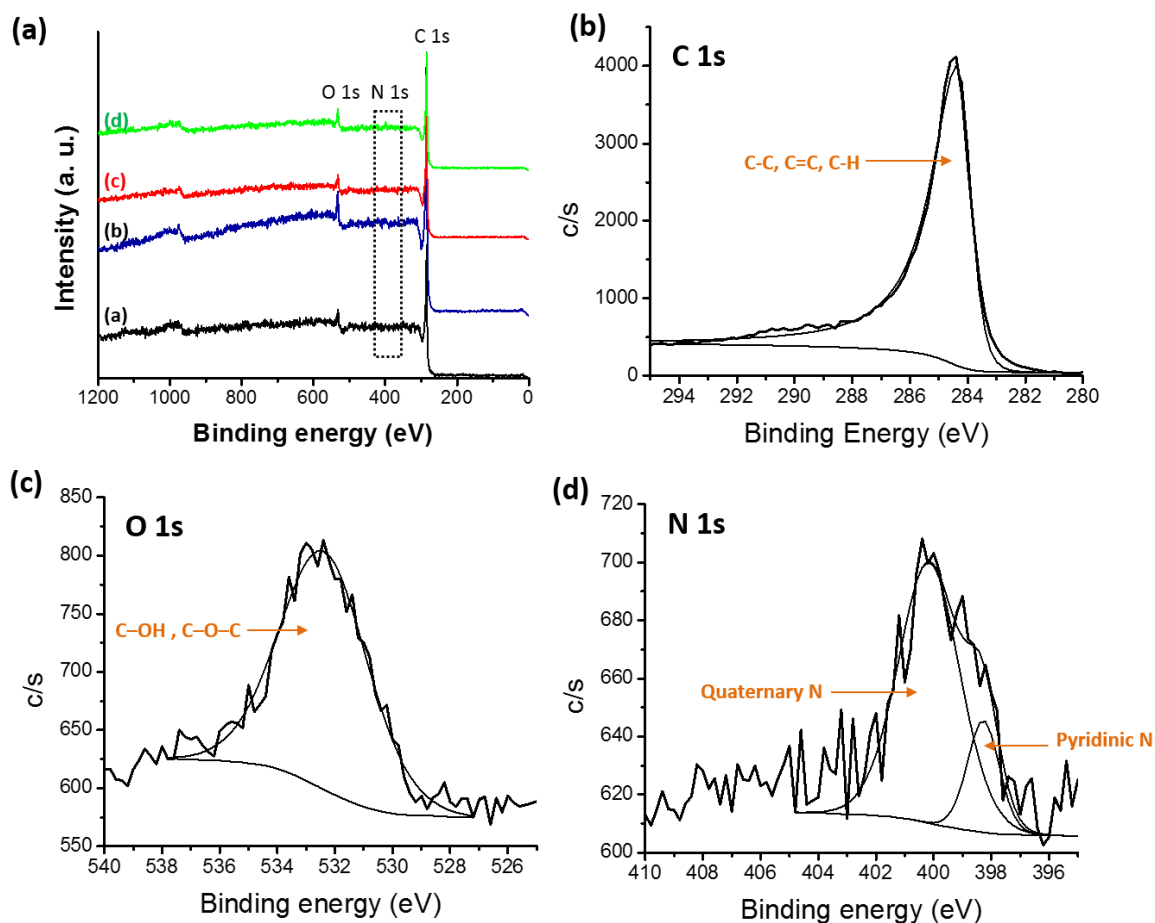


Figure 3.10. (a) XPS survey spectra of all CNFs samples (inset , (a) PBI, (b) PBI:6FDD (90:10), PBI:6FDD (70:30) and (d) PBI:6FDD (50:50), High-resolution deconvoluted (b) C 1s, (c) O 1s, and (d) N 1s, XPS spectra of CNFs derived from PBI:6FDD(70:30).

of C, O and N for all the carbonized samples were shown in Table 3.2. Trace amounts of Fluorine (F) were detected in blends which originated from the CF_3 moiety in 6FDA. Atomic percentage of F 1s was 0.09%, 0.05% and 0.31% for PBI:6FDD (90:10), PBI:6FDD (70:30) and PBI:6FDD (50:50), respectively. Also a trace amount of Si was detected which attributed to the quartz tube used for carbonization. The deconvoluted XPS spectra of C 1s, N1s and O1s for PBI:6FDD (70:30) are shown in the Figure 3.10(b), 3.10(c) and 3.10(d). Figure S3.3, Figure S3.4 and Figure S3.5 show deconvoluted XPS spectra of C 1s, N1s and O1s for PBI, PBI:6FDD (90:10) and PBI:6FDD

(50:50). High resolution XPS spectrum of C 1s for all the samples shows mainly a large peak at a binding energy of 284.3 eV for C-C peak for graphite (sp^2 bonded carbon).⁴⁴ The deconvoluted high resolution O 1s spectrum also mainly consist of one peak at the binding energy of 532.3 eV assigned to the C–OH or C–O–C.⁴⁵ The deconvoluted N 1s spectrum has peaks at 398.2 eV and 401.1eV, are attributed to pyridinic nitrogen and quaternary nitrogen atoms.⁴³

Table 3.2. Chemical composition of C 1s, N 1s and O 1s obtained from the XPS spectra.

Precursor	C 1s(at.%)	O 1s (at.%)	N 1s (at.%)
PBI	94.69	3.09	1.25
PBI:6FDD (90:10)	95.15	3.04	1.60
PBI:6FDD (70:30)	95.55	2.96	1.41
PBI:6FDD (50:50)	93.76	3.58	1.79

3.4.3 Nitrogen adsorption and pore size analysis

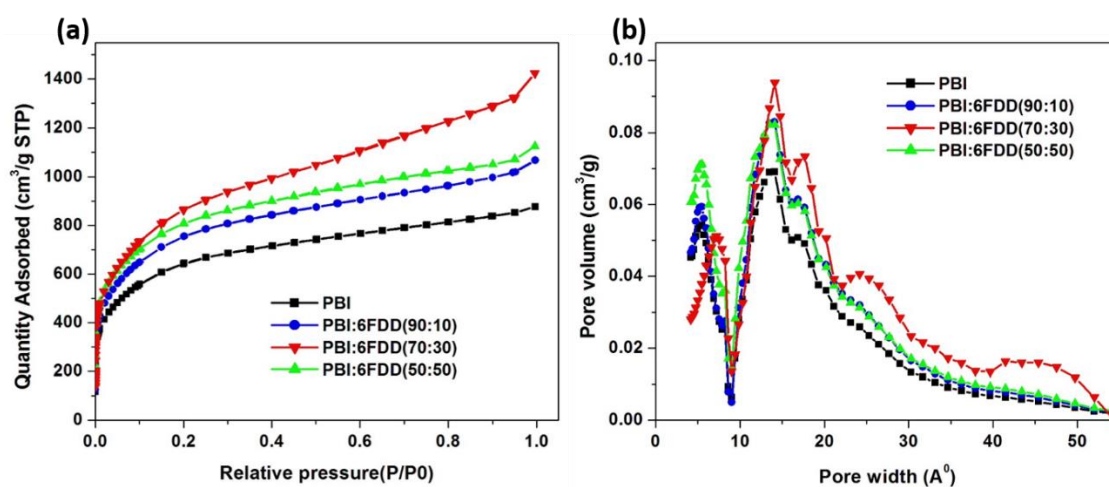


Figure 3.11. (a) Nitrogen adsorption/desorption isotherms and (b) pore size distribution for CNFs derived from ((a) PBI, (b) PBI: 6FDD(90:10), (c) PBI:6FDD(70:30) and (d) PBI:6FDD(50:50).

Table 3.3. Surface area and pore volume of PBI and PBI/6FDD based carbon nanofibers

Precursor	Surface area (m ² /g)	Total pore Volume (cm ³ /g)	V _{micro} (cm ³ /g)	V _{meso} (cm ³ /g)	% micro pores	% meso pores	Micropore /mesopore ratio
PBI	2297	1.1009	0.7345	0.3664	66.7	33.3	2.01
PBI:6FDD (90:10)	2795	1.2998	0.8495	0.4503	65.3	34.7	1.89
PBI:6FDD (70:30)	3010	1.6077	0.9205	0.6872	57.2	42.8	1.34
PBI:6FDD (50:50)	2879	1.3913	0.9279	0.4634	66.7	33.3	2.00

Nitrogen adsorption and pore size analysis were used to investigate the effect of blend compositions on the surface area properties and pore size distributions of the prepared CNFs. Isotherms for the carbon derived from the various precursors are shown in Figure 3.11(a). The adsorption isotherms showed typical type I behavior representing the microporous adsorption with the absence of hysteresis loop. Figure 3.11(b) shows the pore size distribution of activated CNFs. In order to derive maximum capacitance of EDLC, the pore sizes of electrode materials should be similar to the sizes of the electrolyte ions.⁴⁶⁻⁴⁸ Capacitance decreases when the pore size is too small to allow ions to enter the pores. The average pore sizes of the carbonized PBI/6FDD blends (1.3 nm) were close to the cation and anion size of the PYR₁₄TFSI electrolyte which are reported as 1.1 nm and 0.7 nm, respectively.⁴⁹ The matching of the pores of electrodes prepared from PBI/6FDD blends with ion size of electrolyte resulted in the significant increase in the capacitance obtained from the devices. Furthermore, there was a notable difference between the pore size

distribution among the samples, with the 70:30 blend exhibiting a higher percentage of mesopores (42.8%) leading to a micro to mesopore ratio around 1.34. Micropores help to adsorb ions in to the pores to form the double layer whereas mesopores facilitate the ion diffusion to these micropores by providing low resistive pathways for electrolyte ions to pass through the porous carbon structure. Table 3.3 summarizes BET surface areas of CNF of pure PBI and blends with different compositions. The high free volume polymer, 6FDD, clearly contributed to increase in the surface area because all the CNFs prepared from PBI:6FDD blends exhibit higher surface areas (over 2795 $\text{m}^2 \text{g}^{-1}$) compared to the PBI CNFs. High free volume in the precursor matrix may contribute high porosity of the carbonized matrix. The highest surface area was obtained for PBI:6FDD (70:30) at 3010 $\text{m}^2 \text{g}^{-1}$ which is a 31% increase compared to that of pure PBI (2297 $\text{m}^2 \text{g}^{-1}$).

3.4.4 Electrochemical properties of CNFs

Figure 3.12 displays the cyclic voltammetry (CV) curves obtained from the supercapacitors assembled with carbon precursor polymer blends that show rectangular shapes which indicates the ideal capacitive character of the EDLC. PBI:6FDD (70:30) and PBI:6FDD(50:50)also showed very box like CVs even at higher current densities when compared with pure PBI indicating fast charge transfer at the electrode/electrolyte interfaces. Rapid ion transport is facilitated by the significant amount of mesopores in the carbon materials especially in PBI:6FDD (70:30). Since the energy density of supercapacitors varies quadratically with voltage, we used the ionic liquid electrolyte, 1-butyl-1 methylpyrrolidinium bis(trifluoromethyl sulfonyl)imide ($\text{PYR}_{14}\text{TFSI}$) that can operate at high voltage ($\sim 4\text{V}$). The electrolyte used here is a mixture of ($\text{PYR}_{14}\text{TFSI}$), propylene carbonate (PC) and ethylene carbonate (EC) in the volume ratio of 3:3:2

(PYR₁₄TFSI:PC:EC). By mixing with the optimum ratio of PC and EC, the conductivity of PYR₁₄TFSI (1.85 mS cm⁻¹) was increased to 12.5 mS cm⁻¹. This increased conductivity in electrolyte ions helped to decrease the charge transfer resistance between electrode and electrolyte and made the CV plot box-like even in the higher scan rates. The specific capacitance values obtained for the PBI:6FDD blends studied were higher than the pure PBI at all scan rates because of the high surface area of CNF derived from PBI:6FDD blends. The highest specific capacitance of PBI:6FDD (70:30) at 10 mV s⁻¹ was calculated to be 142.8 F g⁻¹ compared to 75.9 F g⁻¹ for the pure PBI, as shown in Table 3.4. The capacitance increases linearly with the surface area. High performance was observed for PBI:6FDD(70:30) is due to high specific surface area and well balanced micro/mesoporosity of this precursor.

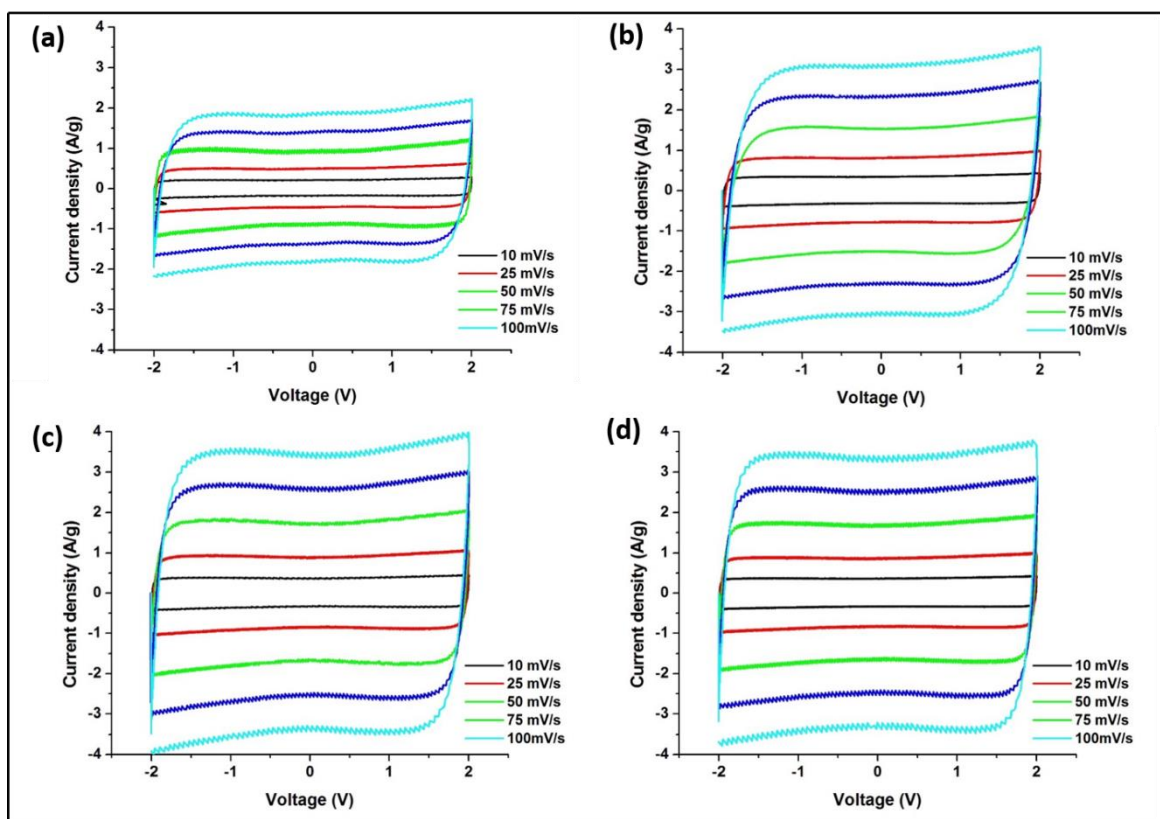


Figure 3.12. Cyclic voltammograms of carbonized nanofibers derived (a) PBI, (b) PBI:6FDD (90:10), (c) PBI:6FDD(70:30) and (d) PBI:6FDD(50:50).

Table 3.4. Specific capacitance of the CNFs derived from the PBI and the PBI/6FDD blends at five different scan rates

Scan rate (mV/s)	Specific capacitance (F/g)			
	PBI	PBI:6FDD	PBI:6FDD	PBI:6FDD
		(90:10)	(70:30)	(50:50)
10	75.9	129.8	142.8	138.3
25	74.6	129.4	141.4	137.5
50	74.5	125.5	140.6	136.9
75	73.7	124.1	140.5	136.7
100	73.3	123.4	138.7	136.2

As shown in the Ragone plot (Figure 3.13(a)) 85-90% of the energy density of the electrodes was retained when the power density increased 10-fold. The energy and power densities of the supercapacitors that were assembled with carbonized PBI/6FDD nanofibers at a current discharge density of 1 A g⁻¹ and 10 A g⁻¹ are listed in the table 3.5. The energy density calculated for at 1 A g⁻¹ was 67.5 Wh kg⁻¹ for PBI:6FDD(70:30) compared to that of PBI (38.4 Wh kg⁻¹) at similar power densities. Also the energy densities and power densities obtained for all the PBI/6FDD blends are much higher than the those reported for PBI blends with other polymers.^{28, 29} Figure 3.13(b) shows the galvanostatic discharging curves for carbonized blends and PBI at 1 A g⁻¹. All the blend-derived fibers exhibited almost linear curves and there was significant difference between the discharge time between PBI and the PBI/6FDD blends, where the blends showed the longer discharge times. PBI:6FDD (70:30) shows the longest discharge time among the blends

studied. Discharge curves of the PBI:6FDD (70:30) at different current densities are plotted in Figure 3.13(c). Discharge curves of the PBI:6FDD (70:30) exhibited almost linear curves with no significant IR drop, which indicates a device with the good performance having high electrochemical stability and reversibility.

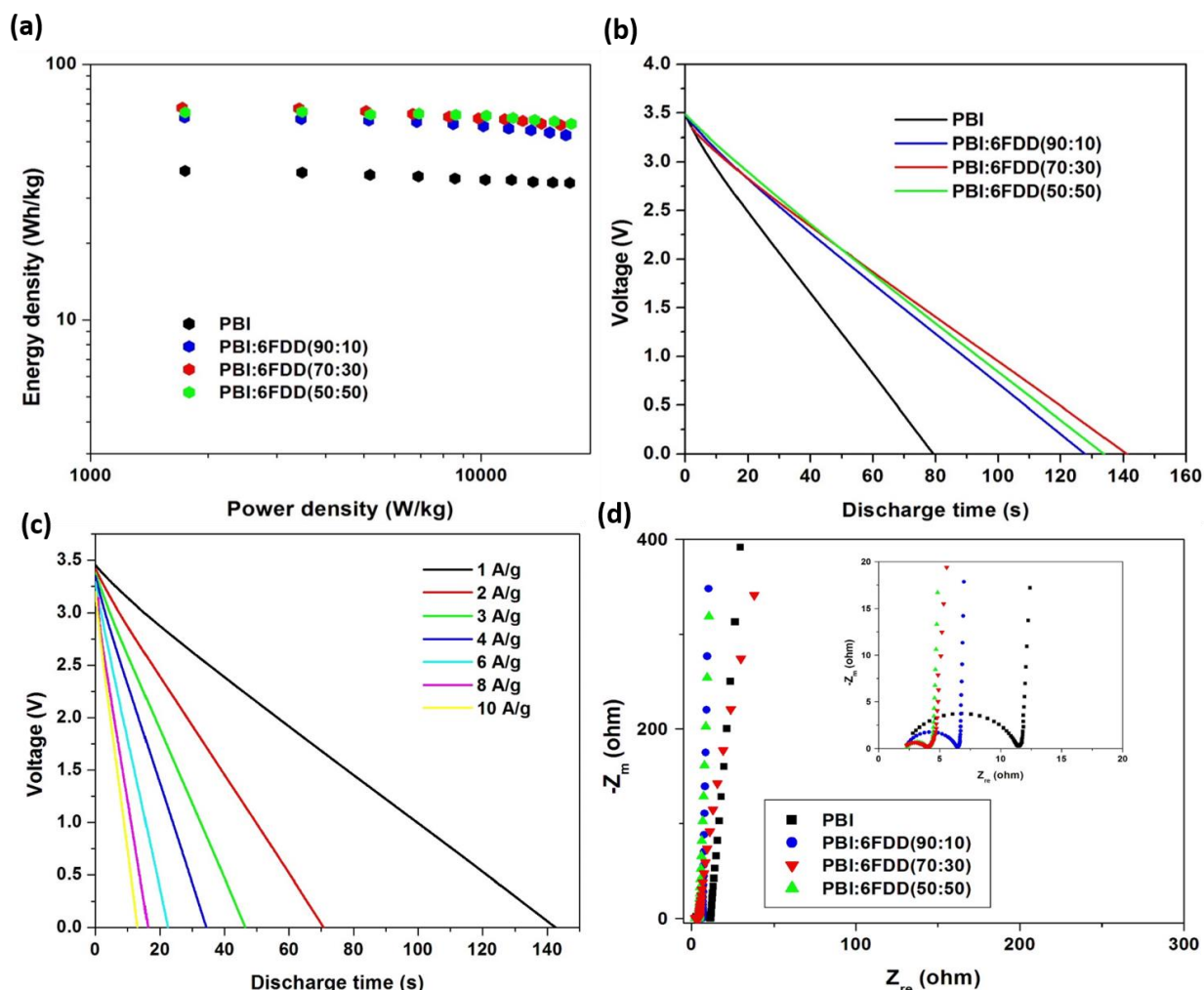


Figure 3.13. (a) Ragone plots (b) galvanostatic discharging curves at a constant current density of 1 A g^{-1} (c) galvanostatic discharging curves for PBI:6FDD(70:30) at different current densities from 1 to 10 A g^{-1} (d) Nyquist plot of carbonized nanofibers derived from PBI and PBI:6FDD blends with different compositions.

Table 3.5. Energy densities and the power densities of the CNFs derived from PBI and the PBI/6FDD blends at current densities of 1 A g⁻¹ and 10 A g⁻¹

Current	Parameters	PBI	PBI:6FDD	PBI:6FDD	PBI:6FDD
Density			(90:10)	(70:30)	(50:50)
(A/g)					
1	Energy density (Wh/kg)	38.4	61.8	67.5	64.7
	Power density (W/kg)	1742.5	1738.3	1713.8	1743.5
10	Energy density (Wh/kg)	34.4	52.8	57.8	58.3
	Power density (W/kg)	16830.7	16451.2	15930.6	16974.4

Figure 3.13 (d) displays the Nyquist plots of carbonized materials obtained from PBI and PBI/6FDD blends with different compositions. The impedance spectra for all the electrode materials displayed ideal capacitive behavior with a semicircle in the high frequency region and a straight line in the low-frequency region. The semicircle corresponds to the charge-transfer process while the linear region related to the diffusion of ions into the bulk of the electrode.⁵⁰ The semicircle in the high-frequency region, is the sum of the resistance of the porous electrode and the interfacial contact resistance between the porous electrode and the current collector while the intercept on the real axis in the high-frequency region provides the resistance of the electrolyte.⁵¹ The diameter of the semicircles obtained for electrodes followed the order of PBI > PBI:6FDD(90:10) > PBI:6FDD(50:50) > PBI:6FDD (70:30) suggesting low charge-transfer resistance of those electrodes was obtained after blending with 6FDD. These enhancements could be due to the shorter ion diffusion routes formed by the mesopores in the pore structure of

PBI:6FDD (70:30), which reduces the resistivity. Furthermore, electrochemical impedance spectroscopy analysis revealed that PBI/6FDD blend has a much smaller charge transfer resistance than PBI.

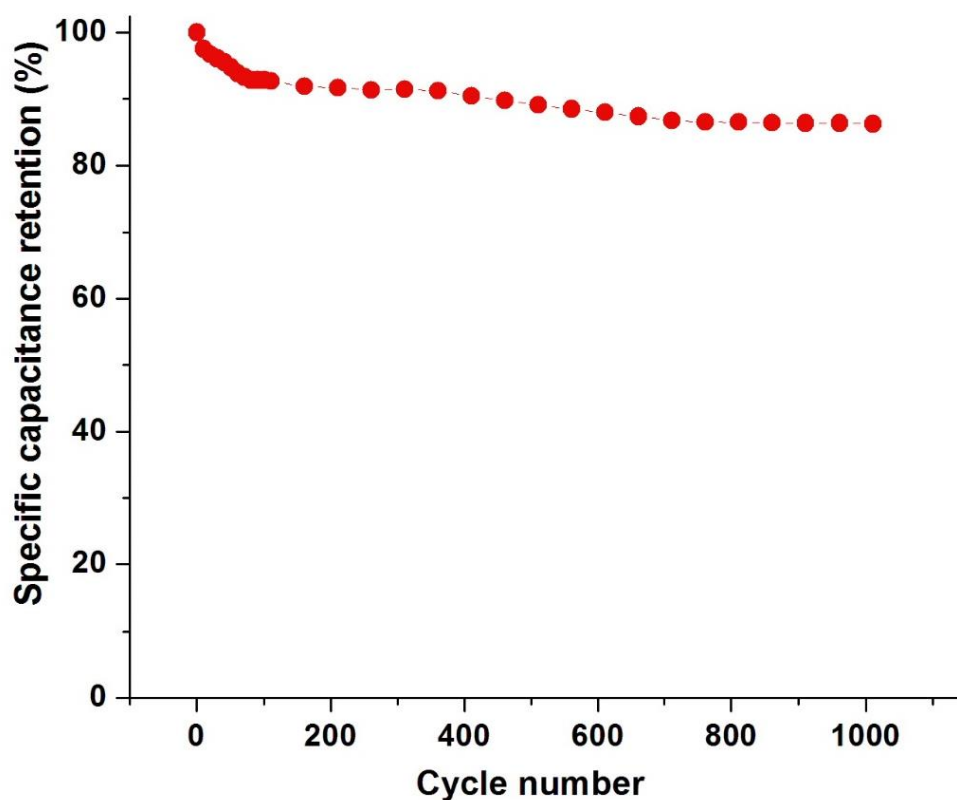


Figure 3.14. Specific capacitance retention of PBI:6FDD(70:30) as a function of cycle number.

Figure 3.14 shows the cycling stability of PBI:6FDD(70:30) at a current density of 1 Ag^{-1} in $\text{PYR}_{14}\text{TFSI}:\text{PC}:\text{EC}$ electrolyte. After the 100th cycle 92.8% of the specific capacitance was retained, which only dropped by 6.5% over the next 900 cycles. These results demonstrate that the activated carbon nanofibers derived from PBI:6FDD(70:30) have high electrochemical stability and reversibility during repetitive charge/discharge cycles in ionic liquid electrolyte system.

3.5 Conclusion

In summary, flexible and freestanding carbon nanofiber mats fabricated by electrospinning immiscible PBI/6FDD polymer blends, followed by subsequent thermal treatments, could be used as electrode materials for supercapacitors in the first time. The addition of 6FDD shows significant effects on the microstructure and surface areas of the CNFs. Binder-free electrodes were assembled into coin cells and tested. The highest capacitance obtained for the PBI:6FDD (70:30) was 142 F g^{-1} at 10 mV s^{-1} which is an 88% increase when compared with the electrode prepared from PBI-based CNF under the same conditions. Supercapacitors based on PBI:6FDD (70:30) exhibit a high energy density of 67.5 Wh kg^{-1} at 1 A g^{-1} . Improvements of the electrochemical performance are attributed to the following factors: more graphitic carbon produced by facilitated carbonization process due to crosslinking of 6FDD of PBI/6FDD blends; the large surface area CNFs derived from PBI/6FDD blends due to addition of high free volume polymer 6FDD; well developed and suitable pore structure of the carbon nanofibers derived from PBI/6FDD blends with the formation of well-balanced micro/mesoporosity with pore sizes very close to those of the electrolyte ions to create more access sites for charge transfer, especially for the PBI:6FDD (70:30) blend. PBI/6FDD blends can be directly carbonized without pre-stabilization, which adds to their attractiveness. This work highlights the potential applicability of immiscible polymer blends of PBI/6FDD to produce electrode materials for high performance energy storage systems.

Acknowledgements

The authors acknowledge the National Science Foundation (Grant no. IIP-1127564) for financial support. We also acknowledge the NSF (CHE-1126177) grant for providing the Bruker AVANCE

IIITM 500 NMR facility. We especially thank Sumudu N. Wijenayake for providing the initial 6FDD sample. We also acknowledge to Dr. Jean Francois Veyan (Department of Materials Science and Engineering, University of Texas at Dallas) for helping with the XPS analysis.

3.6 Appendix - Supporting Information

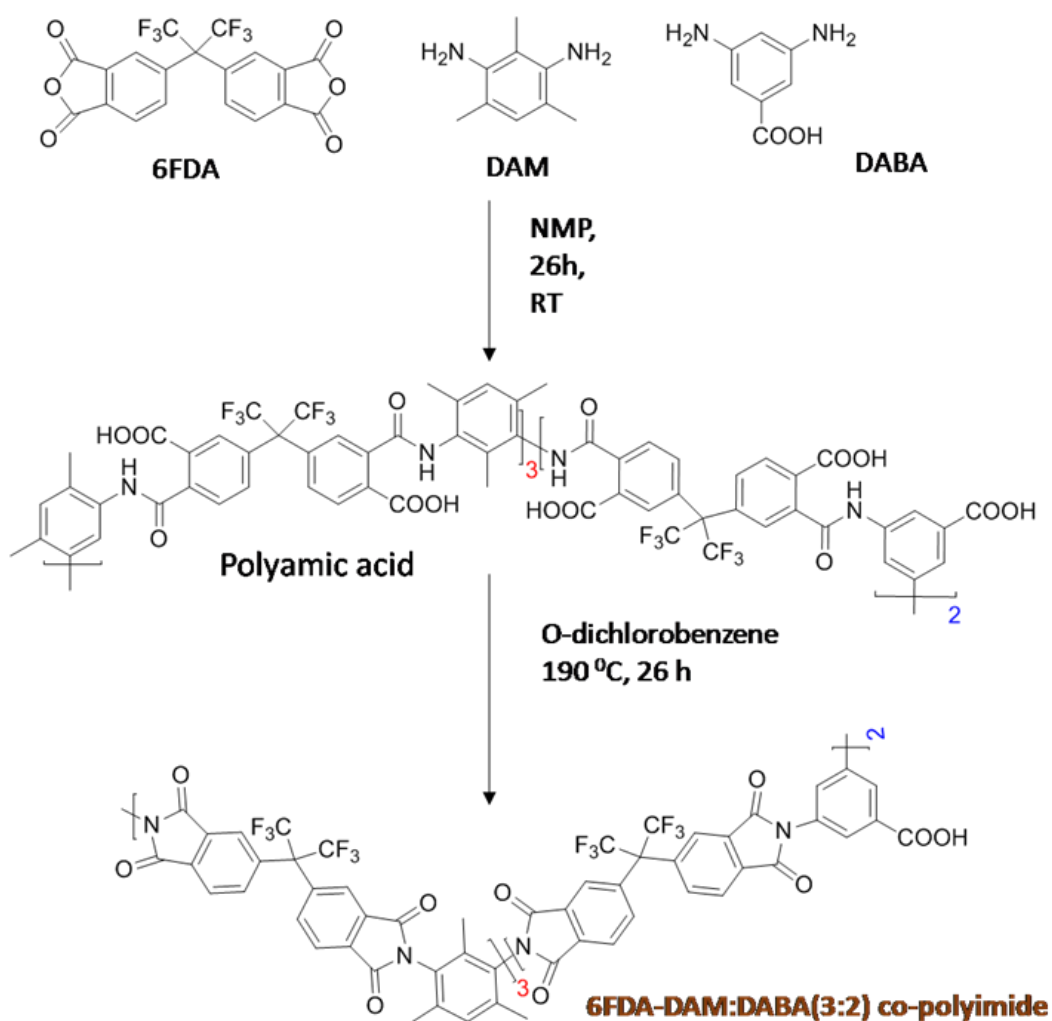


Figure S3.1. Synthesis of 6FDA-DAM:DABA.

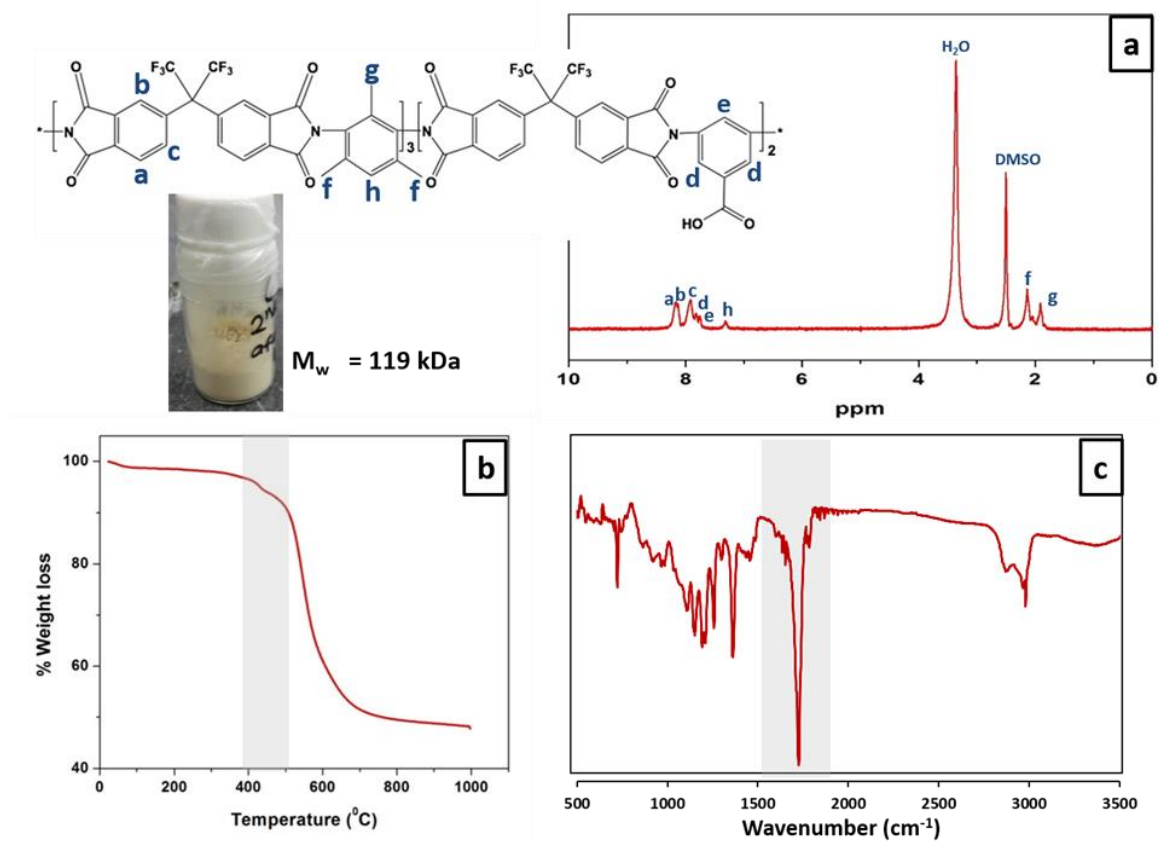


Figure S3.2. Characterizations of 6FDA-DAM:DABA (a) NMR, (b)TGA and (c) FT-IR.

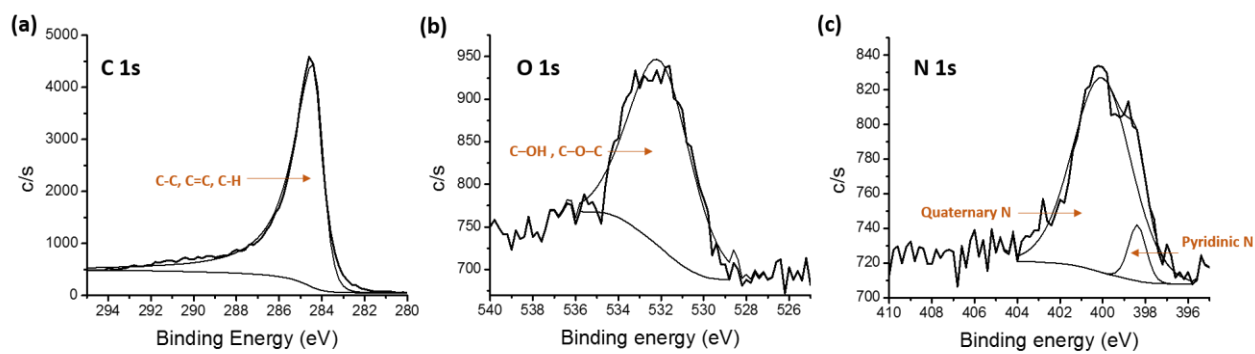


Figure S3.3. High-resolution (a) C 1s, (b) O 1s, and (c) N 1s, XPS spectra of CNFs derived from PBI.

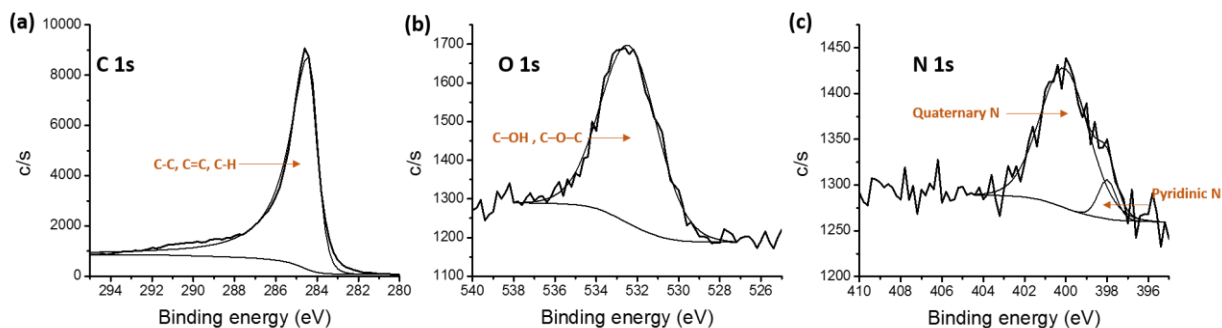


Figure S3.4. High-resolution (a) C 1s, (b) O 1s, and (c) N 1s, XPS spectra of CNFs derived from PBI:6FDD(90:10).

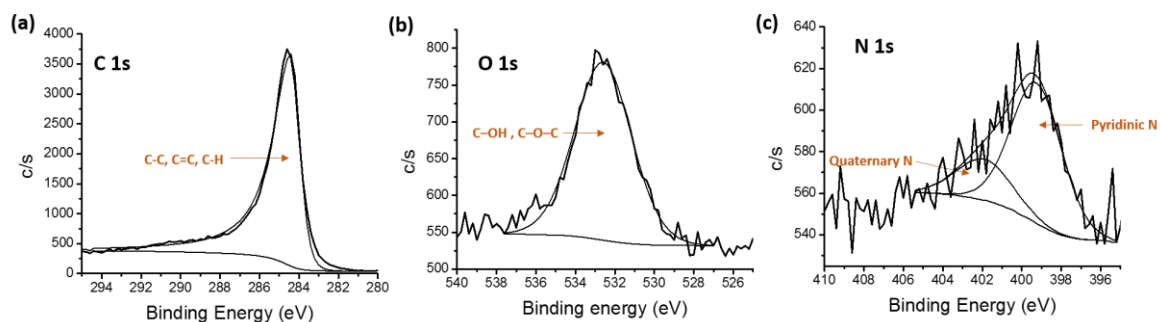


Figure S3.5. High-resolution (a) C 1s, (b) O 1s, and (c) N 1s, XPS spectra of CNFs derived from PBI:6FDD(50:50).

3.7 References

- (1) Simon, P.; Gogotsi, Y. Materials for Electrochemical Capacitors. *Nat. Mater.* **2008**, 7 (11), 845–854.
- (2) Conway, B. E. E.; Birss, V.; Wojtowicz, J. The Role and Utilization of Pseudocapacitance for Energy Storage by Supercapacitors. *J. Power Sources* **1997**, 66 (1–2), 1–14.
- (3) Xie, Y.; Liu, Y.; Zhao, Y.; Tsang, Y. H.; Lau, S. P.; Huang, H.; Chai, Y. Stretchable All-Solid-State Supercapacitor with Wavy Shaped Polyaniline/graphene Electrode†. *J. Mater. Chem. A* **2014**, 2, 9142–9149.
- (4) Winter, M.; Brodd, R. J. What Are Batteries, Fuel Cells, and Supercapacitors? *Chem. Rev.* **2004**, 104, 4245–4269.
- (5) Wang, K.; Xu, M.; Wang, X.; Gu, Z.; Fan, H.; William Gibbons; Croat, J. Porous Carbon Derived from Aniline-Modified Fungus for Symmetrical Supercapacitor Electrodes †. *RSC*

Adv. **2017**, *7*, 8236–8240.

- (6) Zhang, A.; Li, A.; Wang, Y.; Liu, M.; Ma, H.; Song, Z. Controllable Synthesis of Mesoporous Carbon Nanoparticles Based on PAN-b-PMMA Diblock Copolymer Micelles Generated via RAFT Polymerization as Electrode Materials for Supercapacitors. *RSC Adv.* **2016**, *6*, 103843–103850.
- (7) Wang, Q. Environmental Science and Opportunities. *Energy Environ. Sci.* **2016**, *9*, 729–762.
- (8) Inagaki, M.; Yang, Y.; Kang, F. Carbon Nanofibers Prepared via Electrospinning. *Adv. Mater.* **2012**, *24* (19), 2547–2566.
- (9) Zhang, L.; Han, L.; Liu, S.; Liu, S. High-Performance Supercapacitors Based on Electrospun Multichannel Carbon Nano Fibers *RSC Adv.* **2015**, *5*, 107313–107317.
- (10) Peranathan, S.; Bonso, J. S.; Ferraris, J. P. Supercapacitors Utilizing Electrodes Derived from Polyacrylonitrile Fibers Incorporating Tetramethylammonium Oxalate as a Porogen. *Carbon N. Y.* **2016**, *106*, 20–27.
- (11) Cai, J.; Niu, H.; Li, Z.; Du, Y.; Cizek, P.; Xie, Z.; Xiong, H.; Lin, T. High-Performance Supercapacitor Electrode Materials from Cellulose-Derived Carbon Nanofibers. *ACS Appl. Mater. Interfaces* **2015**, *7* (27), 14946–14953.
- (12) Ma, C.; Li, Y.; Shi, J.; Song, Y.; Liu, L. High-Performance Supercapacitor Electrodes Based on Porous Flexible Carbon Nanofiber Paper Treated by Surface Chemical Etching. *Chem. Eng. J.* **2014**, *249*, 216–225.
- (13) Kim, C.; Choi, Y. O.; Lee, W. J.; Yang, K. S. Supercapacitor Performances of Activated Carbon Fiber Webs Prepared by Electrospinning of PMDA-ODA Poly(amic Acid) Solutions. *Electrochim. Acta* **2004**, *50*, 883–887.
- (14) Gong, G.; Wu, J. Novel Polyimide Materials Produced by Electrospinning. *High Performance Polymers-Polyimides Based: From Chemistry to Applications*; 2012, chapter 7, pp 127–144.
- (15) Kim, C. Electrochemical Characterization of Electrospun Activated Carbon Nanofibres as an Electrode in Supercapacitors. *J. Power Sources* **2005**, *142*, 382–388.
- (16) Inagaki, M.; Ohta, N.; Hishiyama, Y. Aromatic Polyimides as Carbon Precursors. *Carbon N. Y.* **2013**, *61*, 1–21.
- (17) Li, Y.; Dong, J.; Zhang, J.; Zhao, X.; Yu, P.; Jin, L.; Zhang, Q. Nitrogen-Doped Carbon Membrane Derived from Polyimide as Free-Standing Electrodes for Flexible Supercapacitors. *Small* **2015**, *11* (28), 3476–3484.

- (18) Hulicova, D.; Oya, A. The Polymer Blend Technique as a Method for Designing Fine Carbon Materials. *Carbon N. Y.* **2003**, *41* (7), 1443–1450.
- (19) Ozaki, J.; Endo, N.; Ohizumi, W.; Igarashi, K.; Nakahara, M.; Oya, A.; Yoshida, S.; Izuim, T. Novel Preparation Method for the Production of Mesoporous Carbon Fiber from a Polymer Blend. *Pergamon Carbon* **1997**, *35* (7), 1031–1033.
- (20) Abeykoon, N. C.; Bonso, J. S.; Ferraris, J. P. Supercapacitor Performance of Carbon Nanofiber Electrodes Derived from Immiscible PAN/PMMA Polymer Blends. *RSC Adv.* **2015**, *5* (26), 19865–19873.
- (21) Jo, E.; Yeo, J. G.; Kim, D. K.; Oh, J. S.; Hong, C. K. Preparation of Well-Controlled Porous Carbon Nanofiber Materials by Varying the Compatibility of Polymer Blends. *Polym. Int.* **2014**, *63* (8), 1471–1477.
- (22) Tian, X. D.; Zhao, N.; Wang, K.; Xu, D. F.; Song, Y.; Guo, Q. G.; Liu, L. Preparation and Electrochemical Characteristics of Electrospun Water-Soluble Resorcinol/phenol-Formaldehyde Resin-Based Carbon Nanofibers. *RSC Adv.* **2015**, *5* (51), 40884–40891.
- (23) Hosseini, S. S.; Chung, T. S. Carbon Membranes from Blends of PBI and Polyimides for N₂/CH₄ and CO₂/CH₄ Separation and Hydrogen Purification. *J. Memb. Sci.* **2009**, *328* (1–2), 174–185.
- (24) Hosseini, S. S.; Teoh, M. M.; Chung, T. S. Hydrogen Separation and Purification in Membranes of Miscible Polymer Blends with Interpenetration Networks. *Polymer (Guildf)*. **2008**, *49* (6), 1594–1603.
- (25) Panapitiya, N. P.; Wijenayake, S. N.; Huang, Y.; Bushdiecker, D.; Nguyen, D.; Ratanawanate, C.; Kalaw, G. J.; Gilpin, C. J.; Musselman, I. H.; Balkus, K. J.; Ferraris, J. P. Stabilization of Immiscible Polymer Blends Using Structure Directing Metal Organic Frameworks (MOFs). *Polymer (Guildf)*. **2014**, *55* (8), 2028–2034.
- (26) Pirouzfard, V.; Moghaddam, A. Z.; Omidkhah, M. R.; Hosseini, S. S. Investigating the Effect of Dianhydride Type and Pyrolysis Condition on the Gas Separation Performance of Membranes Derived from Blended Polyimides through Statistical Analysis. *J. Ind. Eng. Chem.* **2014**, *20* (3), 1061–1070.
- (27) Hosseini, S. S.; Peng, N.; Chung, T. S. Gas Separation Membranes Developed through Integration of Polymer Blending and Dual-Layer Hollow Fiber Spinning Process for Hydrogen and Natural Gas Enrichments. *J. Memb. Sci.* **2010**, *349* (1–2), 156–166.
- (28) Jung, K. H.; Ferraris, J. P. Preparation and Electrochemical Properties of Carbon Nanofibers Derived from Polybenzimidazole/polyimide Precursor Blends. *Carbon N. Y.* **2012**, *50* (14), 5309–5315.

- (29) Jung, K.-H.; Ferraris, J. P. Preparation of Porous Carbon Nanofibers Derived from PBI/PLLA for Supercapacitor Electrodes. *Nanotechnology* **2016**, 27 (42), 425708.
- (30) Kim, J. H.; Koros, W. J.; Paul, D. R. Physical Aging of Thin 6FDA-Based Polyimide Membranes Containing Carboxyl Acid Groups. Part II. Optical Properties. *Polymer (Guildf)*. **2006**, 47 (9), 3104–3111.
- (31) Qiu, W.; Xu, L.; Chen, C.-C.; Paul, D. R.; Koros, W. J. Gas Separation Performance of 6FDA-Based Polyimides with Different Chemical Structures. *Polymer (Guildf)*. **2013**, 54 (22), 6226–6235.
- (32) Kratochvil, A. M.; Koros, W. J. Decarboxylation-Induced Cross-Linking of a Polyimide for Enhanced CO₂ Plasticization Resistance. *Macromolecules* **2008**, 41 (21), 7920–7927.
- (33) Omole, I. C.; Miller, S. J.; Koros, W. J. Increased Molecular Weight of a Cross-Linkable Polyimide for Spinning Plasticization Resistant Hollow Fiber Membranes. *Macromolecules* **2008**, 41 (17), 6367–6375.
- (34) Le, T.; Yang, Y.; Huang, Z.; Kang, F. Preparation of Microporous Carbon Nanofibers from Polyimide by Using Polyvinyl Pyrrolidone as Template and Their Capacitive Performance. *J. Power Sources* **2015**, 278, 683–692.
- (35) Grizzuti, N.; Bifulco, O. Effects of Coalescence and Breakup on the Steady-State Morphology of an Immiscible Polymer Blend in Shear Flow. *Rheol Acta* **1997**, 36, 406–415.
- (36) Christensen, P. A.; Jones, S. W. M. An in Situ FTIR Study of Undoped PolyBenzoImadazole as a Function of Relative Humidity. *Polym. Degrad. Stab.* **2014**, 105 (1), 211–217.
- (37) Zhang, Y.; Liu, X.; Wang, S.; Dou, S.; Li, L. Interconnected Honeycomb-like Porous Carbon Derived from Plane Tree Fluff for High Performance Supercapacitors. *J. Mater. Chem. A* **2016**, 4 (28), 10869–10877.
- (38) Zhao, W.; Lu, Y.; Wang, J.; Chen, Q.; Zhou, L.; Jiang, J.; Chen, L. Improving Crosslinking of Stabilized Polyacrylonitrile Fibers and Mechanical Properties of Carbon Fibers by Irradiating with G-Ray. *Polym. Degrad. Stab.* **2016**, 133, 16–26.
- (39) Liu, W.; Wang, M.; Xing, Z.; Qi, Y.; Wu, G. Radiation-Induced Crosslinking of Polyacrylonitrile Fibers and the Subsequent Regulative Effect on the Preoxidation Process. *RadiatPhys Chem* **2012**, 81(6), 622–627.
- (40) Kim, K.; Lee, H.; An, J.; Kim, B.; Min, B.; Kang, S.; An, K.; Kim, B. Effects of Cross-Linking Methods for Polyethylene-Based Carbon Fibers : Review. *Carbon Lett* **2015**, 16 (3), 147–170.

- (41) Hoefler, M.; Bandaru, P. R. Determination and Enhancement of the Capacitance Contributions in Carbon Nanotube Based Electrode Systems. *Appl. Phys. Lett.* **2009**, *95*(18), 18–20.
- (42) Yang, X.; Yu, J.; Zhang, W.; Zhang, G. RSC Advances High Supercapacitive Performance in Organic. *RSC Adv.* **2017**, *7*, 15096–15101.
- (43) Choudhury, A.; Kim, J.; Mahapatra, S. S.; Yang, K.; Yang, D. Nitrogen-Enriched Porous Carbon Nano Fiber Mat as Efficient Flexible Electrode Material for Supercapacitors. *ACS Sustainable Chem. Eng.* **2017**, *5*(3), 2109–2118.
- (44) Li, X.; Zhao, Y.; Bai, Y.; Zhao, X.; Wang, R.; Huang, Y. Electrochimica Acta A Non-Woven Network of Porous Nitrogen-Doping Carbon Nanofibers as a Binder-Free Electrode for Supercapacitors. *Electrochim. Acta* **2017**, *230*, 445–453.
- (45) Biniak, S. The Characterization Of Activated Carbons With Oxygen And Nitrogen Surface Groups. *Carbon* **1997**, *35* (12), 1799–1810.
- (46) Lazzari, M.; Mastragostino, M.; Pandolfo, a. G.; Ruiz, V.; Soavi, F. Role of Carbon Porosity and Ion Size in the Development of Ionic Liquid Based Supercapacitors. *J. Electrochem. Soc.* **2011**, *158* (1), A22.
- (47) Kim, C. H.; Wee, J.-H.; Kim, Y. A.; Yang, K. S.; Yang, C.-M. Tailoring the Pore Structure of Carbon Nanofibers for Achieving Ultrahigh-Energy-Density Supercapacitors Using Ionic Liquids as Electrolytes. *J. Mater. Chem. A* **2016**, *4* (13), 4763–4770.
- (48) Raymundo-Pinero, E.; Kierzek, K.; Machnikowski, J.; Beguin, F. Relationship between the Nanoporous Texture of Activated Carbons and Their Capacitance Properties in Different Electrolytes. *Carbon N. Y.* **2006**, *44* (12), 2498–2507.
- (49) Pohlmann, S.; Lobato, B.; Centeno, T. a; Balducci, A. The Influence of Pore Size and Surface Area of Activated Carbons on the Performance of Ionic Liquid Based Supercapacitors. *Phys. Chem. Chem. Phys.* **2013**, *15* (40), 17287–17294.
- (50) Subramani, K.; Sudhan, N.; Divya, R.; Sathish, M. On Cobalt Hexacyanoferrate-Derived CoS and. *RSC Adv.* **2017**, *7*, 6648–6659.
- (51) Lei, C.; Markoulidis, F.; Ashitaka, Z.; Lekakou, C. Reduction of Porous carbon/Al Contact Resistance for an Electric Double-Layer Capacitor (EDLC). *Electrochim. Acta* **2013**, *92*, 183–187.

CHAPTER 4

**ELECTROSPUN POLY(ACRYLONITRILE-*CO*-ITACONIC ACID) AS A POROUS
CARBON PRECURSOR FOR HIGH PERFORMANCE SUPERCAPACITOR:
STUDY OF THE POROSITY INDUCED BY IN SITU POROGEN ACTIVITY OF
ITACONIC ACID**

4.1 Abstract

In this study an acrylonitrile based co-polymer, poly(acrylonitrile-*co*-itaconic acid), P(AN-*co*-IA) was synthesized with different amounts of IA (2%, 5% and 8%) to study *in situ* porogen activity of itaconic acid to produce porous carbon nanofibers (CNFs) without any subsequent physical or chemical activation. The concept developed here avoids unnecessary and complex extra activation steps when fabricating carbon nanofibers which ultimately lead to lower char yields and uncontrollable pore sizes. The ability of COOH in P(AN-*co*-IA) to act as an *in situ* porogen by releasing CO₂ during carbonization was verified by TGA-MS analysis comparing to PAN. The surface area of PAN CNFs (<10 m²/g) dramatically increases to 1240 m²/g upon addition of only 8 wt% IA without any *ex situ* activation. Furthermore, we confirmed that the porosity can be tuned by changing the IA content. Conventional CO₂ activation of fiber also carried out to study impact of activation to the electrochemical performances. Electrodes derived from P(AN-*co*-IA) exhibited specific capacitances and energy densities superior to that of PAN derived electrodes with and without CO₂ activation. The best electrochemical performance was obtained from the copolymer containing 8 wt% of IA, which gives a maximum specific capacitance of 131.5 F g⁻¹ (92.9 F g⁻¹) at a scan rate of 10 mV s⁻¹ and energy density of 66.5 Wh kg⁻¹ (45.9 Wh kg⁻¹) at 1 A g⁻¹ with (and without) CO₂ activation, respectively.

4.2 Introduction

Electrochemical capacitors (or supercapacitors) are energy storage devices that are becoming more prominent in applications that require high charge and discharge rates such as consumer electronics, tramways, and energy harvesting systems.^{1,2} Supercapacitors can deliver greater power densities than lithium-ion batteries, though they are unable to store as much energy as batteries.^{3,4,5} Due to their applicability in a large number of energy-related technologies, improving the energy storage capabilities of supercapacitors is of great importance for technological advancement.^{6,7} Utilization of porous carbon electrodes is one approach to increase the capacitance of electrochemical double layer capacitors (EDLCs).⁸ The porosity of the electrodes greatly increases their surface area, and, because capacitance is directly related to surface area, it significantly increases the capacitance of the device. Increased capacitance corresponds to an increase in energy storage capability of supercapacitors.⁹ Porous carbon nanofibers show promise as electrodes for electrochemical double layer capacitor due to their high mechanical strength, high surface area, relatively high electrical conductivity, freestanding nature and flexibility.^{10,11} Activation methods using chemical agents (KOH¹², ZnCl₂^{13,14} and H₃PO₄^{15,16}) and gasses (CO₂¹⁷, NH₃¹⁸ and steam¹⁹) have been applied to the precursor materials to produce porous materials for effective use as electrodes for supercapacitors. However, the main disadvantages associated with these methods are lower char yields due to reaction between carbon and activating agent, additional methods needed to remove residue on fibers after activation and complexity and expense for scale-up due to the multiple steps involved. Besides, harsh chemicals such as ZnCl₂ or KOH result in amorphous carbon that have uncontrollable pore sizes.^{20, 21} This problem can be addressed by an alternative

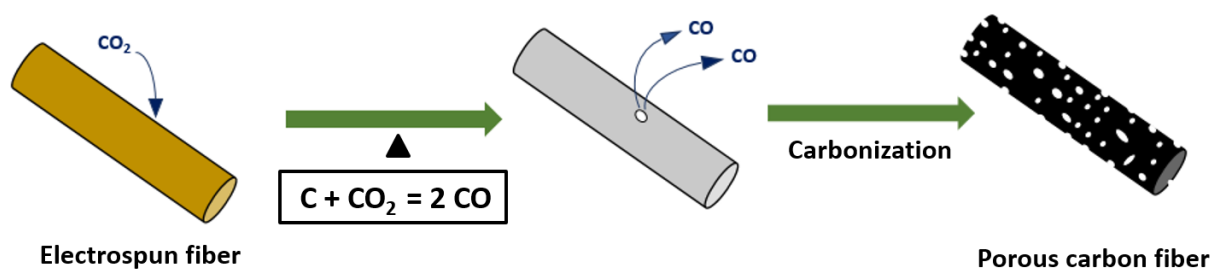
method where introduction of thermally labile porogens that produce porous fibers upon decomposition.^{11,18,20,22}

Direct carbonization of precursor materials without any external activation agent represents the most promising and simple method for the synthesis of porous carbon. Despite these advantages, there is a limited number of reports on the synthesis of high surface area carbon by direct carbonization without adding any external activation agent. Puthusseri et al. has reported direct pyrolysis of interconnected carbon sheets from the poly(acrylamide-co-acrylic acid) potassium salt in inert atmosphere.²³ A high surface area of $1327 \text{ m}^2\text{g}^{-1}$ was obtained without any activation and specific capacitances of 258 Fg^{-1} in $1 \text{ M H}_2\text{SO}_4$ at a current density of 0.5 A g^{-1} . The majority of studies examine carbon forms other than nanofibers without any activation or *in situ* porogen. One of the more common carbon nanofiber sources used for EDLC electrodes polyacrylonitrile (PAN). However, PAN hinders the alignment of polymer chains during spinning and its higher crystallinity is unfavorable to the cyclization step that leads to a less uniform microstructure, which in turn results in poor quality carbon fiber.^{24,25} For these reasons, additional activation methods or porogens are required for the PAN fibers to produce high surface area carbon. Moreover, a crucial thermal stabilization step is need to be performed commonly at 280°C for PAN before conversion to carbon fibers.²⁶

Here in, we present a strategy to produce high surface area carbon by direct carbonization of copolymer incorporating decomposable itaconic acid segments acting as an *in situ* porogen as shown in Figure 4.1. Introduction of the acidic comonomer, itaconic acid (IA), during polymerization of PAN yields the copolymer poly(acrylonitrile-co-itaconic acid) (P(AN-co-IA)). This incorporation of itaconic acid increases the properties of the carbon material derived from

it.²⁷ The presence of IA groups in P(AN-*co*-IA) causes the initiation of the cyclization of nitrile groups at a lower temperature (220 °C) than PAN (280 °C). This allows the use of *ex situ* porogens, which decompose at lower temperatures whenever small porogens are needed to provide additional porosity. There is also an energy saving when overall manufacturing is concerned. Also, P(AN-*co*-IA) has increased spinnability and higher carbon yield of the resulting carbon fibers. Finally the use of *in situ* porogen avoids unnecessary activation steps when fabricating high surface area carbon nanofibers (CNFs). Simultaneous thermo gravimetric analysis- mass spectrometry (TGA-

Ex situ CO₂ activation of fibers (Conventional method of activation)



In situ activation of fiber using IA in copolymer

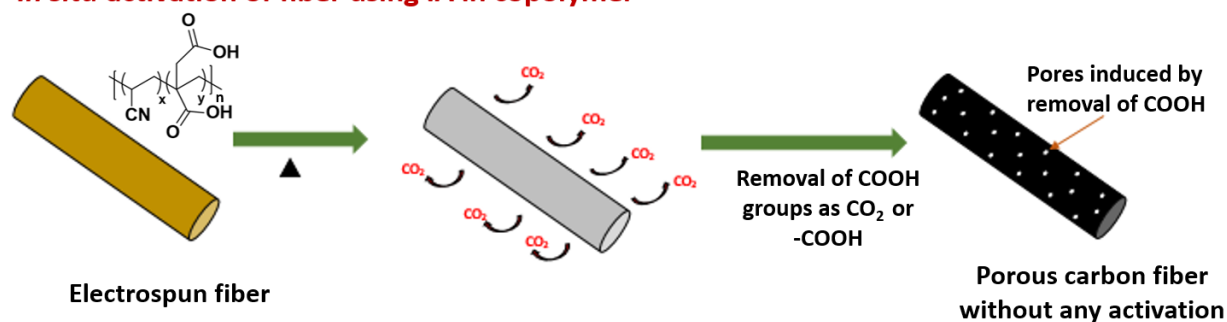


Figure 4.1. Schematic for the strategy of producing porous carbon nanofiber using *in situ* porogen activity of P(AN-*co*-IA) copolymer over conventional CO₂ activation. During carbonization, CO₂ gases produce by decomposition of itaconic acids, which create pores on nanofibers.

MS) of the P(AN-*co*-IA) electrospun nanofiber mats showed that CO₂ gas evolved when the mats were heated to about 220 °C in air. This phenomena was not observed in PAN, suggesting the carboxylic acid moieties on itaconic acid were the source of the CO₂.

The copolymer, P(AN-*co*-IA) was synthesized with different amounts of IA (2%, 5% and 8%), then electrospun into mats and finally carbonized at 1000 °C to afford porous CNFs that were characterized by SEM, surface area analysis and TGA-MS before being incorporated as electrodes in coin cell supercapacitors. The surface area of the electrode material derived from P(AN-*co*-IA), and a concomitant increase in energy storage capability were observed with an increase in itaconic acid content.

4.3 Experimental

4.3.1 Materials

2,2'-Azobis (2-methylpropionitrile) (AIBN), acrylonitrile (AN), and 1-dodecanethiol were purchased from Sigma-Aldrich. Itaconic acid (IA) and anhydrous N,N-dimethylformamide (DMF) was purchased from Alfa Aesar. DMF is used as received for both synthesis as well as the electrospinning. AN was purified by passing through the basic alumina column to remove inhibitor and unless otherwise mentioned, the monomers were used as received. The electrode materials were tested in a coin cell configuration and the coin cell assembly parts were obtained from Shenzhen Yongxingye Precision Machinery Mould Co. Ltd., China. Electrochemical grade EMITFSI (99.5% purity) was purchased from IoLiTec, Inc. and was used without further purification.

4.3.2 Synthesis of P(AN-co-IA)

P(AN-co-IA) was synthesized (Figure 4.2) by radical polymerization in DMF using AIBN as initiator according to the reported literature procedures.²⁸ The free radical solution polymerization of AN and IA with weight feed ratios of AN: IA = 98:2, 95:5 and 92:8 were carried out in 500ml round bottom flasks. The reaction flask was fitted with a thermocouple probe, addition funnel, nitrogen inlet and a condenser. AIBN and IA was dissolved in DMF before mixed them with AN and 1-dodecanethiol to prepare the reaction mixture. The reaction mixture was then poured carefully into an addition funnel attached with a reaction flask. The mixture was added drop wise into a DMF containing preheated (70 °C) the reaction flask over a period of 15 minutes. Upon completion of the addition, all the reactions were carried out at 70 °C with continuous stirring for 48 h. The copolymer from the reaction was precipitated and washed in de-ionized water. The product was then filtered and further washed with methanol and hexane to remove residual unreacted species from the reaction. Finally the copolymer was dried in a vacuum oven at 70 °C for two days till constant weight was obtained.

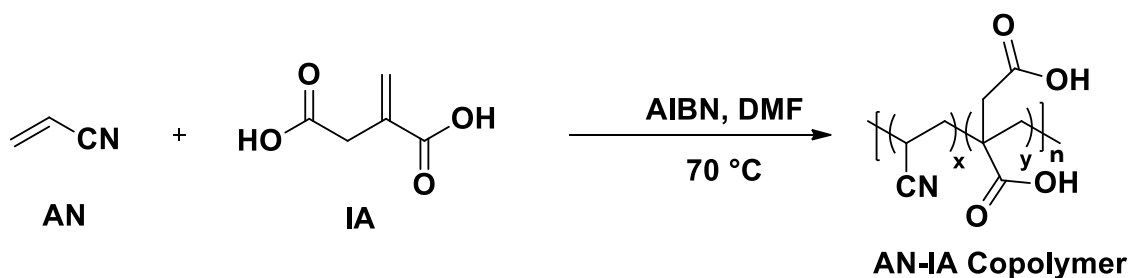


Figure 4.2. Synthesis of P(AN-co-IA).

4.3.3 Preparation of carbon nanofibers (CNFs) and CO₂ activated carbon nanofibers (ACNFs)

The synthesized P(AN-*co*-IA) with different compositions of IA was dissolved in N,N dimethylformamide (DMF) (20 wt.%) at 50 °C for 2 h and then stirred for 24 h at room temperature before electrospinning. The monomer ratio of AN/IA was selected as 98/2, 95/5 and 92/8 by weight and denoted as P(AN-*co*-IA)-2, P(AN-*co*-IA)-5 and P(AN-*co*-IA)-8 respectively. Also, a control solution of PAN was prepared by dissolving PAN in DMF according to the same procedure. The prepared solutions were loaded into the syringe and electrospun in to the nano fibers using a custom-built electrospinner by applying a voltage of 18 kV (Gamma High Voltage Research, Inc., power supply) between the 20G needle tip attached to the syringe and a grounded drum collector wrapped with an aluminum foil rotating at speed of 300 rpm. The needle tip was placed 15 cm away from the grounded drum collector. The spinning solution was delivered a constant rate of 0.5 ml h⁻¹ to the tip. The resulting free standing nanofiber mats were peeled from the aluminum foil and stabilized at 220 °C for 3h under air flow (200 mL min⁻¹) with a heating rate of 2 °C min⁻¹. CNFs were prepared by heating the stabilized mats at a rate of 5 °C min⁻¹ under Helium gas flow (200 mL min⁻¹) from room temperature to 1000 °C and then kept at that temperature for 1 h. After that, the samples were cooled under Helium gas flow. ACNFs were prepared according to the same procedure purging with CO₂ (50 mL min⁻¹) at 1000 °C for 1h.

4.3.4 Characterizations

¹H NMR spectra of the synthesized copolymers were obtained on a Bruker AVANCE III™ (500 MHz) NMR spectrometer using DMSO-d₆ as the solvent. Size exclusion chromatography (SEC)

was used to determine the molecular weights of the polymers synthesized in N, N-dimethylformamide (DMF) at 40 °C at 1 mL min⁻¹ flow rate on Shimadzu HPLC instrument equipped with Agilent polystyrene columns and Shimadzu refractive index detector (RID). Polystyrene standard was used for calibration of SEC. Attenuated total reflectance fourier transform infrared (ATR-FTIR) spectra were recorded on a Nicolet 360 FTIR spectrophotometer. Thermogravimetric behavior of the samples were carried out under nitrogen flow by heating from room temperature to 1000 °C (10 °C min⁻¹ heating rate) on a TA Instruments SDT Q600 Analyzer. Simultaneous thermogravimetric analysis- mass spectrometry (TGA-MS) was performed by a tandem Mettler-Toledo TGA/DSC-1 Pfeiffer QMG 230 mass spectrometer (MS) system from 30 °C to 900 °C at a rate of 10 °C min⁻¹ under nitrogen environment. The MS was scanned from 2 amu to 200 amu for the entirety of the TGA temperature scan. DSC curves for electrospun samples were obtained using a Mettler-Toledo DSC 1 by heating from 50 °C to 350 °C at 5 °C min⁻¹ under 50 mL min⁻¹ nitrogen flow for all the samples. The conductivity of electrospinning solutions was measured using an Oakton CON 11 conductivity meter. The viscosity of electrospinning solutions was measured using a Brookfield digital Viscometer (Model DV-II). Morphological studies of samples were performed with a Zeiss-LEO (Model 1530) Scanning Electron Microscope (SEM) equipped with field emission gun accelerating at 10 keV. All the as-spun and stabilized samples were sputter coated with gold before SEM imaging whereas SEMs of carbonized samples were collected without sputter coating. The surface area of carbon fibers was measured using the Brunauer– Emmett–Teller (BET) surface area analyzer (Autosorb 1, Quantachrome Corporation) at liquid nitrogen temperature (77 K). The pore size distribution (PSD) was obtained by

the Density Functional Theory (DFT). Raman spectroscopy (DXR Raman Spectrometer, Thermo scientific) equipped with 532 nm laser was employed to characterize CNFs and ACNFs samples.

4.3.5 Electrochemical tests

The electrochemical measurements were performed in a two-electrode configuration. For this, the CR2032 coin cell packaging was used. Two identical carbon electrodes were separated by Gore™ PTFE separator. Carbon coated aluminum was used as the current collectors and stainless steel spacers were placed on each side of current collector when packaging. The electrolyte (EMITFSI) was introduced to each electrode and sealed in coin cell using crimper inside a nitrogen-filled glove box. Electrochemical tests, including cyclic voltammetry (CV) and constant current charge/discharge (CDC) were carried out on Arbin Supercapacitor Testing Station (SCTS). CVs were obtained in the range of -2 to 2 V and CDC were recorded between 3.5 V and 0 V. The cells were characterized further by using electrochemical impedance spectroscopy (EIS) at 0 V DC bias in the frequency range of 100 kHz to 10 mHz using a Princeton Applied Research potentiostat/galvanostat (model 2273 A) in a two-electrode configuration.

4.4 Results and discussion

4.4.1 Characterization of the polymer

The ^1H -NMR analysis (Figure S4.1, Figure S4.2 and Figure S4.3) and the molecular weights (Figure S4.4, Table S4.1) of the synthesized P(AN-*co*-IA) copolymers were summarized in the supplementary information.

4.4.2 Characterization of the materials

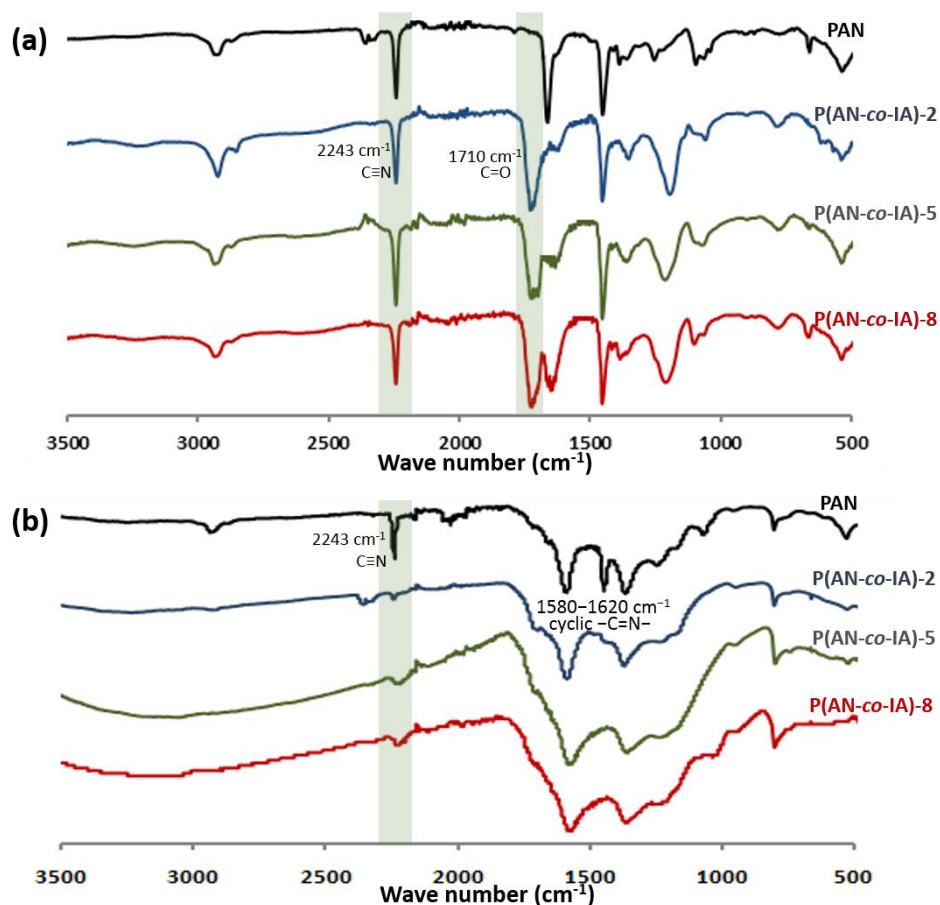


Figure 4.3. FTIR analysis of (a) electrospun fibers (b) stabilized fibers of PAN homopolymer and its copolymers with different ratio of IA.

Figure 4.3(a) depicts the FT-IR spectra of as spun fiber mats of P(AN-co-IA) polymers with different ratios that give rise to similar IR spectra. The absorption band appear in the region 3500-3510 cm^{-1} is assigned to the stretching vibrations of hydroxyl (-OH) groups and strong peaks in the ranges of 1730-1737 cm^{-1} and 1170 cm^{-1} are related to C=O or C-O bonds, which confirms the presence of IA moiety in the copolymers. A sharp strong peak at 2243 cm^{-1} is assigned to the

C≡N stretching in AN unit. The characteristic peak at 2922 cm^{-1} is due to the presence of aliphatic methylene ($-\text{CH}_2$) groups in the copolymers. The intensities of the different bands in IR spectra changed according to the molar ratios of monomers in copolymers. According to the Figure 4.3(a), the C≡N stretching signal is clearly visible at 2243 cm^{-1} with high molar ratio of AN (IR spectrum of P(AN-*co*-IA)-5) but the C=O stretch become dominant upon increasing the ratio of IA compared to AN (IR spectrum of P(AN-*co*-IA)-8). Figure 4.3(b) shows the FT-IR spectra of fibers stabilized at $220\text{ }^{\circ}\text{C}$, 3h. During the stabilization in the linear structure of the precursor polymer converts to an oriented ladder structure the C≡N stretching signal at 2243 cm^{-1} shown in the precursor should disappear with the appearance of peaks in the range of $1580\text{--}1620\text{ cm}^{-1}$ for the cyclic C=N. In Figure 4.3(b), the C≡N stretching band for P(AN-*co*-IA) precursors disappears after stabilization at $220\text{ }^{\circ}\text{C}$ demonstrating that the IA facilitated the cyclization of the PAN leading to the formation of more ordered graphitic structures in the carbon nanofiber later in the carbonization step.²⁹

Thermo-oxidative stabilization is the crucial step when transforming electrospun fibers to carbon fiber, which affects the properties and quality of the resulting carbon fibers. The effect of IA content toward the stabilization of the precursor were studied using DSC analysis (Figure 4.4(a)). According to the DSC, PAN shows a sharp single exothermic peak centered at $280\text{ }^{\circ}\text{C}$, whereas P(AN-*co*-IA) copolymers shows two broad peaks attributed to the two different cyclization mechanisms of PAN and P(AN-*co*-IA) copolymers.³⁰ Cyclization of PAN initiated through a free radical mechanism occurs at the higher temperature because of high activation energy. Incorporation of IA into PAN is an effective way to control stabilization reactions with a significant decrease in the initial temperature and the heat evolved.

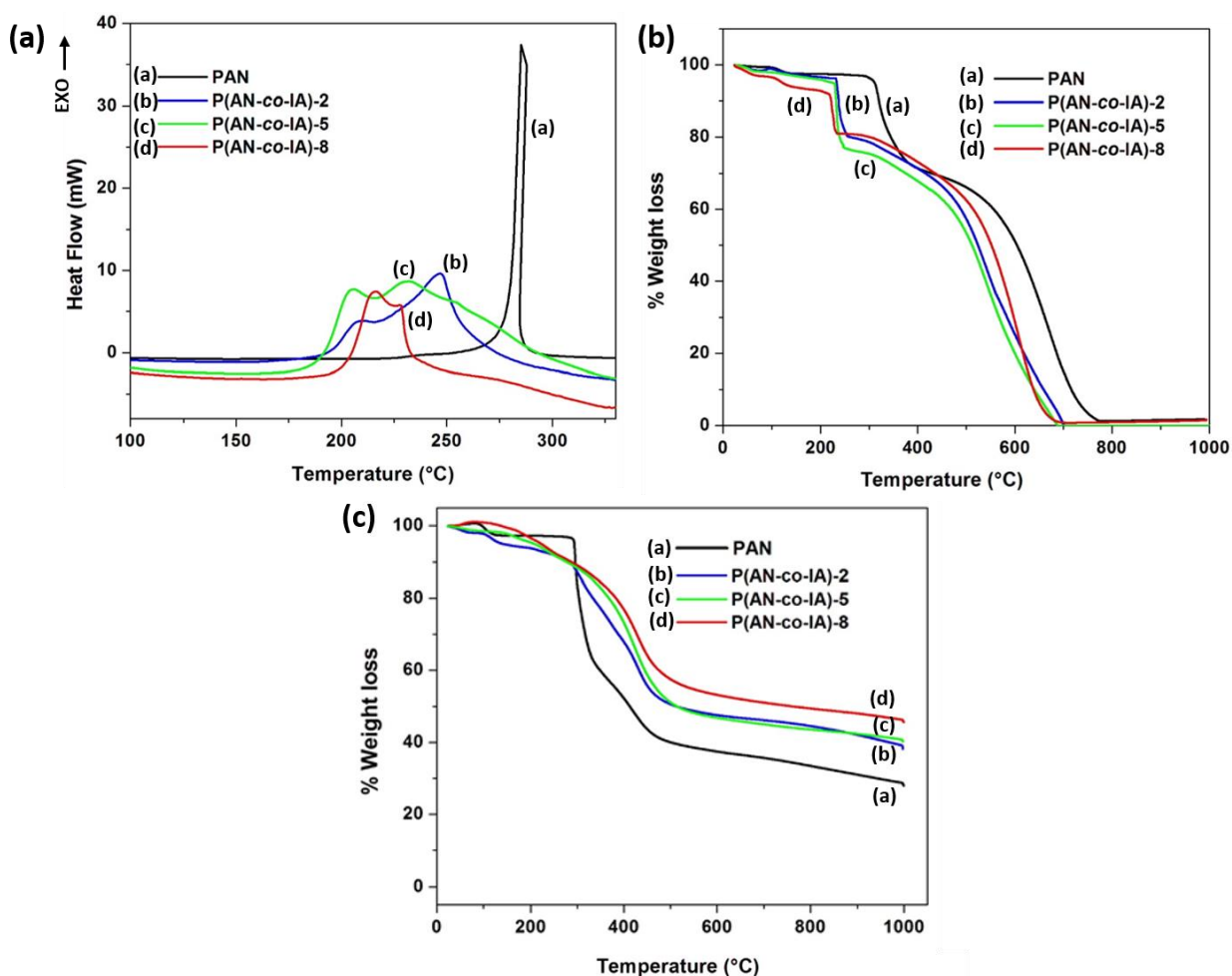


Figure 4.4. (a) DSC analysis in N₂ atmosphere (b) TGA analysis in air atmosphere and (c) TGA analysis in N₂ atmosphere of electrospun samples.

Low temperature cyclization of IA copolymers can be further illustrated by the TGA analysis in air (Figure 4.4(b)). According to the TGA analysis, PAN starts cyclizing above 300 °C but P(AN-co-IA)-2 started the cyclization around 220 °C. The cyclization temperature further decreases when increasing the IA composition in the copolymers. According to the TGA analysis in nitrogen (Figure 4.4(c)), P(AN-co-IA) copolymers have higher carbon yield than the PAN at higher temperatures. More fragmentation occurs during stabilization of PAN because of the centralized

heat release of PAN which causes a lower char yield at high temperature,^{31,32,33} which is not beneficial for production of quality carbon fibers. On the other hand, smooth and gentle release of heat of P(AN-*co*-IA) copolymers leads to high quality carbon fibers with higher yield because of enhanced oxidative reactions. High char yield is one of the main requirements for the materials used as carbon electrodes. The increase in char yield at 1000 °C with increasing IA composition confirms the higher suitability of the copolymer compared to PAN as an electrode material.

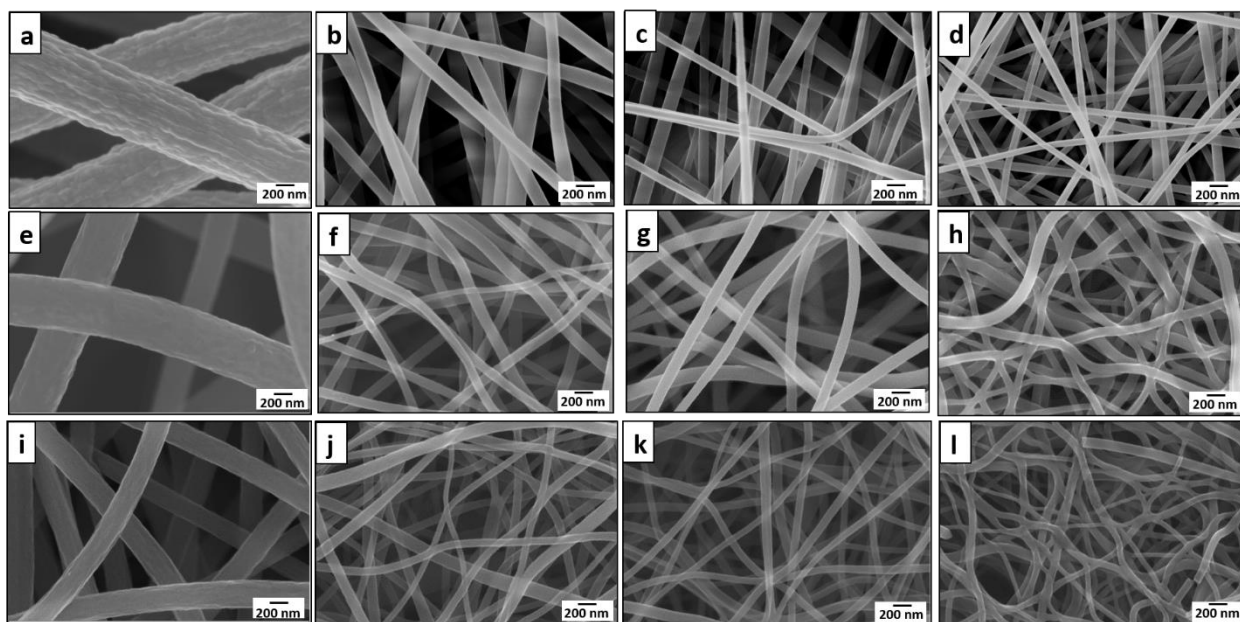


Figure 4.5. SEM images of electrospun (a) PAN (b) P(AN-*co*-IA)-2 (c) P(AN-*co*-IA)-5 (d) P(AN-*co*-IA)-8, carbonized (e) PAN (f) P(AN-*co*-IA)-2 (g) P(AN-*co*-IA)-5 (h) P(AN-*co*-IA)-8, CO₂ activated (i) PAN (j) P(AN-*co*-IA)-2 (k) P(AN-*co*-IA)-5 (l) P(AN-*co*-IA)-8 fibers.

The surface morphology of the samples were investigated using SEM, as shown in Figure 4.5(a) – (l). Average fiber diameters of all fiber samples determined by averaging the diameter of 50 nanofibers of each samples are included in Table 4.1. Figure 4.5(a) – (d) show that the SEM images of electrospun nanofibers. Based on the SEM images, bead free and continuous nanofibers were produced from all the copolymer solutions during electrospinning. Furthermore, when compared

Table 4.1. Average diameters of electrospun fibers, CNF and ACNF

Precursor	As spun fiber diameter (nm)	Carbonized fiber diameter (nm)	Activated fiber diameter (nm)
PAN	727±236	449±86	247±23
P(AN- <i>co</i> -IA)-2	154±33	113±20	70±13
P(AN- <i>co</i> -IA)-5	102±27	99±9	65±11
P(AN- <i>co</i> -IA)-8	66±10	62±13	59±15

with diameter of PAN electrospun fiber (727 nm) spun under the same conditions, the diameter of the fibers in the P(AN-*co*-IA) is much smaller (< 155 nm). The precursor polymer having lowest IA content (2 wt% of IA) exhibited the highest average nanofiber diameter among the P(AN-*co*-IA) fibers and the average nanofiber diameter decreases with increasing IA content (Table 4.1). This may be due to the conductivity and viscosity of electrospinning solution which are critical parameters among the variety of parameters that can strongly influence the morphology and diameters of the electrospun fibers. An increase in conductivity of the spinning solution from 12.2 mS m⁻¹ for PAN homopolymer to 13.9, 14.5 and 16.8 mS m⁻¹ for 2%, 5% and 8% IA, in copolymer, respectively, was observed. Conductivity of the solution increases with an increase in IA contents of copolymers due to dissociation of the carboxylic acid group in the copolymer, This in turn, increases the ionic conduction of charge in the polymer solution. As a result, an increase in the electrospinning current from the tip to the grounded collector during the electrospinning process causes a reduction in fiber diameter.³⁴ Although, all the electrospun solutions were prepared with the same polymer content (20 %), the viscosities of the solutions decreases with increasing IA

content in different copolymers. Viscosity of the spinning solution containing 2 wt% IA was 3260 cP and it decreased to 2930 cP and 1826 cP with an increased IA weight percentage of 5% and 8%, respectively. Hence, increasing IA content of copolymers resulted in decreasing nanofiber diameter which is related to the low viscosity as well as increased conductivity. The fibers become smaller and curly after carbonization due to the removal of COOH which is most obvious at the highest percentage of IA copolymers (8 wt% of IA). The diameters were further reduced by external CO₂ activation. Electrospun fibers, CNFs and ACNFs derived from copolymers falls in the nanometer range (< 100 nm) when compared to commercially available PAN fibers, which is also advantageous in the present application due to increased surface area.

Figure 4.6 shows TGA-MS spectra of PAN and P(AN-*co*-IA) copolymers, which were plotted as ion current vs temperature for selected ions with mass numbers (m/Z) of 14, 16, 18, 28, 32, 44, 45 which correspond to H₂O, N₂, O₂, CO₂, COOH respectively. The ability of the COOH groups in P(AN-*co*-IA) to act as an *in situ* porogen releasing CO₂ ($m/Z = 44$) during carbonization was demonstrated by the increase in ion current around 220 °C during stabilization of the copolymer which is absent from the PAN sample over that temperature range. The evolved CO₂ causes an *in situ* activation leading to high porosity CNFs (Table 4.2). Furthermore, the ion current for CO₂ increases with increasing IA content in the precursor (Figure 4.7(a)). The increasing ion current of COOH with increasing IA ratio as shown in Figure 4.7(b) parallel that of CO₂. Good electrochemical performance could be only obtained from carbonized fiber derived from P(AN-*co*-IA) copolymers and not the PAN homopolymer (vida infra).

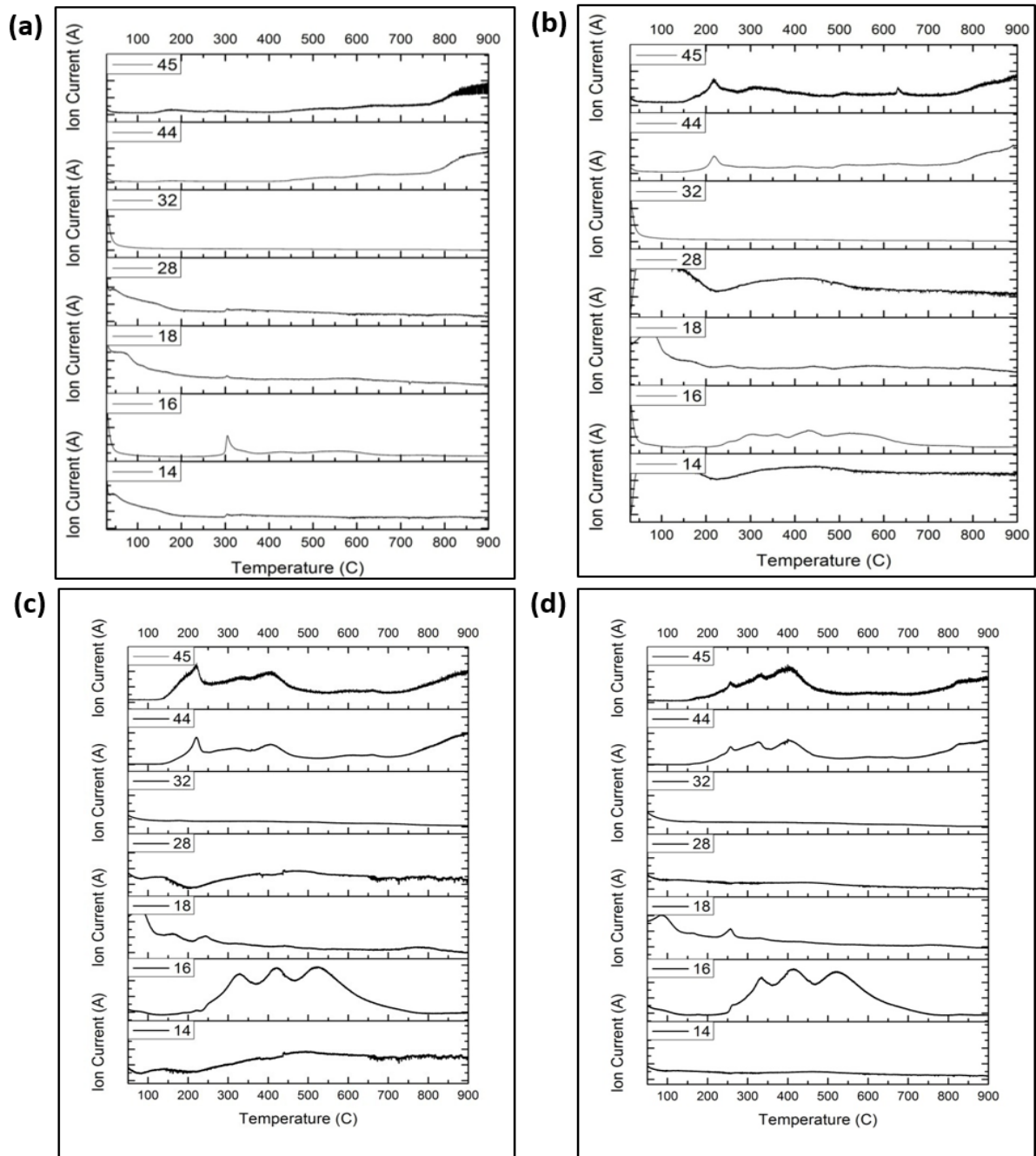


Figure 4.6. The simultaneous TGA -MS spectra of electrospun fibers as a function of IA monomer ratio (a) PAN (b) P(AN-*co*-IA)-2 (c) P(AN-*co*-IA)-5 (d) P(AN-*co*-IA)-8.

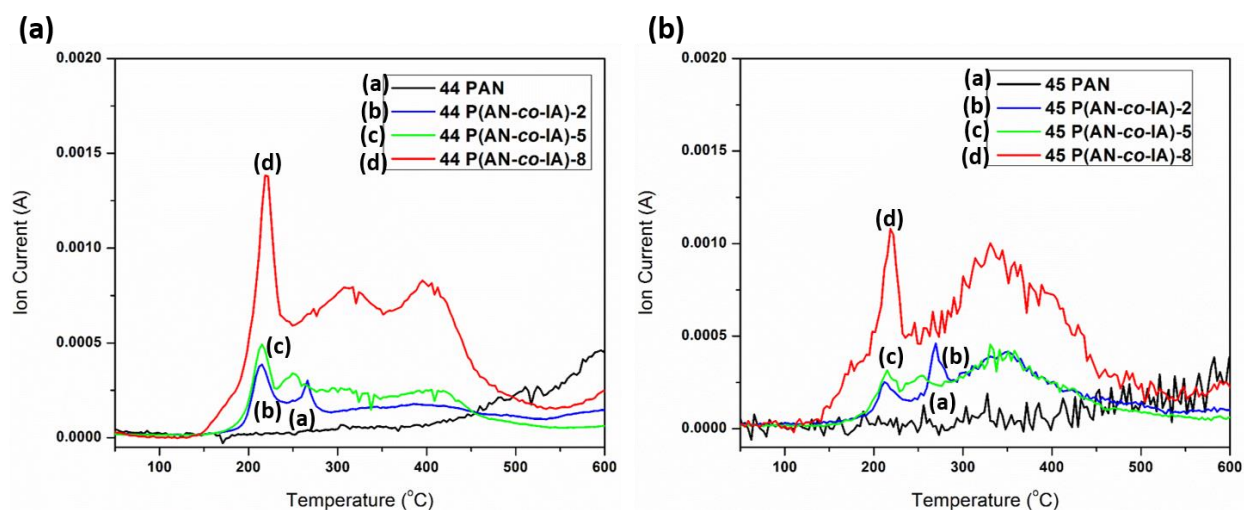


Figure 4.7. (a) CO₂ ion intensity and (b) COOH ion intensity of electrospun fibers as a function of IA monomer ratio derived from TGA-MS spectra.

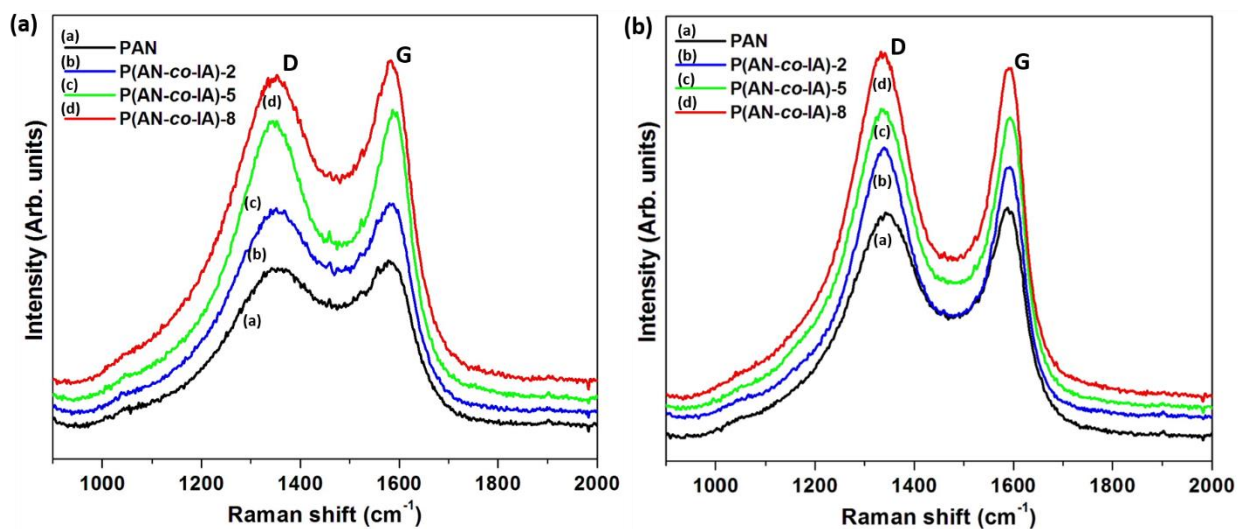


Figure 4.8. Raman spectra of (a) CNF and (b) ACNF.

Raman spectroscopy is a very useful technique for determining the structural properties of nanostructured carbons. The Raman spectra of carbonized fibers and activated fibers of all samples

tested are shown in Figure 4.8 (a) and (b) respectively. All the spectra contain two strong peaks at ~ 1580 and 1350 cm^{-1} assigned to ordered graphitic structures due to sp^2 carbon (G-band) and disordered carbonaceous structures due to sp^3 carbon (D-band) respectively. The I_D/I_G ratio measures disorder in the graphitic structure. A Lorentzian equation was used for peak fitting in order to calculate the ratios of the integrated area intensity of D band to G band (I_D/I_G) of all the spectra shown in Figure 4.8. The I_D/I_G ratio of the CNFs decreased from 2.23, 2.22, 2.03 and 2.01 for 0 wt%, 2wt%, 5wt% and 8wt% of IA copolymers with increasing composition confirming that different carbon structures can be developed from precursors with different compositions when they undergo *in situ* activation. The I_D/I_G ratio decrease with an increase of IA in copolymer and as well as has smaller ratio from copolymer compared to that of PAN indicates that high degree of graphitization of porous carbon materials. This can be attributed to the smooth decomposition of copolymer during carbonization when compared to PAN as evident by DSC. This can result in more fragmentation in PAN hence more defects when carbonized. However, there is a slight increase in disordered carbon with additional CO_2 activation. The I_D/I_G calculated for ACNF increased from 2.73, 2.79, 2.94 and 3.01 for 0 wt%, 2wt%, 5wt% and 8wt% of IA copolymers. Hence a balance must be between graphitic content (conductivity), porosity (capacitance), and char yield.

4.4.3 Nitrogen adsorption and pore size analysis

The nitrogen adsorption-desorption isotherms were used to analyze the pore structures of CNF and ACNF samples as shown in Figure 4.9(a) and (c). It can be seen that most of the N_2 adsorption-

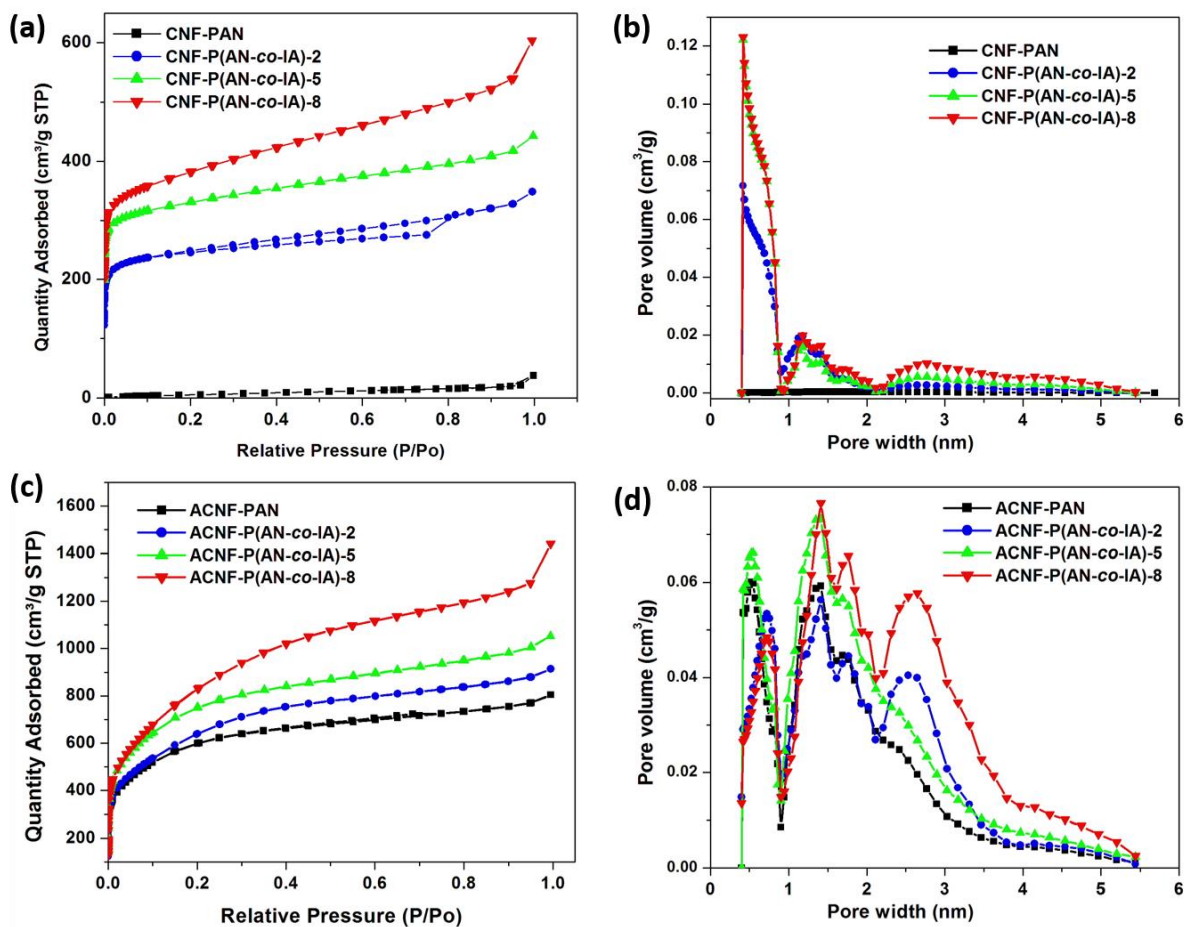


Figure 4.9. (a) Nitrogen adsorption/desorption isotherms and (b) pore size distribution for CNFs (c) Nitrogen adsorption/desorption isotherms and (b) pore size distribution for ACNFs.

desorption isotherms of materials show the typical type-I curves (IUPAC classification). The pore size distribution curves calculated using the DFT method are shown in Figure 4.9(b). Table 4.2 summarizes the surface area of all samples. *In situ* activation of IA copolymer afforded a remarkable increase in the surface area of the nanofibers from $6 \text{ m}^2 \text{ g}^{-1}$ for PAN-derived fibers to $1240 \text{ m}^2 \text{ g}^{-1}$ for those derived from 8 wt% IA incorporation. Surface areas are in good agreement with the TGA-MS analysis. The high surface area induced by removal CO_2 gases and COOH

functionalities from IA moiety in copolymer. On the other hand PAN doesn't show any *in situ* activity like the copolymers, and exhibited a very low surface area. The nanometer sized fibers from P(AN-*co*-IA) also benefits to enhance the surface area. Therefore, the surface areas derived from all the P(AN-*co*-IA) samples exhibited much higher surface areas than the PAN homopolymer. Samples without any *ex situ* activation possessed more micropores which are created by the *in situ* decomposition of the COOH groups and reaction between fibers and evolved CO₂ upon decomposition of COOH. Increasing surface area by the addition of more IA confirm the *in situ* porogen activity of itaconic acid. The changing micro/meso ratio upon increasing IA ratio confirms the tunability of the pore distribution. This approach enables better control of the pore distribution by a straightforward procedure compared to the harsh chemical activation using ZnCl₂ or KOH which results in uncontrollable pore sizes. After external CO₂ activation, the surface areas of the CNFs prepared from P(AN-*co*-IA)-8 further increase to 2972 m² g⁻¹. Upon, external CO₂ activation, both the micro-pore volume and the meso-pore volume are further increased. The ionic liquid electrolyte used in this study is EMITFSI which has ion sizes of 4.3 x 7.6 Å (for EMI⁺) and 2.9 x 7.9 Å (for TFSI⁻). Only the same or larger pore sizes in the fiber compared to the size of electrolyte ions could facilitate better ion diffusion. For all CNF samples derived from the copolymer, more than 90% of the pore volume is accessible to the cations and 100% are accessible to the anions. For the ACNFs more than 94% of the pore volume is accessible to cations and 100% are accessible to anions by considering shortest dimension of anion and cation.

Table 4.2. Surface area and pore volume of PAN and P(AN-*co*-IA) based CNFs and ACNFs

Precursor	Surface area (m ² /g)	Total pore Volume (cm ³ /g)	V _{micro} (cm ³ /g)	V _{meso} (cm ³ /g)	Micropore /mesopore ratio
CNF-PAN	6	0.0129	0.0053	0.0076	0.70
CNF-P(AN- <i>co</i> -IA)-2	912	0.3871	0.3394	0.0477	7.12
CNF-P(AN- <i>co</i> -IA)-5	1041	0.5459	0.4479	0.0980	4.57
CNF-P(AN- <i>co</i> -IA)-8	1240	0.6736	0.4900	0.1836	2.67
ACNF-PAN	2178	1.0035	0.6975	0.3060	2.28
ACNF-P(AN- <i>co</i> -IA)-2	2287	1.1426	0.6724	0.4702	1.43
ACNF-P(AN- <i>co</i> -IA)-5	2406	1.1447	0.7547	0.6900	1.09
ACNF-P(AN- <i>co</i> -IA)-8	2972	1.6260	0.7941	0.8289	0.96

4.4.4 Electrochemical characterizations

The capacitance, C , of the two-electrode device was calculated from the cyclic voltammograms by using the Equations 4.1 and 4.2.

$$C = \int I/vdt \quad (4.1)$$

Where, I is the integrated discharge current over the potential range at a particular scan rate (v).

Specific capacitance, C_{sp} , is related to the cell capacitance as

$$C_{sp} = 4C / m \quad (4.2)$$

Where, m is the mass of both electrodes. Energy densities (E_d) and power densities (P_d) were calculated using Equations 4.3 and 4.4, respectively.

$$E_d = \frac{1}{2} CV^2 \quad (4.3)$$

$$P_d = E_d / t \quad (4.4)$$

Where, V is the Voltage and t is the time it takes to discharge to 0 V from the initial voltage, after considering the IR drop at the beginning of discharge.

Electrochemical properties of CNFs

Free-standing and flexible carbon nanofiber mats were obtained after thermal treatments as shown in Figure 4.10(a). Flexible fiber mats avoid the need for binders which can cause a decrease the performance. Figure 4.10(b)-(d) represents CV curves of carbonized P(AN-*co*-IA) without any subsequent activation at five different scan rate in EMITFSI ionic liquid electrolyte. Carbonized P(AN-*co*-IA) without any activation shows rectangular shaped CVs indicating the ideal capacitive character of the EDLC as compared to carbonized but unactivated PAN which failed to produce significant currents (Figure S4.5). The specific capacitance values obtained for all the P(AN-*co*-IA) with different compositions are higher than the PAN at all scan rates because of their higher surface area as confirmed by surface area analysis. Furthermore, the capacitance increases with increasing IA content as shown in Figure 4.11(a). The highest specific capacitance of P(AN-*co*-IA)-8 at 10 mV s⁻¹ was calculated to be 92.9 F g⁻¹ compared to 1.9 F g⁻¹ for the PAN. Significantly this copolymer precursor with *in situ* porogens shows the same specific capacitance (with high char yield of 35%) as CO₂ activated PAN which has a low char yield of 10% after activation.

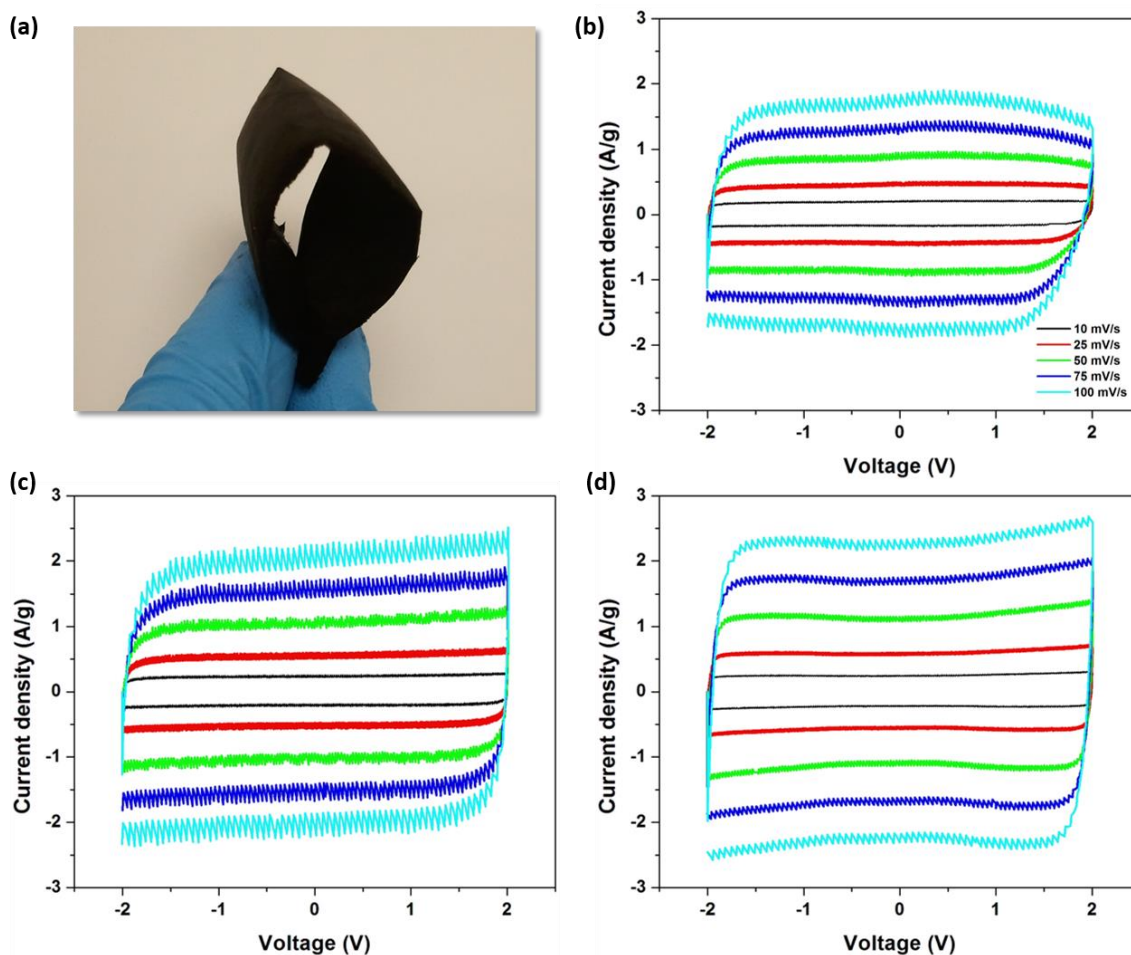


Figure 4.10. (a) Optical image of flexible carbonized mat derived from copolymer P(AN-*co*-IA)-8, cyclic voltammograms of CNFs derived from (b) P(AN-*co*-IA)-2 (c) P(AN-*co*-IA)-5 (d) P(AN-*co*-IA)-8.

Energy and power densities for different charging rates from 1 A g^{-1} to 10 A g^{-1} of all the carbonized samples without activation are shown in the Ragone plot in Figure 4.11(b) and summarized in Table 4.3. P(AN-*co*-IA)-8 electrodes exhibit the high energy density of 45.9 Wh kg^{-1} with a power density of 1.7 kW kg^{-1} . This drops to 31 Wh kg^{-1} at 15 kW kg^{-1} . Significant surface area, and high percentage of mesopores lead to good energy density retention at high current densities of around 68% for P(AN-*co*-IA)-8. Linear discharge plots for samples (Figure 4.11(c)) illustrate the

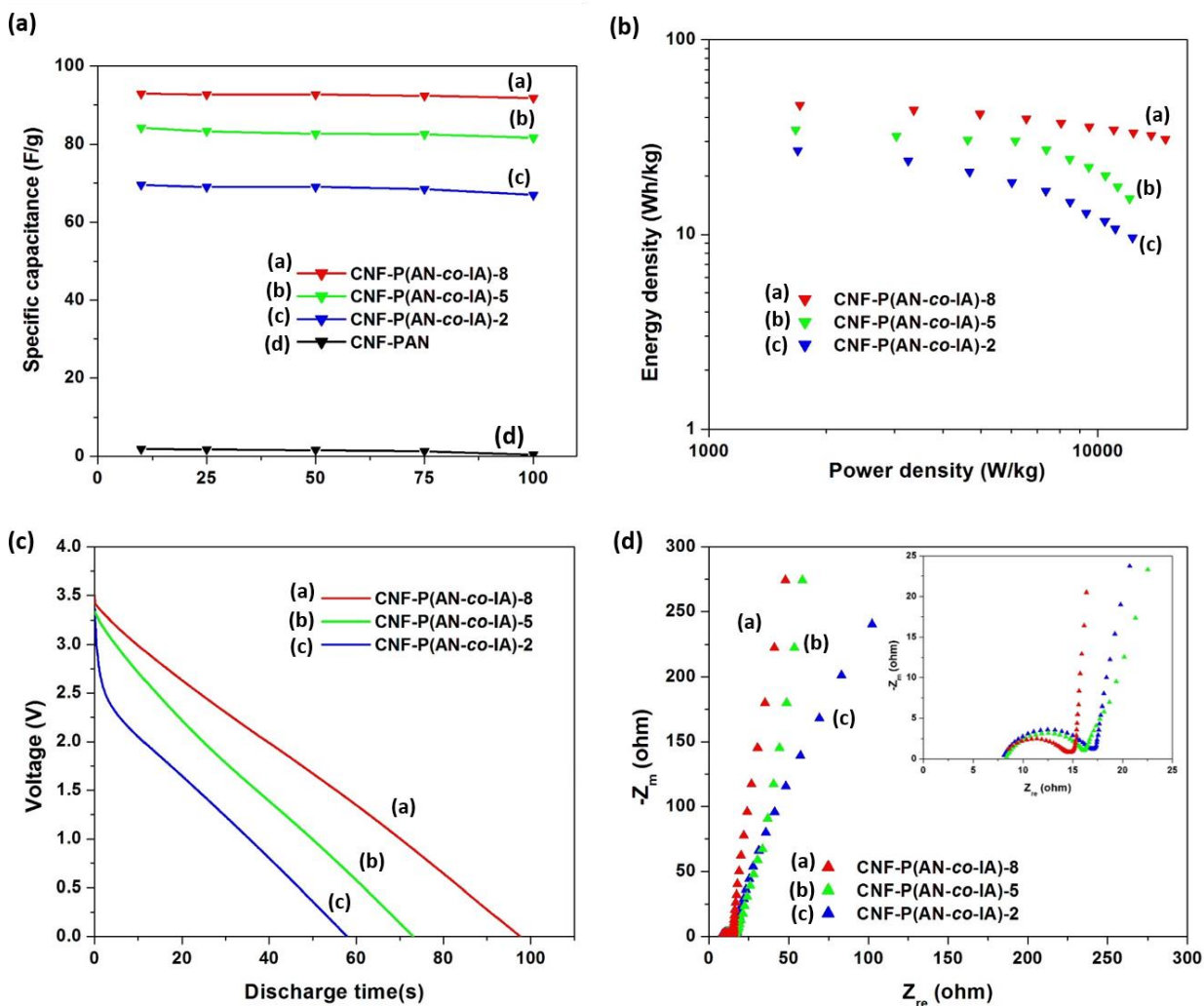


Figure 4.11. (a) Specific capacitance (b) Ragone plot (c) Galvanostatic discharging curves at a constant current density of 1 A g^{-1} (d) Nyquist plots for the CNF samples.

capacitive behavior for P(AN-co-IA)-8 and P(AN-co-IA)-5. These electrodes also show small IR drop at the same current density. Nyquist plots of all electrodes were shown in Figure 4.11(d). At high to medium frequency region, the semi-circle observed corresponds to the sum of the electrical resistance the electrolyte, contact resistance in the electrode/current collector and the charge transfer resistance of the electrolyte. For CNF samples, the ESR values of P(AN-co-IA)-8 was 6.1

Ω , much lower than that of P(AN-*co*-IA)-5 (7.8 Ω) and P(AN-*co*-IA)-2 (8.9 Ω), which depicts the good ion transport of the P(AN-*co*-IA)-8. Almost vertical increase in lower frequency region, indicative of ideal capacitance and the 45° line in all electrodes in the intermediate frequency region reflect the fast of ion diffusion into the electrode materials. As observed commonly in other carbons, activation in all cases led to significant increase of the specific surface area which lead to higher performance but with lower char yields.

Table 4.3. Specific capacitance, energy density and power density of carbonized nanofibers (CNFs)

Precursor	Specific capacitance	Energy density	Energy density
	at 10 mV s ⁻¹ (F g ⁻¹)	(Wh kg ⁻¹) at 1 A g ⁻¹	(Wh kg ⁻¹) at 10 A g ⁻¹
CNF-P(AN- <i>co</i> -IA)-2	69.5	27.0	9.6
CNF-P(AN- <i>co</i> -IA)-5	84.1	34.5	16.2
CNF-P(AN- <i>co</i> -IA)-8	92.9	45.9	30.9

Electrochemical properties of ACNFs (study impact of CO₂ activation)

It is well known that activation of fibers causes an increased surface area in all cases. Carbonized fibers of P(AN-*co*-IA) without any activation show the path to making high performing carbon precursor using the concept of *in situ* porogen without *ex situ* activation for supercapacitors. As a next step, in order to compare with other commonly studied carbon prepared by chemical or physical activation, precursor material previously carbonized at 1000 °C without any activation was subjected to CO₂ activation for 1h at 1000 °C. CO₂ activation caused to further creation of pores which lead to enhanced electrochemical performances.

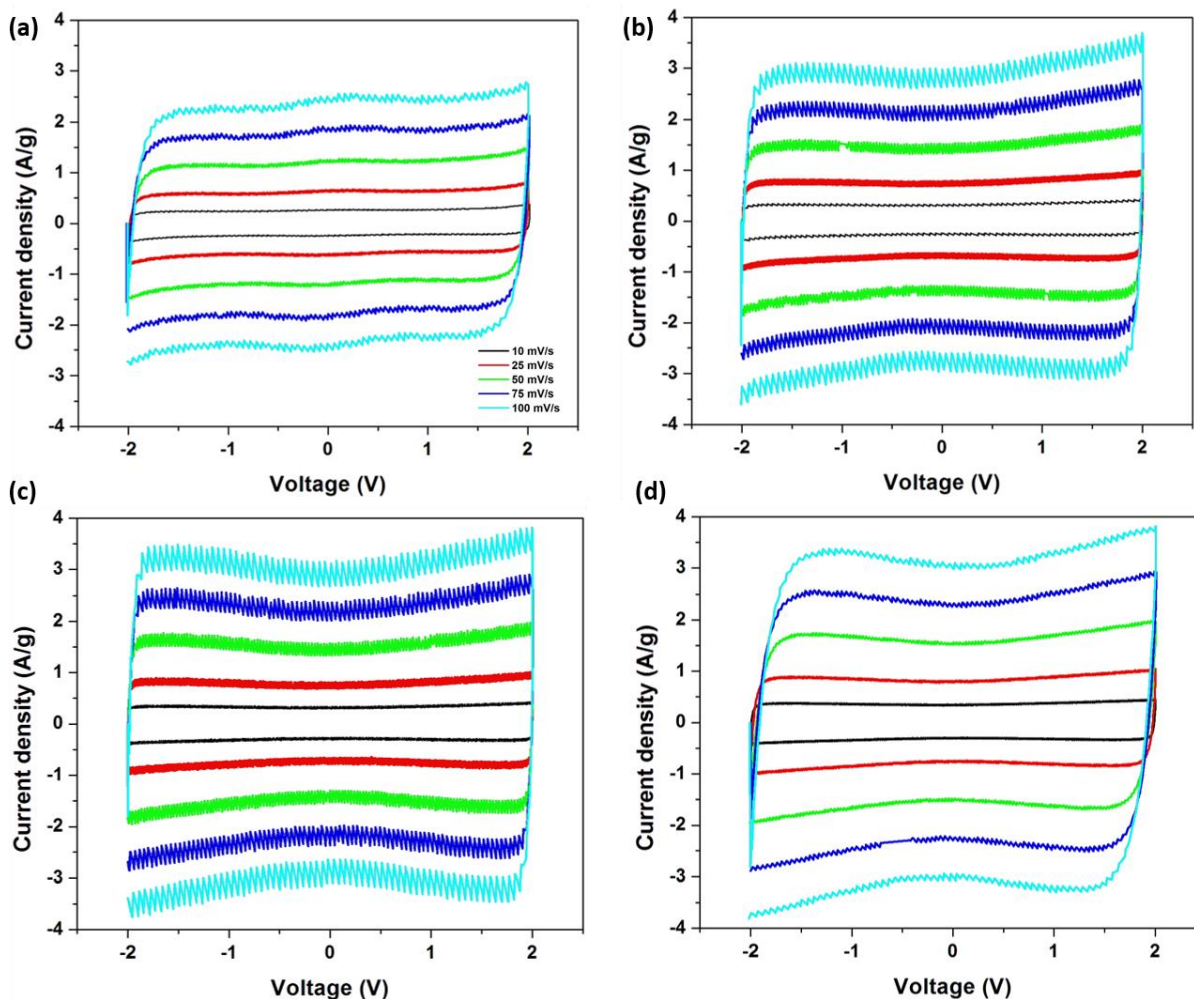


Figure 4.12. Cyclic voltammograms of ACNFs derived from (a) PAN (b) P(AN-co-IA)-2 (c) P(AN-co-IA)-5 (d) P(AN-co-IA)-8.

When these carbonized fibers were CO₂ activated P(AN-co-IA) showed very box like CV (Figure 4.12) even at higher current densities when compared with PAN upon *ex situ* activation. The rectangular shapes of CV curves were retained without dramatic distortions as the scan rate was increased from 25 mV s⁻¹ to 100 mV s⁻¹, showing fast charge transfer at the electrode/electrolyte interfaces.

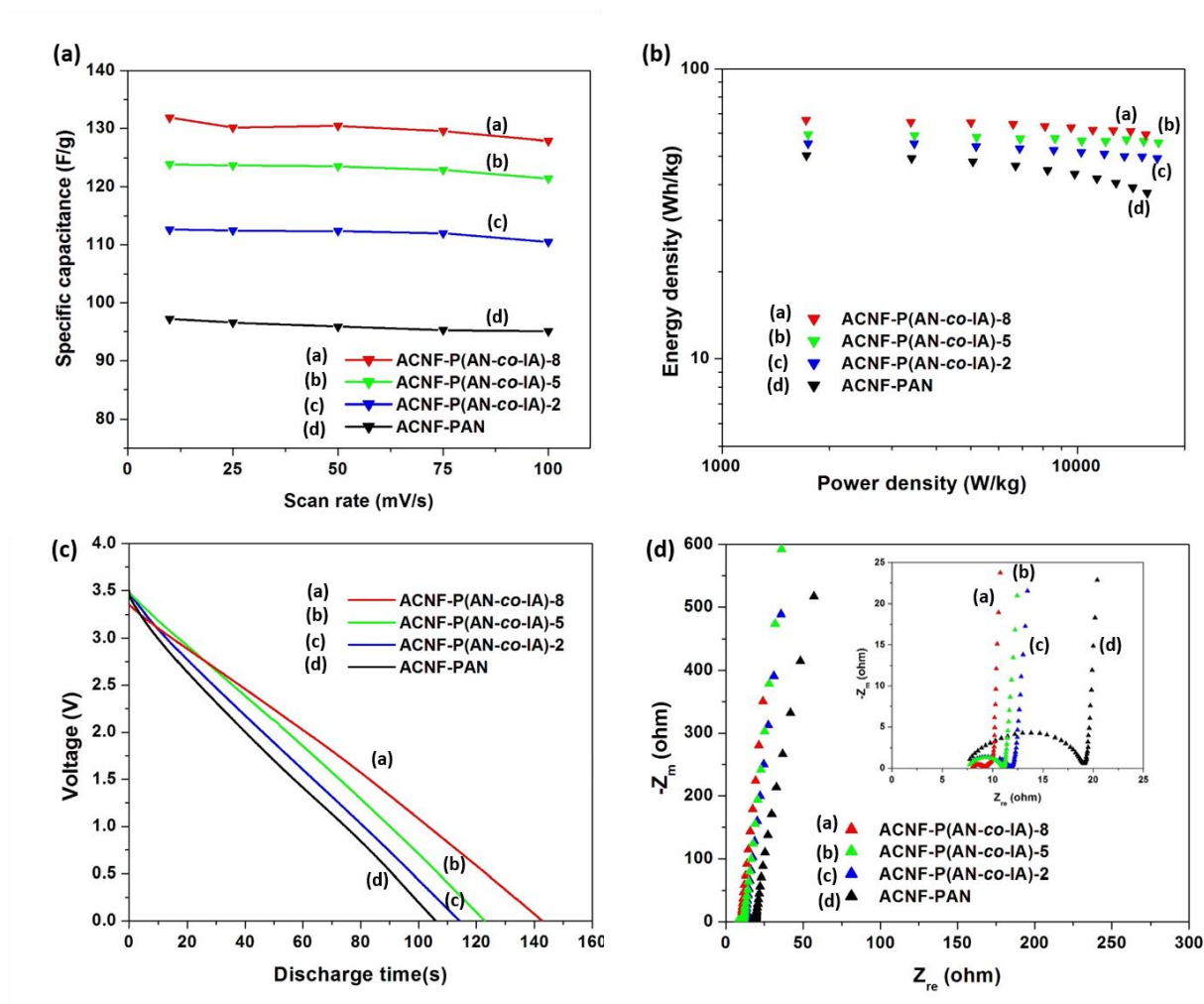


Figure 4.13. (a) Specific capacitance (b) Ragone plot (c) Galvanostatic discharging curves at a constant current density of 1 A g⁻¹ (d) Nyquist plots for the ACNF samples.

As shown in the Ragone plot (Figure 4.13(a)) a very small drop in the energy density of the electrodes from activated samples of P(AN-co-IA) was observed at high power density. In contrast, the energy density of the electrodes from PAN drops fast with increasing current density from 1 A g⁻¹ to 10 A g⁻¹. The energy and power densities of the supercapacitors assembled with CO₂ activated nanofibers at a current discharge density of 1 A g⁻¹ and 10 A g⁻¹ were listed in the Table 3.4. The activation process significantly improves energy and power densities over carbonization

alone. The energy density calculated at 1 A g^{-1} was 55.5 Wh kg^{-1} for P(AN-*co*-IA)-2 compared to that of PAN CNFs (50.1 Wh kg^{-1}) at similar power densities. The highest energy density of 67 Wh kg^{-1} was obtained for P(AN-*co*-IA)-8 sample containing the highest composition of IA. CO_2 activation has advantages such as better capacitance retention (90%) especially at faster discharge rates and lower device ESR. For ACNF samples, the ESR values of P(AN-*co*-IA)-8 was 1.3Ω , P(AN-*co*-IA)-5 (3.3Ω) and P(AN-*co*-IA)-2 (3.9Ω), much lower than that of activated PAN devices which have an ESR around 11.4Ω . Activated carbon electrodes show similar impedance to unactivated ones, however, with very vertical straight line almost parallel to the imaginary axis at the low frequency range.

Table 4.4. Specific capacitance, energy density and power density of carbonized nanofibers (ACNFs)

Precursor	Specific capacitance at 10 mV s^{-1} (F g^{-1})	Energy density (Wh kg^{-1}) at 1 A g^{-1}	Energy density (Wh kg^{-1}) at 10 A g^{-1}
ACNF-PAN	97.2	50.1	37.4
ACNF-P(AN- <i>co</i> -IA)-2	116.4	55.5	49.1
ACNF-P(AN- <i>co</i> -IA)-5	123.9	59.4	55.7
ACNF-P(AN- <i>co</i> -IA)-8	131.9	66.5	59.4

4.5 Conclusion

P(AN-*co*-IA) copolymers were synthesized to develop new precursor polymers for high performance carbon fibers as electrode materials for supercapacitors. Binderless flexible and free-

standing carbon nanofibers were prepared by thermal treatment (with and without subsequent CO₂ activation) of the nanofibers mats obtained by electrospinning the copolymers. The COOH groups in P(AN-*co*-IA) act as an *in situ* porogen from release of CO₂ during the carbonization process to increase the surface area of the CNFs without any extra activation steps. This leads to porous carbon fiber with a simple one step carbonization. We demonstrate that the copolymers without any activation have significantly higher electrochemical performance than PAN with the same condition and exhibit comparable performance as CO₂ activated PAN fiber. This study mainly focused on developing new precursors to achieve electrochemical performance without any subsequent activation that was at least comparable to that derived from conventional activated carbon material. We further studied this new precursor with CO₂ activation to investigate impact of activation on their performance. The highest capacitance obtained for the carbonized P(AN-*co*-IA)-8 was 92.7 F g⁻¹ at 10 mV s⁻¹ and 40.5 Wh kg⁻¹ at 1 A g⁻¹ and further increased to 131.5 F g⁻¹ and 66.5 Wh kg⁻¹ upon CO₂ activation. This work highlights the potential applicability of P(AN-*co*-IA) to produce electrode materials for high performance energy storage systems.

Acknowledgements

We acknowledge the National Science Foundation (Grant no. IIP-1127564) for financial support and Grant no. CHE-1126177 for the purchase of the Bruker AVANCE III™ 500 MHz NMR. We also thank Dr. Manuel Quevedo-Lopez (Department of Material Science and Engineering at The University of Texas at Dallas) for extending his Raman facility to us and Isable Pinter for help with Raman analysis.

4.6 Appendix - Supporting Information

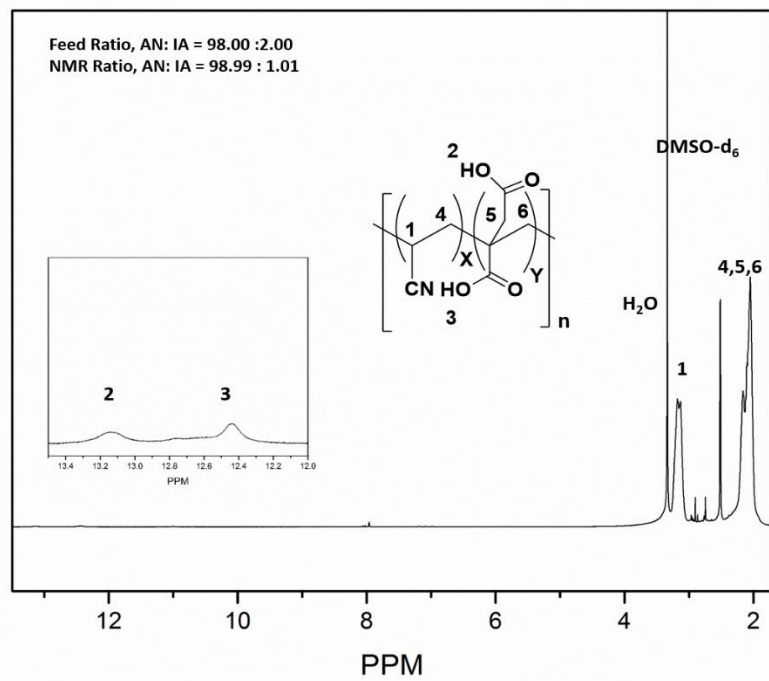


Figure S4.1. ^1H -NMR analysis of P(AN-*co*-IA)-2.

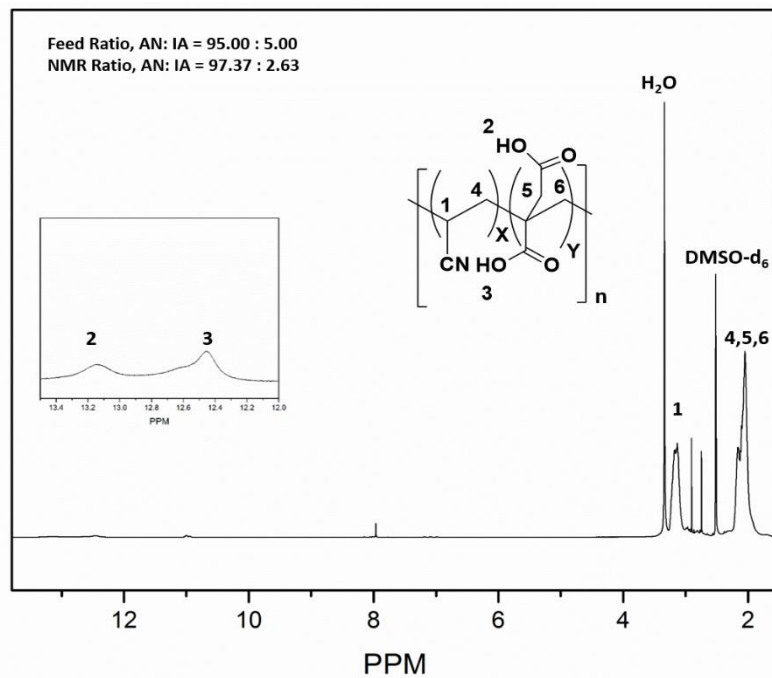


Figure S4.2. ^1H -NMR analysis of P(AN-*co*-IA)-5.

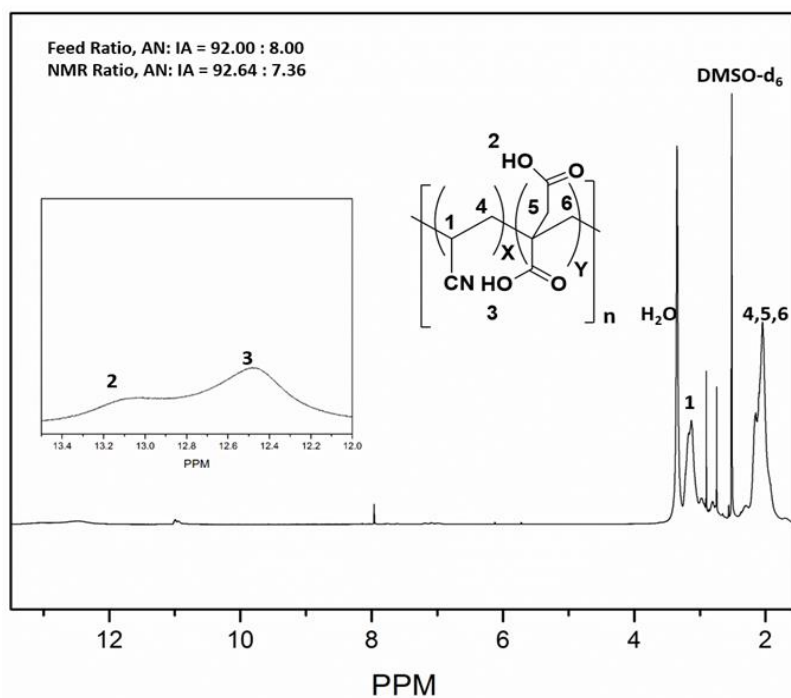


Figure S4.3. ¹H-NMR analysis of P(AN-*co*-IA)-8.

The backbone of CH₂ from IA and AN linkages are indicated by NMR signals at 2 ppm. Peaks at 3.1 ppm represent the backbone CH of the AN. Two peaks at 12.0-13.5 ppm represent the OH groups from the acid groups. There are three small peaks at 8.03, 2.92, and 2.75 ppm for the residual DMF that was used for synthesis of copolymers.

Table S4.1. Molecular weights of the synthesized polymers

Precursor	Molecular weight		PDI
	Mn (KDa)	Mw (KDa)	
P(AN- <i>co</i> -IA)-2	68.1	113.8	1.7
P(AN- <i>co</i> -IA)-5	88.6	128.6	1.5
P(AN- <i>co</i> -IA)-8	108.2	143.4	1.3

Mn = Number-average molecular weight

Mw = Weight-average molecular weight

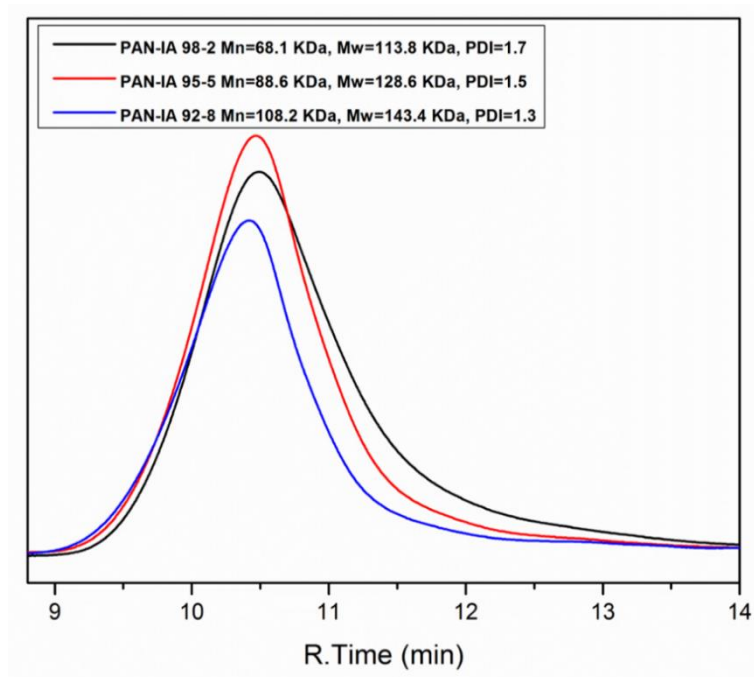


Figure S4.4. SEC analysis of the synthesized polymers.

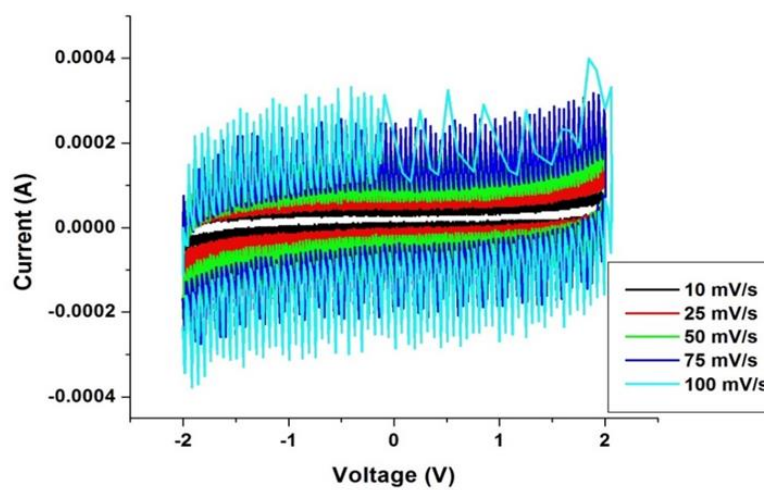


Figure S4.5. Cyclic voltammograms of carbonized nanofibers derived from PAN homopolymer.

4.7 References

- (1) Chen, S.-M.; Ramachandran, R.; Mani, V.; Saraswathi, R. Recent Advancements in Electrode Materials for the High- Performance Electrochemical Supercapacitors: A Review. *Int. J. Electrochem. Sci* **2014**, 9, 4072–4085.
- (2) Arico, A. S.; Bruce, P.; Scrosati, B.; Tarascon, J.; Schalkwijk, W. V. Nanostructured Materials for Advanced Energy Conversion and Storage Devices. *Nat. Mater.* **2005**, 4, 366 - 377.
- (3) Gonzalez, A.; Goikolea, E.; Andoni, J.; Mysyk, R. Review on Supercapacitors : Technologies and Materials. *Renew. Sustainable Energy Rev.* **2016**, 58, 1189–1206.
- (4) Winter, M.; Brodd, R. J. What Are Batteries, Fuel Cells, and Supercapacitors ? What Are Batteries, Fuel Cells, and Supercapacitors ? *Chem.Rev.* **2004**, 104, 4245–4270.
- (5) Conway, B. Transition from “Supercapacitor” to “Battery” Behavior in Electrochemical Energy Storage. *J. Electrochem. Soc.* **1991**, 138 (6), 1539–1548.
- (6) Zhang, S.; Pan, N. Supercapacitors Performance Evaluation. *Adv. Energy Mater.* **2015**, 5, 1401401/1-1401401/19.
- (7) Yan, J.; Wang, Q.; Wei, T.; Fan, Z. Recent Advances in Design and Fabrication of Electrochemical Supercapacitors with High Energy Densities. *Adv. Energy Mater.* **2014**, 4 1300816/1-1300816/43.
- (8) Beguin, F.; Presser, V.; Balducci, A.; Frackowiak, E. Carbons and Electrolytes for Advanced Supercapacitors. *Adv. Mater.* **2014**, 26 (14), 2219–2251.
- (9) Simon, P.; Gogotsi, Y. Materials for Electrochemical Capacitors. *Nat. Mater.* **2011**, 3–5.
- (10) Kim, C.; Yang, K. S. Electrochemical Properties of Carbon Nanofiber Web as an Electrode for Supercapacitor Prepared by Electrospinning. *Appl. Phys. Lett.* **2003**, 83 (6), 1216–1219.
- (11) Abeykoon, N. C.; Bonso, J. S.; Ferraris, J. P. Supercapacitor Performance of Carbon Nanofiber Electrodes Derived from Immiscible PAN/PMMA Polymer Blends. *RSC Adv.* **2015**, 5 (26), 19865–19873.
- (12) Chem, J. M.; Wang, J.; Kaskel, S. KOH activation of carbon-based materials for energy storage. *J. Mater. Chem.*, **2012**, 22, 23710–23725.
- (13) Wang, S.; Yu J. Cotton-Derived Carbon Fibers with High Specific Capacitance by ZnCl₂ Activation for Supercapacitor Application. *Advances in Engineering Research.* **2016**, 63, 358–363.

- (14) Subramanian, V.; Luo, C.; Stephan, A. M.; Nahm, K. S.; Thomas, S. Supercapacitors from Activated Carbon Derived from Banana Fibers. *J. Phys. Chem. C* **2007**, *111*, 7527–7531.
- (15) Sun, X.; Cheng, P.; Wang, H.; Xu, H.; Dang, L.; Liu, Z.; Lei, Z. Activation of Graphene Aerogel with Phosphoric Acid for Enhanced Electrocapacitive Performance. *Carbon*. **2015**, *92*, 1–10.
- (16) Zhi, M.; Liu, S.; Hong, Z.; Wu, N. Electrospun activated carbon nanofibers for supercapacitor electrodes†. *RSC Adv.* **2014**, *4*, 43619–43623.
- (17) Bonso, J. S.; Kalaw, G. D.; Ferraris, J. P. High Surface Area Carbon Nanofibers Derived from Electrospun PIM-1 for Energy Storage Applications. *J. Mater. Chem. A* **2014**, *2* (2), 418–424.
- (18) Jung, K.-H.; Ferraris, J. P. Preparation of Porous Carbon Nanofibers Derived from PBI/PLLA for Supercapacitor Electrodes. *Nanotechnology* **2016**, *27* (42), 425708.
- (19) Jung, K. H.; Ferraris, J. P. Preparation and Electrochemical Properties of Carbon Nanofibers Derived from Polybenzimidazole/polyimide Precursor Blends. *Carbon* **2012**, *50* (14), 5309–5315.
- (20) Ra, E. J.; Kim, T. H.; Yu, W. J.; An, K. H.; Lee, Y. H. Ultramicropore Formation in PAN/camphor-Based Carbon Nanofiber Paper. *Chem. Commun. (Camb)*. **2010**, *46* (8), 1320–1322.
- (21) Moore, B. C.; Macia, J. A. Influence of Carbon Fibres Crystallinities on Their Chemical Activation by KOH and NaOH. *Micropor Mesopor Mat.* **2007**, *101*, 397–405.
- (22) Peranathan, S.; Bonso, J. S.; Ferraris, J. P. Supercapacitors Utilizing Electrodes Derived from Polyacrylonitrile Fibers Incorporating Tetramethylammonium Oxalate as a Porogen. *Carbon* **2016**, *106*, 20–27.
- (23) Puthusseri, D.; Aravindan, V.; Madhavi, S.; Ogale, S. 3D Micro-Porous Conducting Carbon Beehive by Single Step Polymer Carbonization for High Performance Supercapacitors: The Magic of in Situ Porogen Formation. *Energy Environ. Sci.* **2014**, *7* (2), 728–735.
- (24) Jung, K. H.; Deng, W.; Smith, D. W.; Ferraris, J. P. Carbon Nanofiber Electrodes for Supercapacitors Derived from New Precursor Polymer: Poly(acrylonitrile-Co-Vinylimidazole). *Electrochem. commun.* **2012**, *23* (1), 149–152.
- (25) Faraji, S.; Yardim, M. F.; Can, D. S.; Sarac, A. S. And Poly (Acrylonitrile- Co -Itaconic Acid) Based Activated Carbon Nanofibers. *J. appl. polym. sci.* **2017**, *44381*, 1–10.

- (26) Nataraj, S. K.; Yang, K. S.; Aminabhavi, T. M. Polyacrylonitrile-Based Nanofibers - A State-of-the-Art Review. *Prog. Polym. Sci.* **2012**, *37* (3), 487–513.
- (27) Farsani, R. E.; Raissi, S.; Shokuhfar, A.; Sedghi, A. FT-IR Study of Stabilized PAN Fibers for Fabrication of Carbon Fibers. *World Acad Sci Eng Technol.* **2009**, *3* (2), 319–322.
- (28) Mahmood, S. F. Automobile Grade Carbon Fiber Precursor Study: I. Copolymer System and II. Terpolymer System, University of Texas at Dallas, **2015**. (Available from Dissertations & Theses @ University of Texas at Dallas; ProQuest Dissertations & Theses Global. (1712988725). Retrieved from <http://libproxy.utdallas.edu/login?url=http://search.proquest.com/docview/1712988725?accountid=7120>)
- (29) Xue, Y.; Liu, J.; Liang, J. Correlative Study of Critical Reactions in Polyacrylonitrile Based Carbon Fiber Precursors during Thermal-Oxidative Stabilization. *Polym. Degrad. Stab.* **2013**, *98* (1), 219–229.
- (30) Nguyen-thai, N. U.; Hong, S. C. Structural Evolution of Poly (Acrylonitrile- Co -Itaconic Acid) during Thermal Oxidative Stabilization for Carbon Materials. *Macromolecules*, **2013**, *46* (15), 5882–5889.
- (31) Ouyang, Q.; Cheng, L.; Wang, H.; Li, K. Mechanism and Kinetics of the Stabilization Reactions of Itaconic Acid-Modified Polyacrylonitrile. *Polym. Degrad. Stab.* **2008**, *93*, 1415–1421.
- (32) Devasia, R.; Reghunadhan, C. P.; Sivadasan, P.; Katherine, B. K.; Ninan, K. N. Cyclization Reaction in Poly (Acrylonitrile / Itaconic Acid) Copolymer : An Isothermal Differential Scanning Calorimetry Kinetic Study. *J. Appl. Polym. Sci.* **2003**, *88*(4), 915-920.
- (33) Yu, M.; Wang, C.; Zhao, Y.; Zhang, M.; Wang, W. Thermal Properties of Acrylonitrile / Itaconic Acid Polymers in Oxidative and Nonoxidative Atmospheres. *J. Appl. Polym. Sci.* **2010**, *116*(2), 1207-1212.
- (34) Pillay, V.; Dott, C.; Choonara, Y. E.; Tyagi, C.; Tomar, L.; Kumar, P.; Toit, L. C.; Ndesendo, V. M. K. A Review of the Effect of Processing Variables on the Fabrication of Electrospun Nanofibers for Drug Delivery Applications. *J Nanomater.* **2013**, 789289, 22 pp.

CHAPTER 5

HIGH SURFACE AREA CARBON NANOFIBER SUPERCAPACITOR ELECTRODES DERIVED FROM AN *IN SITU* POROGEN CONTAINING TERPOLYMER: POLY(ACRYLONITRILE-*CO*-1-VINYLMIDAZOLE-*CO*-ITACONIC ACID)

5.1 Abstract

Polyacrylonitrile (PAN) is one of the most widely studied precursor polymers for making high performance carbon nanofibers (CNFs) for supercapacitors because of its electrospinnability and high carbon yield. Copolymerization with vinylimidazole (VIM) or acidic monomers such as itaconic acid (IA) comprises an attractive approach to modify the properties of PAN-based fibers. In this study, the terpolymer, poly(acrylonitrile-*co*-1-vinylimidazole-*co*-itaconic acid), P(AN-VIM-IA) was synthesized with different ratios of AN with VIM and/or IA monomers to develop new CNF precursors for supercapacitor applications. Here, IA serve as *in situ* porogen that releases CO₂ during the carbonization process to increase surface area without the need for subsequent activation, thus simplifying the fabrication of these CNFs. The imidazole groups in 1-vinylimidazole (VIM) moieties disrupt the strong dipole-dipole interactions between nitrile groups in pure PAN thus facilitating the processability and thermal stabilization of PAN. A different ratio of AN, VIM with IA was reacted to yield a series of P(AN:VIM:IA) terpolymers, (90:5:5), (85:5:10) and (72:5:23). The terpolymer having the 23 wt% of IA, shows the highest capacitance of 97.0 F g⁻¹ at a scan rate of 10 mV s⁻¹ with energy density of 49 Wh kg⁻¹ at 10 kW kg⁻¹, which was further enhanced to 136.7 F g⁻¹ at 10 mV s⁻¹ and 79 Wh kg⁻¹ at 10 kW kg⁻¹ upon CO₂ activation.

5.2 Introduction

Supercapacitors, also called electrochemical double layer capacitors (EDLC) are among the more promising energy storage devices of today, due to their fast charging and long cycling stabilities. However, supercapacitors have lower energy densities than batteries, which limit their applications.^{1,2} A supercapacitor has two porous electrodes immersed in the electrolyte and can also store much more energy than conventional capacitors. The primary reasons for this difference are the porous carbon electrodes, which have exceptionally high surface areas, as well as the charge storage mechanism, which relies on the interactions between these electrodes and ions dissociated in a electrolyte (electrochemical double layer) to store and release energy.³ Much of the research on supercapacitors is focused around increasing their energy density. Carbon fibers from electrospinning are highly attractive electrode material for supercapacitors because of their ease of preparation, mechanical strength, high surface area, and reasonable conductivity.^{4,5} The preparation of high surface area electrode materials for capacitor applications focuses on careful control of the porous structure.^{6,7} Several strategies were reported to induce pores on the fibers that include activation, templated synthesis, polymer blending and incorporation of porogens.⁸ In the physical activation, NH_3 ,⁹ CO_2 ,¹⁰ and steam¹¹ are used to induce pores and NaOH ,¹² KOH ,¹³ ZnCl_2 ¹⁴ and H_3PO_4 ¹⁵ were used in the chemical activation. Physical activation lowers the char yield at the end of the carbonization because of chemical reaction between precursor material and applied gases.¹⁶ On the other hand, chemical activation results in very high surface area with developed pores on the outer surface, but it also creates very narrow electrolyte- inaccessible pores in the bulk. In addition to that, byproducts generated by chemical activation, remain in the samples and have adverse effects in the later processes. Furthermore, extra steps that are needed to remove

these corrosive etchants and byproducts from the samples usually counteract the advantages.^{8,17,18} Polymer blends consisting of a sacrificial and a carbonizing polymer can also afford a porous structure after carbonization.^{19,20} But optimization of blend compositions are needed to obtain porosity and most of the time additional chemical or physical activations are needed to enhance the performance of polymer blends. Templated synthesis of porous carbon involves multiple steps apart from the extra steps required for the removal of surfactant as well as templates after synthesis. Since all the methods currently used to produce porous fibers are associated with several disadvantages, finding of new precursor which can produce porous fiber without help of above described methods is required. Here, we describe an approach for fabricating porous carbon nanofiber by synthesizing new precursor terpolymer which can induce pores itself by *in situ* decomposition of backbone which does not involve any additive, or any other activation method described above.

In this study, the terpolymer, poly(acrylonitrile-co-1-vinylimidazole-co-itaconic acid), P(AN-VIM-IA) was synthesized with different ratios of AN with VIM and IA monomers to develop new CNF precursors. Polyacrylonitrile (PAN) homopolymer is one of the most widely studied precursor polymers for making high performance carbon nanofibers (CNFs) for supercapacitors because of its electrospinnability and high carbon yield.²¹ But the high crystallinity of PAN makes it unfavorable for the cyclization into ladder-type polymer that precede graphitization which decreases the quality of carbon fibers.²² Also the poor porosity of PAN-based carbon fibers limits its electrochemical performance. In order to increase the surface area, PAN-based carbon fibers are usually activated by extra activation methods (usually steam activation, CO₂ activation or chemical activation) to introduce pores.²³ Because of that, the PAN precursor were modified to

improve its properties by incorporation of a small percentage of suitable co-monomers, P(AN-*co*-VIM) or P(AN-*co*-IA).²² Incorporation of VIM gives several advantages that increase the performance of carbon fiber. A VIM comonomer can disrupt PAN crystallinity by suppressing strong dipole-dipole interactions between nitrile groups in pure PAN, to make it more favorable for cyclization. Furthermore, the unsaturated pendant imidazole groups are thermally cross-linkable which further enhance the stabilization.²⁴ Because of above mention reasons electrodes derived from P(AN-*co*-VIM) showed higher supercapacitive performances than PAN derived electrodes. Supercapacitive performances were reported for the electrodes prepared from steam activated P(AN-*co*-VIM) with surface area of 1120 m² g⁻¹, and highest specific capacitances of 122 F g⁻¹, with maximum energy and power densities of 47.4 Wh kg⁻¹ (at 0.5 A g⁻¹) and 7.2 kW kg⁻¹ (at 5 A g⁻¹), respectively.²² However, these results were reported for the steam activated fibers since one step carbonization did not afforded sufficiently high surface areas. This problem can be addressed by incorporating a third monomer which can act as an *in situ* porogen. This monomer is itaconic acid, which has been shown to create pores in carbon nanofibers, by *in situ* decomposition of COOH in the IA moiety upon carbonization. This eliminates the necessity of extra *ex situ* activation steps thus not only simplifying the fabrication procedure, but also resulting in higher carbon yields. Three different compositions of the terpolymer were synthesized: AN:VIM:IA (90:5:5), (85:5:10) and (72:5:23), which were then electrospun into nonwoven mats and finally carbonized at 1000 °C. The new terpolymers, P(AN-VIM-IA) synthesized in this study produces novel carbon materials, with remarkable properties beyond the range that can be obtained from single homopolymers (PAN) or copolymers (P(AN-*co*-VIM) or P(AN-*co*-IA)) by combining the superior properties of each monomers.

5.3 Experimental

5.3.1 Materials

Acrylonitrile (AN, 99% purity), 1-dodecanethiol, α,α -azobisisobutyronitrile (AIBN, 98% purity) and basic alumina were purchased from Sigma Aldrich. Itaconic acid (IA, 99% purity), 1-vinylimidazole (VIM) and anhydrous N,N-dimethylformamide (DMF) were purchased from Alfa Aesar. AN and VI were purified by passing through the basic alumina column to remove inhibitor and IA was purified by recrystallization from water and dried at 60 °C before the polymerization. AIBN was recrystallized from methanol. Anhydrous N,N'-dimethylformamide (DMF) was purchased from Sigma Aldrich and used as received for both synthesis as well as the electrospinning. Polyacrylonitrile (PAN, $M_w = 150\,000\text{ g mol}^{-1}$) was purchased from Pfaltz and Bauer, Inc. Electrochemical grade EMITFSI (99.5% purity) was purchased from IoLiTec, Inc. and was used without further purification. Coin cell packages (CR2032) were used to assemble all coin cell type supercapacitors and the assembly parts were obtained from Shenzhen Yongxingye Precision Machinery Mould Co. Ltd., China.

5.3.2 Synthesis of P(AN-VIM-IA) terpolymers

Three compositions of PAN terpolymers having AN:VIM:IA weight ratio of 90:5:5, 85:5:10 and 72:5:23 were synthesized (Figure 5.1) by free radical polymerization in DMF using AIBN as the initiator according to the reported literature procedures.²⁵ Polymerizations were carried out in 500ml round bottom flasks. The reaction flask was fitted with a thermocouple probe, addition funnel, nitrogen inlet and a condenser. AIBN and IA were dissolved in DMF before being mixed

with AN, VIM and 1-dodecanethiol to prepare the reaction mixture. The reaction mixture was then poured carefully into an addition funnel attached to the reaction flask. The mixture was added drop wise into a DMF containing preheated (70 °C) reaction flask over a period of 15 min. Upon completion of the addition, the reaction mixture was heated at 70 °C with continuous stirring for 48 h. The terpolymer from the reaction was precipitated and washed with de-ionized water. The product was then filtered and further washed with methanol and hexane to remove residual unreacted species from the reaction. Finally the terpolymer was dried in a vacuum oven at 70 °C for two days till constant weight was obtained. Hereafter the synthesized terpolymer, P(AN-VIM-IA) will be denoted as PVI. And the selected monomer ratios of AN:VIM:IA equal to 95:5:5, 90:5:10 and 72:5:23 by weight will be denoted as PVI-5 , PVI-10 and PVI- 23, respectively.

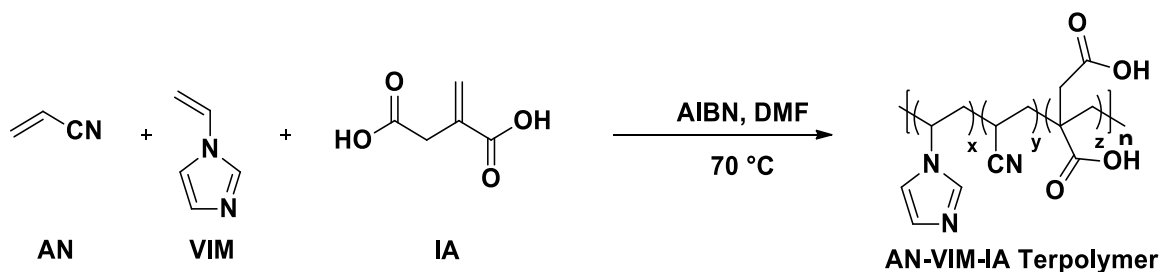


Figure 5.1. Synthesis of PVI terpolymer.

5.3.3 Preparation of CNF and ACNFs

2.5 g of synthesized PVI terpolymers with different compositions of IA were dissolved in DMF at 50 °C with mechanical stirring for 2 h to obtain the spinning solution with a polymer content of 20 wt%. The solution was then cooled to room temperature and was kept stirring 24 h prior to electrospinning. PAN solution was also prepared as a control solution. The solutions were electrospun into a nonwoven mats using a horizontal custom-built electrospinner with a rotating

and translating collector lined with aluminum foil. A feed rate of 0.5 mL h^{-1} through a 20 G needle going across an 18 cm tip-to-collector distance with an applied voltage of 18 kV (Gamma High Voltage Research, Inc., power supply) was used. The obtained electrospun fiber mats would be readily peeled off from the collector foil. After optimizing the stabilization temperature for new precursor polymer using spectroscopic and electrochemical analysis (include in supplementary information), the collected mats were stabilized at $240 \text{ }^{\circ}\text{C}$ for 3 h following heating at $1^{\circ}\text{C min}^{-1}$ in air flow (200 mL min^{-1}) for pre-oxidation and cross-linking, and then carbonized under helium gas flow (200 mL min^{-1}) at $1000 \text{ }^{\circ}\text{C}$ for 1 h at a heating rate of $5^{\circ}\text{C min}^{-1}$ and are denoted as CNFs. Activated carbon fibers (ACNFs) were prepared according to the same procedure purging with CO_2 (50 mL min^{-1}) at $1000 \text{ }^{\circ}\text{C}$ for 1h to further study impact of *ex situ* activation to the electrochemical performances.

5.3.4 Characterization

The ^1H -NMR spectra of synthesized terpolymers were recorded in DMSO- d_6 on a Bruker AVANCE IIITM (500 MHz) NMR spectrometer. Attenuated total reflectance Fourier transform infrared (ATR-FTIR) spectra of PVI terpolymers were recorded on a Nicolet 360 FTIR spectrophotometer. Thermal stability of the samples was investigated with a thermogravimetric analysis (TGA) performed on a SDT Q600 from TA Instruments. The samples were heated between room temperature and $1000 \text{ }^{\circ}\text{C}$ at a heating rate of $10^{\circ}\text{C min}^{-1}$ both under nitrogen (50 mL min^{-1}) and air (100 mL min^{-1}). Simultaneous thermogravimetric analysis- mass spectrometry (TGA-MS) was performed by a tandem Mettler-Toledo TGA/DSC-1 Pfeiffer QMG 230 mass spectrometer (MS) system from $30 \text{ }^{\circ}\text{C}$ to $900 \text{ }^{\circ}\text{C}$ at a rate of $10^{\circ}\text{C min}^{-1}$ under nitrogen. The MS

was scanned from 2 amu to 200 amu for the entirety of the TGA method. Size exclusion chromatography (SEC) was used to determine the molecular weights of the polymers with an N, N-dimethylformamide (DMF) solvent at 40 °C at 1 mL min⁻¹ flow rate using a Shimadzu HPLC instrument equipped with Agilent polystyrene columns and Shimadzu refractive index detector (RID). Polystyrene standards were used for calibration of SEC. The conductivity of electrospinning solutions was measured using an Oakton CON 11 conductivity meter. The viscosity of electrospinning solutions was measured using a Brookfield digital Viscometer (Model DV-II). Raman spectra of the free standing carbon fiber mats were recorded using a DXR Raman microscope (Thermo Scientific) with a 532 nm laser. Scanning electron microscope (SEM) images were acquired using a Zeiss-LEO model 1530 Scanning Electron Microscope (SEM) equipped with field emission gun and an accelerating voltage of 10 keV. Gold coated samples were used for SEM imaging of the electrospun mats whereas images of the carbonized samples were obtained without gold coating. The surface area was determined using a Micromeritics ASAP 2020 surface area analyzer at liquid nitrogen temperature (77K) using nitrogen as the adsorbate and the surface area was determined by using Brunauer–Emmett–Teller (BET) method and the pore size distribution calculated using Density Functional Theory (DFT).

5.3.5 Electrochemical tests

Coin cell packaging (CR2032) was used to assemble all tested supercapacitors. Circular disks which were punched from the carbon fiber mats with 1.1 cm diameters served as both positive and negative electrodes in symmetric coin cell devices. Two electrodes were separated by Gore™ PTFE separator imbibed with EMITFSI ionic liquid electrolyte. Electrodes were sandwiched in

between two carbon coated aluminum current collectors and stainless steel spacers from either side to get better electrode contact with the coin cell parts. All the coin cells were sealed inside the nitrogen filled glove box (Vacuum Atmospheres Company) using a crimper. Cyclic voltammetry (CV) and galvanostatic charge/discharge (CDC) measurements were carried out using these fabricated coin cells on a Supercapacitor Testing Station-SCTS (Arbin). The cells were characterized further by electrochemical impedance spectroscopy (EIS) in a two-electrode configuration mode at 0 V DC bias over a frequency range of 100 kHz to 10 mHz on a 2273A Applied Research Potentiostat/Galvanostat (Princeton).

The capacitance, C , of the two-electrode device was calculated from the cyclic voltammograms was using equations (5.1) and (5.2).

$$C = \int I/v dt \quad (5.1)$$

where I is the integrated discharge current over the potential range at a particular scan rate (v).

Specific capacitance, C_{sp} , is related to the cell capacitance as

$$C_{sp} = 4C / m \quad (5.2)$$

where m is the mass of both electrodes. Energy densities (E_d) and power densities (P_d) were calculated using following Equations (5.3) and (5.4), respectively.

$$E_d = \frac{1}{2} CV^2 \quad (5.3)$$

$$P_d = E_d / t \quad (5.4)$$

5.4 Results and discussion

5.4.1 Characterization of the synthesized terpolymers

The ^1H NMR analysis (Figure S5.1, Table S5.1) and SEC results (Figure S5.2, Table S5.2) of the synthesized PVI terpolymers are summarized in the supplementary information.

5.4.2 Characterization of the samples

Since this is a new precursor material the samples were heated at different temperatures to ascertain the best conditions for stabilization of the electrospun mats. By combining data acquired by FT-IR of stabilized fiber mats and cyclic voltammetry (CV) data for the carbonized mats produced for individual stabilized temperatures the optimized stabilization temperature of 240 °C was established. Optical images of the stabilized nanofiber mats at different temperature (Figure S5.3) and FT-IR analysis of electrospun fiber at different stabilization temperature (Figure S5.4) and CV analysis with specific capacitance (Figure S5.5) obtained for carbonized fibers after different stabilization temperature for PVI-5 are included in supplementary information.

The SEM images of the electrospun, carbonized and activated fibers of different ratio of PVI terpolymers are shown in Figure 5.2. All the polymer samples prepared from synthesized terpolymers showed good electrospinnability, with uniform fibers without beading or aggregation after electrospinning. The fiber diameters of the electrospun, and carbonized and activated nanofibers were measured from the SEM images using ImageJ software.¹⁹ SEM images of nanofibers prepared from PAN are shown in Fig. S6. Average fiber diameters calculated based on 100 individual measurements are summarized in Table 5.1. The diameters of the electrospun fibers

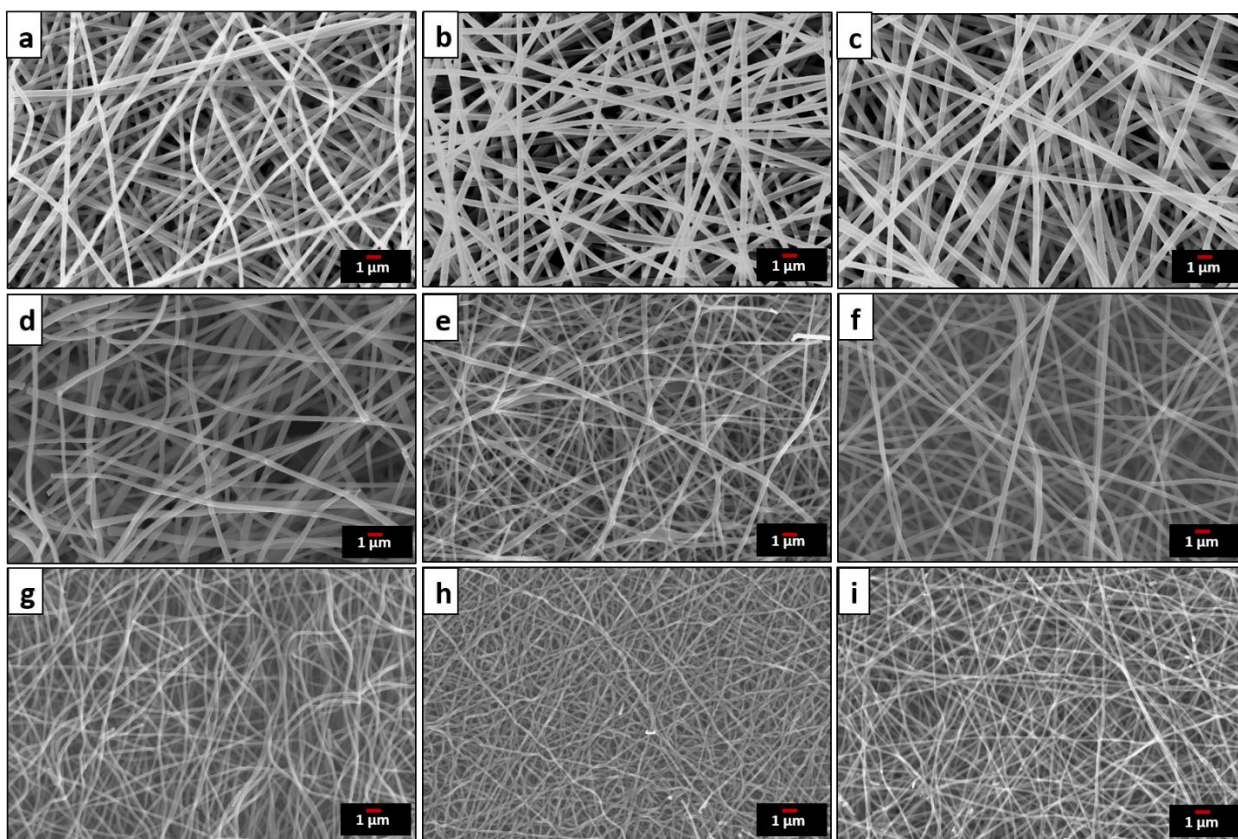


Figure 5.2. SEM images of (a-c) electrospun fibers from (a) PVI-5 (b) PVI-10 (c) PVI-23, (d-f) carbonized nanofiber from (d) PVI-5 (e) PVI-10 (f) PVI-23 (g-i) CO₂ activated nanofibers from (g) PVI-5 (h) PVI-10 (i) PVI-23 samples.

slightly decreased with increasing IA concentration in terpolymers. This is attributed to decrease in the solution viscosity and as a well as increase in conductivity of spinning solutions with increasing IA composition.²⁶ Viscosities of spinning solution for PVI-5, PVI-10 and PVI-23 were determined to be 3020, 2600 and 1050 cp, respectively. Also conductivities of the spinning solutions increased from 14.8 mS m⁻¹ for PVI-5 to 16.3 and 18.4 mS m⁻¹ for PVI-10 and PVI-23. Continuous fibrous morphology of the electrospun fibers was preserved after carbonization as well as *ex situ* CO₂ activation as shown in Figure 5.2 (d-i). Decrement in the standard deviation of nanofiber diameter shows that uniformity of nanofibers is improved by increasing the IA content

in terpolymers. Diameter of as-spun fibers decreases after carbonization and further reduced by *ex situ* CO₂ activation.

Table 5.1. Average diameters of derived from electrospun fibers, CNF and ACNF of PAN homopolymer and different ratio of PVI terpolymers.

Precursor	As spun fiber diameter (nm)	Carbonized fiber diameter (nm)	Activated fiber diameter (nm)
PAN	727±236	449±86	247±23
PVI-5	364±45	265±52	147±19
PVI-10	353±39	222±42	123±17
PVI-23	333±35	213±27	114±13

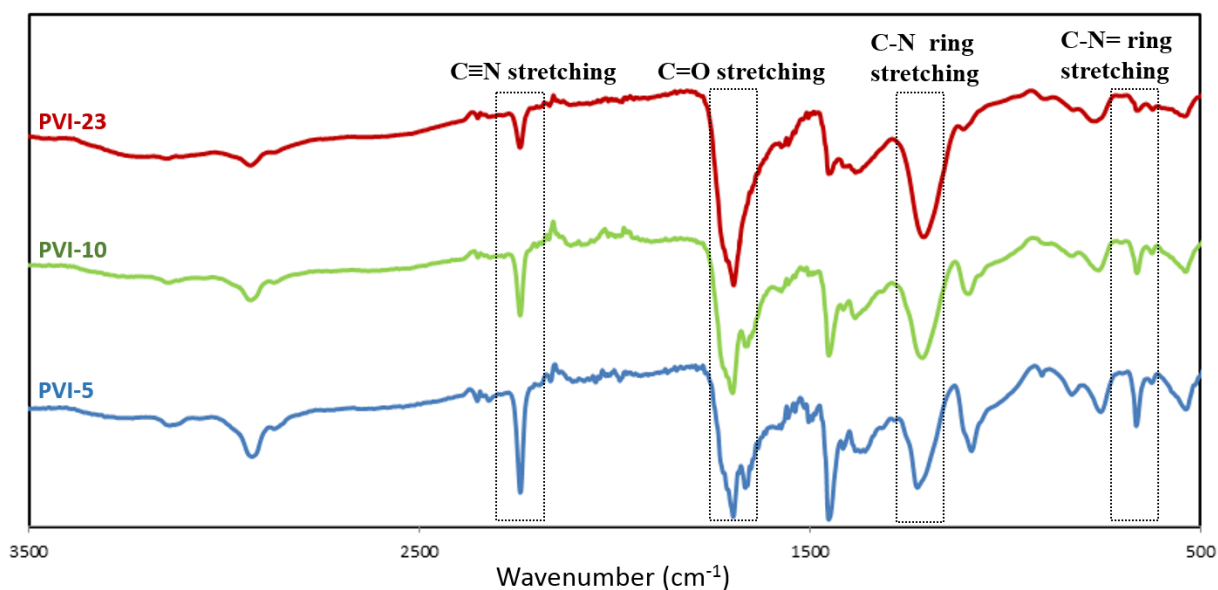


Figure 5.3. FTIR analysis of electrospun samples derived from PVI terpolymers.

ATR-FTIR spectra of electrospun P(AN-VIM-IA) terpolymers are shown in Figure 5.3. Backbone CH₂ stretching occurs at 2930 cm⁻¹, C≡N stretching is shown at 2242 cm⁻¹ for AN segments. OH stretching at 3200 cm⁻¹ and the C=O stretching at 1720 cm⁻¹ are clearly visible for the IA unit, at 3118 cm⁻¹. C-H ring stretching, at 1229 cm⁻¹, C-N ring stretching at 1082 cm⁻¹, and C-H ring in-phase bending at 665 cm⁻¹ for the imidazole ring are observed for the VIM groups. The presence of all the bands corresponding to the each monomer unit in FT-IR spectra for all the compositions confirms that the definite combination of AN, VIM and IA in electrospun samples.

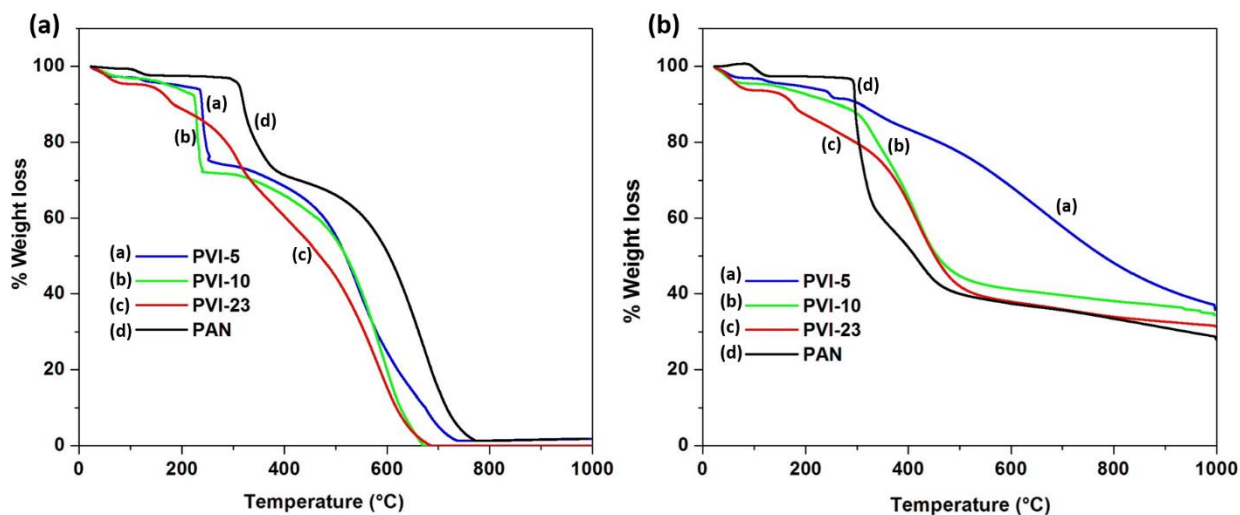


Figure 5.4. TGA analysis of PAN homopolymer and electrospun PVI terpolymer samples in (a) air atmosphere and (b) N₂ atmosphere respectively.

Thermogravimetric analysis (TGA), carried out to investigate the effect of monomer ratios toward the thermal stability and also to determine the char yields of the terpolymers at high temperature, is shown in Figure 5.4. As shown in Figure 5.4(a), terpolymer (PVI-23) with the highest IA content has lowest stabilization temperature around 170 °C which can lead to energy saving. It also allows of porogens that decompose at low temperature. Furthermore, it is also important to note that the

smooth weight loss occurring in PVI-23 in air without a sudden weight loss at the stabilization temperature helps produce higher quality carbon fibers. Char yields of various PVI terpolymers were obtained by TGA under nitrogen and shown in Figure 5.4(b). All the terpolymers studied displayed larger weight retention at high temperature compared to the PAN homopolymer. This trend is attributed to the smooth and gentle release of heat during pyrolysis of the PVI terpolymers after incorporating IA into the backbone that resulted in less fragmentations during pyrolysis.²⁷

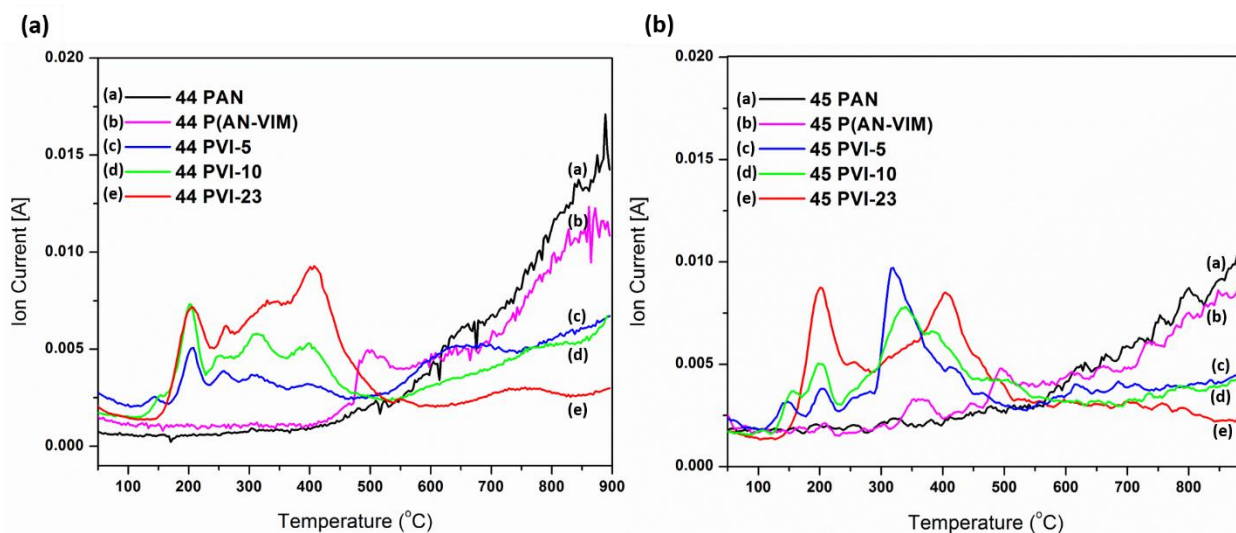


Figure 5.5. The simultaneous TGA and mass spectrometry of electrospun terpolymers.

Figure 5.5 shows the analysis of simultaneous TGA and mass spectrometry of electrospun fiber samples of the terpolymers to confirm our hypothesis of *in situ* porogen activity of IA in terpolymers. For comparison, the analysis was also performed for PAN and P(AN-*co*-VIM) as presented in the same Figure 5.5. Here, the mass spectra are only shown for the two evolved gases, CO₂ ($m/Z = 44$) and COOH ($m/Z = 45$) among the various gases analyzed, to confirm *in situ* porogen activity of terpolymers. PAN or P(AN-*co*-VIM) fail to emit any CO₂ or COOH until 600

°C as shown in the Figure 5.5 (a) and (b) which is consistent with the absence of pendent COOH groups in their structures. All the terpolymer samples shows the emission of CO₂ as well as COOH starting from 100 °C and intensity of those two gases increased with increasing IA content. The CO₂ evolution is ascribed to the decarboxylation of COOH in IA unit, which selectively decomposes to make pores in the fiber to activate the fibers *in situ*. Thus, the carbonized (CNFs) terpolymers shows higher porosities with increasing IA monomer ratio in terpolymers, which is in good agreement with the surface area analysis (Table 5.2).

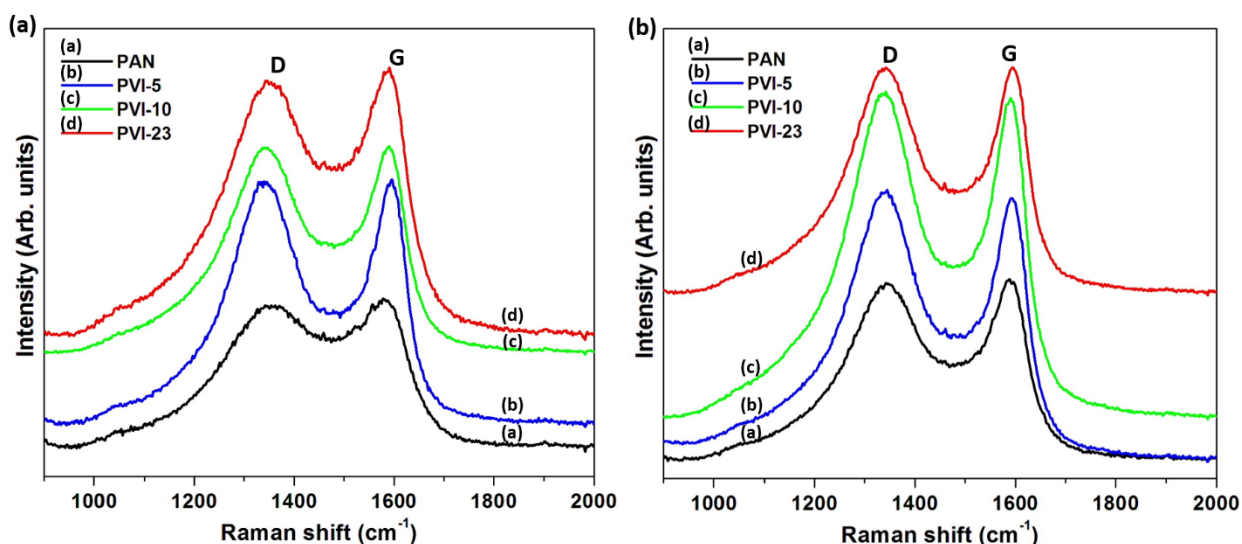


Figure 5.6. Raman spectra of (a) CNF and (b) ACNF derived from PVI copolymers.

Raman analysis, shown in the Figure 5.6 was used to further characterize the carbon fibers derived from terpolymers and PAN. The presence of two prominent Raman active peaks for the disordered sp³ carbon ‘D-band’ (~1360 cm⁻¹) and the sp² bonded carbons ‘G-band’ (~1590 cm⁻¹) in all the carbonized samples are evidence for the formation of graphitic structures.²⁸ The intensity ratio of the D band relative to the G band (I_D/I_G values) depends on the degree of graphitization and the

alignment of the graphitic planes. I_D/I_G ratio can be calculated by peak fitting using Lorentzian equation. The calculated I_D/I_G values for CNFs and ACNFs were 2.91, 2.43 and 2.26 for carbonized PVI-5, PVI-10 and PVI-23 and 3.24, 3.03 and 3.01 for *ex situ* CO₂ activated PVI-5, PVI-10 and PVI-23 fibers, respectively. The decreased I_D/I_G value reflects the increase of ordered graphitic carbon with the increasing amount of IA in terpolymer. This is mainly attributed to the smooth decomposition of terpolymer during carbonization with increasing IA that results in fewer defects in the carbonized samples when compared to the PAN homopolymer.

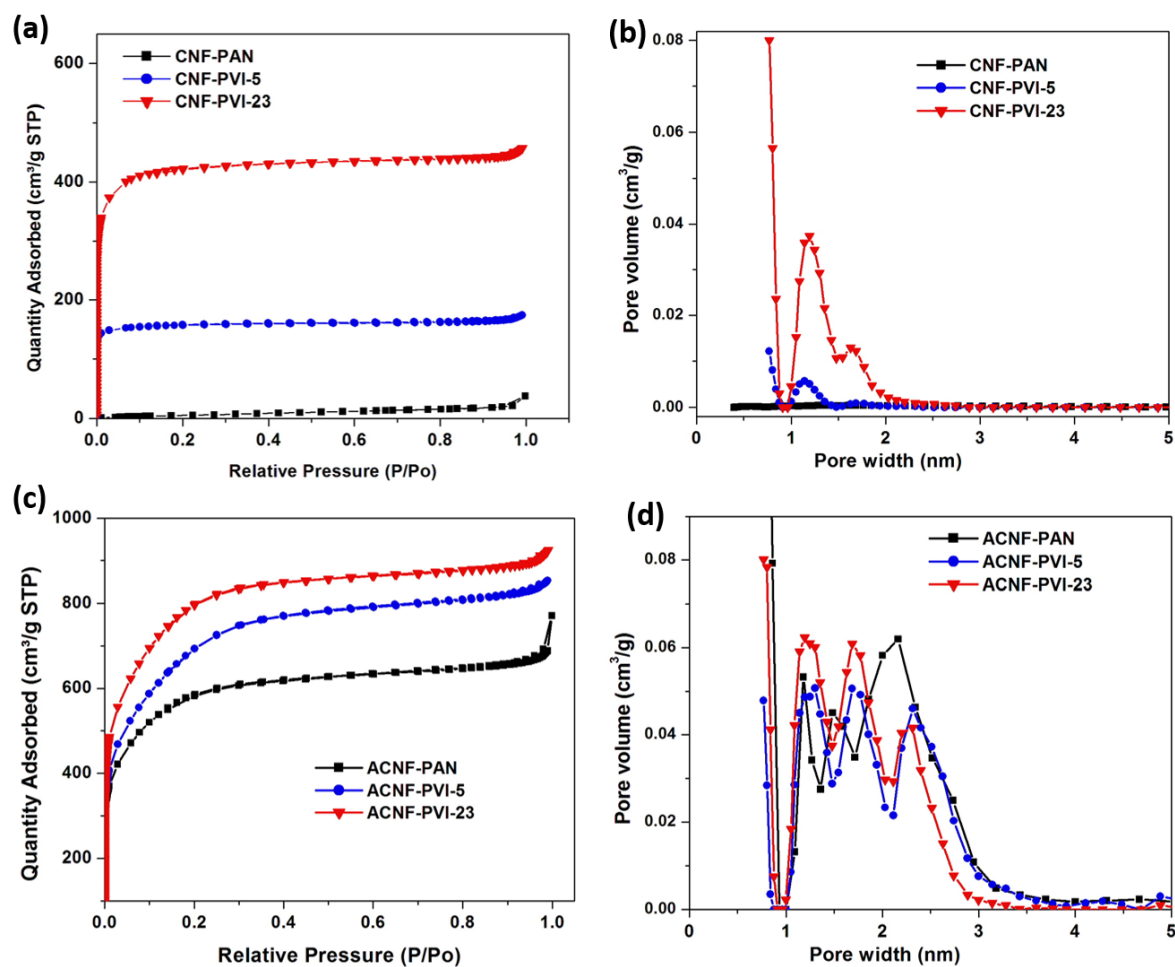


Figure 5.7. Nitrogen adsorption/desorption isotherms and pore size distribution for (a, b) CNFs (c, d) ACNFs respectively.

Table 5.2. Surface area and pore size analysis of carbonized nanofibers (CNFs) and CO₂ activated carbon nanofibers (ACNFs) derived from PVI terpolymers

Precursor	Surface area (m ² /g)	Total pore Volume (cm ³ /g)	V _{micro} (cm ³ /g)	V _{meso} (cm ³ /g)
CNF-PAN	6	0.0129	0.0053	0.0076
CNF- PVI-5	605	0.4132	0.2259	0.1873
CNF- PVI-23	1630	0.7923	0.6047	0.1876
ACNF-PAN	2026	1.0884	0.6502	0.4383
ACNF- PVI-5	2380	1.2598	0.7972	0.4626
ACNF- PVI-23	2815	1.3590	1.0307	0.3283

The nitrogen adsorption/desorption isotherms shown in Figure 5.7 (a and c) for the carbon nanofibers both with and without activation exhibit type I curves according to the IUPAC classification. The specific surface area of carbon nanofibers was calculated using the BET method and the results are shown in Table 5.2. The addition of IA in terpolymers used to prepare nanofibers resulted in an increase in the surface area upon carbonization compared to CNFs derived from PAN because of this *in situ* porogen activity of IA. Furthermore, surface area increases with increasing IA content with CNFs of PVI-23 showing a surface area of 1630 m² g⁻¹. External CO₂ activation of fibers increased the surface area in all cases. Surface area of ACNFs prepared from all terpolymer samples were higher than PAN even with external CO₂ activation. Pore size distributions of CNFs and ACNFs were shown in Fig.7 (b and d). According to the Table 5.2, it is clearly demonstrated that pore size, especially micro/meso pore volume can be tailored by using

different compositions in terpolymers. For porous carbon electrodes, the match between pore size and the electrolyte ion size is essential to acquire maximum utilization of electrode materials in supercapacitors. The pore size distribution in Figure 5.7 (b and d) shows varying the monomer ratio of terpolymer (i.e. increasing IA percentage) increase the percentage of pores around 1–2 nm for both CNFs and ACNFs. This creates appropriate pore size to match with EMITFSI ionic liquid electrolyte. Since the ion sizes are 0.43×0.76 nm for EMI^+ and 0.29×0.79 nm for TFSI^- , an increase in pore size on the fibers could better facilitate ion diffusion which provides more accessible surface and sites for electrochemical energy storage.²⁹

5.4.3 Electrochemical characterization

The cyclic voltammograms (CVs) generated for carbonized fibers without any *ex situ* activation at five different scan rates between 10 and 100 mV S^{-1} of symmetric device in EMITFSI are shown in Figure 5.8. Energy can be increased by using high working potential as shown in equation 5.3. In this study, ionic liquid electrolyte (EMITFSI) were selected as the electrolyte because this electrolyte has a stable potential window up to 4.1 V.³⁰ All electrodes derived from different amount of terpolymers show rectangular CVs suggesting typical electric double layer capacitive energy storage compared to the carbonized but unactivated PAN which failed to produce significant currents. Terpolymers synthesized with higher amounts of IA shows higher current density resulting in increased capacitance. Among the carbon samples, PVI-23 shows the highest specific capacitance due to its highest specific surface area generated by *in situ* activation by decomposition of COOH. Interestingly, all the CV curves maintained their rectangular shapes even at the very highest scan rates tested, indicating fast charge transfer and low resistance during

charging and discharging process. In this work, the specific capacitance values of electrodes derived from terpolymers has been dramatically increased compared to PAN electrodes. Specific

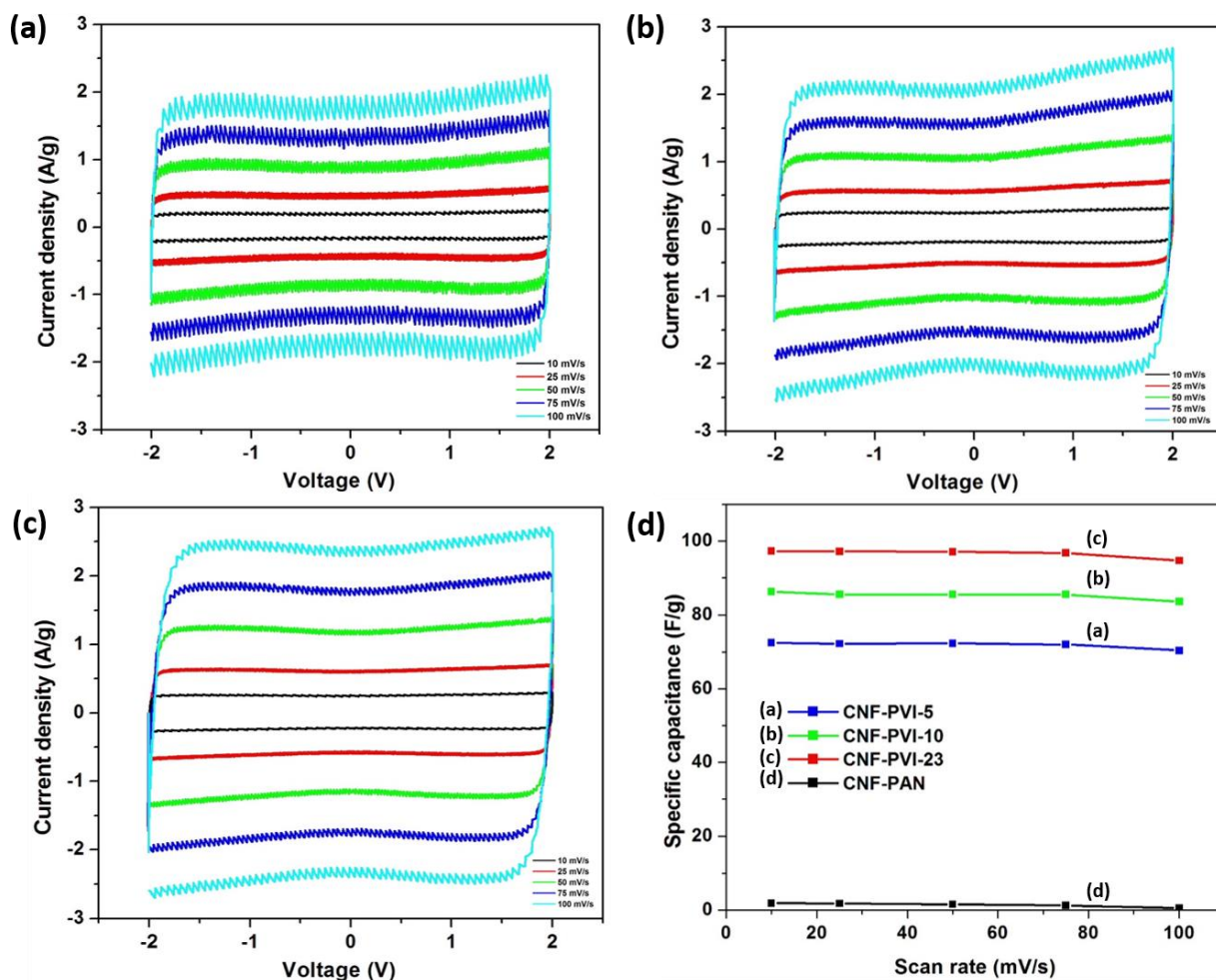


Figure 5.8. Cyclic voltammograms of CNFs derived from (a) PVI-5 (b) PVI-10 (c) PVI-23 (d) Specific capacitance of CNF derived from PVI terpolymers and PAN homopolymer as a function of the scan rate.

capacitance obtained from electrode materials at various scan rates were plotted in Figure 5.8 (d). The specific capacitance of electrodes remains almost constant at high scan rates as shown in

Figure 5.8 (d). The specific capacitances of the electrode obtained CNFs were calculated to be 1.9, 72.5, 86.3 and 97.0 F g^{-1} at the scan rate of 10 mV s^{-1} for PAN, PVI-5, PVI-10 and PVI-23, respectively.

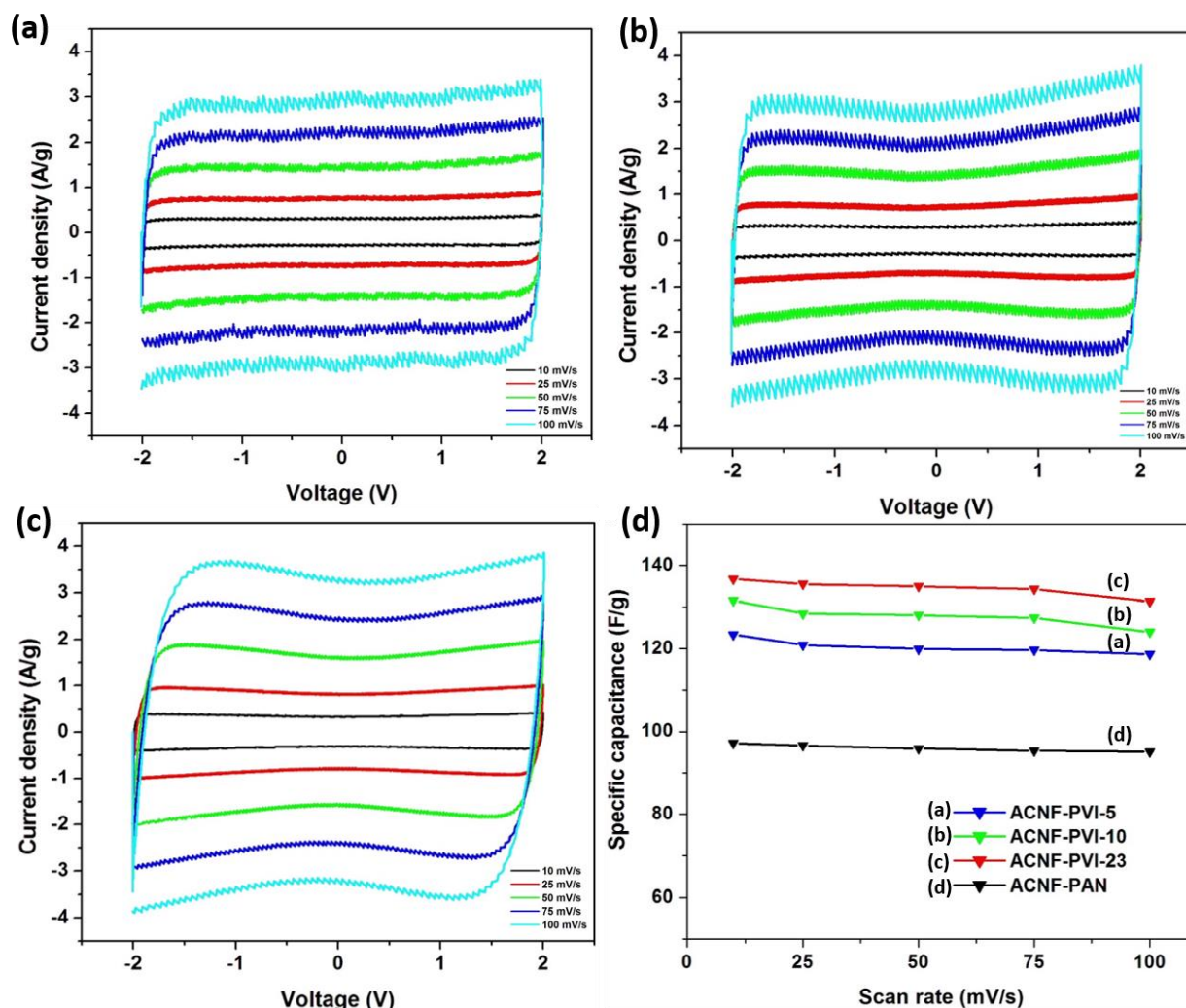


Figure 5.9. Cyclic voltammograms of ACNFs derived from (a) PVI-5 (b) PVI-10 (c) PVI-23 (d) Specific capacitance of ACNF derived from PVI terpolymers and PAN homopolymer as a function of the scan rate.

The cyclic voltammograms generated for carbonized fibers with CO₂ activation are shown in Figure 5.9. The CV plots gave a box-like shape, showing very little resistance in the charge/discharge interface. CV obtained for ACNF-PAN is shown Figure S5.7. The specific capacitances of the electrode obtained ACNFs were summarized in Table 5.3.

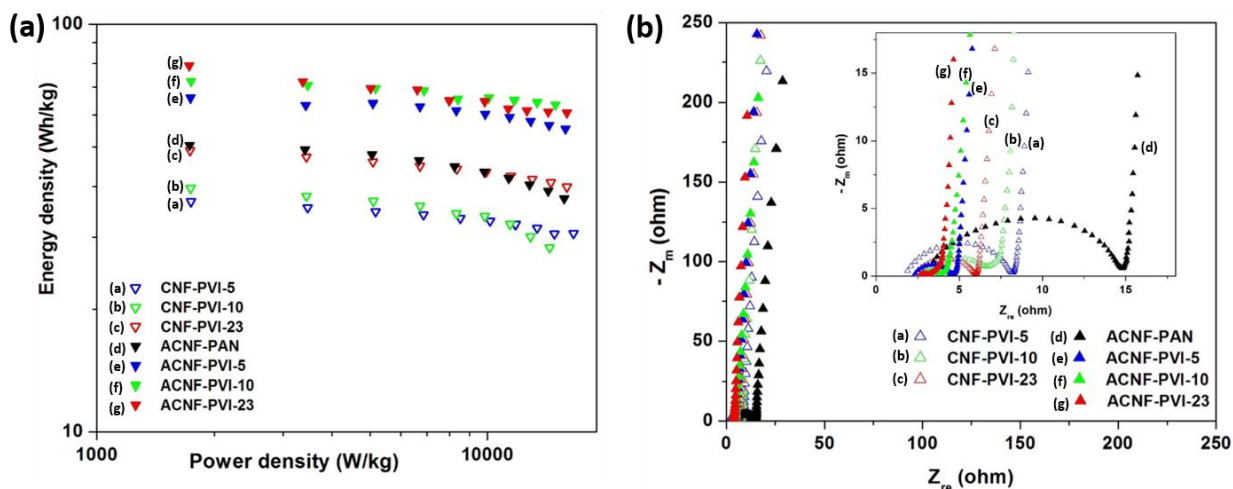


Figure 5.10. (a) Ragone plots of electrode materials measured at various current densities (b) Nyquist plots for the samples prepared from both CNFs and ACNFs.

The Ragone plot at different current densities, ranging from 1 to 10 A g⁻¹ in Figure 5.10(a) shows that both CNFs and ACNFs have high energy retention with increasing power densities. Energy density of CNFs was further enhanced after CO₂ activation due to porosity and high surface areas created by reaction between carbon and CO₂ during activation (Table 5.3). It is interesting to note that the same electrochemical performance was obtained from PVI-23 without any activation (yielding good char yield of 28%) in that of PAN with CO₂ activation (low char yield of 10%).

Table 5.3. Electrochemical performance of CNFs and ACNFs electrodes derived from PAN and PVI terpolymers in EMITFSI

Precursor	Specific		Current density			
	Capacitance		1 A g ⁻¹		10 A g ⁻¹	
	(F g ⁻¹)					
	10	100	Energy	Power	Energy	Power
	mVs ⁻¹	mVs ⁻¹	density	density	density	density
			(Wh kg ⁻¹)	(W kg ⁻¹)	(Wh kg ⁻¹)	(W kg ⁻¹)
CNF-PVI-5	72.5	70.4	36.7	1741	30.7	16568
CNF-PVI-10	86.3	83.7	39.6	1732	26.8	15614
CNF-PVI-23	97.0	94.7	49.0	1730	39.9	15918
ACNF-PAN	97.2	95.1	50.1	1725	37.4	15664
ACNF-PVI-5	123.4	118.7	65.9	1733	55.4	15800
ACNF-PVI-10	131.6	124.1	72.4	1741	63.4	15630
ACNF-PVI-23	136.7	131.3	79.0	1721	60.6	15947

Here the significant pore formation by *in situ* porogen activity of IA in terpolymer resulted a very porous carbon without any external activation. Furthermore, CNF-PVI-23 shows an 82% energy retention compared to 75% for ACNF-PAN at 10 kW kg⁻¹. These results confirms advantage of PVI terpolymers as supercapacitor electrode materials.

Electrochemical impedance spectroscopic (EIS) analysis of electrode materials both with and without activation were carried out to further investigate and shown in Figure 5.10(b). All the electrode materials display similar overall shapes, consisting of a semicircle at high frequency

region and vertical line in the low frequency region.³¹ The numerical values of charge transfer resistance which can be derived from the diameter of the semicircle, were very low for both CNFs and ACNFs and show 3.38 Ω for CNF-23 and a significantly low resistance of 0.50 Ω for ACNF-23 compared to ACNF-PAN (11.39 Ω). Vertical line appearing in the low-frequency region represents an ideal capacitive behavior of electrode material. It is important to notice that vertical line obtained for the CNF materials prepared without any activation, indicate very good diffusion of ions into the bulk. This is attributed to the induced porous structure with large amount of meso prepared by decomposition of COOH during carbonization. Compared with the results obtained for PAN homopolymer and P(AN-*co*-VIM)/ P(AN-*co*-IA) copolymers,²² PVI terpolymer exhibit superior electrochemical performance due to the combination of desirable properties from each co monomers .

5.5 Conclusion

Flexible, freestanding and binder free supercapacitor electrodes with high surface areas were prepared with one step carbonization of a novel precursor terpolymer, P(AN-VIM-IA). The high surface area carbon fibers were obtained, without the use of any additive or *ex situ* activation. Decomposition of the COOH in itaconic acid provides *in situ* porogen activity to create porosity as high as 1630 m² g⁻¹. CNFs derived from PVI-23 exhibit 97.0 F g⁻¹ at a scan rate of 10 mV s⁻¹ with energy density of 49 Wh kg⁻¹ at 10 kW kg⁻¹ which is the same as CO₂ activated PAN. CO₂ activation was also performed to investigate the impact of *ex situ* activation. An increase in surface area up to 2815 m² g⁻¹ along with increased electrochemical performance was observed. Remarkable energy density of 79 Wh kg⁻¹ at 10 kW kg⁻¹ and 136.7 F g⁻¹ at a scan rate of 10 mV

s⁻¹ were obtained for ACNF-PVI-23. This demonstrates the potential of poly(acrylonitrile-*co*-1-vinylimidazole-*co*-itaconic acid), P(AN-VIM-IA) as a novel carbon nanofiber precursor as electrodes for supercapacitor applications.

Acknowledgements

We acknowledge the National Science Foundation (Grant no. IIP-1127564) for financial support and Grant no. CHE-1126177 for the purchase of the Bruker AVANCE III™ 500 MHz NMR. We especially thank Dr. Ronald A. Smaldone and Sampath B. Alahakoon for help with the surface area analysis. We also thank Dr. Manuel Quevedo-Lopez (Department of Material Science and Engineering at The University of Texas at Dallas) for extending his Raman facility to us and Isable Pinter for help with Raman analysis.

5.6 Appendix - Supporting Information

The backbone of CH₂ from VIM, IA and AN linkages are indicated by NMR signals at 2 ppm. Peaks at 3.1 and 4.4 ppm represent the backbone CH of the AN and VIM groups respectively. Signals from 7.8-6.8 ppm represents the unsaturated CH groups in VIM group. Peak at 11.0 ppm represent the OH from the acid group. There are three small peaks at 8.03, 2.92, and 2.75 ppm for the residual DMF that was used for synthesis of copolymers. Table S1 shows the summary of NMR analysis.

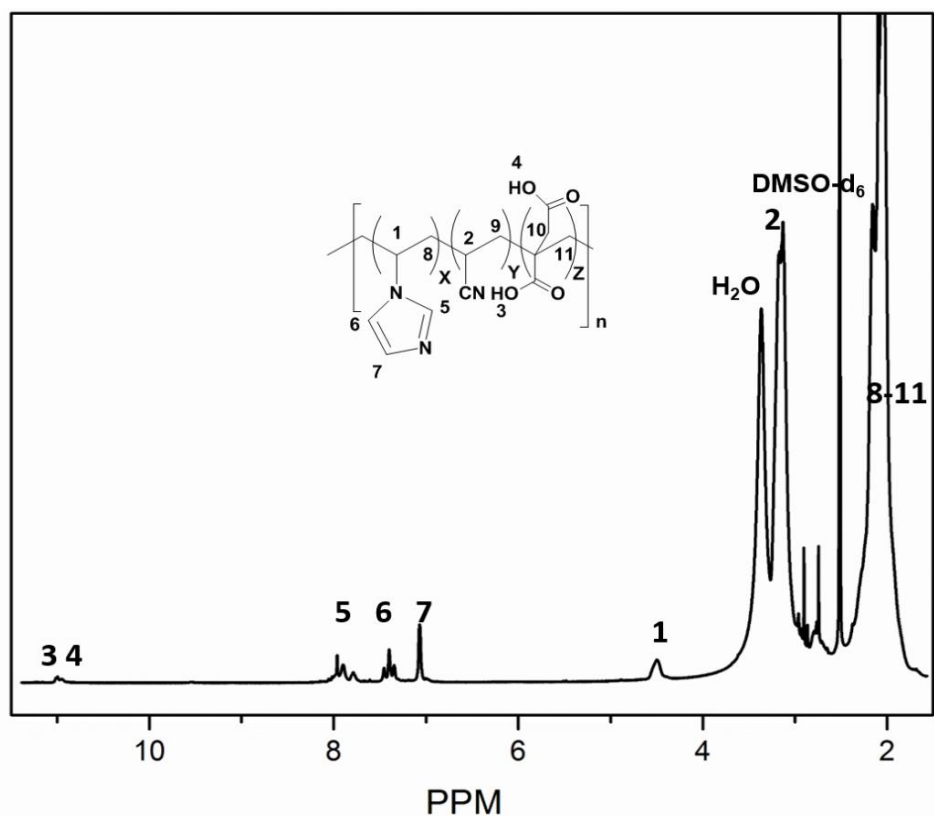


Figure S5.1. ^1H NMR of PVI-5 terpolymer.

Table S5.1. Summary of NMR analysis of P(AN-VIM-IA) terpolymers

Precursor	Feed monomer ratio			Calculated monomer ratio		
	AN, mol% , (wt%)	VIM, mol%, (wt%)	IA, mol%, (wt%)	AN, mol%, (wt%)	VIM, mol%, (wt%)	IA, mol%, (wt%)
PVI-5	94.8 (90.0)	3.0 (5.0)	2.2 (5.0)	96.5 (94.0)	3.2 (5.6)	0.2 (0.4)
PVI-10	92.5 (85.0)	3.0 (5.0)	4.5 (10.0)	95.4 (91.8)	3.7 (6.4)	0.8 (1.8)
PVI-23	85.5 (72.0)	3.4 (5.0)	11.1 (23.0)	81.4 (69.2)	13.7 (20.7)	4.8 (10.1)

Table S5.2. Molecular weights of the synthesized polymers

Precursor	Molecular weight		PDI
	Mn (KDa)	Mw (KDa)	
PVI-5	80.2	120.3	1.5
PVI-10	98.0	126.0	1.3
PVI-23	106.0	131.2	1.2

Mn = Number-average molecular weight

Mw = Weight-average molecular weight

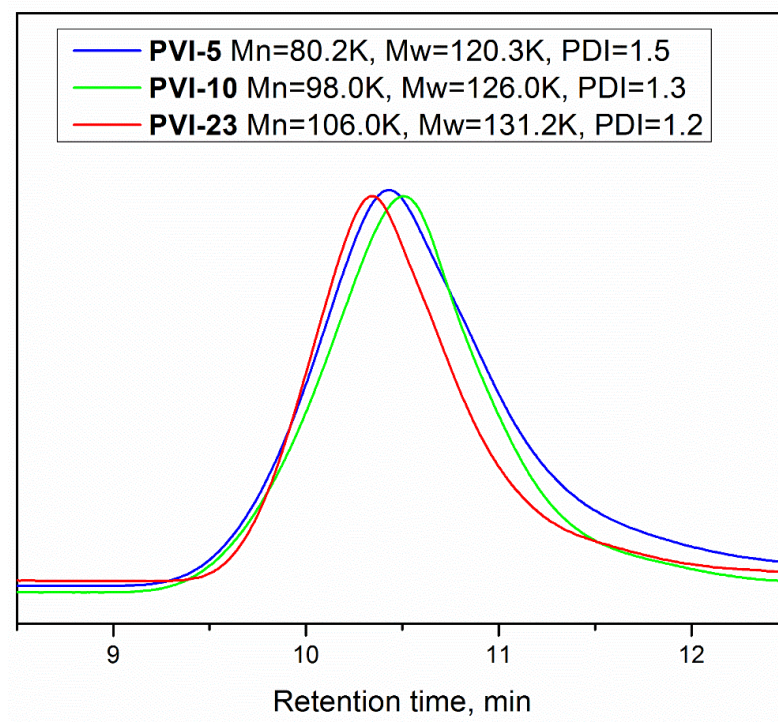


Figure S5.2. SEC analysis of the synthesized polymers.






Electrospun Nanofiber mat				
Temperature	200 °C	220 °C	240 °C	260 °C
Color of stabilized nanofiber				

Figure S5.3. Optical images of the electrospun of PVI-5 nanofiber mat (top) and stabilized nanofiber mats of PVI-5 at different temperature (bottom).

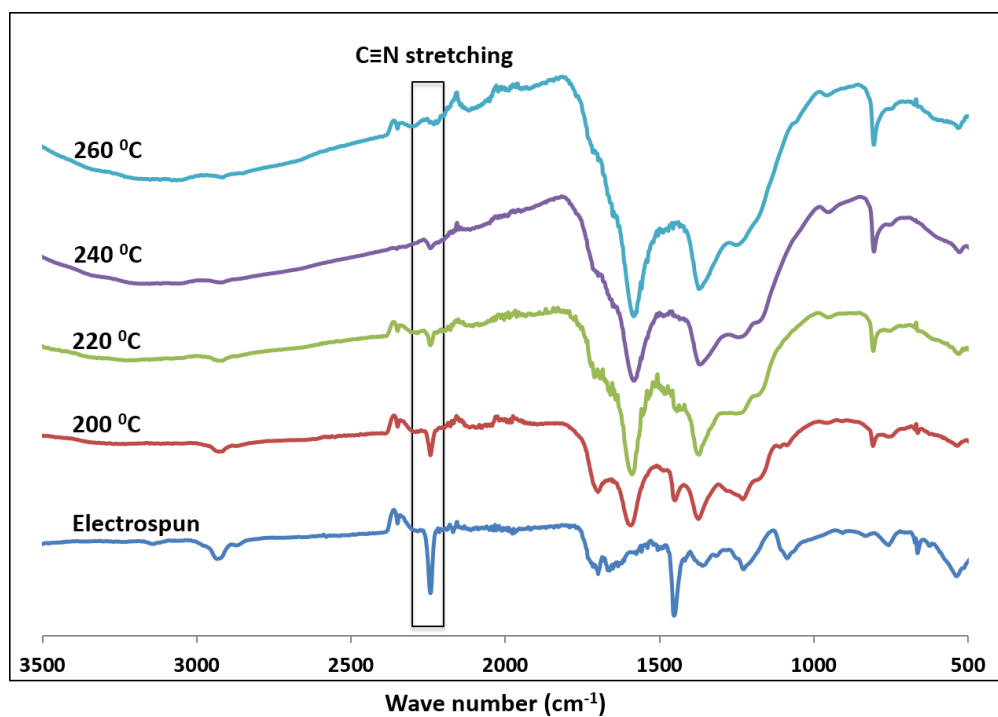


Figure S5.4. FTIR analysis of stabilized fibers of PVI-5 at different stabilized temperature.

The fiber mats become more dark brown in color with increasing temperature as shown in Fig. S3. FT-IR spectra of electrospun fiber mats of PVI-5 with different heating temperature shows that during stabilization, the peak related to $C\equiv N$ bonds is reduced sharply (Fig. S4). This reduction are mainly related to cyclization where nitrile groups ($C\equiv N$) groups converted to cyclic $-C=N-$ and $-C-N-$ groups. Gradual disappearance of the $C\equiv N$ peaks at 2240 cm^{-1} (Fig. S4) and the appearance of broad peaks at $1580\text{--}1620\text{ cm}^{-1}$ represented the formation of cyclic $-C=N-$ group

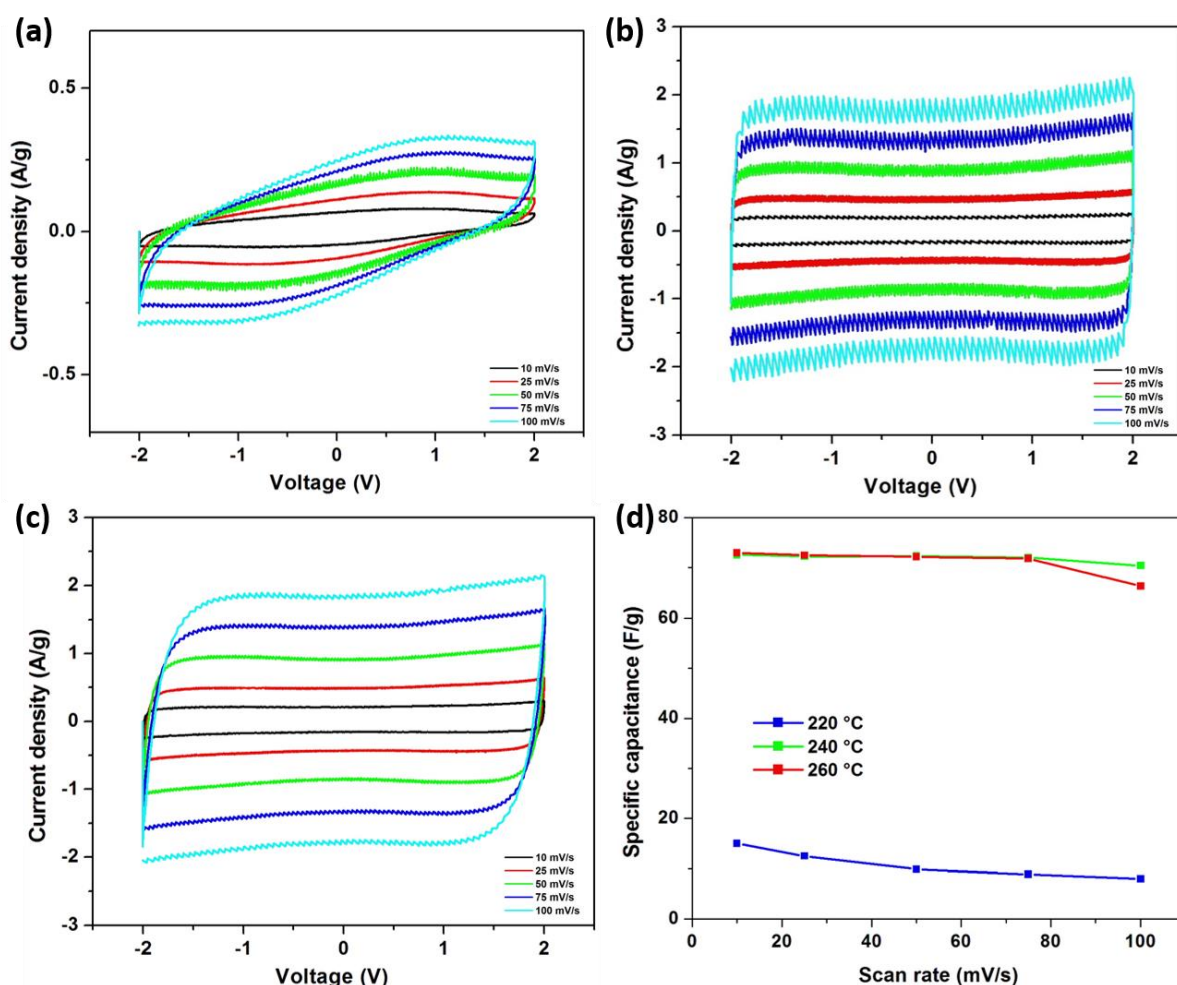


Figure S5.5. Cyclic voltammograms of CNF derived from PVI-5 terpolymer stabilized at (a) 220 °C (b) 240 °C (c) 260 °C and (d) Specific capacitance of CNF derived from PVI-5 terpolymers at different stabilization temperatures.

which indicates successful cyclization. According to the spectra, $\text{C}\equiv\text{N}$ peaks at 2246 cm^{-1} is completely removed after stabilizing at $240\text{ }^{\circ}\text{C}$. Therefore $240\text{ }^{\circ}\text{C}$ was selected as the suitable temperature for stabilization of PVI terpolymer.

The CV curves obtained PVI-5 stabilized at $240\text{ }^{\circ}\text{C}$ and $260\text{ }^{\circ}\text{C}$ show a very box like shapes at different scanning rates with higher specific capacitance than other two stabilization temperatures ($200\text{ }^{\circ}\text{C}$ and $220\text{ }^{\circ}\text{C}$), indicting a typical characteristic of double-layer capacitor behavior. This is because of high degree of stabilization obtained after $240\text{ }^{\circ}\text{C}$ as evident by FT-IR analysis produce graphitic carbon. CVs obtained for those stabilized at $220\text{ }^{\circ}\text{C}$ display non ideal shapes and stabilization at $200\text{ }^{\circ}\text{C}$ failed to produce significant currents which is mainly related to only partial or not well cyclized structures. Performance leveled upon heating above $240\text{ }^{\circ}\text{C}$, so it was selected as best temperature for stabilization.

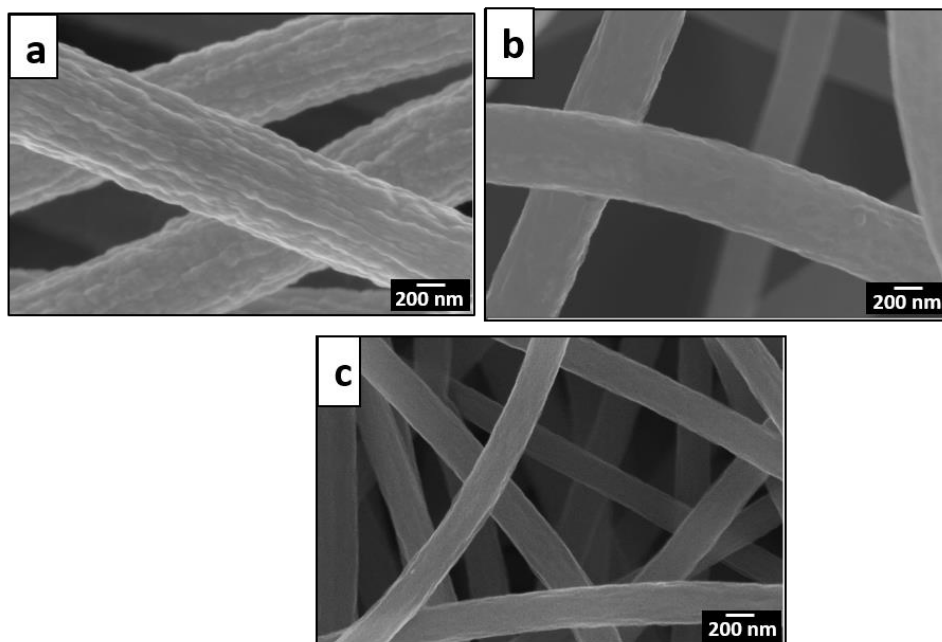


Figure S5.6. SEM images of (a) electrospun (b) carbonized (c) CO_2 activated nanofibers from PAN homopolymer.

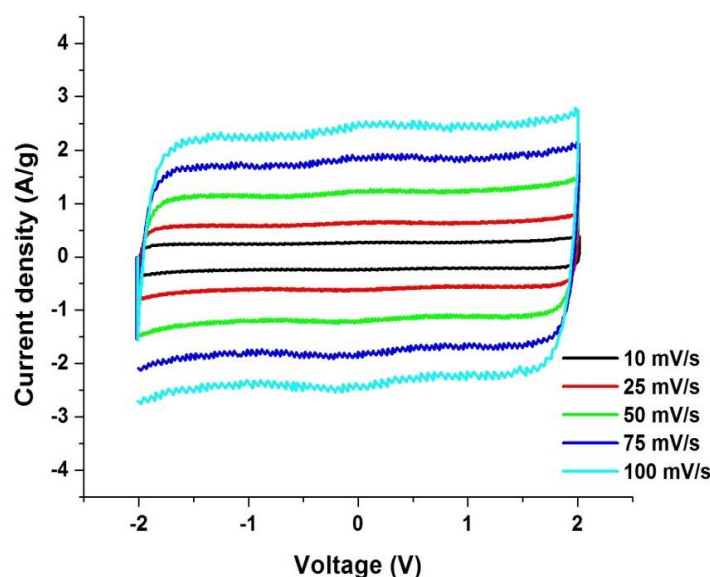


Figure S5.7. Cyclic voltammograms of CO₂ activated nanofibers derived from PAN homopolymer (ACNF-PAN).

5.7 References

- (1) Kotz, R.; Carlen, M. Principles and Applications of Electrochemical Capacitors. *Electrochim. Acta* **2000**, *45* (15–16), 2483–2498.
- (2) Burke, A. Ultracapacitor; Why, and Where Is the Technology. *J. Power Sources* **2000**, *91*, 37–50.
- (3) Gonzalez, A.; Goikolea, E.; Andoni, J.; Mysyk, R. Review on Supercapacitors : Technologies and Materials. *Renew. Sustainable Energy Rev.* **2016**, *58*, 1189–1206.
- (4) Kim, C.; Yang, K. S. Electrochemical Properties of Carbon Nanofiber Web as an Electrode for Supercapacitor Prepared by Electrospinning. *Appl. Phys. Lett.* **2003**, *83* (6), 1216–1219.
- (5) Lu, X.; Wang, C.; Favier, F.; Pinna, N. Electrospun Nanomaterials for Supercapacitor Electrodes : Designed Architectures and Electrochemical Performance. *Adv. Energy Mater.* **2017**, *7*, 1–43.
- (6) Zhi, M.; Yang, F.; Meng, F.; Li, M.; Manivannan, A.; Wu, N. Effects of Pore Structure on Performance of An Activated-Carbon Supercapacitor Electrode Recycled from Scrap Waste Tires. *ACS Sustainable Chem. Eng.* **2014**, *2*, 1592–159.

- (7) Pohlmann, S.; Lobato, B.; Centeno, T.; Balducci, A. The Influence of Pore Size and Surface Area of Activated Carbons on the Performance of Ionic Liquid Based Supercapacitors. *Phys. Chem. Chem. Phys.* **2013**, *15* (40), 17287–17294.
- (8) Hernandez-montoya, V.; Garcia-servin, J.; Bueno-lopez, J. I. Thermal Treatments and Activation Procedures Used in the Preparation of Activated Carbons. *Lignocellul. Precursors Used Synth. Act. Carbon - Charact. Tech. Appl. Wastewater Treat. Dr. Virginia Hernández Montoya (Ed.)*, ISBN 978-953-51-0197-0, InTech, Available from <http://www.intechopen.co> **2012**.
- (9) Jung, K.-H.; Ferraris, J. P. Preparation of Porous Carbon Nanofibers Derived from PBI/PLLA for Supercapacitor Electrodes. *Nanotechnology* **2016**, *27* (42), 425708.
- (10) Peranathan, S.; Bonso, J. S.; Ferraris, J. P. Supercapacitors Utilizing Electrodes Derived from Polyacrylonitrile Fibers Incorporating Tetramethylammonium Oxalate as a Porogen. *Carbon N. Y.* **2016**, *106*, 20–27.
- (11) Bonso, J. S.; Kalaw, G. D.; Ferraris, J. P. High Surface Area Carbon Nanofibers Derived from Electrospun PIM-1 for Energy Storage Applications. *J. Mater. Chem. A* **2014**, *2* (2), 418–424.
- (12) Volperts, A.; Dobelev, G.; Zhurinsk, A.; Zalane, Z.; Ozolinsh, J.; Vervikishko, D.; Shkolnikov, E. Supercapacitor Electrodes from Activated Wood Charcoal. *Bulg Chem Commun.* **2016**, *48*, 337–341.
- (13) Yoon, S.; Lim, S.; Song, Y.; Ota, Y.; Qiao, W.; Tanaka, A.; Mochida, I. KOH Activation of Carbon Nanofibers. *Carbon N. Y.* **2004**, *42*, 1723–1729.
- (14) Chang, B.; Wang, Y.; Pei, K.; Dong, X. RSC Advances Surface Area and Superior Mesoporous Structure as an Efficient Supercapacitor Electrode. *RSC Adv.* **2014**, *4*, 40546–40552.
- (15) Elmouwahidi, A.; Bailón-garcía, E.; Perez-cadenas, A. F.; Maldonado-hódar, F. J.; Carrasco-marín, F. Electrochimica Acta Activated Carbons from KOH and H₃PO₄ - Activation of Olive Residues and Its Application as Supercapacitor Electrodes. *Electrochim. Acta* **2017**, *229*, 219–228.
- (16) Xue, R.; Yan, J.; Liu, X. Effect of Activation on the Carbon Fibers from Phenol – Formaldehyde Resins for Electrochemical Supercapacitors. *J Appl Electrochem.* **2011**, *41*, 1357–1366.
- (17) Ra, E. J.; Kim, T. H.; Yu, W. J.; An, K. H.; Lee, Y. H. Ultramicropore Formation in PAN/camphor-Based Carbon Nanofiber Paper. *Chem. Commun. (Camb).* **2010**, *46* (8), 1320–1322.

- (18) Moore, B. C.; Macia, J. A. Influence of Carbon Fibres Crystallinities on Their Chemical Activation by KOH and NaOH. *Micropor Mesopor Mat.* **2007**, *101*, 397–405.
- (19) Abeykoon, N. C.; Bonso, J. S.; Ferraris, J. P. Supercapacitor Performance of Carbon Nanofiber Electrodes Derived from Immiscible PAN/PMMA Polymer Blends. *RSC Adv.* **2015**, *5* (26), 19865–19873.
- (20) Zhang, L.; Han, L.; Liu, S.; Liu, S. RSC Advances High-Performance Supercapacitors Based on Electrospun Multichannel Carbon Nano Fibers *RSC Adv.* **2015**, *5*, 107313–107317.
- (21) Rahaman, M. S. A.; Ismail, A. F.; Mustafa, A. A Review of Heat Treatment on Polyacrylonitrile Fiber. *Polym. Degrad. Stab.* **2007**, *92*(8), 1421–1432.
- (22) Jung, K. H.; Deng, W.; Smith, D. W.; Ferraris, J. P. Carbon Nanofiber Electrodes for Supercapacitors Derived from New Precursor Polymer: Poly(acrylonitrile-Co-Vinylimidazole). *Electrochem. commun.* **2012**, *23* (1), 149–152.
- (23) Wang, K.; Teng, H. The Performance of Electric Double Layer Capacitors Using Particulate Porous Carbons Derived from PAN Fiber and Phenol-Formaldehyde Resin. *Carbon N. Y.* **2006**, *44*(15), 3218–3225.
- (24) Deng, W.; Lobovsky, A.; Iacono, S. T.; Wu, T.; Tomar, N.; Budy, S. M.; Long, T.; Hoffman, W. P.; Smith, D. W. Poly (Acrylonitrile E Co -1-Vinylimidazole): A New Melt Processable Carbon Fiber Precursor. *Polymer (Guildf).* **2011**, *52* (3), 622–628.
- (25) Mahmood, S. F. Automobile Grade Carbon Fiber Precursor Study: I. Copolymer System and II. Terpolymer System, University of Texas at Dallas, **2015**. (Available from *Dissertations & Theses @ University of Texas at Dallas; ProQuest Dissertations & Theses Global*. (1712988725). Retrieved from <http://libproxy.utdallas.edu/login?url=http://search.proquest.com/docview/1712988725?accountid=7120>)
- (26) Pillay, V.; Dott, C.; Choonara, Y. E.; Tyagi, C.; Tomar, L.; Kumar, P.; Toit, L. C.; Ndesendo, V. M. K. A Review of the Effect of Processing Variables on the Fabrication of Electrospun Nanofibers for Drug Delivery Applications. *J Nanomater* **2013**, 789289, 22 pp.
- (27) Ouyang, Q.; Cheng, L.; Wang, H.; Li, K. Mechanism and Kinetics of the Stabilization Reactions of Itaconic Acid-Modified Polyacrylonitrile. *Polym. Degrad. Stab.* **2008**, *93*(8), 1415–1421.
- (28) Liu, Y.; Zhou, J.; Chen, L.; Zhang, P.; Fu, W.; Zhao, H.; Pan, X.; Zhang, Z.; Han, W.; Xie, E. Highly Flexible Freestanding Porous Carbon Nano Fibers for Electrodes Materials of High-Performance All-Carbon Supercapacitors. *ACS Appl. Mater. Interfaces* **2015**, *7*(42), 23515–23520.

- (29) Largeot, C.; Portet, C.; Chmiola, J.; Taberna, P.; Gogotsi, Y.; Simon, P. Relation between the Ion Size and Pore Size for an Electric Double-Layer Capacitor. *J. Am. Chem. Soc* **2008**, *130*(9), 2730–2731.
- (30) Balducci, A.; Soavi, F.; Mastragostino, M. The Use of Ionic Liquids as Solvent-Free Green Electrolytes for Hybrid Supercapacitors. *Appl Phys A Mater Sci Process*.**2006**, *82*(4), 627–632.
- (31) Taberna, P. L.; Simon, P.; Fauvarque, J. F. Electrochemical Characteristics and Impedance Spectroscopy Studies of Carbon-Carbon Supercapacitors. *J. Electrochem. Soc.* **2003**, *150* (3), A292-A300.

CHAPTER 6

COMPATIBILIZATION OF IMMISCIBLE POLYMER BLENDS USING SMALL MOLECULES TO TAILOR PORE DISTRIBUTION OF CARBON FIBERS FOR SUPERCAPACITOR ELECTRODES

6.1 Abstract

In this study, porous carbon nanofibers were fabricated from blends of polybenzimidazole (PBI) and 6FDA-DAM:DABA (6FDD) compatibilized with different loadings of 2-Methylimidazole (2-MI), (5 wt%, 10 wt%, and 20 wt%). Compared to the uncompatibilized blend very uniform and small domains of 6FDD were observed for the electrospun blend fibers containing 2-MI. This results in a balanced micro/mesopore ratio after CO₂ activation to better match the ion size of electrolyte used for electrochemical testing. To our knowledge, this is the first report of *controlling the nanostructure of the electrospun fibers to control the porosity by capitalizing on the different CO₂ etch rates of the resulting carbonized blend fibers*. The highest specific capacitance of 139.4 F g⁻¹ at a scan rate of 10 mV s⁻¹, and an energy density of 67.7 Wh kg⁻¹ at a current density of 1 A g⁻¹ were observed for the compatibilized PBI:6FDD (50:50) blends with 20 wt% of 2-MI. A remarkable energy retention of 96.3% was obtained at high current densities (10 A g⁻¹) after compatibilizing the polymer blend compared to 78% for same blend without 2-MI. Moreover the concepts developed here may be generally applicable to the design of new low cost high performing electrodes with stable energy densities at high power from immiscible polymer blends that exhibit lower performance due to high degree of phase separation.

6.2 Introduction

Supercapacitors are electrochemical storage devices that have high power and superior cycle lives that make them attractive for applications requiring rapid charge/discharge such as hybrid vehicles and consumer electronics.¹ However, supercapacitors have lower energy densities than batteries, which limit their application.² The energy of a supercapacitor is determined by the surface area of its electrodes and its operating voltage.^{3,4} If surface area that is accessible to electrolyte is increased, the energy is increased.^{5,6} Consequently, in order to make supercapacitors a commercially competitive energy storage device, the electrode surface area and porosity must be enhanced. This has motivated the search for new electrode materials, with a pore size distribution that can be tailored by simple methods.⁷

Polymer blends have been employed for supercapacitor applications. The blending of polymers result in controlled and optimized pore architectures. Additionally, can be cost effective by avoiding the complexity of new materials design and synthesis.⁸ The simplest polymer blends are binary but many of these are immiscible, tending to phase separate due to the unfavorable entropy of mixing.⁹ Unfortunately, the macrophase separation of polymer blends after leads to a deterioration of the electrochemical as well as mechanical properties.¹⁰ Despite that, carbonized immiscible polymer blends have been used as electrodes for supercapacitors, usually where, one polymer serves as a sacrificial component due to lower thermal stability and decomposes to induce pores in the carbonizing polymer at high temperature.^{11,12} A different approach would be blending of immiscible polymers that can both serve as carbonizing polymers. Relaxing the miscibility constraint also broadens the library of eligible polymers. However, immiscibility of polymers could limit the electrochemical properties of the blend carbons because of the non-uniform

microstructure. Compatibilizers, allow control of the microstructure of the blend. Which often take the form of copolymers/terpolymers^{13,14,15,16} and nanoparticles/nanosheets.^{17,18,19} Compatibilizers increase compatibility by lowering the interfacial tension, suppressing coalescence and improving the miscibility between the two polymers.^{20,21,22} This concept is commonly used in many application to overcome limitations due to immiscibility of polymer blends, including enhancing the mechanical properties of polymeric materials.^{23,24} Wang et al. reported a new approach for compatibilization of immiscible polyvinylidene fluoride (PVDF)/polylactic acid (PLLA) blends using *in situ* formed Janus nanomicelles at the polymer-polymer interface.²⁵ However, the synthesis of novel polymeric or inorganic compatibilizer materials is time-consuming, expensive and applicability range of these compatibilizers are limited. This problem can be overcome by using commercially available small molecules as a compatibilizers. Thin film membranes fabricated using small molecule compatibilized immiscible polymer blends have recently been reported in the literature for gas separation application.²⁶ This approach has yet to be applied to electrospun fibers derived from compatibilized immiscible polymer blends or the carbon fibers derived from them. Zhao et al. reported improved mechanical properties of immiscible polylactide/poly(ϵ -caprolactone)/ multi-walled carbon nanotubes electrospun nanofibers prepared by electrospinning.²⁷

Herein, we report, the use of commercially available and inexpensive small molecule to compatibilize immiscible blends to produce a uniform microstructure in electrospun fibers. The subsequent carbonization and CO₂ activation of these spun fibers to fabricate binder free electrodes with improved supercapacitive performance is reported. Furthermore, by varying the amount of the small organic molecules, different morphologies of the electrospun fibers can be obtained. The

small molecule compatibilizers have the advantage of simplicity and versatility compared to using the traditional compatibilization methods employing copolymers or nanoparticles. Commercially available 2-methylimidazole (2-MI) was used as the small molecule compatibilizer. The polymer blend components were selected so that polymers contribute to the overall nanostructure (surface area, pore size, etch rate, and graphitic content) of the resulting carbon composite nanofibers. The first carbonizing polymer used in this study is polybenzimidazole (PBI), which is a commercially available polymer that has a high carbon yield (~50%) and produces mechanically stable carbon fibers even without thermal stabilization, which is a required for other commonly used polymers such as polyacrylonitrile (PAN).²⁸ The second polymer, 6FDA-DAM:DABA(3:2), (6FDD) is a copolymer of 4,4'-hexafluoroisopropylidene dipthalic anhydride (6FDA), with 2,4,6-trimethyl-1,3-phenylenediamine (DAM) and 3,5-diaminobenzoic acid (DABA). It is a member of an important class of polyimides and has a large fractional free volume (18%) that can potentially result in highly porous carbon materials upon carbonization.²⁹ In addition, the carboxylic acid groups of the DABA moieties can be act as *in situ* porogens upon carbonization to further increase the surface area. Finally, 6FDD undergoes intermolecular cross-linking at ~450 °C, which could contribute to better mechanical properties of the carbonized materials. The CO₂ etch rate at 1000 °C of the carbonized 6FDD is approximately 20% faster than that of the carbonized PBI. CO₂ etch rates of two polymers were determine by comparing mass loss of two polymers after 30 min CO₂ activation (at 1000 °C) of membranes prepared from two polymers individually. A uniform dispersion of 6FDD in the PBI polymer phase of electrospun fibers, can be achieved by compatibilizing the blend with 2-MI (Figure 6.1). Thus offers the opportunity for controlling the porosity upon CO₂ activation to achieve high surface area by capitalizing on the different CO₂ etch

rates for the component carbons. The optimum porosity and morphology in the carbonized fibers were determined with different loadings of 2-MI to obtain best the electrochemical performance.

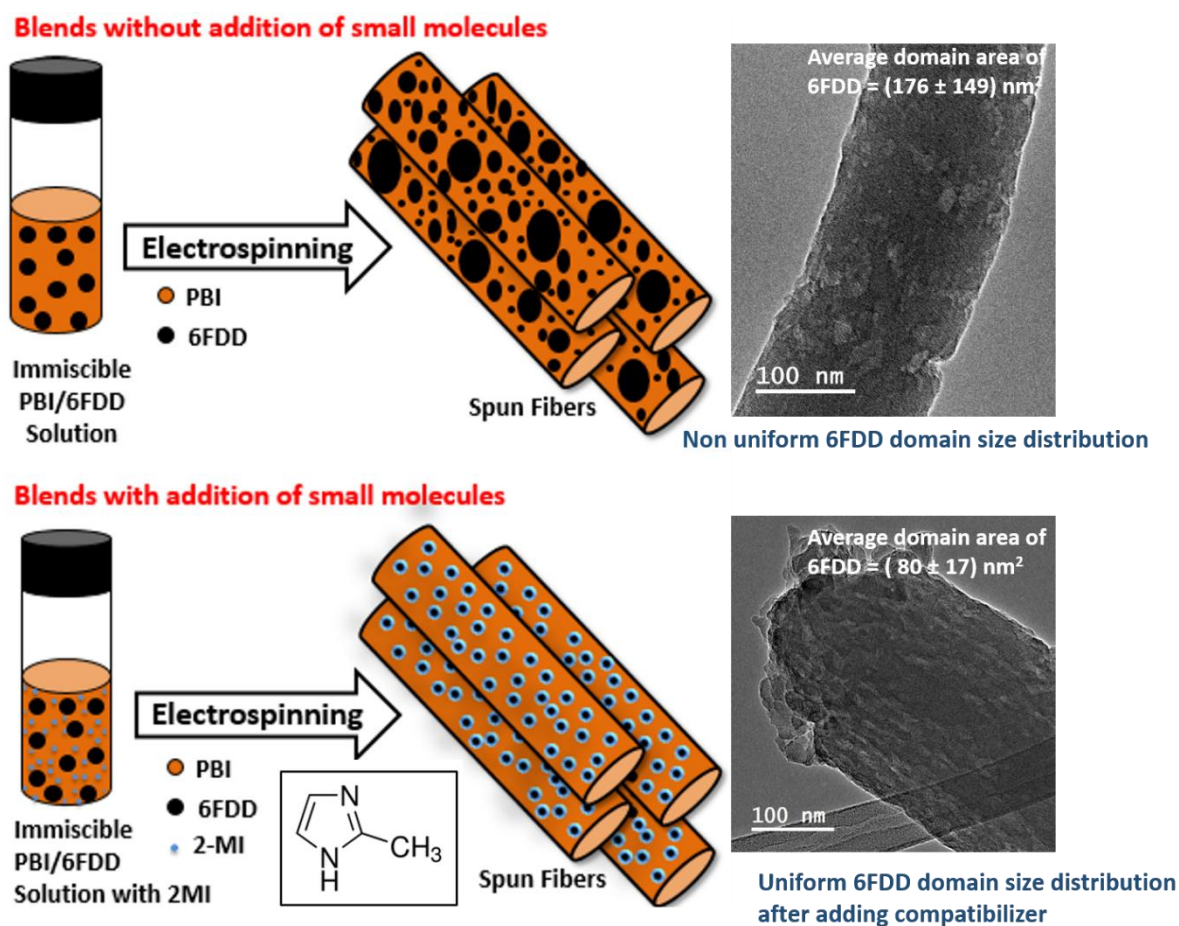


Figure 6.1. Schematic illustration of for electrospinning PBI:6FDD (50:50) blends with and without small molecule (2-MI) compatibilizers and their corresponding microstructures on fibers.

6.3 Experimental

6.3.1 Materials

4,4-Hexafluoroisopropylidene diphthalic anhydride (6FDA, >99% purity) was purchased from Akron Polymer Systems Inc. 2,4,6-Trimethyl-1, 3-phenylenediamine (DAM, >97% purity) was

purchased from TCI America. 3,5-Diaminobenzoic acid (DABA, 98% purity), 1,2-dichlorobenzene (ODCB) and 2-Methylimidazole (2-MI) was purchased from Sigma Aldrich. Anhydrous 1-methyl-2-pyrrolidone (NMP, 99.8% purity) was purchased from Sigma Aldrich and was dried over activated 4A molecular sieves purchased from Sigma Aldrich. Polybenzimidazole (PBI) was purchased from PBI Performance Inc. (26 wt% in DMAc, 1.5% (w/w) LiCl, Mw 30,000) and was used as received. Anhydrous N, N-dimethylacetamide (DMAc, 99.8% purity) was purchased from EMD chemicals and used for the electrospinning solutions. Electrochemical grade 1-Butyl-1-methylpyrrolidinium bis(trifluoromethylsulfonyl)imide (PYR₁₄TFSI, 99.5% purity) was purchased from IoLiTec, Inc. and ethylene carbonate (EC), (99.5% purity) and propylene carbonate PC, (99.5% purity) were purchased from Sigma Aldrich, and were used without further purification to prepare the electrolyte mixture.

6.3.2 Synthesis of 6FDA-DAM:DABA (6FDD)

6FDD was synthesized according to a reported literature procedure (Figure S6.1).³⁰ All the monomers were purified prior to the synthesis. DAM was purified by recrystallization using hexane. The purified monomer was dried in a vacuum oven at 80 °C for 12 h. DABA was purified by recrystallization using HPLC grade water and vacuum dried at 80 °C for 12 h before use. Prior to the synthesis of 6FDD, 6FDA was vacuum dried at 120 °C for 24 h. All glassware was vacuum dried at 120 °C for 24 h prior to the synthesis. A 250 mL three neck flask was sealed and purged with nitrogen gas, then air evacuated while being heated with a hot air gun. This was repeated two more times in order to ensure that the flask was completely dry and free of air. DABA (0.274 g)

and 6FDA (2.000 g) were then both dissolved separately in 2.5 mL and 8.5 mL NMP, respectively. The dissolved DABA and 6FDA were injected into the round bottom flask and stirred at room temperature for 1h. Then, DAM dissolved in NMP was injected into the round bottom flask and stirred at room temperature for 24 h. Then, 12 mL of o-dichlorobenzene (ODCB) were added and the solution was refluxed using a Dean Stark trap at 190 °C for 24 h. The polymer was precipitated by adding the solution dropwise to methanol. The polymer was isolated using vacuum filtration and vacuum dried at 120 °C for 24 h.

6.3.3 Preparation of CNF and ACNFs

A 50:50 ratio of PBI:6FDD was used for all electrospinning solutions. The PBI and 6FDD polymers were dissolved separately in dimethylacetamide (DMAC) for 4 h at 80 °C. For the solutions containing 2-MI, the compatibilizer was measured as a weight percentage (5 wt %, 10 wt%, 20 wt%) of the total mass of two polymers and was also dissolved in DMAC separately for 4 h at 80 °C. After 4 h, for the control, the 6FDD was added dropwise to the PBI solution and the combined solution was stirred overnight at 80 °C until just before electrospinning. This control solution of PBI:6FDD(50:50) will be denoted as BL-0. For the 2-MI solutions, the 2-MI solution was first added to the PBI solution and the combined solution was alternately stirred and bath sonicated for 30 min twice. After the PBI and 2-MI solutions were combined, the 6FDD was added dropwise to the PBI/2-MI solution and then the combined solution was stirred overnight at 80 °C until just before electrospinning. Compatibilized immiscible blends of PBI:6FDD(50:50) prepared with 5 wt %, 10 wt% and 20 wt% of 2-MI will be denoted as BL-5, BL-10 and BL-20 respectively.

The prepared polymer blend mixture was inserted into a 10 mL syringe. The mixture was then set to dispense at 0.2 ml h^{-1} onto a rotating and translating collector that was covered by aluminum foil. A 15 cm tip-to-collector distance and an applied voltage of 20 kV between the tip and grounded rotating mandrel was used. After electrospinning, an unwoven, flexible mat of nanofibers was obtained. The mat was then carbonized under Helium flowing at 200 mL min^{-1} by heating at $5 \text{ }^{\circ}\text{C min}^{-1}$ to $1000 \text{ }^{\circ}\text{C}$ and then holding at that temperature for 1 h followed by activation at $1000 \text{ }^{\circ}\text{C}$ for 30 min under CO_2 (50 mL min^{-1}) and then allowed to cool to room temperature.

6.3.4 Characterization

NMR spectra were obtained on a Bruker AVANCE IIITM (500 MHz) in $(\text{CD}_3)_2\text{SO}$ with TMS (^1H) as internal standard to confirm the structure of 6FDD. The molecular weight of as-synthesized 6FDD was determined by gel permeation chromatography (Viscotek GPCmax, VE2001) using two ViscoGEL columns in series (I-MBHMW 3078, Viscotek) and a Triple Array Detector (Module TDA 320, Viscotek). THF was used as the mobile phase at a flow rate of 1 mL min^{-1} and polystyrene standards (Polymer Laboratories) were used for calibration. Attenuated total reflectance Fourier Transform infrared (ATR-FTIR) spectra were acquired using a Nicolet 380 FTIR equipped with Omnic 7.3 software (Thermo Electric Corp.) Morphologies and microstructures of electrospun and carbonized samples were observed by Zeiss-LEO (Model 1530) scanning electron microscope (SEM) using an accelerating voltage of 10 kV. Electrospun samples for SEM imaging were sputtered-coated with gold while carbonized samples were used without sputter coating. Transmission electron microscope (TEM) images were obtained using a JEOL JEM-2100 TEM at 200 kV (JEOL Co Ltd). Samples were prepared by dispersing electrospun

fibers in methanol and a fishing technique was used to obtain fibers on a 300 mesh Cu Lacey carbon grid. Thermogravimetric analysis (TGA) measurements were taken using a TA Instruments SDT Q600 Analyzer with a heating ramp rate of $10\text{ }^{\circ}\text{C min}^{-1}$ up to $1000\text{ }^{\circ}\text{C}$, under 50 mL min^{-1} nitrogen flow. Raman spectroscopy was performed using a DXR Raman Spectrometer (Thermo Scientific) equipped with a 532 nm laser. Dynamic light scattering (DLS) technique was used to determine the size of particles in electrospinning solutions using a Zetasizer Nano ZS (Malvern Instruments) at a scattering angle of 90° .

6.3.5 Electrochemical tests

The freestanding carbon nanofiber mats were used directly as electrodes for supercapacitors by punching out circular electrodes 1.1 cm in diameter ranging from 1-2 mg in weight. The electrodes were presoaked in the ionic liquid electrolyte mixture ($\text{PYR}_{14}\text{TFSI}:\text{PC}:\text{EC}$ (3:3:2)) and placed on top of the carbon coated aluminum current collectors. Then electrodes with current collectors were placed in vacuum desiccator for 2 h at $100\text{ }^{\circ}\text{C}$ to ensure the penetration of the electrolyte into the pores. The wet electrodes were assembled into symmetric coin cell devices (CR2032) using porous PTFE (GoreTM) thin films as separator. All the coin cells were assembled inside an argon filled glovebox (Vacuum Atmospheres Company) using a crimper. Cyclic voltammetry (CV) and constant current charge/discharge tests (CDC) were performed using an Arbin SCTS Supercapacitor Testing System. The cells were first equilibrated for 10 cycles at 50 mV s^{-1} using cyclic voltammetry (CV), and then followed by three cycles each at 10, 25, 75, 100 mV s^{-1} in the voltage range of 2 V to -2 V. The galvanostatic charge-discharge studied from 3.5 V to 0 V with

10 different current rates ranging from 1 A g⁻¹ to 10 A g⁻¹ for 10 cycles each were performed to calculate the energy and power densities. Electrochemical impedance spectroscopy (EIS) was done using a PARSTAT 2273 potentiostat (Princeton Applied Research) equipped with a PowerSuite software from 100 kHz to 10 mHz at 0 V DC potential.

6.4 Results and discussion

6.4.1 Characterization of the 6FDD polymer

Characterization of the 6FDD polymer is included in the supplementary information. The molecular weight of the polymer (Mw) was 60 000 with PDI of 2.9. The structure of the 6FDD was confirmed by the ¹H-NMR spectroscopy (Figure S6.2), FT-IR spectroscopy (Figure S6.3) and TGA (Figure S6.4).

6.4.2 Material characterization

SEM images in Figure 6.2 show the morphology of the electrospun fibers derived from 6FDD:PBI(50:50) with different weight percentages of 2-MI. Fiber structure, uniformity, and size all play a role in the electrochemical performance of supercapacitor materials. The SEM images show that the incorporation of 2-MI increases the diameter of electrospun fibers. The control (Figure 6.2 (a)) showed the smallest fibers (232 ± 51 nm), followed by the 5% 2-MI (276 ± 62 nm), the 10% 2-MI (311 ± 48 nm), and the 20% 2-MI (414 ± 46 nm). This trend can be attributed

to the increased conductivity of the polymer solution due to the incorporation of 2-MI that caused large increase in mass flow and thus increased the nanofiber diameters.³¹

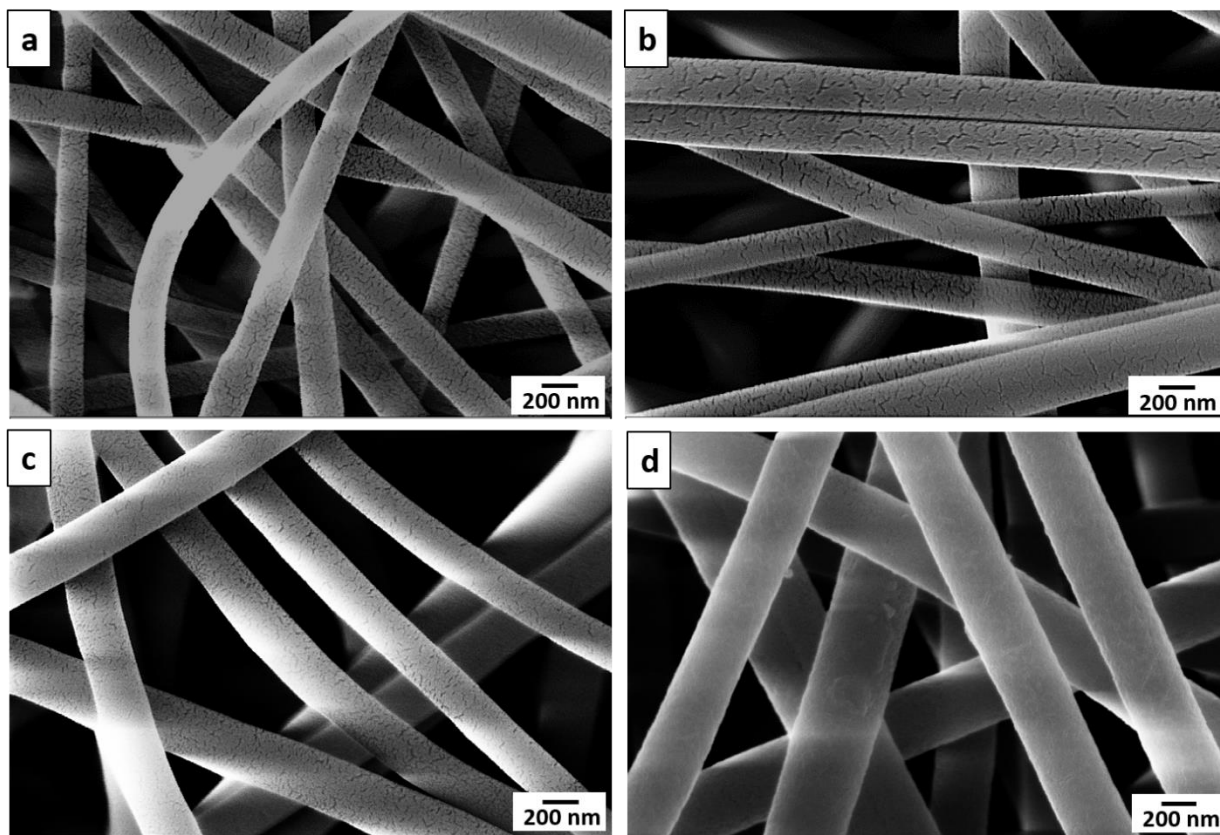


Figure 6.2. SEM images of electrospun fibers derived from (a) BL-0, (b) BL-5 (c) BL-10 and (d) BL-20.

Figure 6.3 shows carbonized and CO₂ activated fibers derived from 6FDD:PBI (50:50) with different weight percentages of 2-MI. The fibrous morphology was well-preserved. After carbonization and CO₂ activation the fiber diameters decreased due to carbon fibers reacting with the CO₂.³² The diameters of the carbon fibers were 228 ± 52 nm for the control (BL-0) and 213 ± 52 nm, 194 ± 42 nm and 183 ± 44 nm for BL-5, BL-10 and BL-20, respectively. While the addition

of 2-MI increased the diameter of fibers in the as spun mats, the carbonized fibers containing 2-MI exhibited smaller fiber diameters than the control. This may be attributed to the uniform morphology achieved by compatibilization allowing more etching with CO₂ thus a more reduced diameter of fiber (vide infra).

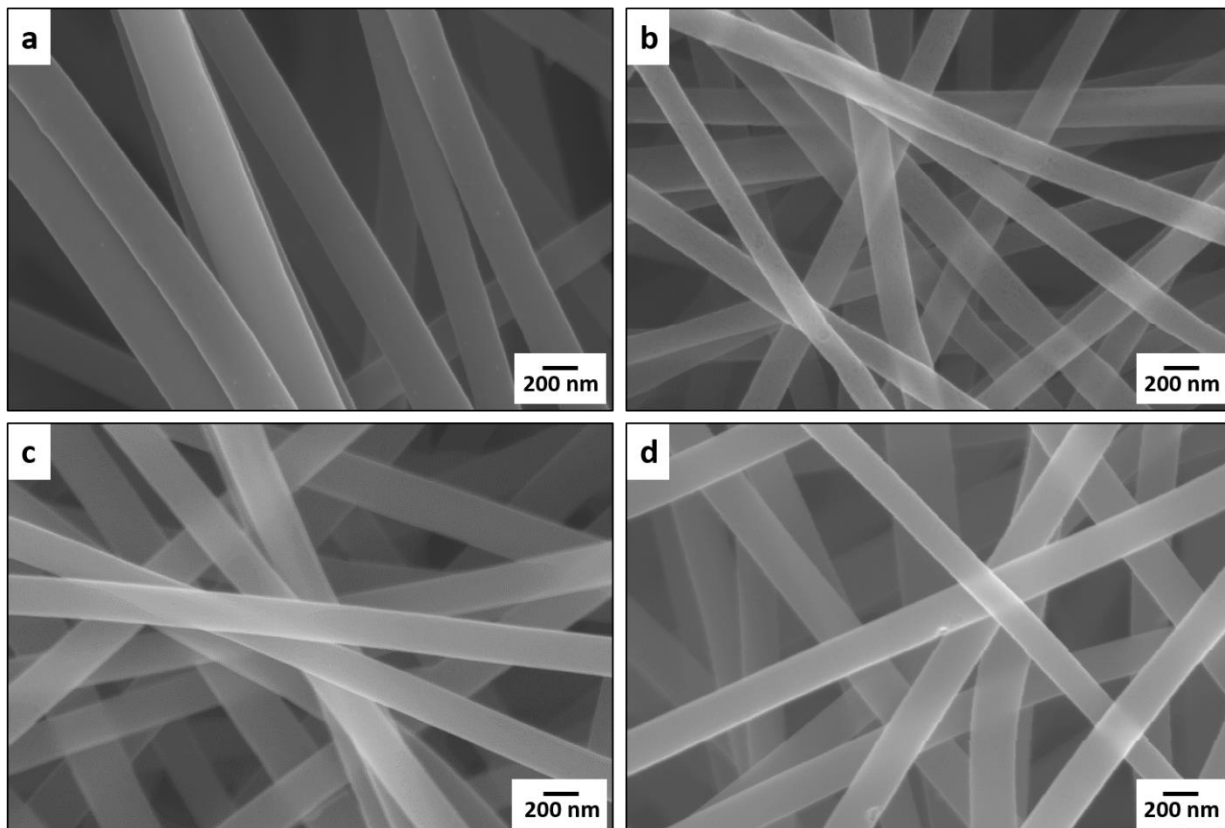


Figure 6.3. SEM images of carbonized fibers derived from (a) BL-0, (b) BL-5 (c) BL-10 and (d) BL- 20.

The microstructure of the blend membranes cast directly from the electrospinning solutions with different amounts of 2-MI are shown in Figure 6.4. All samples display the matrix-droplet morphology. In PBI:6FDD(50:50) blend, 6FDD polymer is dispersed in the continuous PBI polymer matrix and this was confirmed by selective removed of 6FDD using soxhlet extraction

with THF. Droplets of the dispersed 6FDD become very small and uniform in size with compared to pure blend with increasing loading of 2-MI. The PBI:6FDD(50:50) blend without 2-MI shows large and non-uniform 6FDD domains. Compatibilizers for two immiscible polymers work by inhibiting coalescence. Greater inhibition of coalescence is observed with increasing amount of compatibilizer.³³ Localization of 2-MI occurs at the interface during phase separation of the polymers. 2-MI forms hydrophobic and π - π interactions with PBI and hydrogen bonds with 6FDD as previously reported.²⁶ Thus 2-MI can suppress the coalescence due to its interaction with both polymer phases by lowering the interfacial energy.

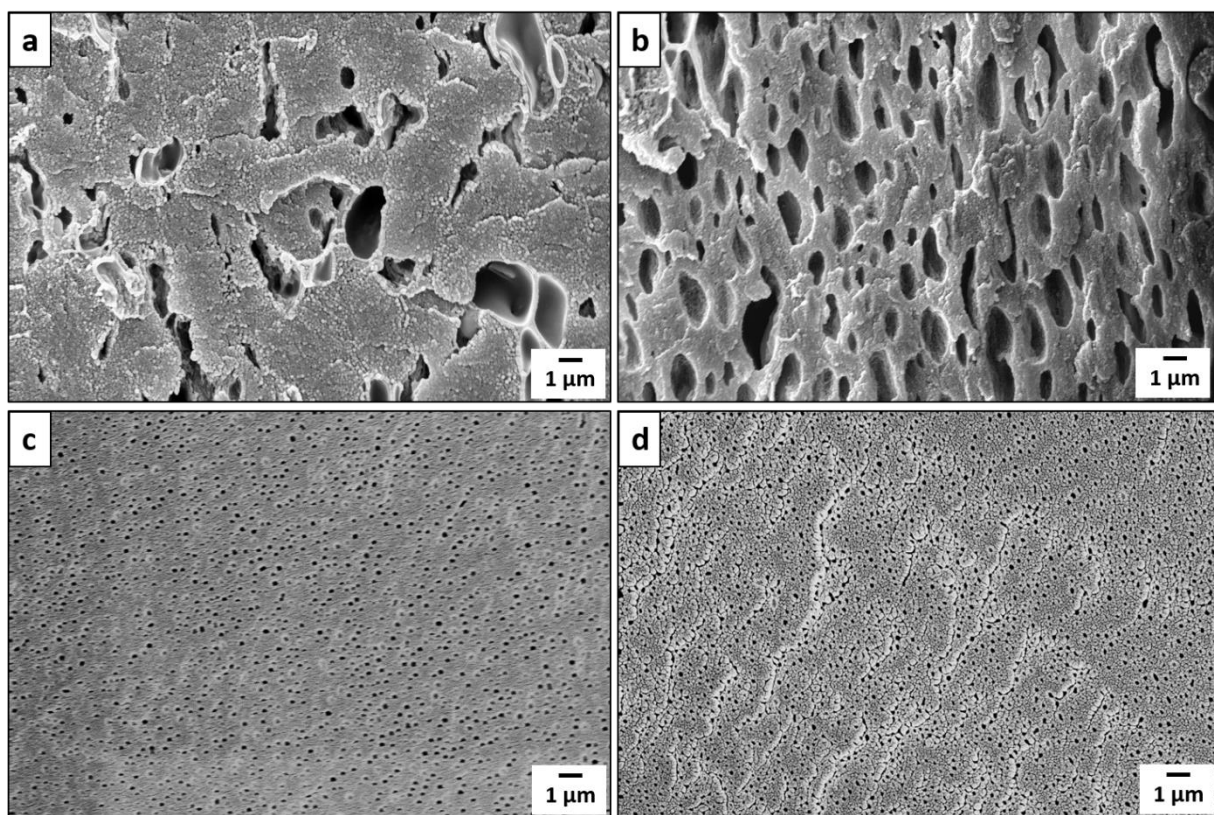


Figure 6.4. SEM images of the cross-section of the membranes cast from electrospinning solutions of PBI:6FDD blends compatibilized with (a) 0 wt% (b) 5 wt% (c) 10 wt% and (d) 20 wt% 2-MI after extraction with THF.

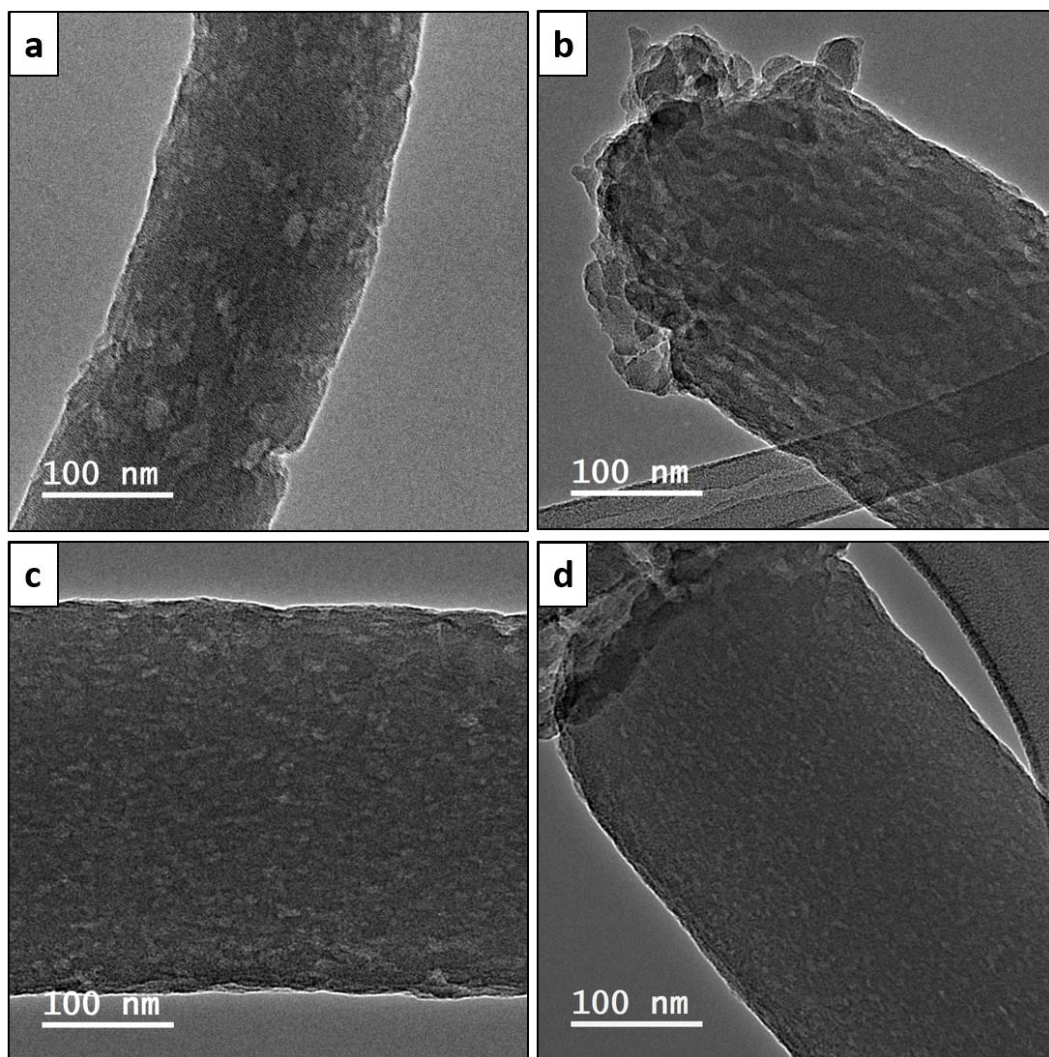


Figure 6.5. TEM images of electrospun fibers derived from (a) BL, (b) BL-5 (c) BL-10 and (d) BL-20.

We further analyzed the electrospun and carbonized fibers using TEM to ascertain the microstructure in the fibers. We observed the same trend of nanophase-separated domains in the electrospun fibers as observed by SEM images of membranes after compatibilization, but with somewhat smaller and more elongated domains resulting from electrospinning. This was surprising at first given the great time difference between solvent casting (on the order of minutes

to hours) and electrospinning which occurs within microseconds. This suggest the domains are set the electrospinning solutions. This was confirmed using DLS analysis of the electrospinning solutions prepared from blends without 2-MI and with 5wt% 2-MI. Bimodal distributions were obtained due to the polydispersity of electrospinning solutions which accounts for different size particles in a mixture. The average particle sizes obtained for the PBI:6FDD(50:50) blends without 2-MI (BL-0) were higher than the average particle sizes of compatibilized blends with 2-MI (BL-5) as shown in Figure S6.5. The Z- Average particle size obtained for the blend without 2-MI was 219.9 nm versus 87.9 nm for the compatibilized blend with 5wt% of 2-MI (Table S6.1). This indicates the small domains are already in the solution after compatibilization with 2-MI before electrospinning and are reflected in the domain sizes in the electrospun fibers. The Non uniform, larger domains of 6FDD ($176\pm149\text{ nm}^2$) were observed for the blend fibers without 2-MI (Figure 6.5(a)). A strong dependence on the size of dispersed phase (6FDD) on the fiber and the compatibilizer concentration is evident in the TEM images of the blend fibers at 5 wt %, 10 wt % and 20 wt % of 2-MI loading (Figure 6.5(b), (c) and (d)). The size of the dispersed phase become smaller and more uniform with 5 wt % of 2-MI ($80\pm17\text{ nm}^2$), which decreased even more for BL-10($65\pm17\text{ nm}^2$). At the highest concentration of 2-MI (20 wt%), the droplet size of dispersed phase in the fiber ($44\pm9\text{ nm}^2$) was dramatically reduced. Thus, the loading of 2-MI plays a critical role in obtaining smaller morphology of 6FDD domains on electrospun fibers.

TEM images of carbonized and CO₂ activated nanofibers of BL-0 and BL-20 are shown in Figure 6.6 at different magnifications. More intense, uniformly distributed white circular spots were observed for the fibers derived from the compatibilized blend (BL-20) than the blend without 2-MI, can be seen more clearly at 20 nm in Figure 6.6(d). This may be the 6FDD remaining after the

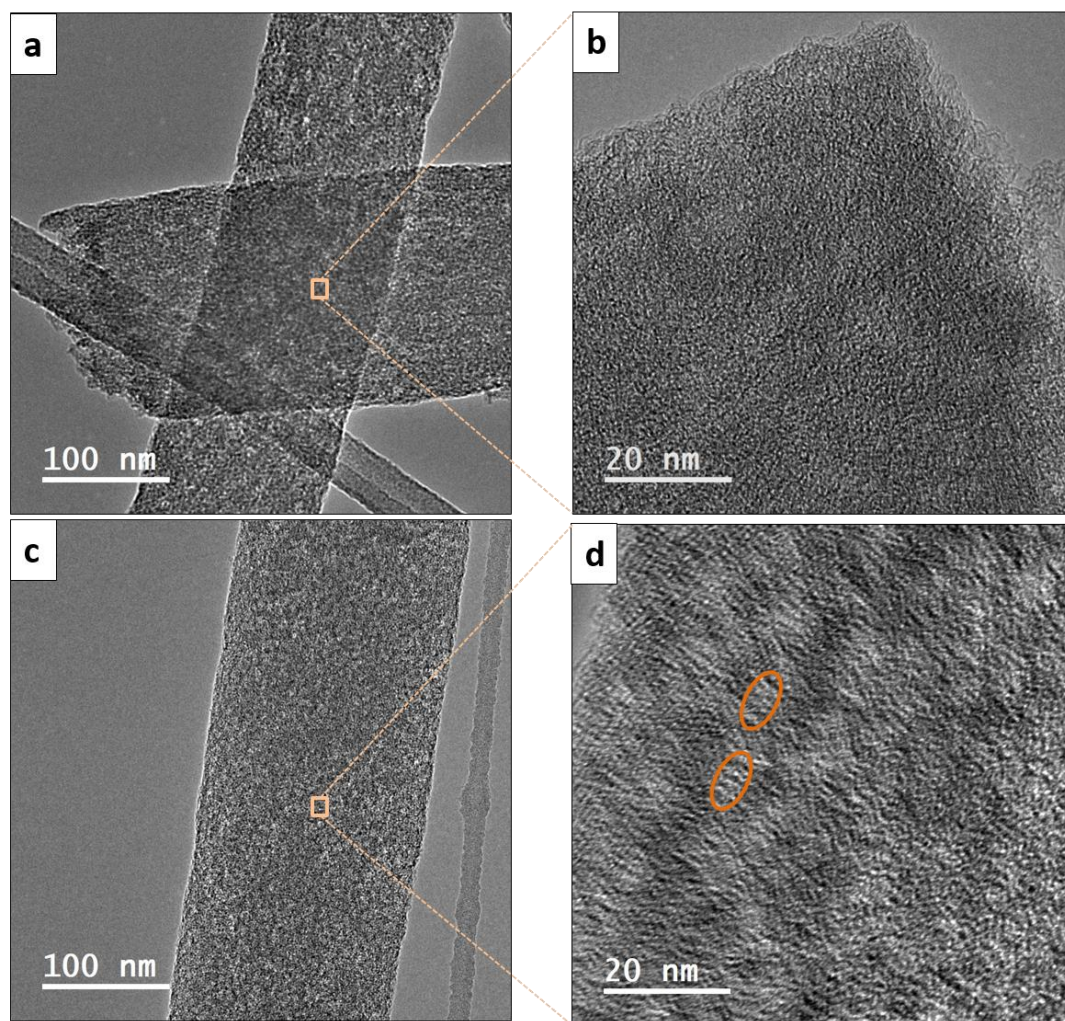


Figure 6.6. TEM images of carbonized fibers derived from BL-0 (a) 100 nm, (b) 20 nm and BL-20 (c) 100 nm, (d) 20 nm.

etching with CO_2 because the size of spots comparable to the domains sizes of 6FDD in the electrospun fibers. Because 6FDD has higher etch rates (20%) over PBI, uniform distribution of 6FDD domains in the fibers derived from compatibilized blend could result in more uniform pore sizes and distributions in the carbonized samples. Since changing the amount of compatibilizer results in different microstructures for the fibers as evident by TEM analysis, this approach could be used to obtain pore sizes optimized for access by electrolyte ions.

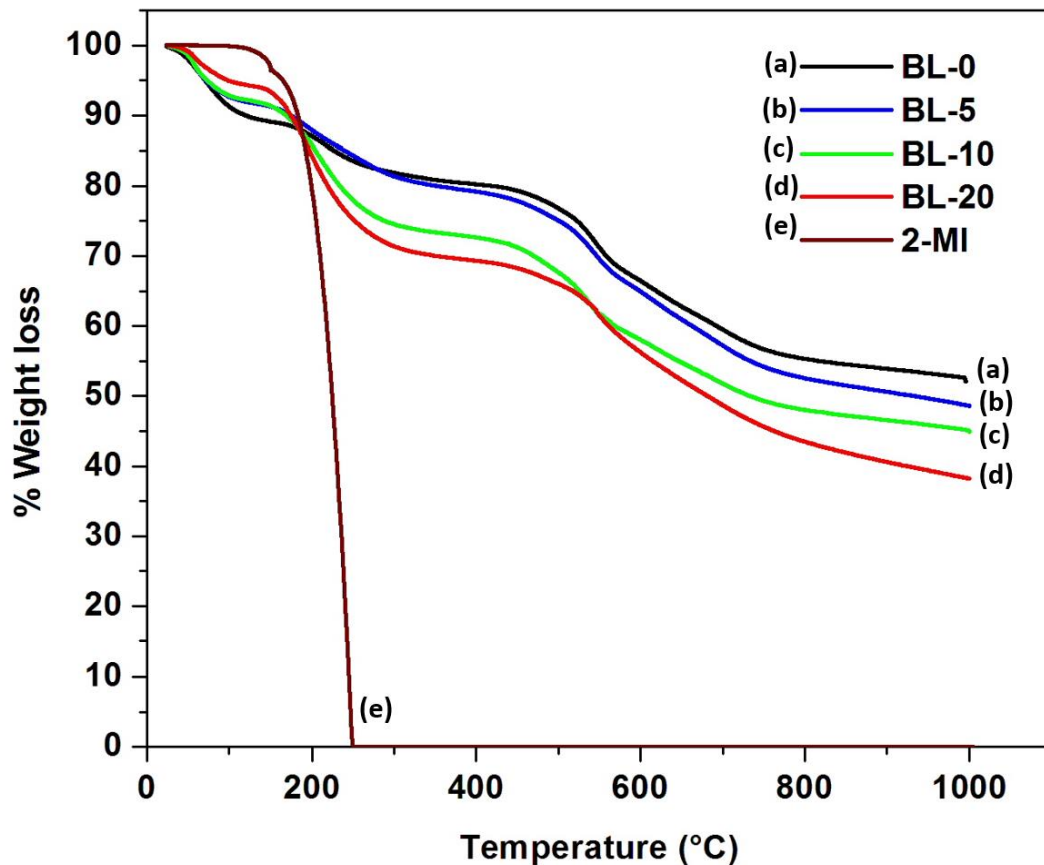


Figure 6.7. TGA curves of electrospun fibers derived from blend without 2-MI and blends compatibilized with different weight percentages of 2-MI.

The thermal decomposition of all of the samples was studied using TGA analysis (Figure 6.7) in order to confirm the presence of 2-MI in the fibers and to determine the carbon yield of PBI:6FDD with different weight percentages of 2-MI at 1000 °C. The PBI:6FDD without 2-MI showed two main stages of weight loss between 100-250 °C and 300-400 °C. The first stage was due to evaporation of residual solvent and the second stage was due to decarboxylation of DABA (weight loss ~ 3%). The 2-MI starts to evaporate at 250 °C. Therefore, samples with higher weight percentages of 2-MI had lower carbon yields. The pure blend of PBI:6FDD without 2-MI had the

highest char yield of 52.1% followed by 48.6% , 44.9% and 38.2% for BL-5, BL-10 and BL-20, respectively.

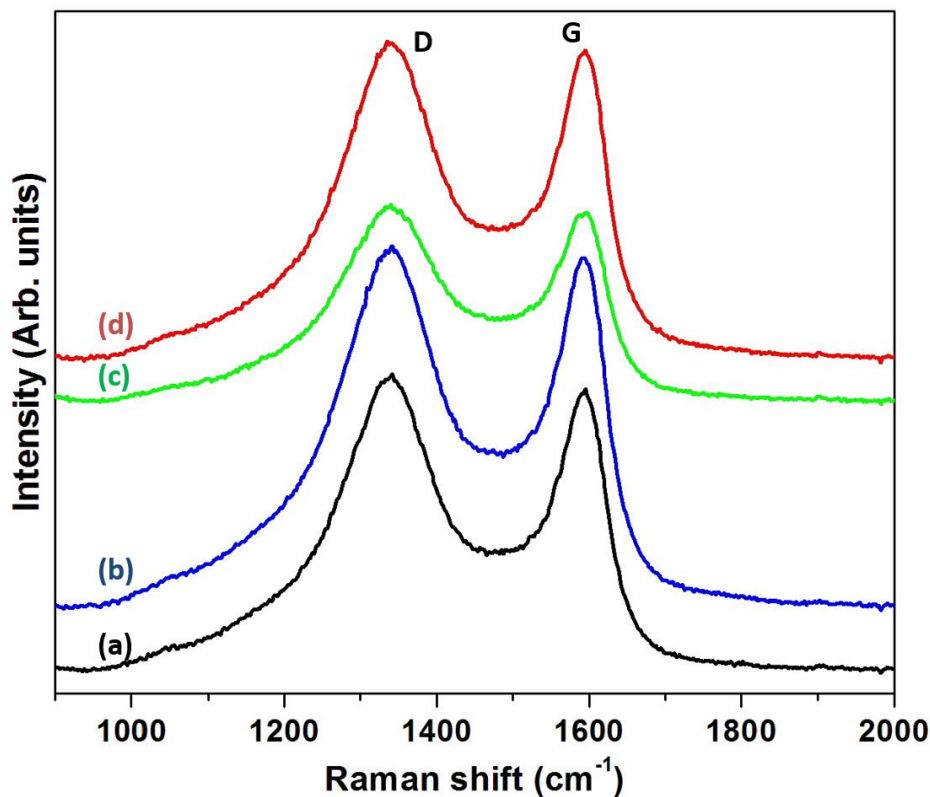


Figure 6.8. Raman spectra of ACNFs derived from (a) BL-0, (b) BL-5 (c) BL-10 and (d) BL-20.

Figure 6.8 shows the Raman spectra of PBI:6FDD containing different weight percentages of 2-MI. The spectra was used to determine the amount of graphitic carbon in activated samples. The first peak centered around 1350 cm⁻¹ contains carbonaceous and amorphous carbon and is called the D-band and the second peak centered on 1590 cm⁻¹ contains ordered, graphitic structures and is called the G-band.³⁴ The area under each of these curves were measured in order to determine the I_D/I_G ratio of each blend. These ratios calculated by peak fitting using Lorentzian equation. The

I_D/I_G ratio increased slightly after addition of 20 wt% of 2-MI compared to BL-0 but there is no significant difference observed between BL-0 and BL-5 or BL-10 (Table 6.1). Defects are possible by decomposition of 2-MI. Thus large amounts of 2-MI may an increase in amorphous carbon. Results obtained for compatibilized blends indicate that the addition of small amounts of 2-MI does not significantly increase the amount of disordered carbon.

Table 6.1. Ratios of peak intensities of ACNFs derived from blends with different ratio of 2-MI

Precursor	I_D/I_G Ratio
BL-0	2.96
BL-5	2.97
BL-10	3.01
BL-20	3.24

6.4.3 Electrochemical characterization of activated carbon nanofiber electrodes

Cyclic voltammetry (CV) curves were taken for the carbon fibers derived from the PBI:6FDD blends containing different weight percentages of 2-MI at five different scan rates between 10-100 mV between the voltage range of -2 and 2 V as shown in Figure 6.9. The electrolyte was $\text{PYR}_{14}\text{TFSI}:\text{PC}:\text{EC}(3:2:2)$ because of its high conductivity (12.5 mS cm^{-1}) and high voltage window ($\sim 5\text{V}$). All four electrodes exhibit a rectangular shaped CV as expected from a typical double layer capacitor. A box-like shape for the CV indicates good adsorption and desorption of ions on the surface of carbon electrodes without any faradic redox reactions. The rectangular shapes of the CV curves for BL-20 derived carbons were retained without distortions at higher

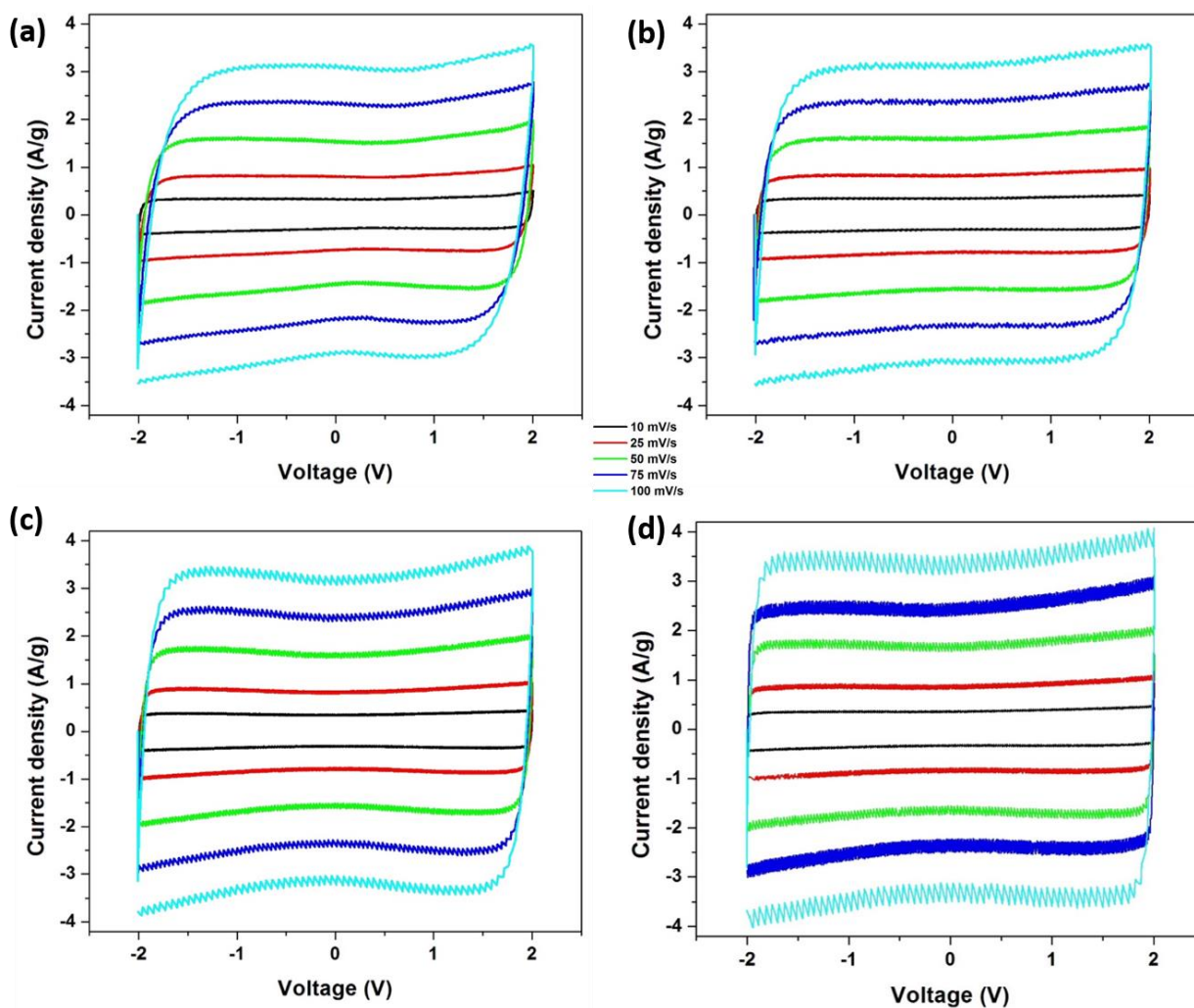


Figure 6.9. Cyclic voltammograms of ACNFs derived (a) BL-0, (b) BL-5 (c) BL-10 and (d) BL-20.

scan rate, showing fast charge transfer at the electrode/electrolyte interfaces. Figure 6.10(a) shows that specific capacitance of the ACNFs derived from the blend without 2-MI and compatibilized polymer blend with varying ratio of 2-MI at five different scan rates. It is important to note that higher specific capacitance was observed as the 2-MI was increased in each sample. Additionally, the specific capacitance did not drop upon increasing the scan rate by order of magnitude. This is an advantage since the specific capacitance typically drops at high scan rates as shown by the blend

without 2-MI (Table 6.2). BL-20 showed the highest capacitance which was followed by BL-10, BL-5, and BL-0.

Table 6.2. Specific capacitance of the ACNFs derived from blends with different ratio of 2-MI at five different scan rates

Scan rate (mV/S)	Specific capacitance (F g^{-1})			
	BL-0	BL-5	BL-10	BL-20
10	125.4	130.7	135.6	139.4
20	123.1	130.4	134.2	138.8
50	122.3	129.1	134.1	138.7
75	121.1	129.0	133.5	138.4
100	120.0	128.3	133.1	138.1

Energy densities and power densities were calculated from galvanostatic charge-discharge curves over the discharge current range of 1-10 A g^{-1} and shown in Figure 6.10(b). The results are summarized in Table 6.3. The specific energy densities for BL-0, BL-5, BL-10, and BL-20 derived carbons at 1 A g^{-1} were 61, 62, 66, and 69 Wh kg^{-1} , respectively. In general, both the power and energy densities improved with higher weight percentages of 2-MI. It is important to note the remarkable energy retention at high current densities after compatibilizing the polymer blend compared with the blend without 2-MI. The pure blend without 2-MI shows a very rapid decay in the energy density when the current density increased to 10 A g^{-1} from 1 A g^{-1} with only 77.8%

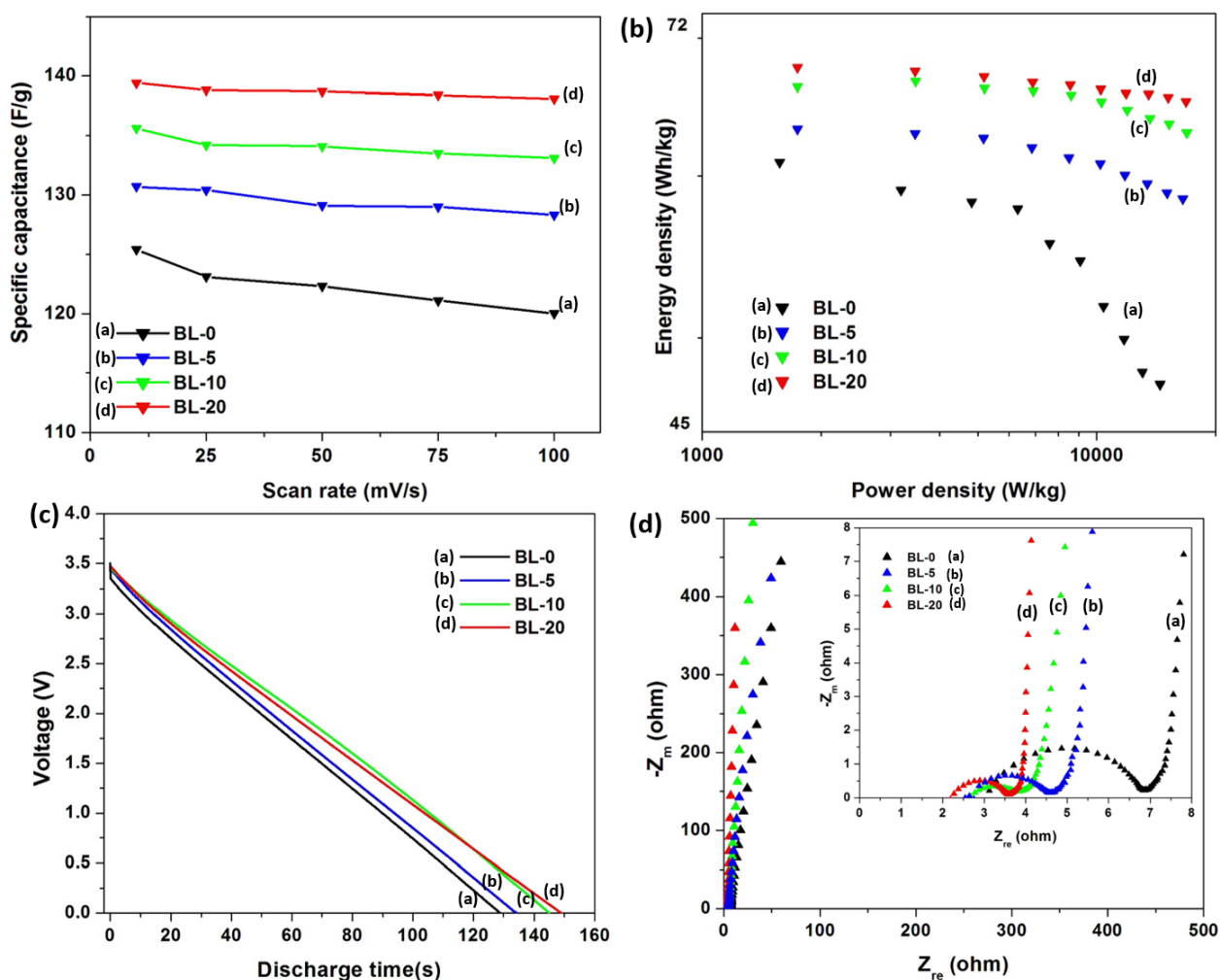


Figure 6.10. (a) Specific capacitance with five different scan rates (b) Ragone plots (c) galvanostatic discharging curves at a constant current density of 1 A g⁻¹ (d) Nyquist plot of carbonized nanofibers derived from BL with different wt% of 2-MI.

retention. The addition of the 2-MI resulted in retention of energy density with increasing current density. The blend compatibilized with 20 wt% of 2-MI showed an energy retention around 96.3% at the highest discharge currents. The blends compatibilized with 5 wt% and 10 wt% of 2-MI also showed relatively high energy retentions of 92.5% and 95.1%. In Figure 6.10(c), the galvanostatic discharge curves of carbonized and CO₂ activated PBI:6FDD nanofibers and compatibilized

PBI:6FDD with different weight percentage 2-MI are shown. The Blend compatibilized with 20 wt% of 2-MI showed the longest discharge time. Linear discharge curves with no significant IR drop were observed for the compatibilized blends. A higher IR drop was observed for the uncompatibilized blend (BL-0) compared to compatibilized blends (Table 6.3).

Table 6.3. IR drops obtained for the he ACNFs derived from blends with different ratio of 2-MI

Precursor	IR drop (V)
BL-0	0.16
BL-5	0.05
BL-10	0.04
BL-20	0.02

EIS measurements were carried out to further investigate electrochemical properties of electrodes. All plots shown in Figure 6.10(d) displayed a semicircle in the high-frequency region and a straight line in the low-frequency region. The diameter of the semicircle was assigned to the charge transfer resistance at the interface of electrode/electrolyte.³⁵ The estimated values of the semicircle diameters for compatibilized blends with 5 wt%, 10 wt% and 20 wt% were 1.87 Ω , 1.39 Ω , 1.16 Ω and 3.73 Ω for the blend without 2-MI, respectively. The lower charge transfer resistance for the carbon nanofiber electrode obtained from the 2-MI compatibilized blends compared to those derived from blend BL-0, is indication of higher conductivity and well developed pores with desired pore sizes which are accessible to electrolyte ions. The electrode derived from blend compatibilized with 2-MI exhibits the smallest value for the resistance which is in good agreement

with the CV and CDC data. The vertical line in the low frequency region is attributed to the ion diffusion into the electrode materials. Vertical lines nearly parallel to the imaginary axis are an indication of an ideal capacitive behavior.

Table 6.4. Energy densities and the power densities of the CO₂ activated fibers derived from blends with different loading of 2-MI

Current					
Density	Parameters	BL-0	BL-5	BL-10	BL-20
(A/g)					
1	Energy density (Wh/kg)	60.9	63.2	66.3	67.7
	Power density (W/kg)	1571	1740	1743	1741
10	Energy density (Wh/kg)	47.3	58.5	63.0	65.2
	Power density (W/kg)	14421	16507	16868	16800

6.5 Conclusion

A cost-effective and simple method is demonstrated to prepare highly porous and binderless carbon materials with enhanced electrochemical performance using compatibilization of phase separated polymer blend of PBI/6FDD with commercially an available small molecule 2-MI, and subsequent CO₂ activation. To our knowledge, this is the first report controlling the nanostructure of the electrospun fibers derived from an immiscible polymer blend using small molecules compatibilizers to control the porosity that can capitalize on the different CO₂ etch rates of the component polymers in the blend. With the addition of only 5 wt% 2-MI, the domain size of the

dispersed phase (6FDD) on electrospun fibers is dramatically reduced and it was further reduced by adding more 2-MI, to form different morphologies and pore distributions in the carbon nanofiber after etching with CO₂. The electrochemical performance of the electrodes improved after compatibilization. Electrodes from carbonized blends with 20 wt% of 2-MI showed a maximum specific capacitance of 139.4 F g⁻¹ at a scan rate of 1 mV s⁻¹ and energy density of 67.7 Wh kg⁻¹ at 1 A g⁻¹. Excellent energy retention of 96.3% at 10 A g⁻¹ are obtained for blends with 20 wt% of 2-MI in comparison to 77.8% retention for the carbon derived from the blend without 2-MI indicated promising results for use in stable high energy density supercapacitors. We are exploring the generality of this simple approach which often compatibilized immiscible polymer blends.

Acknowledgements

We acknowledge the National Science Foundation (Grant no. IIP-1127564) for financial support and Grant no. CHE-1126177 for the purchase of the Bruker AVANCE III™ 500 MHz NMR. We also thank Dr. Manuel Quevedo-Lopez (Department of Material Science and Engineering at The University of Texas at Dallas) for extending his Raman facility to us and Isable Pinter for help with Raman analysis.

6.6 Appendix - Supporting Information

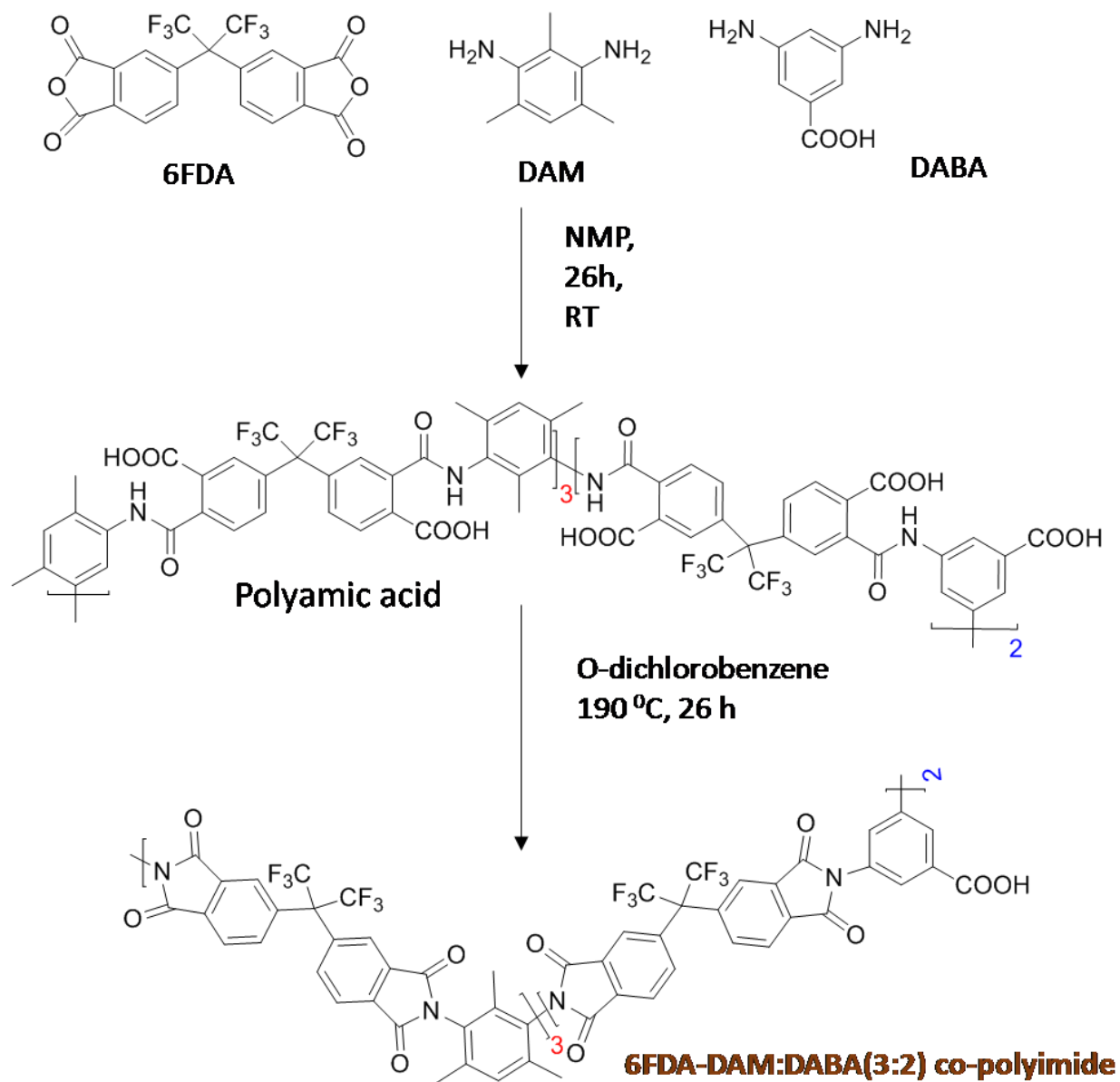


Figure S6.1. Synthesis of 6FDA-DAM:DABA(3:2).

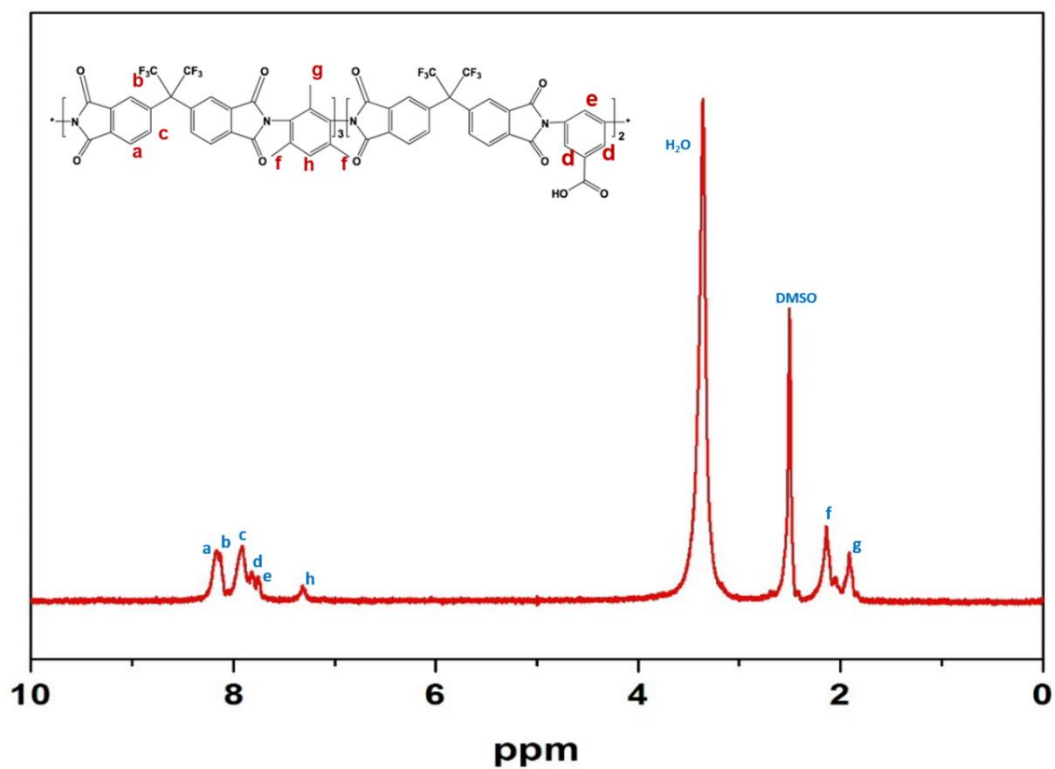


Figure S6.2. ^1H NMR spectrum of 6FDD.

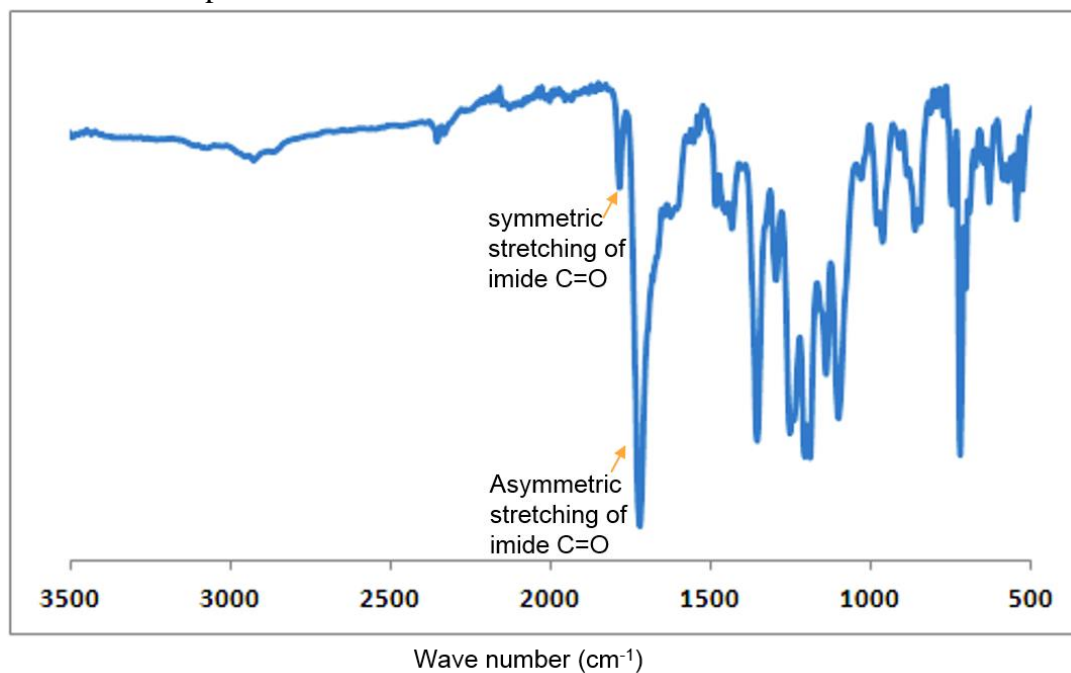


Figure S6.3. FTIR spectrum of 6FDD.

The two absorption peaks appearing at 1780 cm^{-1} and 1720 cm^{-1} in the FT-IR spectrum of 6FDD, attributed to symmetric and asymmetric stretching vibrations of the imide $\text{C}=\text{O}$, respectively, indicates complete conversion of the poly(amic acid) to the polyimide.

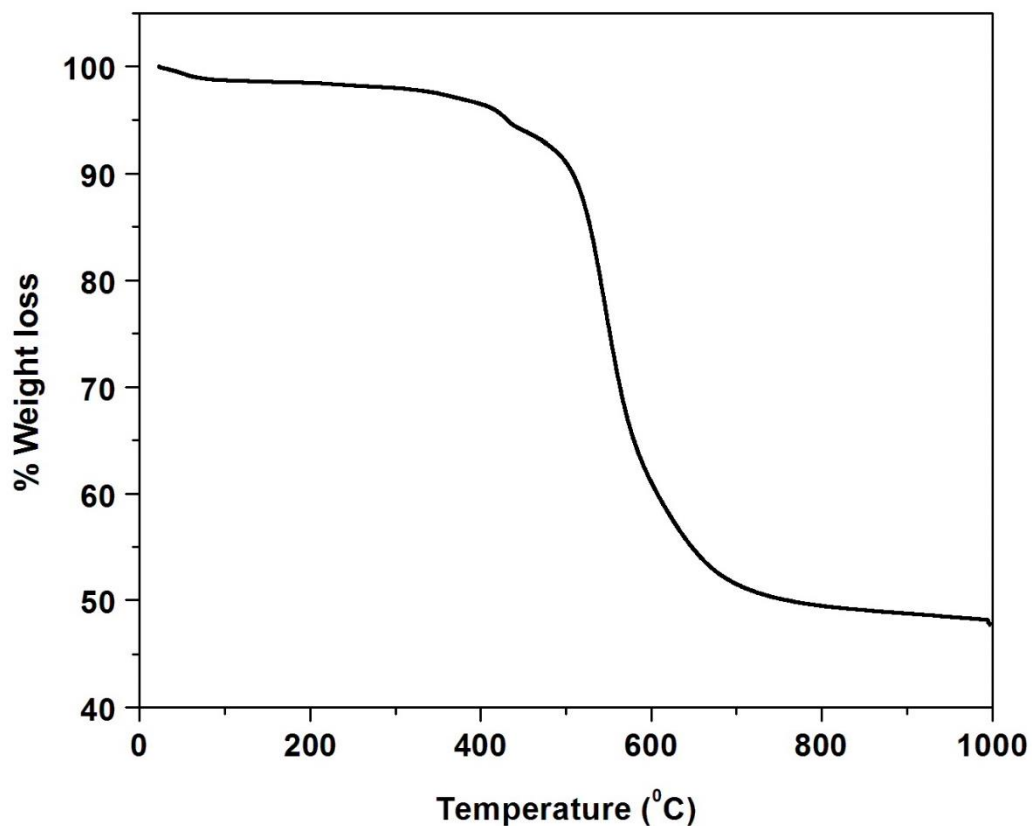


Figure S6.4. TGA curve of 6FDD.

According to the TGA 6FDD polymer is thermally stable up to $450\text{ }^{\circ}\text{C}$ and shows char yield around 47.8% at $1000\text{ }^{\circ}\text{C}$. The carbon yields for PBI at $1000\text{ }^{\circ}\text{C}$ was 58.2%.

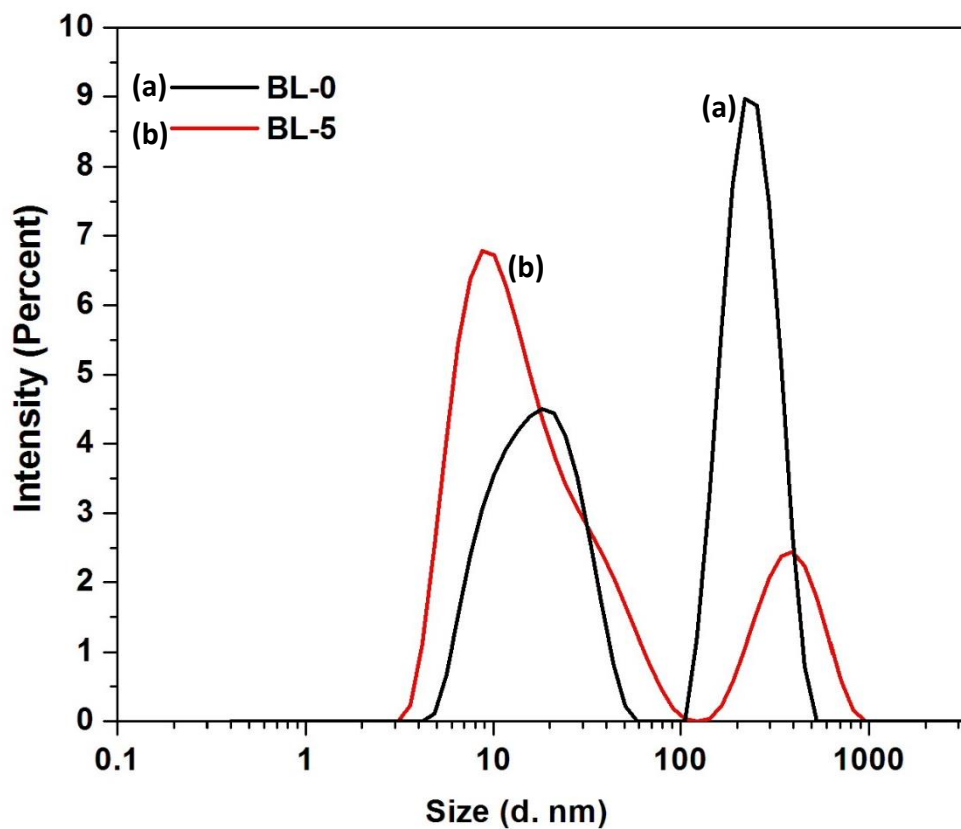


Figure S6.5. Size distribution by intensity of BL-0 and BL-5 using DLS analysis.

Table S6.1. Z- Average particle size obtained from DLS analysis

			Size (d. nm)	% Intensity	St. Dev (d. nm)
BL-0	Z-Average (d.nm) = 219.9	Peak 1	16.30	45.8	6.48
	PDI = 0.25	Peak 2	243.6	51.8	74.3
BL-5	Z-Average (d.nm) = 87.98	Peak 1	17.08	74.2	12.63
	PDI = 0.21	Peak 2	445.3	18.9	154.2

6.7 References

- (1) Shukla, A. K.; Banerjee, A.; Ravikumar, M. K.; Jalajakshi, A. Electrochimica Acta Electrochemical Capacitors : Technical Challenges and Prognosis for Future Markets. *Electrochim. Acta* **2012**, *84*, 165–173.
- (2) Conway, B. Transition from “Supercapacitor” to “Battery” Behavior in Electrochemical Energy Storage. *J. Electrochem. Soc.* **1991**, *138* (6), 1539–1548.
- (3) Mombeshora, E. T.; Nyamori, V. O. A Review on the Use of Carbon Nanostructured Materials in Electrochemical Capacitors. *Int. J. Energy Res.* **2015**, *39*, 1955–1980.
- (4) Burke, A. Ultracapacitor; Why, and Where Is the Technology. *J. Power Sources* **2000**, *91*, 37–50.
- (5) Pohlmann, S.; Lobato, B.; Centeno, T. a; Balducci, A. The Influence of Pore Size and Surface Area of Activated Carbons on the Performance of Ionic Liquid Based Supercapacitors. *Phys. Chem. Chem. Phys.* **2013**, *15* (40), 17287–17294.
- (6) Largeot, C.; Portet, C.; Chmiola, J.; Taberna, P.; Gogotsi, Y.; Simon, P. Relation between the Ion Size and Pore Size for an Electric Double-Layer Capacitor. *J. Am. Chem. Soc.* **2008**, *130*, 2730–2731.
- (7) Wang, Q.; Yan, J.; Fan, Z. Carbon Materials for High Volumetric Performance Supercapacitors: Design, Progress, Challenges and Opportunities. *Energy Environ. Sci.* **2016**, *9*, 729–762.
- (8) Hulicova, D.; Oya, A. The Polymer Blend Technique as a Method for Designing Fine Carbon Materials. *Carbon N. Y.* **2003**, *41* (7), 1443–1450.
- (9) Koning, C.; Duin M.V; Pagnouille, C.; Jerome R. Strategies for Compatibilization of Polymer Blends. *Prog. Polym. Sci.* **1998**, *23* (97), 707–757.
- (10) Kar, G. P.; Biswas, S.; Bose, S. Tailoring the Interface of an Immiscible Polymer Blend by a Mutually Miscible Homopolymer Grafted onto Graphene Oxide : Outstanding. *Phys. Chem. Chem. Phys.* **2014**, *17*, 1811–1821.
- (11) Abeykoon, N. C.; Bonso, J. S.; Ferraris, J. P. Supercapacitor Performance of Carbon Nanofiber Electrodes Derived from Immiscible PAN/PMMA Polymer Blends. *RSC Adv.* **2015**, *5* (26), 19865–19873.
- (12) Jung, K.-H.; Ferraris, J. P. Preparation of Porous Carbon Nanofibers Derived from PBI/PLLA for Supercapacitor Electrodes. *Nanotechnology* **2016**, *27* (42), 425708.

- (13) Braun, D.; Fischer, M.; Hellmann, G. P. Block-Graft Copolymers as Compatibilizers in Polymer Blends. *Polymer (Guildf)* **1996**, *37* (17), 3871–3877.
- (14) Xu, Y.; Thurber, C. M.; Lodge, T. P.; Hillmyer, M. A. Synthesis and Remarkable Efficacy of Model Polyethylene-graft- Poly(methyl Methacrylate) Copolymers as Compatibilizers in Polyethylene/Poly(methyl Methacrylate) Blends. *Macromolecules* **2012**, *45*, 9604–9610.
- (15) Schmalz, H.; Müller, A. H. E.; Bahrami, R.; Tina, I. L. Micromechanics of “ Raspberry ” Morphology in PPE / SAN Polymer Blends Compatibilized with Linear ABC Triblock Terpolymers. *Polymer (Guildf)* **2015**, *80*, 52–63.
- (16) Mickiewicz, R. A.; Ntoukas, E.; Avgeropoulos, A.; Thomas, E. L. Phase Behavior of Binary Blends of High Molecular Weight Diblock Copolymers with a Low Molecular Weight Triblock. *Macromolecules* **2008**, *41*, 5785–5792.
- (17) Zhang, W.; Lin, M.; Winesett, A.; Dhez, O.; Kilcoyne, A. L. D.; Ade, H.; Rubinstein, M.; Shafi, K. V. P. M.; Ulman, A.; Gersappe, D.; Tenne, Rafailovich, R. M.; Sokolova, J.; Frisch, H. L. The Use of Functionalized Nanoparticles as Non-Specific Compatibilizers for Polymer Blends. *Polym. Adv. Technol.* **2011**, *22*, 65–71.
- (18) Kwon, T.; Kim, T.; Ali, F.; Kang, D. J.; Yoo, M.; Bang, J.; Lee, W.; Kim, B. J. Size-Controlled Polymer-Coated Nanoparticles as Efficient Compatibilizers for Polymer Blends. *Macromolecules* **2011**, *44*, 9852–9862.
- (19) Cao, Y.; Zhang, J.; Feng, J.; Wu, P. Compatibilization of Immiscible Polymer Blends Using Graphene Oxide Sheets. *Acs nano*, **2011**, *7*, 5920–5927.
- (20) Rafailovich, M.; Sokolov, J.; Zhu, S.; Brook, S.; Chu, B. Compatibilizer for Immiscible Polymer Blends. **2002**, *1* (12), US patent 6,339,121 B1.
- (21) Abdellah A.; Utracki, L. A. Interphase and Compatibilization of Polymer Blends. *Polym. Eng. Sci.* **1996**, *3* (12), 1574-1585.
- (22) Sinha, S.; Pouliot, S.; Bousmina, M.; Utracki, L. A. Role of Organically Modified Layered Silicate as an Active Interfacial Modifier in Immiscible Polystyrene / Polypropylene Blends. *Polymer (Guildf)* **2004**, *45*, 8403–8413.
- (23) Yuan, K.; Chen, Y. Nanostructuring Compatibilizers of Block Copolymers for Organic Photovoltaics. *Polym Int.* **2014**, *63*, 593–606.
- (24) Li, Y.; Shimizu, H. Compatibilization by Homopolymer : Significant Improvements in the Modulus and Tensile Strength of PPC / PMMA Blends by the Addition of a Small Amount of PVAc. *ACS Appl. Mater. Interfaces* **2009**, *1* (8), 1650-1655.

- (25) Wang, H.; Dong, W.; Li, Y. Compatibilization of Immiscible Polymer Blends Using in Situ Formed Janus Nanomicelles by Reactive Blending. *ACS Macro Lett.* **2015**, *4*, 1398–1403.
- (26) Panapitiya, N. P.; Wijenayake, S. N.; Nguyen, D. D.; Huang, Y.; Musselman, I. H.; Balkus, K. J.; Ferraris, J. P. Gas Separation Membranes Derived from High-Performance Immiscible Polymer Blends Compatibilized with Small Molecules. *ACS Appl. Mater. Interfaces* **2015**, *7* (33), 18618–18627.
- (27) Zhao, X.; Luo, J.; Xiong, J. Investigation of polylactide/poly(3-Caprolactone)/ Multi-Walled Carbon Nanotubes Electrospun Nanofibers with Surface Texture. *RSC Adv.* **2015**, *5*, 99179–99187.
- (28) Kim, C. Electrochemical Characterization of Electrospun Activated Carbon Nanofibres as an Electrode in Supercapacitors. *J. Power Sources* **2005**, *142* (1–2), 382–388.
- (29) Qiu, W.; Xu, L.; Chen, C.-C.; Paul, D. R.; Koros, W. J. Gas Separation Performance of 6FDA-Based Polyimides with Different Chemical Structures. *Polymer (Guildf)*. **2013**, *54* (22), 6226–6235.
- (30) Omole, I. C.; Miller, S. J.; Koros, W. J. Increased Molecular Weight of a Cross-Linkable Polyimide for Spinning Plasticization Resistant Hollow Fiber Membranes. *Macromolecules* **2008**, *41* (17), 6367–6375.
- (31) Mit-uppatham, C.; Nithitanakul, M.; Supaphol, P. Ultrafine Electrospun Polyamide-6 Fibers: Effect of Solution Conditions on Morphology and Average Fiber Diameter. *Macromol. Chem. Phys.* **2004**, *6*, 2327–2338.
- (32) Xue, R.; Yan, J.; Liu, X. Effect of Activation on the Carbon Fibers from Phenol – Formaldehyde Resins for Electrochemical Supercapacitors. *J Appl Electrochem.* **2011**, *41*, 1357–1366.
- (33) Puyvelde, P. V.; Velankar, S.; Moldenaers, P. Rheology and Morphology of Compatibilized Polymer Blends. *Curr. Opin. Colloid Interface Sci.* **2001**, *6*, 457–463.
- (34) Ferrari, A. C.; Basko, D. M. Raman Spectroscopy as a Versatile Tool for Studying the Properties of Graphene. *Nat. Publ. Gr.* **2013**, *8* (4), 235–246.
- (35) Fan, L.; Yang, L.; Ni, X.; Han, J.; Guo, R.; John, C. Nitrogen-Enriched Meso-Macroporous Carbon Fiber Network as a Binder-Free Flexible Electrode for Supercapacitors. *Carbon N. Y.* **2016**, *107*, 629–637.

BIOGRAPHICAL SKETCH

Nimali Chathurika Abeykoon was born in 1985 in Kandy, Sri Lanka. She obtained her Bachelor's degree in Chemistry from University of Peradeniya, Sri Lanka in 2010. Then she entered The University of Texas at Dallas in fall 2012 to pursue a Doctor of Philosophy Degree in Chemistry. In 2013 she started working under the supervision of Dr. John P. Ferraris. Her research was focused on "Supercapacitor electrode materials from highly porous carbon nanofibers with tailored pore distributions".

CURRICULUM VITAE

Nimali C. Abeykoon

EXPERTISE

Synthetic Skills:

- Multistep organic synthesis: Experimental design
- Synthesizing and characterizing novel polymeric materials for polymer supercapacitors and Li-ion batteries
- Expert in synthesis of metal oxides, nanoparticles, carbon nanofibers, and CVD synthesis of carbon nanotubes

Characterization/ Devices:

- Fabrication and characterization of battery cells
- Hands-on experience using battery test instruments and software (Arbin, Potentiostat/Galvanostat) and electrochemical measurements including EIS, CV and cycling measurements /charge discharge
- Materials Characterization techniques (SEM/EDX, XRD, FT-IR, Raman spectroscopy, TGA, DSC, NMR, UV/Vis, HPLC, ICP-MS, GC-MS, Fluorescence and surface area analysis) including interpreting and analyzing data
- Proficient in Origin Pro, Bruker topspin, Image J, Microsoft Office, SciFinder

EDUCATION

PhD in Chemistry, University of Texas at Dallas (UTD), USA

2012-2017

Title: Supercapacitor electrode materials from highly porous carbon nanofibers with tailored pore distributions

Advisor: Dr. John P. Ferraris

B.Sc. in Chemistry, University of Peradeniya, Sri Lanka

2006-2010

Title: Investigation of atmospheric pollution through precipitation studies at Peradeniya

Advisor: Dr. H. N. D Namal Priyantha

RESEARCH EXPERIENCE

PhD, University of Texas at Dallas

2012-2017

Project I : Supercapacitor performance of carbon nanofiber electrodes derived from immiscible PAN/PMMA polymer blends

Project II : High surface area carbon nanofibers from incompatible polymer blends of PBI/ 6FDA-DAM:DABA as binder-free electrode materials for supercapacitors

Project III : Immiscible PBI/ 6FDA-DAM:DABA polymer blends compatibilized with small molecules for supercapacitor applications

Project IV : Electrospun poly(acrylonitrile-*co*-itaconic acid) as porous carbon precursor for high performance supercapacitors: Study of in-situ porogen activity of itaconic acid in copolymers

Project V : High surface area carbon nanofiber electrodes derived from an in-situ porogen containing terpolymer: P(AN-VIM-IA)

Project VI : Carbon nanofibers with nanostructured MnO₂ and SnO₂ for high performance supercapacitors

Project VII : Carbon nanofibers functionalized with heteropolyacids as an electrode materials for supercapacitor

Project VIII : Supercapacitor performance of carbon nanofibers prepared from PBI with colloidal ZIF-8

Project IX : Perylene-Polyether Block Polyimides as Redox Active Electrode Materials for High Performing Lithium-Organic Batteries

OTHER SKILLS

Research mentoring for undergraduate and high school students

TEACHING EXPERIENCE

Graduate Teaching Assistant, University of Texas at Dallas

2012-2017

- Graduate teaching assistant for Introduction to Organic chemistry Lab I and Lab II, Instrumental analysis Lab, General chemistry Lab II, General chemistry I (Lecturing & Grading) –Three semesters for each lab

Graduate Teaching Assistant, The Open University of Sri Lanka, Sri Lanka **2011-2012**

- Graduate teaching assistant for Organic chemistry, Physical chemistry, Inorganic chemistry and Analytical chemistry
- Conducted lectures and supervision of assessment tests and final examinations

Graduate Teaching Assistant, University of Peradeniya, Sri Lanka **2010-2011**

- Graduate teaching assistant for Organic chemistry and Inorganic chemistry

PUBLICATIONS

- (1) **Abeykoon, N. C.**; Bonso, J. S.; Ferraris, J. P.; Supercapacitor performance of carbon nanofiber electrodes derived from immiscible PAN/ PMMA polymer blends, *RSC Adv.*, **2015**, 5, 19865–19873.
- (2) **Abeykoon, N.C.**; Garcia, V.; Jayawickramage, R. A.; Perera W.; Balkus, K.J.; Ferraris, J.P.; Novel binder-free electrode materials for supercapacitors utilizing high surface area carbon nanofibers derived from immiscible polymer blends of PBI/6FDA-DAM:DABA, *RSC Adv.*, **2017**, 7, 20947–20959.
- (3) **Abeykoon, N.C.**; Mahmood, S.F.; Ferraris, J. P., Electrospun poly(acrylonitrile-*co*-itaconic acid) as porous carbon precursor for high performance supercapacitor: study of insitu porogen activity of itaconic acid in copolymer, *Preprints-American Chemical Society, Division of Energy & Fuels*, **2016**, 61(2), 134-136.

PRESENTATIONS

- (1) **Abeykoon, N.C.**; Garcia, V.; Balkus, K.J.; Ferraris, J.P.; High surface area carbon nanofibers from incompatible polymer blends of PBI/ 6FDA-DAM:DABA as binder-free electrode materials for supercapacitors, **ACS Southwest Regional Meeting**, Galveston, TX, November 10-13, **2016**.
- (2) **Abeykoon, N.C.**; Mahmood, S.F.; Ferraris, J.P.; Electrospun poly(acrylonitrile-*co*-itaconic acid) as porous carbon precursor for high performance supercapacitor: Study of in-situ porogen activity of itaconic acid in copolymer, **252nd ACS National Meeting & Exposition**, Philadelphia, PA, United States, August 21-25, **2016**.

- (3) **Abeykoon, N.C.**; Mahmood, S.F.; Ferraris, J.P.; High surface area carbon nanofiber electrodes derived from an in situ porogen containing terpolymer: P(AN-VIM-IA), **49th ACS DFW Meeting in Miniature**, Denton, Texas, April 25, **2016**.
- (4) Ferraris, J.P.; **Abeykoon, N.C.**; Bonso, J.S.; Mahmood, S.F.; High surface area carbon nanofiber supercapacitor electrodes derived from an in-situ porogen containing terpolymer:P(AN-VIM-IA), **251st ACS National Meeting & Exposition**, San Diego, CA, United States, March 13-17, **2016**.
- (5) **Abeykoon, N.C.**; Sanchez, E.; Bonso, J.S.; Ferraris, J.P.; High surface area carbon nanofiber electrodes derived from an in-situ porogen containing copolymer: Poly(acrylonitrile-*co*-itaconic acid), **48th ACS DFW Meeting in Miniature**, Arlington, Texas, April 25, **2015**.
- (6) Ferraris, J.P.; **Abeykoon, N.C.**; Bonso, J.S.; Perananthan, S.; High energy density supercapacitors utilizing carbon nanofibers derived from electrospun porogencontaining polyacrylonitrile, **247th ACS National Meeting & Exposition**, Dallas, TX, United States, March, 16-20, **2014**.
- (7) **Abeykoon, N.C.**; Ferraris, J.P.; Preparation of porous carbon nanofiber material from PAN /PMMA polymer blend for supercapacitor application, **247th ACS National Meeting & Exposition**, Dallas, TX, United States, March 16-20, **2014**.
- (8) **Abeykoon, N.C.**; Bonso, J.S.; Ferraris, J.P.; Supercapacitor performance of carbon nanofiber derived from immiscible PAN/PMMA polymer blends, **47th ACS DFW Meeting in Miniature**, Fort Worth, Texas, April 26, **2014**.
- (9) Khong, M.; **Abeykoon, N.C.**; Chaturvedi, S.; Ferraris, J.P.; Supercapacitor performance of carbon nanofibers prepared from PBI with colloidal ZIF-8 , **47th ACS DFW Meeting in Miniature**, Fort Worth, Texas, April 26, **2014**.
- (10) **Abeykoon, N.C.**; Wijenayake S.N; Bonso, J.S.; Ferraris, J.P.; Supercapacitor performance of carbon nanofiber prepared by selective removal of one polymer phase from blends of immiscible polymers, **46th ACS DFW Meeting in Miniature**, Commerce, Texas, April 27, **2013**.

LANGUAGES

English and Sinhalese

AWARDS AND HONORS

Chemistry Department Travel Award	2016
UTD Graduate Studies Scholarship	2012-2017
Second Class Upper Honors, BSc, University of Peradeniya	2010

PROFESSIONAL MEMBERSHIPS

Member, American Chemical Society	2014-present
-----------------------------------	--------------